Towards an understanding of high strength metastable β titanium alloy machinability

Alex Graves

Department of Materials Science and Engineering

The University of Sheffield

Thesis submitted for the degree of Doctor of Engineering

September 2021

Abstract

Metastable β titanium alloys are used within the aerospace industry due to their high strength, fracture toughness, hardenability and low density. Utilisation of these alloys is expensive due to their poor machinability. To improve the machinability cutting tool wear and machined surface quality must be better understood. To this end, drilling, turning and orthogonal cutting studies have been conducted on the metastable β titanium alloy, Ti-5Al-5Mo-5V-3Cr. The titanium alloys; Ti-6Al-4V, Ti-6Al-2Sn-4Zr-6Mo and Ti-5Al-2Sn-2Zr-4Cr-4Mo were also investigated to provide comparability. Emphasis was placed on; 1) Characterising microstructural deformation in the workpiece. 2) Analysing force and torque response. 3) Assessing machined surface quality. 4) Understanding how the chemical interaction between titanium and WC-Co influences crater wear. In this work, a novel surface response methodology enabled subsurface damage to be characterised for multiple alloys, the results showed how subsurface damage depth decreased with increasing alloy strength and how the depth varied for PVD-TiAlN coated and uncoated tools. Uncoated tools resulted in a more efficient cutting process compared to coated tools at the start of drilling: but as the tools started to wear, the efficiency of uncoated tools decreased, while the efficiency of coated tools increased. Built up edge (BUE) was prominent in Ti-5Al-5Mo-5V-3Cr machining, resulting in poor machined surface quality and reducing process stability. Analysis of Ti-5Al-5Mo-5V-3Cr and WC-Co interfaces using transmission electron microscopy showed that during crater wear Co diffused rapidly from the tool substrate once titanium had adhered and this was followed by decarburisation and subsequent breakdown of the WC. The methods developed in this thesis can help speed up the tool-design process efficiency while the knowledge can help tool designers to make intelligent design decisions for tools used to machine titanium alloys, both of which can contribute to improving the cost effectiveness of using metastable β alloys within industry.

Contents

Preface

Submitted for the degree of Doctor in Engineering at the University of Sheffield, this thesis describes the research carried out in three locations: (1) the Depeartment of Materials science and Engineering under the supervison of Prof Martin Jackson, (2) the Advanced Manufacturing Research Centre (AMRC) under the supervison of Dr Pete Crawforth and (3), at various Sandvik Coromant sites in the UK and Sweden under the supervison of Prof Susanne Norgren.

Sections of this thesis have been published in the following research papers:

A. Graves, S. Norgren, P. Crawforth, and M. Jackson, "A novel method for investigating drilling machinability of titanium alloys using velocity force maps," Adv. Ind. Manuf. Eng., vol. 2, no. September 2020, p. 100043, 2021. (Chapter 5)

A. Graves, W. Wan, S. Singh, M. Kritikos, C. Xiao, S. Norgren, P. Crawforth, and M. Jackson "On the mechanism of crater wear in a high strength metastable beta titanium alloy," Wear, vol. 484–485, no. March, p. 203998, 2021. (Chapter 7)

A. Graves, S. Norgren, P. Crawforth, and M. Jackson, "Surface roughness response to drilling of Ti-5Al-5Mo-5V-3Cr using Ti-Al-N coated and uncoated WC/Co tools," Procedia CIRP, vol. 87, pp. 170–175, 2020. (Chapter 6)

A. Graves, M. Teike, S. Norgren, P. Crawforth, and M. Jackson, "The effect of Titanium Alloy Composition and Tool Coating on Drilling Machinability," World Conference on Titanium (Ti-2019), MATEC Web Conf., vol. 321, p. 13002, 2020. (Chapter 4 and 5)

Acknowledgments

It is difficult to put into words how the guidance, time and attention of my supervisors; Martin Jackson, Pete Crawforth and Susanne Norgren, has helped me in this journey. They are the best supervisors I could have ever hoped for. Their continual contribution to my growth and development has been invaluable for my work and my future.

I would like to thank the staff at the AMRC, University of Sheffield and Sandvik Coromant who I have worked with over the last four years. I am especially thankful to Raphael Royer for all his time, support and advice. I am also extremely grateful to everyone in the IDC, D1 and at Sandvik Coromant, who have enriched my experience throughout my time as a postgraduate.

This doctorate would have been a different experience for me without the close support of my childhood friends, they know who they are! For those who I have shared the journey with; Joseph Pinchbeck, Jack Rooke and Lewis Blackburn: I hope their doctorates have been fulfilling and that I have contributed to their experience, as much as they have to mine!

It goes without saying that the last 4 years would have been a lonely road without my other half, Zoe Ku. She has supported me in all the ways that matter, blunting all those hard edges that came at along the way, and alleviating those inescapable stresses we all feel from time to time. For this, she will always have a place in my heart.

I truly appreciate the love and memories that my sisters, Teresa and Yvonne, have shared with me over the last 4 years; they have helped more than they know along the way.

Finally, I need to thank my parents, whose patience, generosity and kindness knows no bounds. It would have been impossible without them. Anita and Jon, I dedicate this thesis to you.

List of Figures

List of Tables

Nomenclature

α	Hexagonal close packed alpha phase
β	Body centered cubic beta phase
η	Friction angle
λ_n	Cutting edge angle
μ_T	Friction coefficient
Ψ	Rake angle
σ_0	Normal stress
φ	Shear angle
a_p	Depth of cut
ASP	Arbitary strain path
bcc	Body centered cubic
BUE	Built up edge
CFD	Chip flow direction
CMM	Coordinate measuring machine
CNC	Computer numerical control
CVD	Chemical vapour deposition
CW	Crater wear
DC	Cutting diameter
EDM	Electronic discharge machining

EDP	Electron diffraction pattern
EDS	Energy dispersive spectroscopy
$EELS$	Electron energy loss spectroscopy
$EMPA$	Electron microprobe analyser
$ER, \Delta R$	Edge rounding
F_α	Resultant thrust force
F_η	Normal shear force
F_c	Cutting force
F_s	Shear force
F_{rev}	Feed rate in mm per rev
fcc	Face centered cubic
FIB	Focused ion beam
Fx	Force in the x-axis
Fy	Force in the y-axis
Fz	Thrust force
hcp	Hexagonal close packed
KM	Crater center to tool edge distance
KT	Maximum crater depth
Mo_{eq}	Molybdenum Equivalency
MRR	Material removal rate
Mz	Torque
NW	Nose wear
NW	Notch Wear
OD	Outer diameter
PD	Plastic deformation

PDZ	Primary deformation zone
PVD	Physical Vapour deposition
R^2	Standard error
R_{max}	Surface roughness (Maximum deviation)
Ra	Surface roughness (arithmetical mean deviation)
RPM	Revolutions per minute
S_0	Shear stress under no normal stress
S_s	Shear stress
SD	Standard deviation
SE	Standard error
SEM	Scanning electron microscopy
$STEM$	Scanning transmission electron microscopy
t	chip thickness
t_1	Uncut chip thickness
t_2	Cut chip thickness
T_β	Beta transus temperature
T_β	The β transus temperature
TEM	Transmission electron microscopy
$TiAlN$	Titanium aluminum nitride
V_f	Feed rate in mm per minute - v_f in industry
V_g	Sliding velocity
V_s	Cutting speed - v_c in industry
Var	Variation
VB	Average flank wear
VB_{max}	Maximum flank wear

VFM Velocity force map

WDS Wavelength dispersive spectroscopy

$X-EDS$ X-ray energy dispersive spectroscopy

XRD X-ray diffraction

Chapter 1

Introduction

1.1 Titanium alloys in the aerospace and tooling manufacture industries

Current sales by the tool manufacturer Sandvik Coromant are in excess of £80 million annually for the titanium machining industry [1]. Expenditure has increased in recent years due to growth of titanium usage within the aerospace industry. Such growth is due to economic pressure on aerospace manufacturers to improve sustainability by reducing environmental impact. Their key goals include reducing weight and improving fuel efficiency whilst maintaining and improving the reliability and service life of aircraft. This has required the implementation of high strength, low density materials. In addition to being high strength and low density, titanium alloys have several key properties which make them ideal for aerospace applications; Low chemical reactivity; performance at elevated temperatures and high cycle fatigue. Titanium also has exceptional compatibility with carbon fibre reinforced polymers (CFRPs), which are rapidly being implemented in higher quantities within commercial single aisle aircraft. The increase in the amount of titanium being used and the amount of aircraft being produced, as forecasted by Longbow [2], is shown in Figure 1.1. Such growth, coupled with the ever rising percentage use of titanium as gross empty weight, as shown in Figure 1.2, demonstrates the rapid increase in demand for titanium within the aerospace industry [2, 3, 4]. The balanced strength, ductility, weldability and workability exhibited by Ti-6Al4V, coupled with favourable creep characteristics and thermal processability, has culminated in this alloy being incorporated successfully into low temperature engine parts such as the fan blades, engine casings and airframe structural components [5]. As the titanium forging and casting industries have moved forward, alloying and heat treatment techniques have developed to a point where alloy properties and microstructure can be closely controlled through the balancing of α and β phases to produce alloys with superior

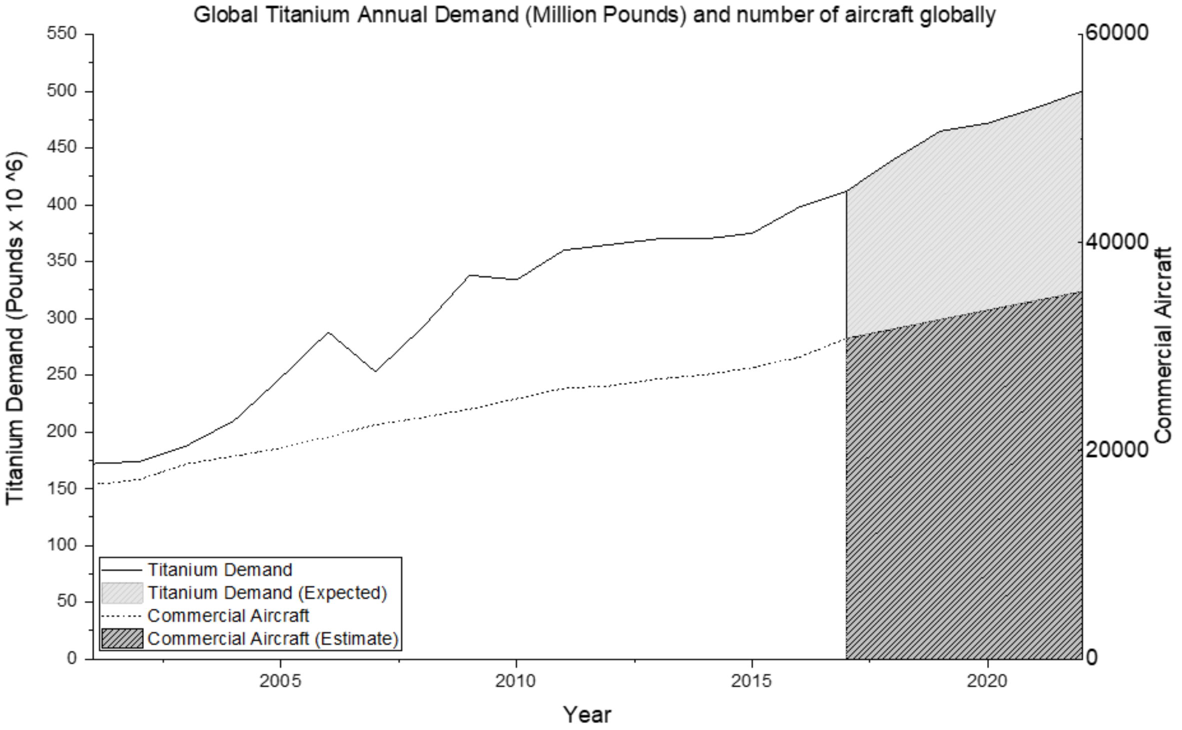

Figure 1.1: Titanium Annual Demand by Longbow and global number of aircraft by CAPA [2].

strength, toughness or fatigue characteristics [6, 7]. As a result, many aerospace components where Ti-6Al4V is inadequate, but where steels are still used, are being targeted for production using more suitable or even tailor designed titanium alloys. In particular there is significant pressure to utilise high strength, fatigue resistant, metastable β alloys which have versatile process-ability, some notable examples include; Ti-13V-11Cr-3Al, used in the SR-71 “Blackbird”. Ti-5Al-2Sn-2Zr-4Cr-4Mo (Ti-17) and Ti-6Al-2Sn-4Zr-6Mo (Ti-6246), β rich α+β alloys with deep hardenability and moderate temperatures characteristics, used for engine mount fittings. Alloy C, which was used in the F-22 nozzle requiring high burn resistance performance. Ti-5Al-5V-5Mo-3Cr (Ti-5553), used for the lower bracers, torque links, bogie and slider of the Boeing 787 landing gear [8]. In the coming years, aerospace companies will be looking to introduce more CFRP titanium hybrid parts and more high strength titanium in critical components, however the extent to which the latter can be done depends on reducing the high cost of implementing such material. As a result of the increasing commercial interest in metastable β alloys, the subject area has become more prominent within academia. The extent to which this has taken place over the past 50 years is demonstrated in Figure 1.3, which shows the number of publications listed in the Web of Science database for each 5 year period since 1965: before this point there were only 26 publications

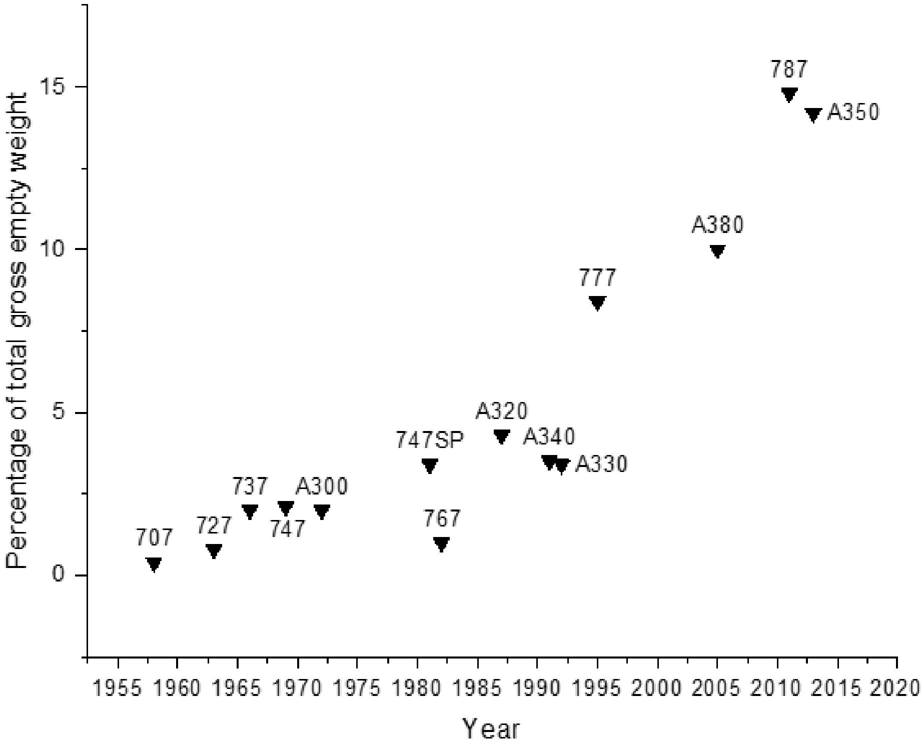

Figure 1.2: The amount of titanium that was used as a percentage of the total gross empty weight in Boeing and Airbus aircraft since 1950 [4].

in total [9]. The expensive and time consuming process of machining is a critical obstacle in using more titanium alloys for aircraft components. The machining stage involved in the production of critical aerospace components accounts for 60% of the total cost. The two main reasons for this are; 1) Parts often requires the majority (95%) of the work piece to be machined away, which is costly from a buy-to-fly perspective and typically requires a lot of machining time and tools [10]. 2) Poor machinability due to the high strength, low thermal conductivity and chemical reaction with tool materials results in rapid tool wear and failure even when slow machine speeds are used.

Increasing titanium usage within the aerospace industry has resulted in higher revenue for tool manufacturers. As a result, they have increased their expenditure on grade and process improvement for products which are utilised for titanium machining. Many of the targeted improvements have been tool-system centric. For example, in turning, systems utilising compressed air, lasers, high pressure jets and cryogenic cooling have been investigated [11, 12, 13, 14, 15]. In drilling, some areas showing promise for improving material removal rate (MRR) include using coolants such as MQL, liquid nitrogen and CO_2 cryogenics and using low frequency vibrational assisted drilling [13, 16, 17]. At the leading edge of turning

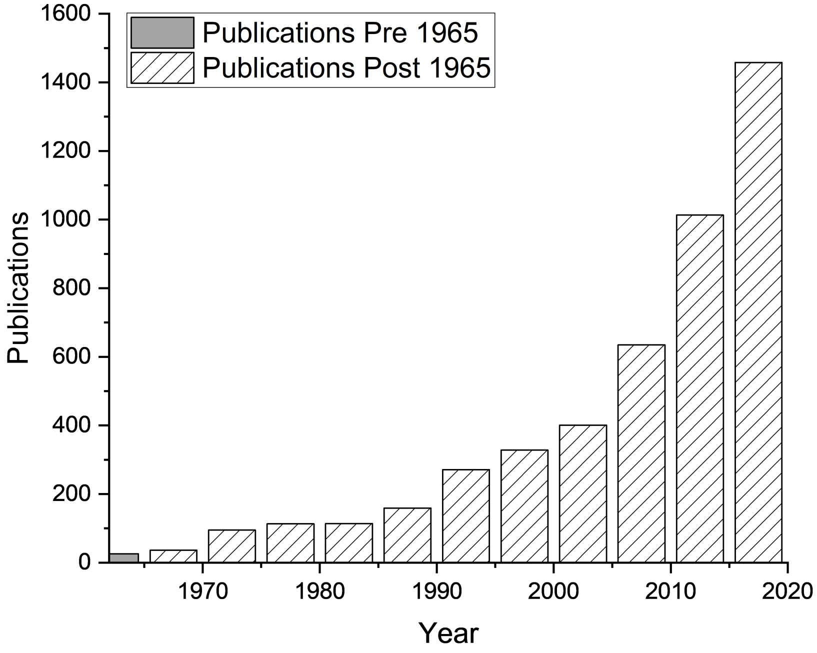

Figure 1.3: Number of publications on web of science within topic heading ‘beta titanium’ since 1960 [9].

insert design, polycrystalline diamond (PCD) tools can improve surface integrity in finish operations [12], whilst cubic boron nitride (CBN) tools show promise in extending tool life [18]. Both PCD and CBN tools are expensive and currently do not offer the means to replace tungsten carbide cobalt binder tools (WC-Co) as the prime tool material for machining titanium alloys. In addition to this, both hard metal and ceramic tools have been disregarded as replacements due to their very high reactivity with the titanium workpiece [19]. Most turning operations involving titanium are carried out using uncoated inserts as many coatings have a negative impact on tool life because they react with the titanium and accelerate tool wear. In some turning operations, physical vapour deposited (PVD) TiAlN coatings are recommended for high speeds [20], but often the benefits to life are minimal and do not warrant the extra cost. In drilling, PVD-TiAlN is almost always used to machine titanium alloys, despite very little research into its effectiveness in alloys other than Ti-64, where it has been shown to reduce the amount of tool wear and improve surface finish [21]. In the area of mill machining, some studies suggest uncoated tools outperform coated counterparts in near-α alloys [22], but that TiAlN coatings provide tool life and productivity benefits for α+β alloys like Ti-64 [23]. The variance in results and lack of mechanistic conclusions seen in studies investigating the workpiece tool and coating system for different machine applications, portends the complicated nature of the tool-workpiece interaction. From a tooling supplier perspective, knowledge regarding tooling systems will help in optimising tools, but if the interactions taking place within said systems are not fully understood, tool substrates and coatings cannot be improved.

In titanium machining, the most utilised cutting tool material is the composite WC-Co (WC with a Co binder). Such materials have excellent sinterability due to; the Co dissolving significant proportions of WC, the low dihedral angle of the WC-Co system and the fact that they can be sintered at temperatures below the Co melting point [24]. Typically the WC grain size and binder content can vary but grain sizes between 0.2 and 3.5 microns are normally used: the binder percentage is often around 6 wt.% Co. WC-Co inserts used for turning titanium alloy components are subject to several different types of wear due to adhesion, plastic deformation, abrasion and reactions between the component and WC-Co composite insert [25]. As a result of such reactions the phenomenon of crater wear tends to occur. Crater wear has been determined by Hartung and Kramer to be the critical wear type involved in the failure of turning inserts [26]. They found that when machining at cutting speeds (V_s) = 61-122 m/min, that solution diffusion driven crater wear reaches a critical point which starts to affect the rate of flank wear on the tool: such flank wear soon becomes significant enough to consider the tool failed. With this knowledge, further studies on various WC-Co and titanium alloys (often Ti-64) systems have been investigated in order to identify the exact mechanism of how crater wear develops. Some methods take advantage of diffusion coupling the system at relevant temperatures and high pressures to understand the static inter-diffusivity within the system. Results have identified some principle properties of the elemental diffusion between WC-Co and titanium, including the formation of interfacial species. However, static methods are not enough on their own to further understand the mechanism by which crater wear occurs in the dynamic machining process [27]. Hartung and Kramer hypothesised that the formation of a TiC at the tool workpiece interface created a protective barrier between the tool and workpiece/chip material which mediated diffusion and therefore the rate of crater wear. Recent work by Hatt et al., used static diffusion couples to mimic the crater interface between WC-Co and different titanium alloys and found that Mo inhibits such formation of TiC. As Mo is a common β stabiliser, it could be a contributing factor to why crater wear is more prominent for alloys containing more Mo [28]. Odelros et al., used diffusion couples in combination with turning trials and thermodynamic modelling to demonstrate that there are C-rich compounds within the crater region resultant from the C depletion of the WC, which leaves embrittled W(bcc) [29]. It is thought that it is this layer of W(bcc), and not a layer of TiC, which mediates decarburisation and therefore rate of crater wear during machining, as a consistent TiC interface has yet to be demonstrated within a crater. Other studies such as the work by Jang Hal et al., have found some success modelling and analysing the dynamic situation and have determined the importance of the Co binder in the chemical reactions that facilitate crater wear [30]. In order to further understand and propose the explicit mechanism by which crater wear manifests in titanium alloy turning with WC-Co tools, higher resolution imaging and elemental mapping techniques must be used at the crater interface for inserts used for different lengths of time to turn titanium.

State of the art metastable β alloys, such as Ti-5553 are well known to be exceptionally difficult to machine. Very slow V_s are required to stop unpredictable tool failure and /or damage to surface integrity [31]. It has been shown that alloy chemistry can drastically change the chemical interaction between the tool and workpiece [28]. For this reason the tool inserts used to machine β rich titanium alloys should be different to those inserts used for Ti-64. Despite this, since Ti-64 is the dominant alloy in the aerospace industry, tools are almost solely designed and optimised for the machining of Ti-64. However, with a shifting market focus to introduce more high strength metastable β alloys into aircraft, there is pressure on tooling suppliers to improve tool life for metastable β alloys, which means there is more scope for designing specialised tools. Up to now, there has been very little focus to optimise tools for β and near-β titanium alloys due to the high quantity of expensive alloy required to iteratively develop and improve tool design. However, if tool optimisation can be achieved at lower costs to tooling manufacturers, there is a substantial opportunity for cost savings for both the tooling and aircraft manufacturers. One way of achieving this would be to develop methods of tool machinability assessment: if cheaper benchmarking and testing was avalible, the cost risk associated with designing new tools for tool manufacturers could be reduced. If such methods also enable the development of a clearer understanding of the interaction mechanisms between WC-Co tools and near β titanium alloys, this could allow significant design step improvements to be made, such as tool coating, WC grain size and Co binder content for different alloys.

The decreasing buy-to-fly ratios, due to the increased titanium usage means tool value becomes more important for maintaining the suppliers distribution network. Due to this, the economic value in titanium machinability research, that enables improvements in production speed and tool cost reduction has never been greater. The current methods of comparing and investigating the machinability of materials, often fail to assess the various characteristics that are important when considering the design of new tools for similar alloys. Therefore, new methods of machinability testing are required to enable rapid material comparison that can draw clarity to the critical factors in the tool-workpiece system that influence tool wear and surface integrity. This project endeavours to achieve both of these objectives. To improve on machinability investigative methods, a detailed study into the drilling machinability of Ti-5553, Ti-6246 and Ti-64 has provided the means to develop a comprehensive method of machinability investigation. The importance of examining both the mechanical and material aspects of the machining process, has resulted in both the differences in tool wear characteristics and hole surface integrity being addressed for a range of titanium alloys. In addition, the VFM "surface response" methodology developed, provides a method of alloy machinability comparison of Ti-64, Ti-6246 and Ti-5553 based just on data from the initial holes drilled. The application of this technique will enable cost reduction when benchmarking the machinability of hard metal tools for new alloys: this in turn would allow tool suppliers to (1) improve their tolerances and (2) test new tool design for a fraction of the current cost. Results which showed increased levels of BUE and higher levels of adhesive wear in Ti-5553 drilling, highlighted the importance of understanding how titanium interacts with WC-Co at the temperatures and pressures that occur during machining. Since prior research has identified the critical failure mechanism of WC-Co tools when turning titanium alloys is due to chemical crater wear, and that such wear results from the interaction of titanium and WC-Co, it was imperative to investigate this phenomenon. Within literature the exact mechanism by which crater wear manifests is not yet fully understood, and therefore, essential work elucidating the mechanisms by which crater wear develops was executed. In this work scanning transmission electron microscopy (STEM), energy dispersive spectroscopy (EDS), wavelength dispersive spectroscopy (WDS) and electron energy loss spectroscopy (EELS) enabled the mechanism by which WC-Co tools degrade when in contact with adhered Ti-5553 to be further understood.

Chapter 2

Literature Review

The literature review will address the principle concepts and knowledge required for discussion of the work presented throughout the thesis. This will include; an overview of titanium alloys and the way they are classified, current machining processes with emphasis on both drilling and turning operations, tool materials and the mechanisms of tool wear with emphasis on WC-Co tools and the current understanding of how titanium alloys interact with tungsten carbide tools in high temperature environments. The final section discusses methods of machinability assessment used in industry and key aspects of machinability in the context of titanium alloys.

2.1 Titanium alloys: Classification and application

Discovered in 1791, titanium has been found to exist in large quantities within the earth's crust, mostly as titanium dioxide and titanium tetrachloride. Although first refined industrially in 1910 using the Hunter process, this was rapidly replaced in 1920 with the development of the Kroll process, which enabled large scale pyrometallurgical refinement of titanium tetrachloride into ductile pure titanium [32, 33]. The dual-phase nature of titanium alloys makes possible the manipulation of material properties via the addition of alloying elements and thermomechanical processing. This enables a high level of versatility when considering structural applications for titanium alloys. At room temperature, a hexagonal close packed (hcp) α-phase exists (Figure 2.1a), whilst at increased temperatures, above the β-tranus (T_β), 100% of the lattice is transformed to a body cantered cubic structure (bcc) (Figure 2.1b). In general there are 5 classifications of titanium alloy; α, near-α, α+β, metastable β and β [10]. Alloying elements also have their own classification in titanium metallurgy; neutral, α-stabilising and β-stabilising.

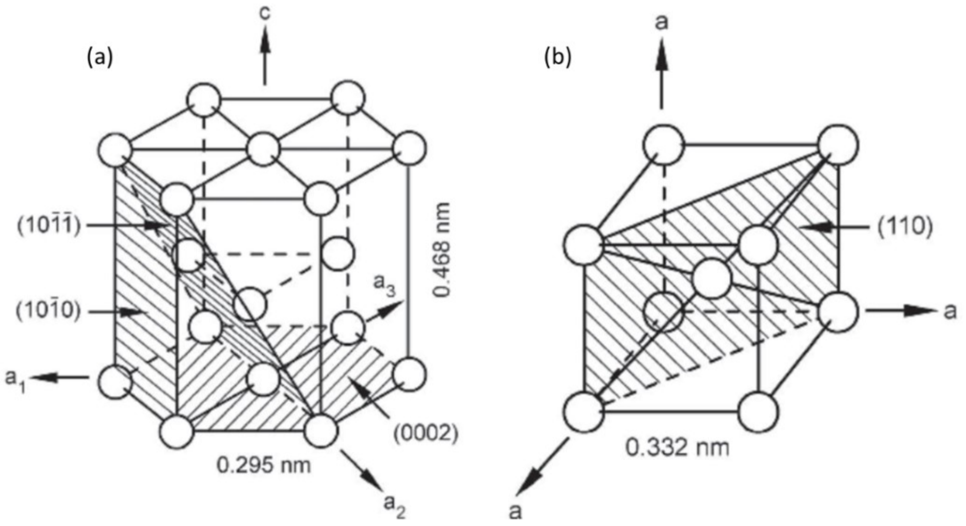

Figure 2.1: (a) and (b) are the unit cell diagrams of the α (hcp) and β (bcc) phases respectively [10].

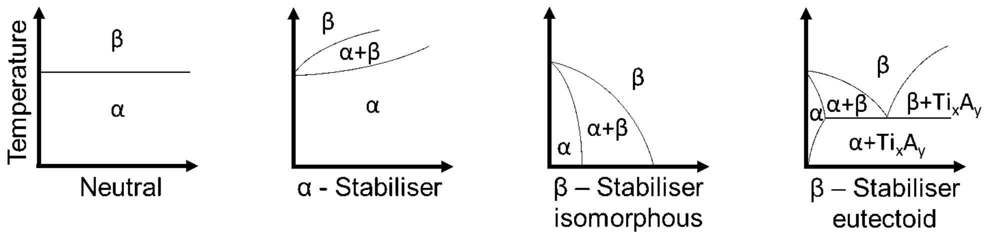

Figure 2.2: Phase diagrams showing phase behaviour due to addition of α and β stabilising elements for titanium alloys [10].

The phase diagrams in Figure 2.2 show how elements affect the phase behaviour of titanium depending on whether they are neutral, an α stabiliser, a β (isomorphous) stabiliser or β (eutectoid) stabilisers. Elements that are considered to be α-stabilising such as Al, O, N and C increase T_β, whilst isomorphous, often expensive, β-stabilisers like Mo, V, Nb, Ta and W lower T_β. β stabilisers require addition of aluminium to mediate their high densities and melting points. Titanium alloys are classified based depending on the relative amount of β stabilising elements, the isomorphous pseudo phase diagram in Figure 2.3 identifies the α, α+β, metastable β and stable β regions. The near-α and near-β regions are identified on the phase diagram and the martensitic start (Ms) and martensitic finish (Mf) lines, labelled Ms/Mf [8]. There are a range of eutectoid β stabilising elements like Fe, Mn, Cr and Co which can increase T_β, whilst due to restricted solubility form intermetallic phases via eutectoid β phase decomposition. Often such elements can only be considered for use in commercial alloys if the rate of decomposition is slow enough to be avoided during industrial fabrication. Neutral alloying elements do not alter T_β, despite this, small additions of elements like Sn and Zr are used for grain refinement and provide solid solution, enabling material properties like yield strength and hardness to be controlled. [34, 35].

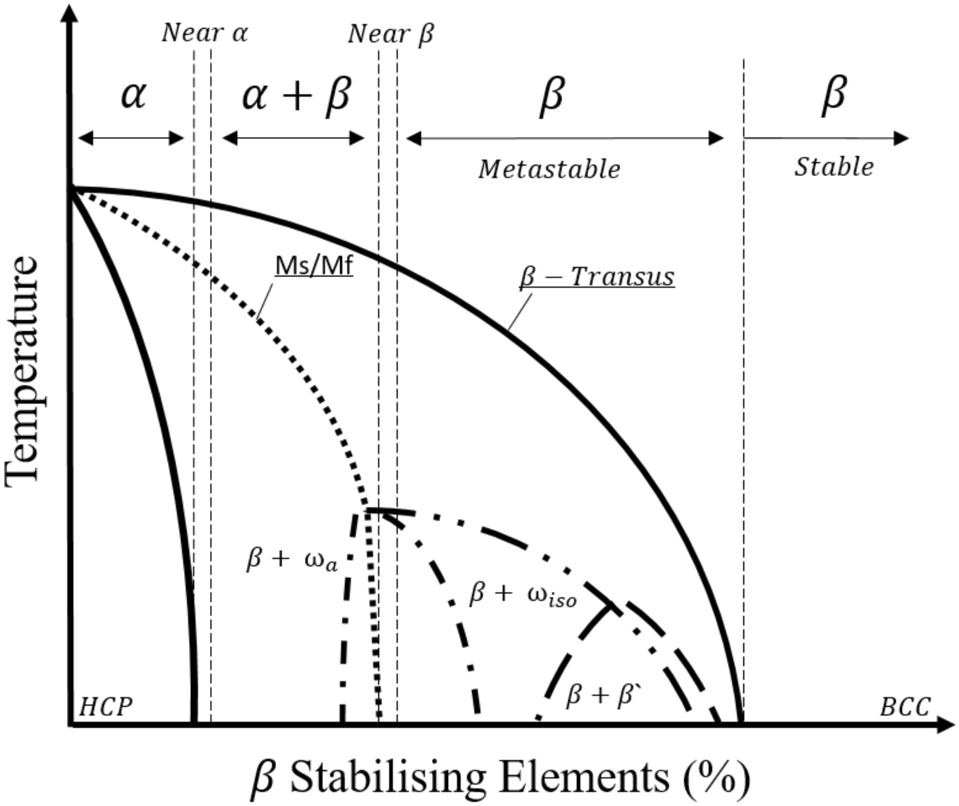

Figure 2.3: Pseudo binary phase diagram showing various classifications of titanium alloys with increasing β stabilisation. Reproduced from [8].

2.1.1 α alloys

Ti-O, also known as commercially pure (CP) titanium is the most widely used α alloy. In the case of Ti-CP oxygen is added during the process of solution hardening, in which the single phase alloys are quenched to obtain a highly martensitic microstructure. In some cases, substitutional solution hardening is used in α alloys like Ti-5Al-2.5Sn to improve strength. Alternatively, cold working can also provide improvements to strength [36]. Heat treatments are largely ineffective on such alloys due to them being mostly hcp, however, this does mean they exhibit excellent properties within welding applications. Within α alloys a very small % of β stabilising elements, often Fe, are included to maintain a consistent grain size during recrystallisation due to their relatively poor solubility in the hcp lattice. The corrosion resistance, creep stability, tensile properties and weldability of α alloys at a relatively lower cost compared to other titanium alloys lending their use to chemical process engineering and biomedical applications. In particular, the weldability and the corrosion resistance make α alloys ideal for wire and piping, especially in hard to maintain environments like off shore oil rigs or submarines.

2.1.2 Near α alloys

Often with less than 2% β stabilising elements, near α alloys have a relatively small amount of β phase precipitates within their microstructure. The small amount of retained β not only makes these materials useful for applications at elevated temperature, but also ensures they have a large stable $\alpha + \beta$ phase field which improves their workability. During processing of near-α alloys, manipulating the α to β ratio can help yield high creep resistance and low crack propagation. These alloys are used for elevated temperature applications that require high fatigue and fracture toughness. As an example Ti-6Al-2Sn-4Zr-2Mo (Ti-6242) is a near α alloy that can be used at operating temperatures up to 550°C for aircraft compressor disks and impellers and more recently has been used as the blade fins on the Space X Falcon 9 rocket.

2.1.3 $\alpha + \beta$ alloys

The most commonly used titanium alloy, accounting for over half of the world's titanium alloy sales is Ti-6Al-4V - an $\alpha + \beta$ alloy. Such alloys are utilised extensively within the aerospace industry due to superior yield stress, fatigue strength, corrosion resistance, modulus of elasticity when compared to alternatives like high strength aluminium alloys. $\alpha + \beta$ alloys are also generally effective at higher temperatures. Generally $\alpha + \beta$ alloys are versatile and can be used within a range of applications. This is because various thermomechanical processing routes can yield very distinct microstructures, namely; fully lamellar, bi-modal, fully equiaxed and mill-annealed. Each microstructure has its own benefits over the others. Lamellar microstructures have high crack propagation resistance and although the β annealing process required to produce such a microstructure is expensive, it is required for components such as bulkheads and cockpit window frames which are critical for passenger safety. Bi-modal microstructures, for which mechanical properties are primarily controlled by the cooling rate after β homogenisation, have excellent fatigue crack nucleation resistance, high cycle fatigue (HCF) and low cycle fatigue (LCF) strength. The stress that fan and compressor blades undergo during flight requires both high HCF and LCF, which is why such components are often made of Ti-6Al-4V recrystallised to a bi-modal microstructure. In addition, disks which need good LCF and microcrack propagation resistance are often manufactured from $\alpha + \beta$ alloys with a bi-modal miocrostructure. Mill annealing can be achieved by avoiding a recrystallisation step during processing. Although mill annealing does not provide a well-defined microstructure, it often imbues excellent formability and therefore is used for component casings and other such parts where fatigue life is less important. Fully equiaxed microstructures can be produced through a similar processing route to the bi-modal structure, with a lower recrystallisation annealing temperature, allowing only the growth of α' grains and no lamellar. Another method of getting fully equiaxed microstructures consists of eliminating all the α lamellar during the recrystallisation stage by using a sufficiently low temperature. Fully equiaxed microstructures can be converted to bi-modal and visa-versa by heating into the $\alpha + \beta$ phase field and using different cooling strategies. Fully equiaxed microstructures are evident in aero manifolds due to the slow cooling required in their construction; this requires both superplastic forming and diffusion bonding. Some $\alpha + \beta$ alloys are used for higher temperature applications. For the case of these alloys, the β phase fraction is reduced due to the elevated diffusion that occurs for the bcc lattice. Ti-6242 is α stabilised, hence has 5% less β phase fraction when compared to Ti-64 at 800°C, meaning it can be used for applications like compressor blades and disks because it maintains good creep properties even when the temperature is constantly exceeding 350°C.

2.1.4 β alloys

There are two key distinctions made when considering titanium β alloys. Those alloys like Ti-5553 which lie close to the $\alpha + \beta$ classification are high strength β alloys, often described as either near-β alloys or metastable β alloys. Other β alloys, often regarded as stable β alloys contain higher quantities of β stabilisers. A key characteristic of β alloys is a continuous layer of α phase at β grain boundaries. Often processing of such alloys is done to control the size, formation and impact of α layers which preferentially nucleate at the β grain boundaries. The precipitated α at grain boundaries is often termed the GB α layer. The key properties of the β alloy microstructure is the β grain size and the strength difference between the GB α and the neighbouring precipitate free zone (PFZ). Control of these properties has the most impact on material properties which are dependent on preferential plastic deformation along the GB α. β grain size is primarily controlled by increasing the recrystallisation temperature above the T_β, whilst controlling the GB α, and the distribution and volume fraction of α platelets, is done via controlling the heating rate and temperature during ageing.

2.1.5 Metastable β alloys

In recent years titanium β alloys have been gaining popularity with aerospace manufacturers. This is because age hardening of alloys within this region produces higher yield stresses than those achievable in $\alpha + \beta$ alloys. The volume of high strength β alloys being utilised within aircraft is increasing steadily. The elimination of α layers at grain boundaries is not possible, but as thick layers are detrimental to strength, processing routes are often used to minimise the layer size and create fine precipitate layers. Maintaining strength is especially important for the high strength β alloys since they are often used for safety critical applications. When processing, controlling the ageing temperature and rate can enable homogenisation and mediate α platelet formation which produces adequate creep properties at higher temperatures within metastable β alloys, improving their applicability for higher temperature applications. Small β grain sizes are advantageous for improved ductility due a reduced slip length between β grain boundaries. Incredible strength, good ductility and fracture toughness are ideal for many landing gear components. For the Boeing 777 landing gear, Ti-10V-2Fe-3Al (Ti-10-2-3) is processed via β forging, with subsequent $\alpha + \beta$ forging, which creates a plastic strain above 15%. In the Boeing 787, Ti-5553 has replaced Ti-10-2-3 for most of the landing gear components as in addition to slightly higher strength and toughness, the processing is easier [8, 31, 37].

2.1.6 β stabilised alloys

β alloys, with significant amounts of β stabilising elements, such as Ti-15V-3Cr-3Al-3Sn (Ti-15-3) or Beta-C, cannot be processed to as high strength as the near β alloys. Heavily β stabilised alloys such as Ti-15-3 and Beta-C have been chosen to be used for aircraft springs since the 1980s. More recently, Beta 21S has been implemented for the elevated temperature application of the Boeing 777 engine nozzle. Other applications for heavily β stabilised alloys with low modulus include an increasing utilisation for biomedical applications which involve load sharing between bone and implanted structures [38].

2.2 Machining processes

Modern machining processes utilising hard tools are often exploited to remove material from forged parts or billets. Such processes are subject to stringent shape and tolerance requirements which vary from component to component, these requirements are particularly high for aerospace components [39]. Rough machining is a term that describes processes which require large amounts of material to be removed. Finish machining is considered to be the final stage of machining. During finish machining using the correct V_s, cutting feed (V_f) and depth of cut (a_p) is extremely important for achieving a good surface finish. It is understood that poor surface finish, e.g. when there is adhered material and/or a high surface roughness (Ra) on the machined surface, can significantly reduce the fatigue life of components, this is unacceptable for critical components within aircraft, such as many of those made using titanium alloys [40]. Since maintaining surface integrity is so essential for many metal removal processes, in recent years there have been significant advances in the understanding and experimental techniques used to characterise and monitor surface integrity, this subject is well reviewed by Jawahir et al., [41]. Three of the most important machining operations used within the aerospace industry are turning, milling and drilling. Turning is the process of turning a work piece (often billet material), while bringing a static tool into contact with said workpiece to remove material. Operations involving removal of material from the outer diameter are known as OD turning while removing material from the top face of the workpiece is known as face turning. Face and peripheral milling processes are the most common type of material removal operations and can be described as the process of advancing a rotating tool, often with several cutting edges, into a fixed workpiece. On most milling machines the axis of movement can be varied in several directions. Drilling, like milling, uses as rotating cutting tool, but with this operation the axis of motion for the tool is fixed during the process. Drilling that is used to create holes: holes that go through entire work pieces are known as "through holes", while holes that go part way into a workpiece, are known as "blind holes". Each machining operation can be explained using well identified mechanics of cutting. These mechanics will be briefly discussed for both turning (§2.2.2), and drilling (§2.2.3), as both feature prominently within this thesis. To introduce general cutting mechanics the relatively simple process of orthogonal cutting will be addressed (§2.2.1).

2.2.1 Orthogonal cutting and the Merchant model

Orthogonal cutting, in terms of machining, occurs when the cutting tool is perpendicular to the workpiece. The forces involved in orthogonal cutting can be described by considering the two dimensional Merchant model [42]. In the merchant model there are several key assumptions; the cutting edge is always normal to the V_f direction, the cutting edge is perfectly sharp, the shear plane is always considered to be acting upwards from the workpiece and the following are constant; a_p, coefficient of friction, chip width, tool geometry and pressure in the shear band. Figure 2.4 shows a merchant circle overlaid onto an orthogonal cutting operation. The merchant circle provides a method of considering the different forces involved in orthogonal cutting when the tool is moved into the workpiece along the feed direction; the cutting force (F_c), the resultant thrust force (F_Ψ), the shear force (F_s) the normal shear force (F_η), the normal force N and the friction force F. The resultant force is labelled R and its magnitude is the diameter of the merchant circle. The uncut chip thickness is t_1 and the cut chip thickness is t_2, often a cutting ratio is defined as $r=t_1/t_2$. The cutting ratio r, can be obtained through the geometric relationship between the shear angle (φ) and the rake angle (Ψ) as in equation (2.1). Based on these angles a larger shear angle will increase t_1 and decrease t_2 while increasing rake angle will increase t_2.

$$r = \frac{sin(\varphi)}{cos(\varphi - \Psi)} \tag{2.1}$$

As labelled, the tool is incident at an angle Ψ to the workpiece. This angle Ψ is referred to as the rake angle as it is between the rake face and the perpendicular to the workpiece. The shear angle, φ, is the angle between the F$_s$ which lies along the shear plane and the workpiece and results from the severe deformation that occurs in chip formation. The friction angle η lies between N and R. By considering φ the F$_s$ and the friction force (F$_\eta$), can be be related to F$_c$ and F$_\Psi$ through equation (2.2).

$$\begin{bmatrix} \frac{F_s}{F_\eta} \end{bmatrix} = \begin{bmatrix} cos(\varphi) & -sin(\varphi) \\ sin(\varphi) & sin(\varphi) \end{bmatrix} \begin{bmatrix} \frac{F_c}{F_\Psi} \end{bmatrix} \tag{2.2}$$

Similarly Ψ can be used to relate N and F to F$_c$ and F$_\Psi$ as in equation (2.3).

$$\begin{bmatrix} \frac{N}{F} \end{bmatrix} = \begin{bmatrix} cos(\Psi) & -sin(\Psi) \\ sin(\Psi) & sin(\Psi) \end{bmatrix} \begin{bmatrix} \frac{F_c}{F_\Psi} \end{bmatrix} \tag{2.3}$$

To calculate the shear stress (S$_s$) for the 2D orthogonal case, Merchant uses a combination of the shear stress under no normal stress (S$_0$), and the gradient (K) of the shear stress vs the normal stress (σ_n) through addition as in equation (2.4). It should be noted that this method does not account for temperature and strain rate which must be set from prior literature results.

$$S_S = S_0 + K\sigma_n \tag{2.4}$$

In reality the system is always three dimensional and by introducing the width of cut (L) the average S$_s$ can be calculated using F$_s$ and φ using equation (2.5).

$$S_S = \frac{F_S + sin(\varphi)}{Lt_1} \tag{2.5}$$

2.2.2 Turning

Turning is carried out using rotational lathe machines. The first automatic lathe was developed in 1842. Since then, the technology has progressed significantly and modern industrial lathes are often automated using computer numerical controllers (CNCs). In turning, the workpiece (often cylindrical) is mounted in a fixture and rotated while a single point cutting tool is brought into contact with the rotating material. A diagram of the process is shown in Figure 2.5 [39]. The clamped billet is being rotated at a speed V$_s$ controlled by the RPM of the spindle, the tool is advancing at the feed rate, V$_f$ through the workpiece, the depth of cut

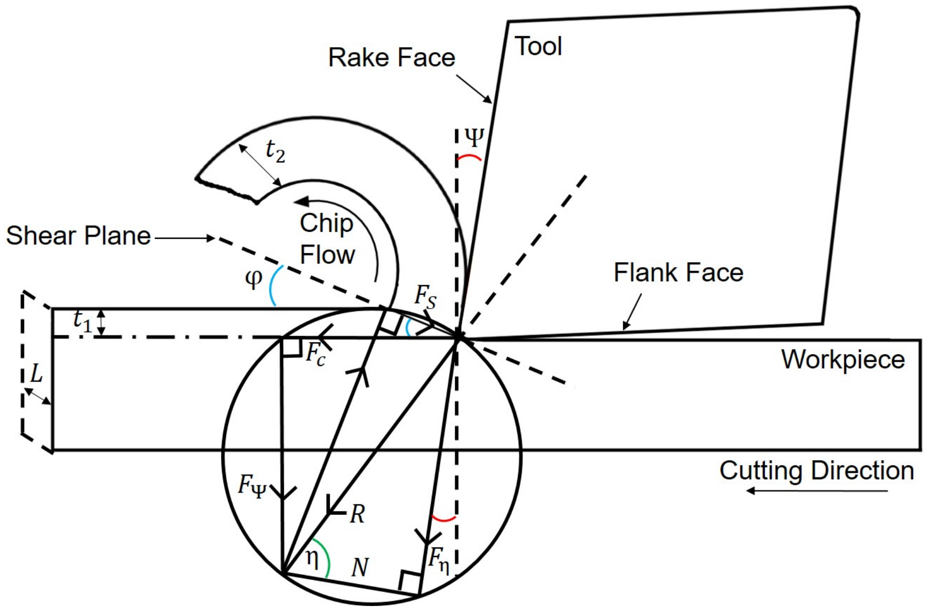

Figure 2.4: Merchant circle diagram - adapted from [42].

a_p, is the distance radially removed from the billet. The material removal rate (MRR) can be calculated using these three parameters MRR $= V_s V_f a_p$. MRR is often used to compare the efficiency of different tools and tooling systems when turning, especially for roughing operations. For machinists V_s, V_f and a_p are important parameters that must be controlled carefully to reduce tool wear and not impart unwanted damage into the work piece whilst maintaining efficiency and productivity. For this reason V_f and a_p often vary significantly for different tool and workpiece material combinations. Depending on the type of turning or the geometry of the final part there is less freedom to vary the a_p often to account for this further changes to V_s and V_f are made to maintain efficiency and quality. In the bottom right of Figure 2.5 there is a top view of the tool and tool holder. As the tool intersects the rotating workpiece the chips flow over the rake face of the cutting insert. In the top right of Figure 2.5 a magnified view of the chip flow is shown. The rake and shear plane angles are labelled and dictate how long the chip remains in contact with the tool and hence the size of the chip-tool contact zone. The shear angle is dependent on material properties, therefore, to mediate the chip flow in for workpiece materials, different tool geometries are used. There are several different types of turning and although face and OD turning are two of the most common types of material removal, turning can also be used to create grooves, tapers, or other profiles. The process of boring can also be considered to be a turning like operation but done on the inside of the rotating cylinder and allows creation of holes and tubular geometries. Most modern turning applications can be considered to be oblique cutting systems. The main difference of the oblique case to the orthogonal case discussed previously is the inclination angle γ which measures the offset of the cutting edge from orthogonality of the V_f plane [43]. The introduction of γ causes chip flow to be offset from the orthogonal plane.

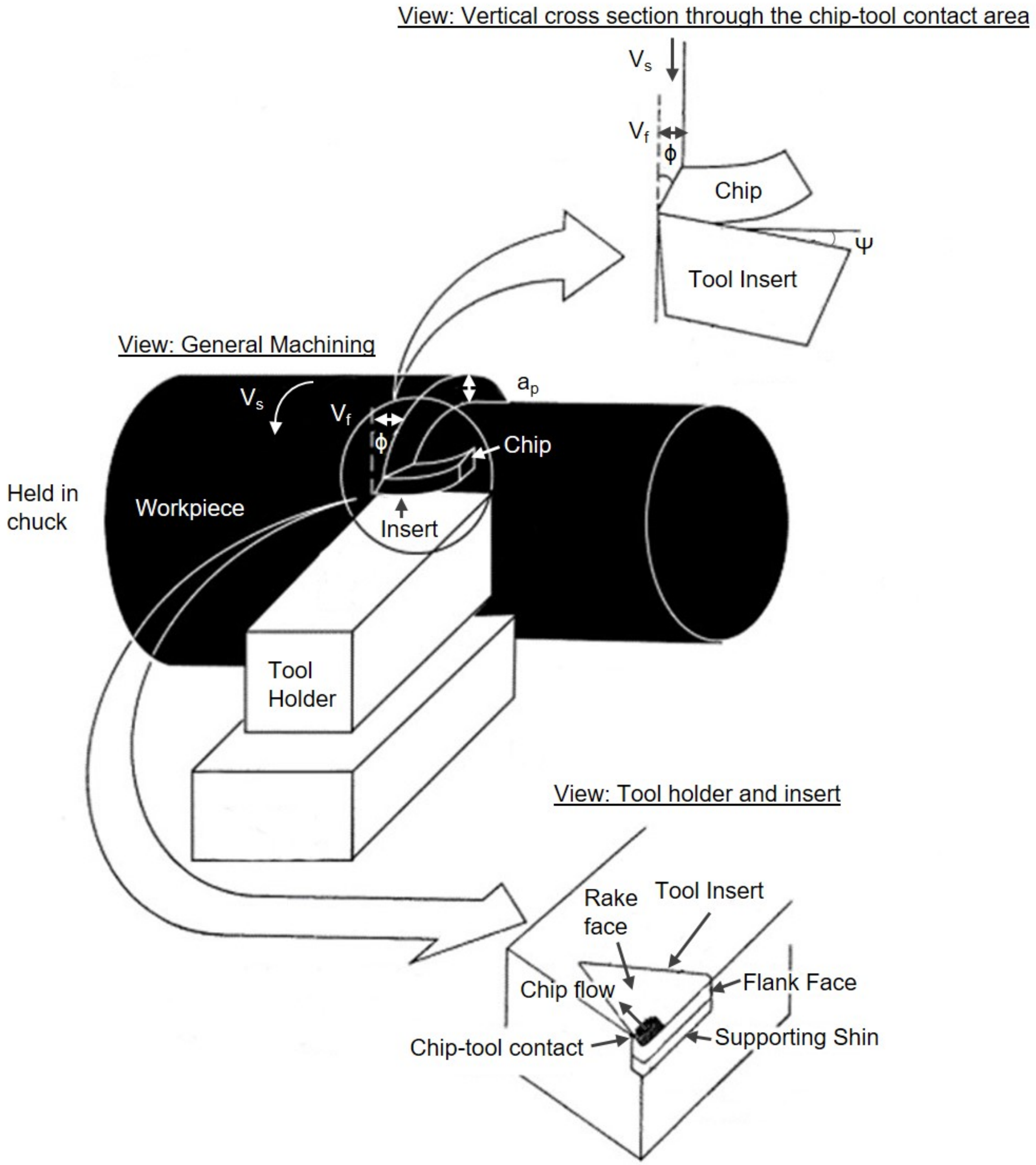

Figure 2.5: Diagram showing the turning process on a lathe. Top right shows a magnified view of the chip, tool and work material contact. Bottom right shows details about the insert. This figure is adapted from [39].

In turning the chip flow angle from this plane can be increased by increasing the tool nose radii [44], or the restricted cutting effect which is resultant from cutting and chip formation interference between the primary and auxiliary cutting edges [45].

2.2.3 Drilling

The history of drilling

Drill technology is evident throughout human history: evidence of drilled holes can be found as early as the palaeolithic period [46]. The earliest rotary drill machine system to be used was the bow drill in the ancient Harappa and Egyptian civilizations [47]. Through the ages bow drills were somewhat automated using Greek water mills and wind mills in combination with belts to transfer torque to rotary tools. Evidence of manual machines used for rock drilling and coring can be found up to 3000 years ago, these drills are used to remove a core of material from a solid body. The Romans also made use of similar drills for construction. Until the advent of steam power and electric motors not many significant advances in drilling technology were made as there wasn't sufficient power or infrastructure available to produce drills useful for other applications. The first non-rotary steam powered drill was used to drill oil wells in 1859 [48]. The main breakthrough for rotary powered steam drills came in 1901 when Anthony Francis Lucas used a steam powered system for rotary drilling at the spindle top oil field. The electric motor made possible the invention and production of power drills in the early 1900s these tools combined with electric powered table top drilled enabled the production of complex structural parts which helped drive structural technology to where it is today. In the modern era there are many types of drill tools but the most common is the application of twist drills for drilling holes in a vast range of materials including wood, plastic, metals and various rock types. Modern twist drill bits were first invented in the 1860s by Steven Ambrose Morse, he theorised it should be possible to drill more accurate holes using a tool with a sharpened point and fluting that helps the evacuation of material while the drill was in operation [49]. His first iteration included a sharp metal bar with large helical grooves hatched in either side, the flute. This was then rotated using high torque and a pressure was applied along the longitudinal axis of rotation. The key characteristics of modern twist drills are a tool shank to be gripped by a torque producing machining centre, a cylindrical shaft with helical flutes, and a cutting tip which can have a multitude of geometries depending on the application.

The use of twist drills in aerospace production

One of the most advanced areas of twist drill application is those used for machining aerospace alloys for aircraft assembly. There are three main hole types associated with twist drills: (1) Through holes, which are holes that exit one side of the workpiece. (2) Blind holes, which terminate within the workpiece. (3) Deep holes which are considered to be holes 4 or more times the diameter the drill. This is because precision and accuracy are essential within aerospace, especially where critical components are concerned. Twist drills must be able to withstand the excessive forces required to deform and shear strongest and most advanced structural alloys whilst maintain high hole tolerances. Often, such drills have to be made from extremely hard materials like tungsten carbide, so the cutting edge does not break or deform during action. Twist drills are used extensively in the production of landing gear parts such as gear legs and beams [50]. One popular method of maintaining accuracy and precision in such parts is to drill holes undersized and then ream them precisely to meet specification. The geometry of twist drills is vital from both a tolerance and tool life standpoint. Tool manufacturers are constantly improving and innovating on current twist drill design for different applications and materials. The changes to drill geometry range from very subtle to extensive, some of the key characteristics will be discussed in more detail: subtle changes are required for drills used in similar materials but with different diameters in order to maintain optimal chip flow characteristics. Often the intricacies of such differences are company trade secrets and are not widely distributed. On the other hand some drills require significant geometric variations, such as drills used to machine deep holes [51]. In some cases, for very deep holes twist drills are not applicable due to instability and consequently increased risk of fracture, for such applications gun drills may be employed instead.

Twist drill geometry

Not every aspect of the geometry will be explained in this section but the main features of the tools will be addressed and where relevant, their effect on the drilling operation will be discussed. Figure 2.6 shows a twist drill schematic [52].

Body

The drill body is measured from the point to the end of the neck, the upper body is the cutting portion of the tool. Sometimes there can be a back taper applied to the body in which the diameter at the point of the drill is larger than at the neck. The flute, land and top or point of the drill are all located in this cutting region. The top of the drill contains the major and minor cutting edges and the key terms are included below.

Neck

The neck connects the body and shaft of the drill and has a smaller diameter than both.

Shank

The tool shank can be either straight or tapered and functions as the section of the drill that is held within a chuck and rotated by the spindle. Different size chucks have to be used for different size drills with varied shank sizes. The clamping mechanisms used in chucks can

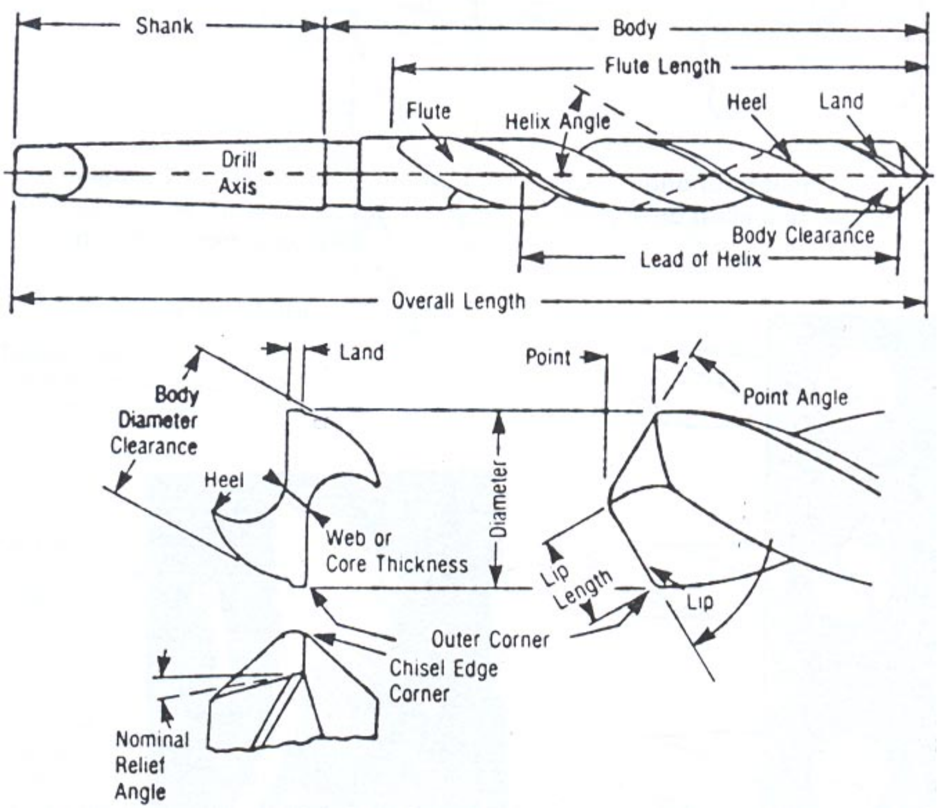

Figure 2.6: A schematic showing the geometric features of twist drills from [52].

also vary, examples include mechanical heat shrink and vacuum methods which are selected depending on the type of application to be carried out, and the type of drill employed.

Chisel Edge and Chisel Edge Angle

The chisel edge is located on the point of the tool along the web and is normally created through grinding. The chisel edge connects the cutting lips of the drill and often has no influence on cutting. However, it is required for connecting cutting edges and helping enter the material.

Clearance

The clearance and clearance diameter refers to the portion of the land that had been ground away to avoid excessive contact with the work piece.

Core

The core of the drill is the region not intersected by the helical flute in the centre of the drill. Large cores offer better drill stability and are necessary for high torque drilling operations such as those used in drilling aerospace alloys.

Flute

The flutes extend from the rake faces of the cutting edges on the top of the drill. Their main purposes are to facilitate chip flow and evacuation from the cutting region and in some cases to help coolant reach the cutting edges during the process. Generally drills that can accommodate a larger flute are better for chip extraction. Advanced twist drills contain coolant holes which extend as helical tubes down the flutes so that coolant can be transported at optimal pressure to the cutting region. Some drills have 3 or 4 flutes, although this reduces the maximum stresses the drill can tolerate it aids chip evacuation and is often utilised for increasing the diameter of pre drilled holes.

Helix angle

The helix angle determines the angle at which the flute helix propagates along the drill. It is an essential consideration in most twist drill designs as it dictates the chip formation and flow.

Land

The land is the region of the drill which is ground to a cylindrical shape to either side of the flutes. The defining purpose of the land is to maintain drill alignment and hole size. Often the land diameter is slightly smaller than that of the drill to maintain some clearance and prevent jamming.

Margin

This region is located on the land and is the region not ground away. The margin helps provide clearance for the drill during operation.

Outer Corner

The outer corners of the point experience the most torque during the drilling action. Excessive torque and poor chipping can cause chipping on these regions which can prematurely fail the tool.

Point and Point Angle

The point refers to the cutting region of the drill. It can also be referred to the very first point of contact. The point angle is the angle made by the point when viewed from between the drill lips. Generally, tougher materials are required to have shallower point angles as less stress will be put on the point and breakage will not occur.

Web

The web is the part of the drill which connects the land areas between flutes. The web extends to the chisel edge for two flute drills. The web thickness normally refers to the size of the web at the point.

Drilling processes and hole generation

Before the stages of generating a hole are discussed, the cutting parameters that govern the mechanics of the drilling action must be explained. The V_s in drilling, normally measured in metres per minute (m/min) is the speed at which the outer corner (or any point on outer diameter) is moving while in cut. The chosen V_s is critical in determining the life of the tool but the optimal speed can vary significantly for different tool and workpiece materials, as well as different types of hole and tool geometry [53, 54]. Tooling manufacturers expend a lot of resource on determining the correct V_s for drilling operations so they can offer the best tool efficiency to manufacturers and machinists. Some key parameters to consider when choosing the V_s are the diameter of the drill, the rigidity of the drill and chuck, the properties of the material and the required hole quality. The feed rate, describes how fast the drill propagates through the material and is most often expressed in millimetres per revolution f_{rev} (mm/rev) or mm per minute V_f (mm/min). Again, the correct V_f depends on material properties, selected V_s, drill type or size and the stability of the setup. The combination of the V_f, V_s and tool geometry make the mechanics of the drilling operation fairly complex. The drilling process can be split into several stages: For through holes these are; Centring, steady state drilling and breakthrough. In blind hole drilling only the centring and steady state cutting are stages occur. The centring stage is important to ensure the hole is drilled precisely at the correct location. Centring can be considered to be the first contact of the drill point and chisel edge with the workpiece. The centering stage ends once the cutting edge is fully engaged and the resultant force and torque become constant. Consequences of poor centring include; unbalanced stresses which can cause accelerated tool degradation and breakage or holes not drilled to specification. Once the thrust force and rotational torque are constant and the whole tool is engaged in cutting, the operation enters the steady state drilling phase. During this phase the corners of the drill will experience high thermomechanical loads which are determined by the material properties and the V_s and V_f involved. Consequently, it is important that the cutting parameters used do not cause the drill to experience excessive forces which could cause breakage and critical failure. The breakthrough phase consists of plastic deformation in the tool and workpiece material as the tool tip penetrates and exist the workpiece. In this stage, wear and chipping of the tool can be caused by the release of stored elastic energy. The drilling V_s and V_f are again important to consider in order to avoid excessive damage during the breakthrough stage [39, 55].

Shear mechanics in twist drilling

In this section the mechanics of twist drilling will be explained using the previously discussed merchant theorem §2.2.2. The merchant model allows for effective comparison between drilling and turning results which complements the work of this thesis. Modified merchant models, as that of Naisson et al., have been shown to be successful in modelling the thrust force and torque in drilling [56]. In their model they used the shear stress bridgeman type model [57], as described previously in equation 2.4, to link the shear stress to the shear stress under zero normal stress and the shear stress vs normal stress. As the merchant model does include some limitations which would have resulted in poor experimental and model similarity, they modified and/or approximated some aspects to improve accuracy. One limitation is that shear stress calculated from equation (2.4) omits factors such as temperature and strain rate, so for these values, Naisson refers to other values that have previously been experimentally proven in literature. Another such limitation, is that in the merchant model, the friction coefficient (μ_T) is constant and there is no V_s. In machining the V_s is one of the most important parameters and heavily influences the μ_T [58]. In order to include a more accurate representation of μ_T, the sliding velocity (V_g) must be considered at the tool chip interface as demonstrated by Zemzemi et al [59]. In addition, since both V_s and chip thickness (t) are constant in the merchant model there is no consideration of chip compression as this would make calculation of μ_T more complicated. To account for the above, Naisson et al., developed equation (2.6) which includes values for the uncut chip thickness (t_1) and the cut chip thickness (t_2), to approximate for the coefficient of friction.

$$\mu_T = 0.26\left(\frac{t_1}{t_2}\frac{V_g}{V_{ref}}\right) \tag{2.6}$$

They then modified the equation for shear angle based on the principle of minimising the power dissipated in cut to create equation (2.7) where $\lambda_T = tan^{-1}(\mu_T)$.

$$\varphi = \frac{\pi}{4} + \frac{\Psi - \lambda_T}{2} \tag{2.7}$$

Experimental studies such as that by Moufki et al., have found calculation of the shear angle using the merchant theory are not accurate unless material dependant properties are accounted for [60]. They improved upon the model by including material dependant coefficients A1 and A2 in their shear angle calculation as in equation (2.8). A1 and A2 are calculated by comparing t_1 and t_2 using $S = tan^{-1}(cosA_n/(t_2/t_1 - sinA_n))$.

$$\varphi = A1 + A2(\Psi - \lambda_T) \tag{2.8}$$

To relate this to the variation in chip thickness the geometric relationship in equation (2.1) is used. In order to account for the plastic behaviour involved the parameters k and S_0 are related to S_s' and C in equation (2.9) and (2.10).

$$S_s' = \frac{S_0}{1 - k \cdot tan(\varphi + \lambda_T - \gamma_n)} \tag{2.9}$$

$$C = 2\varphi + \lambda_T - \gamma_n \tag{2.10}$$

Where γ_n is the cutting edge angle.

2.3 Tool wear

Tool wear is a key factor in the machinability of any material. Rapid tool wear of high end tools, such as those used to machine titanium alloys, contributes significantly to the overall cost of machining. The high affinity for titanium and oxygen/carbon, coupled with high strength and good fracture toughness at increased temperatures, promotes excessive tool wear and thus contributes to the poor machinability associated with titanium alloys. Tool suppliers must continually improve their tools within this market in order to stay competitive. This is because tool life contributes significantly to cost efficiency for aerospace manufacturers. In order to do this, the suppliers must first understand how and why their tools are wearing. In this section, the important aspects of tool wear will be discussed in two sub sections: §2.3.2 will explain the various wear mechanisms. §2.3.3 will address the way such mechanisms contribute to different wear types. In most cases the knowledge in this section will be collated from Thomas Childs metal machining [55], Trent and Wright metal cutting [39], and from the Sandvik Coromant educational wear guide [61]. Where other sources have been used, the reference will appear in the text as normal.

2.3.1 Taylor model for tool wear

The simplified Taylor model for tool wear is a description of how wear develops over time [62]. Figure 2.7 shows the so called Taylor curve. In this figure there are three key regions: region 1, known as the break in period where there is initial rapid flank wear of the tool, region 2, in which a steady wear rate is reached and region 3 where the flank wear rate accelerates and the tool approaches total failure. It is important to note that although the Taylor method specifically focuses on one type of wear; typically flank wear. Such wear is often resultant from a combination of the wear modes and mechanisms which will be discussed within this section.

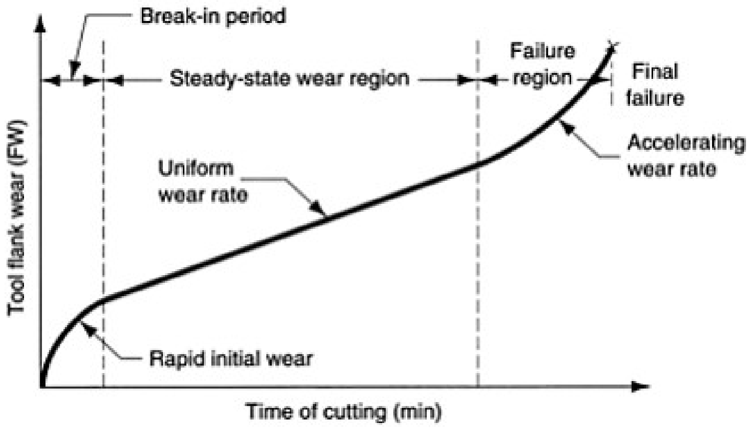

Figure 2.7: A graph showing the Taylor wear curve which indicates how flank wear develops over time. The key regions have been labelled [62].

2.3.2 Wear mechanisms

Various loads are imparted on tools during all machining processes. In many cases, and especially for titanium, these loads create a violent environment which causes degradation to the most advanced tool materials. The different wear mechanisms; thermo-mechanical, abrasive, adhesive and chemical, can often be discussed using different terminology. In this case, each mechanism will be described in the context of the load that the tool is put under. Before the mechanisms can be discussed, the role of contact temperature must be defined.

Contact Temperature

Temperature is a significant contributor to tool wear. The temperature is generated from the three shear zones shown in Figure 2.8 [63]. The first zone, the primary shear zone, is related to the shear angle discussed in §2.2 and is the shear that causes the chip to separate from the workpiece contributing to the majority of the thermal energy within the system. The secondary shear zone refers to the shear resultant from the chip material sliding against the tool rake face. The tertiary zone is located under the cutting edge on the flank face of the tool between the work piece and tool. The contributions of chemical, adhesive and abrasive wear mechanisms to the overall tool wear vary with different temperatures as shown in Figure 2.9. Chemical wear increases exponentially with temperature. Adhesive wear peaks at a certain temperature, determined by the tool and workpiece materials. Abrasive wear is fairly independent of temperature but has a slight negative linear relationship. There is a linear relationship between cutting temperature and V_s and so they are interchangeable on the X axis of Figure 2.9 assuming all other parameters remain the same.

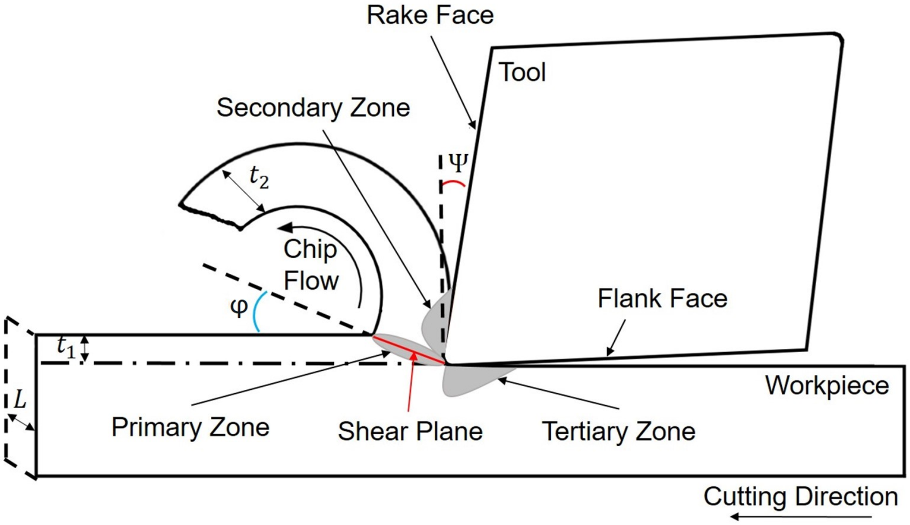

Figure 2.8: Diagram showing the primary, secondary and tertiary shear zones resultant from machining.

Thermomechanical Loading

The primary load on the cutting tool induces both mechanical and temperature stresses and is the main cause of thermomechanical wear. Depending on the cutting parameters and what workpiece or tool material is being used, the contribution of temperature to mechanical induced stress varies. One of the main parameters that influences thermal load is the V_s, hence why it is linked to the x-axis in Figure 2.9. Cutting fluids are often required to limit the thermal loads. If the V_s is maintained and V_f or a_p is increased, the mechanical load on the tool will increase due to the increasing feed force or shear angle respectively. Although tooling materials, are by design, made to withstand high thermal and mechanical loads, when they are raised above the tool's threshold the tool compressive strength is overcome and results in plastic deformation. Such plastic deformation can either be macroscopic, on the cutting edge of the tool due to the primary shear zone, or, microscopic in the secondary shear zone due to chip tool contact. The above discussed response to thermomechanical loading is often resultant in continuous cutting operations like turning. When machining intermittently, the loads can result in excessive tensile stresses at the surface and compressive stresses deeper into the tool. This is due to the heating and cooling cycle. Comb cracks, perpendicular to the cutting edge, start to form when the tensile stresses become greater than the material strength. This can be exacerbated by thermal expansion within the tool substrate. In some machining operations, cyclic loads can be induced by cyclic variation in the a_p, for example, if a billet is slightly off centre in a turning operation, the tool will experience increased mechanical loads when the a_p is larger. A similar phenomenon occurs when tools are taken

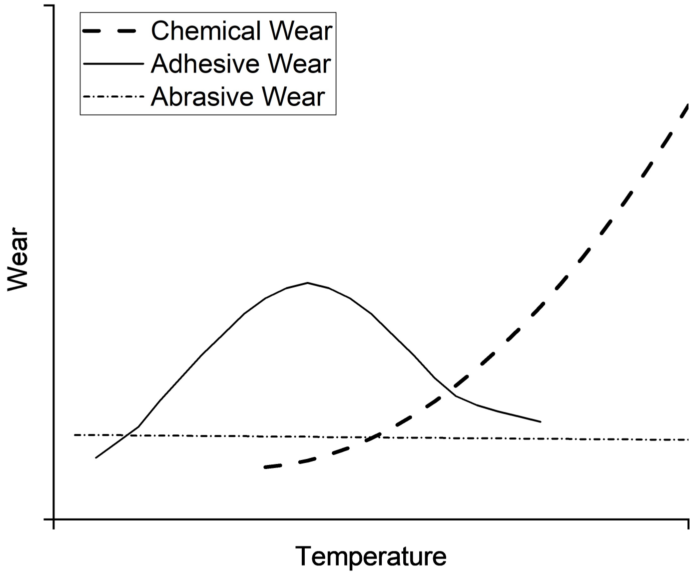

Figure 2.9: Graph showing the relationship between temperature and wear mechanism. Cutting speed (V_s) can also be substituted for temperature on the x-axis since the faster the cutting speed the higher the temperature. Adapted from [61].

in and out of cut which can occur in milling operations.

Chemical Wear

Diffusion wear can occur due to chemical interaction between certain workpiece and tool materials. In some cases oxidation can be an issue, causing corrosive wear for which the oxidation reaction accelerates the removal of wear debris from the tool [64]. In titanium machining, the titanium reacts with the Co binder in the tool and has been determined to be a critical proponent of the tool wear [26]. This is discussed in detail in the crater wear type section. Chemical wear is heavily dependent on temperature as shown in Figure 2.9 as it increases the energy of the system which promotes both diffusion and oxidation. The highest temperatures in the cutting system are evident in the secondary shear zone where crater wear occurs. At the edge of this region, for uncoated carbides and ceramics, notch wear can be promoted by the workpiece and tool coming into contact with oxygen.

Adhesive Wear

Adhesive wear, sometimes referred to as attrition wear, occurs when there is significant strong adhesion of workpiece or chip material to the cutting tool material. The interface that forms between the materials controls the characteristics of such wear. This is because these characteristics depend on the strength of the interface compared to that of the tool and workpiece materials. Adhesive wear can cause several types of damage, including but not limited to; chipping, fracture and flaking of the tool material. These types of damage often occur during the repeated cycle of tool, workpiece and chip material adhesion that result in tool material being torn away. The process causes wear when the cutting forces in certain locations cause uneven metallic junctions to form, putting strain on the tool material and causing wear in the aforementioned ways [65]. In the case without lubricant, the amount of wear is proportional to the relative ratio of hardness of the materials [66]. Adhesion can in some cases protect the tool, one such phenomenon is when the adhered material creates an impenetrable barrier which stops any oxidation occurring. Another case is that of BUE, which can sometimes replace the worn flank with an edge that has a more favourable geometry than the worn tool, helping maintain a more stable cut for longer. Note: it is only a special case when BUE is beneficial and often can cause significant parts of the coating and tool substrate to be torn away, especially if the cutting is somewhat unstable. Figure 2.9 shows the contribution of the adhesion mechanism to wear is heavily influenced by temperature. At low temperatures the regions of adhesion tends to form weaker junctions. Whereas, at elevated temperatures the adhesion zone is soft. At higher temperatures the weakest region of the adherence zone is in the workpiece material, therefore for this case tool material is less likely to be damaged or torn away.

Abrasive Wear

The abrasive wear mechanism is similar in nature to the grinding process. Hard particles from the workpiece material like Ti(C, N) from stainless steel or WC from the tool get between the tool and the workpiece/chip material causing abrasion during sliding. In cases of strong adhesion this sliding will occur within chip material and not at the interface, thus limiting the abrasive wear. Tool manufactures try to ensure that the amount of abrasive wear is only determined by the distance of material that has been machined and not by the V_S and temperature. When this is the case, the relationship shown in Figure 2.9 occurs.

2.3.3 Wear types

The different types of visible wear are identified as "wear types" and include; flank wear, plastic deformation, cracking, fracture, chipping, notching, BUE and crater wear. Each of these will be discussed in its own section. Figure 2.10 is included to aid the description of the aforementioned wear types within each section: (a, b) are 3D diagrams of turning inserts with various types of wear, (c) is a cross section with indication of nomenclature for average flank wear (VB), maximum crater depth (KT) and crater centre to tool edge (KM), and (d) show 2 types of plastic deformation. Crater wear and the chemical interaction that causes such wear as a result of machining titanium is discussed in §2.4. In this section only the general case of crater wear is addressed.

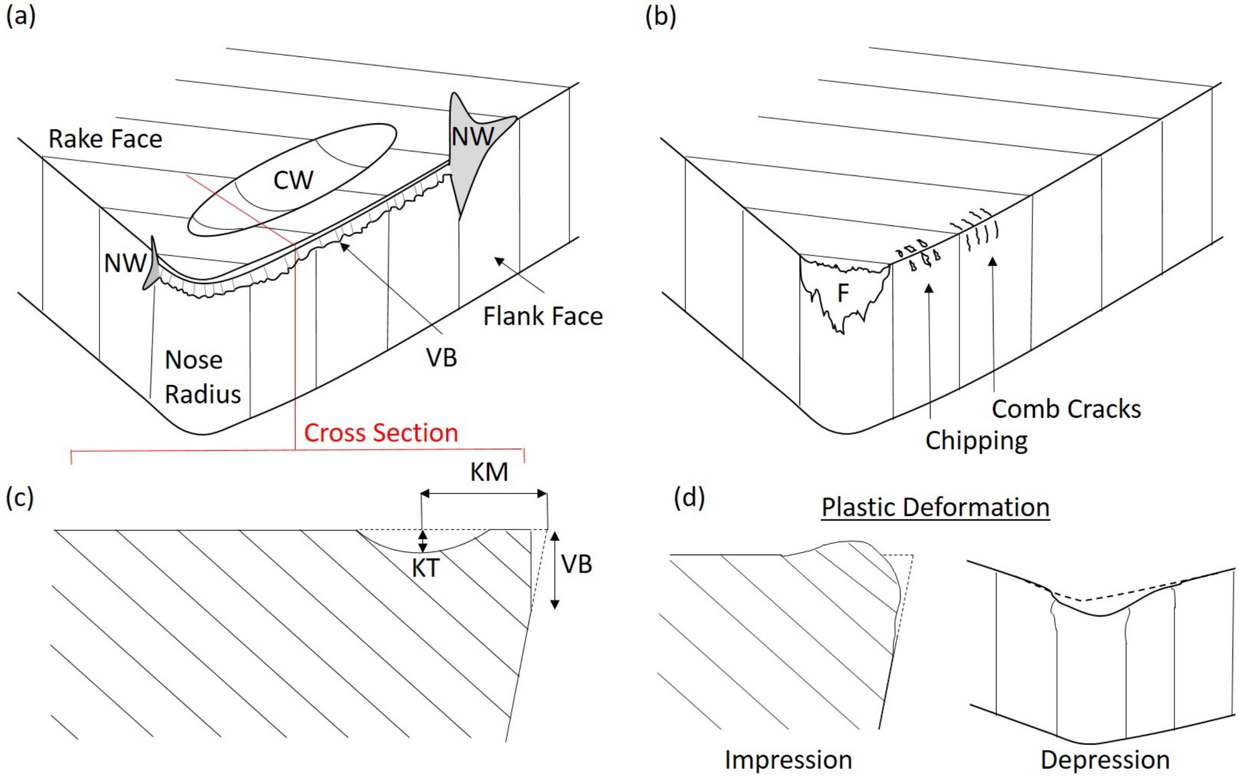

Figure 2.10: Tool wear types: (a, b) - Highlight various wear types on 3D diagram of turning insert. (c) - Cross section marked in (a) and nomenclature for Flank Wear (VB), maximum crater depth (KT) and crater centre to tool edge (KM). (d) - Impression and depression plastic deformation. Diagrams are recreated from [67, 39].

Flank Wear

Flank wear is the most commonly examined wear and can be caused by all major machining processes. The chemical and abrasive wear mechanisms are the main contributors to flank wear. The contributions of each, vary significantly for different material and tool combinations. Flank wear occurs when cutting tool material is lost from the flank face during the sliding of the tool against the machined workpiece surface. Figure 2.10c shows where the flank wear, labelled as VB, occurs on a turning insert for a parallel intersection along the cutting edge. Such wear normally starts at the cutting edge and develops perpendicular to this, eventually encompassing the nose and corner radius and some of the secondary cutting edge. As the tool is normally in constant contact with the workpiece flank wear is very common. If only flank wear is evident it often increases linearly. Normally flank wear is uniform on the flank face, however, if there are other wear types happening within the same region, or the insert has unusual geometry, the wear can become irregular. Often cracks due to high thermomechanical loading occur and exacerbate the flank wear by degrading protective coatings. As it often hard to discern different wear types from each other within the flank region, typical measurements of the average flank wear (VB) in industry, tend to take these other wear types into account in the average and maximum measurements. This is often a point of contention between different machinists who may measure the amount of flank wear using subtly different methods, especially for the cases of different tool and workpiece material combinations. Variation of tool substrate, assuming suitable hardness, can be said to have less contribution to the flank wear. Often flank wear is controlled and reduced using protective coatings for many machining operations [68, 69].

Plastic deformation

Plastic deformation of the tool material results in permanent deformation and change in geometry of the cutting edge without loss of tool material. Plastic deformation is mainly due to thermomechanical loading. This occurs when the stress state in the tools edge is raised above that of the cutting tool materials yield strength for the cutting temperature. This means plastic deformation (PD) happens when there are high cutting forces and high temperatures acting simultaneously on the cutting edge. Figure 2.10d shows examples of plastic deformation on the flank and rake faces. As labelled, these are known as PD impression and depression. Impression causes the inward deformation of the cutting edge and progresses down the flank face of the tool near the nose. Extensive plastic deformation leads to tools breaking along the deformed edges due to extreme stresses. To control the amount of PD impression and depression, the main influences on the characteristics of plastic deformation must be controlled. These are: (1) the hardness of the workpiece material which increases PD by causing higher cutting temperatures. (2) The V_s since increasing this (in isolation) directly increases cutting temperature. (3) The type of coolant/lubricant and the method of delivery for said coolant. One of the major concerns with plastic deformation is fact that the cutting edge and chip breaker geometry will no longer be as designed. If the edge rounding (ER) is altered via PD depression, and/or impression, the forces at the cutting edge will not be balanced optimally as designed and cutting temperatures will rise, accelerating PD. Tool designers must balance susceptibility to PD: one way to reduce PD impression is by lowering the tool ER, however, doing so can simultaneously raise susceptibility to PD depression. Another way to increase tool PD resistance is to modify the binder, for WC-Co tools decreasing the Co binder % will improved PD resistance but result in a more brittle tool, and visa-versa, increasing the amount of Co can improve tool toughness but increase susceptibility to plastic deformation. For the case of titanium machining tool suppliers must not only balance the PD resistance using Co% but also consider that increasing the Co within the tool will accelerate the chemical crater wear [70].

Flaking

Flaking refers to the removal of parts of the coating and the exposure of the substrate. Flaking does not occur consistently in a linear fashion and therefore is a non-continuous wear type. The main wear mechanisms that contribute to flaking are adhesive and thermo-mechanical. The adhesive load on the tool can cause the removal of the coating when the coating-tool bond is the weakest link in the sliding system. As the strength of the adhesion is controlled by the substrate and workpiece material, the coatings plasticity and adhesion must be considered depending on the application. Generally the thicker the coating, the higher the propensity to flake. Also, the tools surface finish can impact the propensity of flaking: tools with poor surface finish will result in higher local cutting forces and increase the likelihood of the bond between coating and substrate breaking. As previously described, cyclic thermomechanical loads can cause cracks, these can reduce the coating substrate contact and exacerbate flaking.

Cracking

Different types of cracks can occur on machine cutting tools. For the case of coated inserts there can be cracks that only penetrate the coating, and others, which extend below the coating and into the substrate. Deeper cracks that run parallel to the cutting edge and are mainly caused by mechanical fatigue, whereas, cracks that run perpendicular to the cutting edge, such as the ones seen in Figure 2.10b are called comb cracks. Comb cracks are resultant from cyclic temperature fatigue and occur in tools used for intermittent machining processes. They can be exacerbated depending on the type of thermal control (liquid or cryogenic coolant). Cyclic thermodynamic loading causes cracks in the direction of highest stress, often perpendicular to the cutting edge. Such cracks are more common when using CVD coated inserts but can still occur when using uncoated PVD cemented carbide inserts. For example, in WC-Co inserts comb cracks are caused by differences in the thermal expansion rate of the WC compared to the Co matrix. This is one of the reasons why the WC-Co binder ratio is very important in cemented carbide inserts: if the Co content is too high, the stress state difference between carbide and binder will be large and increase the likelihood of cracking. For coated inserts, CVD coatings can cause cracks to develop even before the inserts are used to cut material. This happens during incorrect temperature control during the cooling process of CVD application. Generally PVD coatings have better resistance to comb cracking due to relatively higher residual stresses resultant from PVD application.

Chipping

Chipping can be somewhat of an ambiguous term. Different terminologies are often used by tool designers and machinists to describe chipping, such as attrition or frittering. Chipping results from several factors; the fatigue during cyclic loading of the insert, adhesive wear or in chip hammering and jamming putting very high loads on specific locations on the insert. Chipping due to cyclic loading often arises in intermittent cutting processes. Chips caused by adhesion happen when machining particularly adhesive materials. This is one issue that is unresolved in terms of tool design for the titanium alloy Ti-5553. Chip hammering can happen when chips break too rapidly whilst still in contact with the insert, this causes instantaneous loading and de-loading of the insert which can lead to instantaneous chipping. Chip jamming is more prone to happening in closed machining processes like drilling where the chip becomes jammed during extraction. If this occurs it can cause unwanted instantaneous loads which can chip the tool and even cause fracture of the tool in severe cases. Neither chip jamming nor hammering occur for materials with very small chips, titanium chips however, are extremely problematic as they either break abruptly and cause chip hammering or become long and can snarl and jam. Titanium chips and swarf generation is discussed further in §2.5. In general, chipping can occur due to many combinations of wear mechanisms and often it is unclear as to the exact reason for a specific chip on the tool face. It is important to control all machining parameters to avoid this type of damage. However, selecting the correct parameters can be expensive for tooling suppliers due to the cost of identifying optimum tool parameters for different materials.

Fracture

Breakage of the cutting edge can occur due to high mechanical loads incident on a weakened cutting edge. Often an un-weakend cutting edge can resist fracture unless especially violent cutting parameters are used. Figure 2.10b shows fracture on the nose of the tool. This is a typical location for fracture due to weakening of the tool substrate in this region, additionally, it is where the highest forces occur. Weakening can be caused by any wear mechanism and depends on the tool material combination. Within industry chipping and fracture are often used synonymously, however, fracture normally attains to the failure of a tool while small chips are tolerated in some cutting applications before a tool is retired. In titanium turning the wear before fracture often occurs on the rake face and is chemical in nature. This weakens the cutting edge and causes plastic deformation that in turn accelerates flank wear and eventually results in fracture. In most machining processes tools are retired before fracture due to a VB limit. Again, the best control to avoid fracture is to use the optimum cutting parameters for the specific material and cutting tool being used.

Built up edge (BUE)

“Sticky” workpiece material from the chip can adhere to the cutting insert causing smearing. When such smearing occurs on the cutting edge and work hardening occurs it causes a

BUE. BUE damages the tool via the adhesive wear mechanisms. In some cases a BUE can retain an optimal geometry on inserts and improve tool life. The balance between a beneficial and detrimental BUE is hard to define but it can be said that an irregular BUE is often bad for the cutting operation. Materials with high smearing terminologies must be benchmarked thoroughly by tool suppliers so they can recommend cutting parameter and temperature control strategies to ensure the BUE does not limit the tool life. In titanium machining BUE can be a big problem. One major issue for tool manufacturers is that titanium alloys often have different adhesive tendencies depending on alloying elements. For example tools designed for the turning of Ti-64 at a specific parameter set cause extensive BUE in the machining of Ti-5553 [71, 72]. Machinists can often overlook that they are machining a different titanium grade and use the wrong parameters Therefore it is important that suppliers not only make clear what the optimum parameters are, but also have tested each alloy to find these parameters. Since it is an interaction between alloying elements and tool workpiece that governs BUE characteristics, it is extremely difficult, if not impossible to use simulation and modelling to identify the correct cutting parameters. For this reason tool manufacturers have to rely on time intensive and expensive benchmarking trials for parameter identification. For titanium alloys, which exhibit elevated adherence, the BUE can often be deposited on the machined surface which essentially welds fracture sites onto the part greatly reducing fatigue life [73].

Crater Wear

Sliding and sticking of the chip over the rake face with high thermomechanical loads causes crater wear. Most commonly formed during continuous engagement of the tool chip and workpiece, crater wear is often constant and the rate can be predicted. Applications where crater wear is a major issue often make use of coated tools. For such, the first stage of crater wear is the wear and removal of the coating on the rake face, correct cutting parameters must be used to ensure this does not happen too fast and void the benefits of the coating. Once the coating is removed, the crater increases in size gradually. The crater geometry and location are often similar to the one in Figure 2.10a labelled CW. The rate of crater growth is controlled by the magnitude of the thermomechanical loading and the tool and workpiece material affinity. Both abrasive and chemical wear mechanisms can contribute to the craters growth. On the rake face closest to the cutting operation the latter is more likely to occur as this is the sticking zone and instead of sliding the chip shears. Further from the cutting edge there is more likely to be abrasive wear caused by the sliding of the chip against the tool substrate. For the case of titanium turning with WC-Co tools temperatures in the sticking zone can exceed 1000°C [26, 67]. This causes accelerated diffusion-dissolution and decarburisation of the WC tool, which drives the crater wear rate [29]. The mechanism by which the dissolution and decarburisation occurs is discussed in §2.4.2 on the diffusion and chemical interaction of titanium with WC-Co.

2.4 Chemical interaction between titanium and WC-Co tools

The chemical interaction between titanium and WC-Co tools is extremely important; WC-Co is the most common tool material used in titanium machining and the interaction between the tool and workpiece governs the characteristics of the machining process. To understand the interaction between the tool and workpiece materials the diffusion behaviour of titanium must first be addressed.

2.4.1 Diffusion in the α and β phases

Diffusion within the β phase in titanium is drastically increased compared to the α phase. The self-diffusion of titanium at 1000°C (analogues to machining temperatures), is of order 10^{-13} (m^2s^{-1}) for β, but 10^{-15} (m^2s^{-1}) for α [74]. Diffusion within cubic lattice systems is isotropic, whereas for hcp phases it is anisotropic.

For titanium alloys the influence of different alloying elements on mechanical properties is often related to their diffusive properties within titanium. Generally, slower diffusion within the α-phase corresponds to lower deformability and ductility, but higher creep and oxidation resistance. The specific diffusion characteristics of certain elements can be used to enhance certain material properties, for example, Si improves the creep performance of near α alloys due to either its interaction via diffusion with regions of high dislocation density [75], or by precipitating silicides [76]. Other elements can have deleterious effects, introducing interstitial elements like hydrogen, which has rapid diffusion in both α and β phases, can significantly reduce fatigue via embrittlement [10]. Other interstitial elements like Fe can cause similar detrimental effects such as hindering the diffusion of alloying elements such as Al with the α-phase, thus Fe is often kept as low as possible.

As a result of the relationship between diffusivity and mechanical properties it is important that during the design of alloys, the various self-diffusion of differing substitutional elements in both phases is understood. Nakajima and Koiwa have reviewed both the self and impurity diffusion for the α and β phases and the influence of phase transformation, diffusion anisotropy, atomic size and correlations between solubility and diffusivity [77]. They make clear that the diffusion of transition elements within the α-phase is rapid, almost three to five orders of magnitude faster than self-diffusion which is facilitated by the vacancy mechanism. For Fe, Co and Ni interstitial diffusion is suggested as the probable diffusion mechanism. The interstitial diffusion mechanism (dissociative mechanism) was originally proposed by Frank and Turnball as a mechanism of diffusion of copper and germanium [78]. The difference in the self-diffusion of titanium, compared to that of the transitional elements, is evidenced by the relative increase in self diffusion rate when α to β phase transformation occurs.

2.4.2 The interaction of titanium and WC-Co during crater wear

From the point of view of machinability, it is important to address the relationship and current knowledge regarding the interaction of titanium with WC-Co, the most commonly used tooling material for most titanium alloy machining applications. Seminal research by Hartung and Kramer (1982), identifies that although flank wear may be the defining factor of whether a tool reaches the end of its life, it is actually crater wear which is critical in determining tool life, because as the crater develops, the flank is more prone to plastic deformation and so will begin to wear faster [26]. Crater wear is driven by chemical interaction between adhered workpiece chip material on the rake face of the tool. Hartung and Kramer proposed that between the tool and adhered material a reaction layer formed via dissolution of tool constituents into the chip. They declared the rate of crater wear would be dictated by the balance of tool dissolution and diffusion rates. They hypothesised that the reaction layer would be primarily TiC, formed by the diffusion of C from the tool material whilst dissolution occurs. They detected TiC for polycrystalline diamond and WC-Co tools when turning Ti-64 by using hydrofluoric etchant, EDS and augar spectroscopy. In their experiment they also employed thermocouples to measure cutting temperature which have been used and cited frequently within subsequent work by many authors.

The current understanding is that the temperature on the rake face of the tool, within the crater region, is between 900°C and 1050°C [26, 79, 80]. In 1986 Dearnley et al. tested a range of coated and some uncoated WC-Co straight and steel cutting grade inserts for the turning of Ti-64 [67]. They found that the dissolution diffusion mechanism was present for all of the uncoated WC-Co inserts, but only some of the coated counterparts. The wear was measured to be more extensive for coated tools which wore via dissolution diffusion in some cases and attrition in others. Hartung and Kramer reported that the dissolution diffusion mechanism wears tools slower than if attrition and sliding mechanisms are permitted to dominate. Dearnley et al., also found that tools with roughly 6% Co binder content performed best, those with more than 6% were observed to have increased plastic deformation at the cutting edge and those with less had increased notch wear on the tool flanks. This supports Hartung and Kramer's hypothesis that as the crater develops, the flank is more likely to wear via plastic deformation. Sun et al., found that as crater size increased so did the cutting forces incident on the flank and cutting edge of the tool which would correspond to more serious plastic deformation [81].

In several instances static diffusion couple methodologies have been utilised to investigate the interaction between WC-Co tools and titanium alloys. Hatt et al., identified that the system is much more complicated than the simple mediation of diffusion via TiC which was proposed by Hartung and Kramer. Their initial work identified that there are a range of

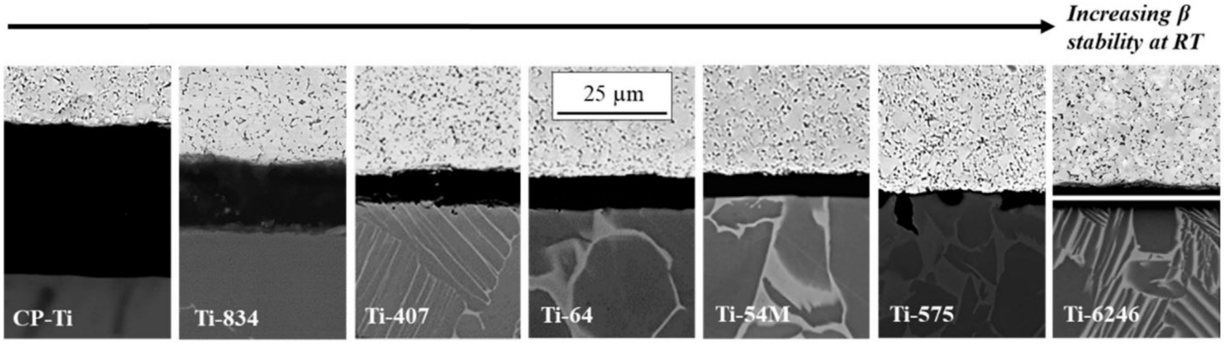

Figure 2.11: BSE micrographs of the TiC layer at the interface between the WC-Co(6%) tool insert and CP-Ti; Ti-5.8Al-4Sn-3.5Zr-0.7Nb-0.5Mo-0.35Si (Ti-834); Ti-3.9V-0.85Al-0.25Si-0.25Fe (Ti-407); Ti-64; Ti-5Al-4V-0.8-Mo-0.5Fe (Ti-54M) and Ti-5Al-7.5V-0.5Si (Ti-575) from Figure 4 in [84].

phases that could form at the interface depending on what alloying elements are present and the temperature distribution [82, 83, 28]. In particular they found the formation of brittle eta (Co_xW_yC) phases , M_6C ($x + y$=6) and $M_{12}C$ at the interface to be detrimental to stable formation of TiC protective layers. This work highlighted the need for tool designers to make tools and coatings which promote stable interfacial phases at the interface. In later work, Hatt et al., identified some key features of the interaction by investigating the effect that Al, Mo, Cr and V have on TiC formation at 1000°C using WC-Co(6%) [84]. They found that increasing any of the aforementioned alloy additions, decreases the size of TiC at the interface. They also identified that commercial alloys with increasing Mo equivalency yield smaller TiC reaction layers, as shown in Figure 2.11. Their conclusion was that a reduction in TiC formation reduces the resistance to crater wear and so alloys with higher Mo equivalency experience more rapid crater wear during machining - due to more rapid dissolution diffusion of the tool material into the adhered material within the crater. Ramirez et al., have also employed diffusion couples to investigate the reaction between a WC-Co(10%) tool and Ti-54M, a Ti-64 variant produced by TIMET as a more machinable alternative [85]. Tests were performed at 1100°C and identified a Co rich region, a TiC layer and significant dissolution of the WC within the Ti-54M. Alongside this, they ran experimental tests which somewhat validated the results obtained from diffusion couples by identifying W within adhered titanium on their tools.

Although static diffusion couples provide valuable insight into the interaction between alloying elements and the tool material for the titanium and WC-Co system, they cannot be used to define the exact mechanism by which crater wear proceeds in the dynamic machining process. As a result, detailed analysis of the crater region on WC-Co tools has been carried out by several researchers. They have found the dynamic situation to be more complicated than the results obtained from analysing diffusion couples suggest. Odelros et al., analysed both WC-Co Ti-64 diffusion couples and the crater wear on inserts used to machine Ti-64

[29]. They used scanning electron microscopy (SEM), energy-dispersive X-ray spectroscopy (EDS), wavelength-dispersive X-ray spectroscopy (WDS) and X-Ray diffraction (XRD). As expected, in the crater, they found titanium and carbon enrichment, indicating TiC. However, in their SEM images they did not find a TiC layer, but instead found disparate TiC at the interface and within the adhered material in the crater. Through comparing the crater wear interface to WDS data obtained from the diffusion couple sample shown in Figure 2.12, they saw a significant difference between the dynamic and static cases; a more recognisable TiC layer was shown to form in the static case. The WDS carried out on the diffusion showed that the transition of WC to W(bcc); the resultant fringe-like morphology at the interface was similar for both the static and dynamic cases. This also highlighted the rapid diffusion of Co into the titanium which is difficult to detect in the dynamic process. Odelros et al., proved that the WC within the crater had been transformed to W(bcc) using XRD. They also proposed that local equilibria were forming between the titanium and Co which facilitated the formation of metallic carbides. DICTRA analysis of such local equilibria identified the possibility of a liquid phase forming at the interface and enhancing decarburisation. There was no other evidence that such a phase existed at the interface except for an exceptionally smooth crater. Regarding the decarburisation of the WC, molecular dynamic simulation has shown that the more C that is lost from the WC the faster C will be depleted subsequently [86]. Kaplan et al., have evidenced the fringe-like morphology at the interface of the crater on inserts used to turn Ti-64, they also showed XRD evidence that reaction products such as (Ti,V,Al)C were forming within the adhered material and appearing as black precipitates within the adhered layer [87]. An SEM image of the dark precipitates is shown in Figure 2.13, which has been taken at the crater interface on a tool that is WC-Co(6%), used to machine Ti-64. By testing tools with different Co binder they suggested that the less Co, the higher the propensity for such reaction products to form. Kaplan et al., also showed that there are specific locations, enriched in titanium, where (Ti,V)C forms. Figure 2.14 shows a top down image of the crater with such locations highlighted in red. Saketi et al., have shown that temperature enhances the rate at which the WC is decarburised by imaging the interface of inserts used at different cutting speeds (V_s) [88]. Below 60 m/min the interface in the crater had no definitive fringe-like morphology and attrition was shown to dominate. On the other hand, at 90 m/min the fringe-like morphology was evidenced and the diffusion driven dissolution of the WC dominates.

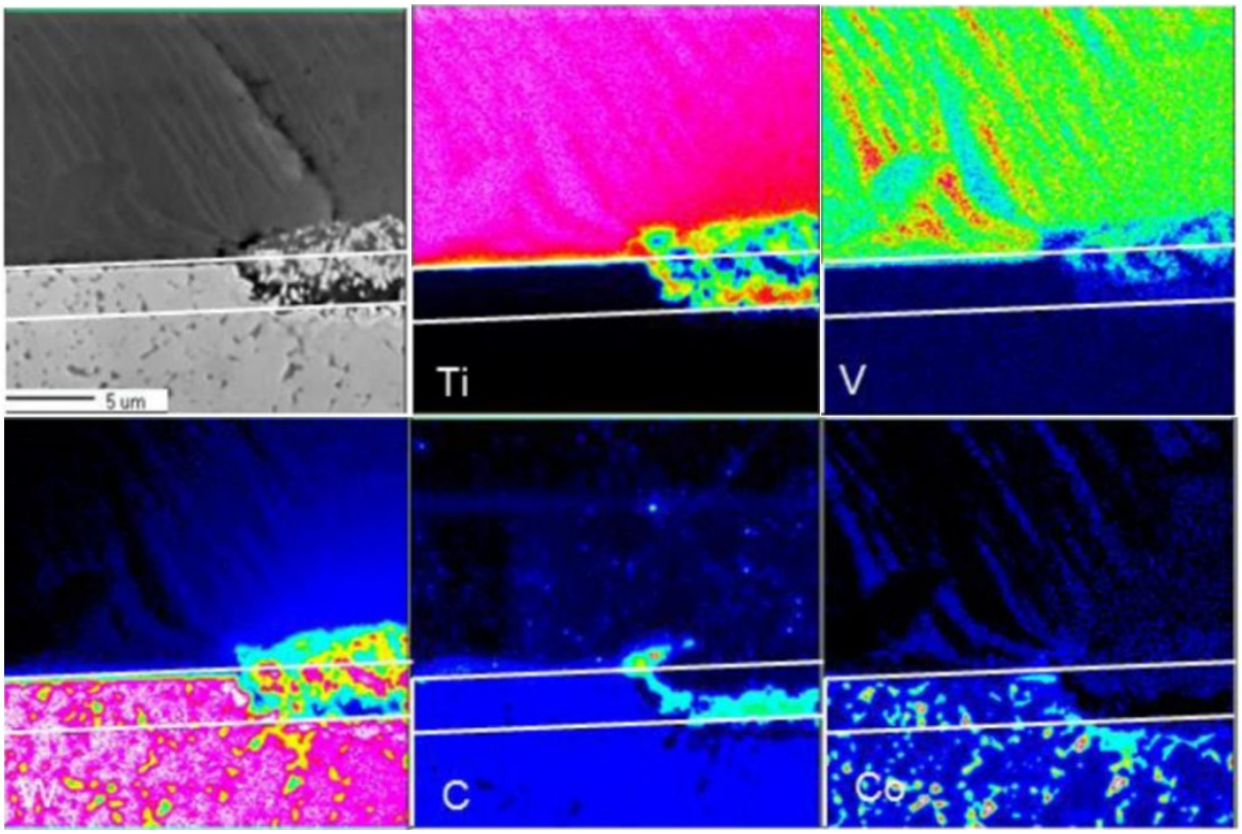

Figure 2.12: WDS map for Ti64 WC-Co diffusion couple adapted from Odelros et al., (2017). Modified from Figure 11 in [29].

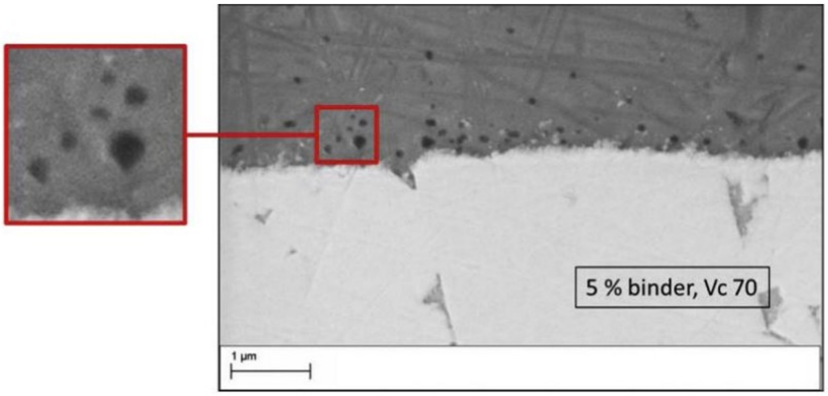

Figure 2.13: SEM images of the crater cross section of a WC-Co insert with 5% Co, used to turn Ti-64 at 70 m/min. Modified from Figure 2 in [87]

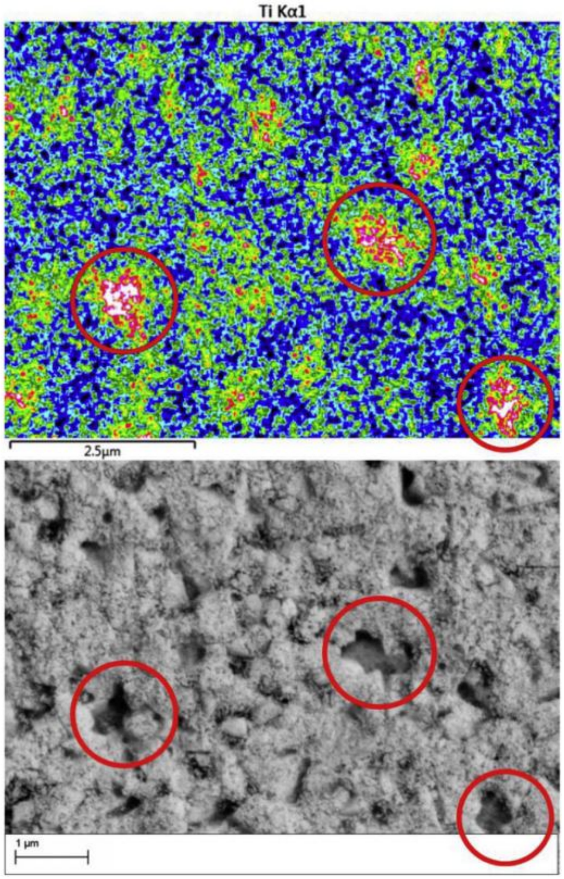

Figure 2.14: EDS map and corresponding BSE micrograph showing titanium enrichment within a crater on the rake face of a WC-Co tool used to machine Ti-64 at $V_s = 115$ m/min. (red = high, blue = low). From Figure 4 in [87].

Unlike in steel turning, where crater wear rate is governed by the chip-tool contact temperature and flow rate [89], crater wear rate in titanium machining is heavily influenced by Co. One reason for this is because the transition metal Co, is known to diffuse fast in titanium via the interstitial diffusion mechanism. As a result, when WC-Co is used to machine titanium the Co is the fastest constituent to diffuse into the chip material and controls the rate of tool degradation. This is supported by the work of Hua et al., who successfully modelled diffusion of Co in combination with the contact temperature and flow rate to predict the rate of crater wear in titanium machining [70]. Sadik et al., found in the turning of Ti-5553 crater wear rate is slower when using a tool that has 3% Co binder on the tool rake face and 6% in the body of the tool, demonstrating that tailoring the Co content for specific regions of the tool can improve performance [90]. Thus far transmission electron microscopy (TEM) has had limited use within the field of crater wear, however, where it has been utilised TEM has been used to investigate the WC-Co and adhered titanium interface within the crater region there is evidence that the Co, which exists between WC grains is facilitating more rapid decarburisation of the substrate than elsewhere [91].

2.4.3 Coating technology in titanium machining

Tool coatings are used within the machining industry to provide tool life or productivity benefits. Of course, this depends on the material and type of machining as each significantly changes the conditions at the cutting edge(s). For titanium, most coating technology is investigated and targeted for Ti-64 since it is by far the most used alloy (up to 50% of all titanium machining).

Both CVD and PVD coatings are used in titanium machining. The deposition method can be considered to affect coating performance; CVD, deposited at high temperatures generally between 800°C and 1000°C, enables creation of high purity thin films. For example, to reduce flank wear, thin films of TiCN can be formed to improve abrasive wear resistance. On the other hand, depositing via PVD (at lower temperatures, up to 600°C), can induce residual streses within the edge line of the tool, improving the edge line toughness. The PVD-TiAlN coating, was designed to have good flank wear resistance, which is given by a high proportion of aluminium in the coating. In titanium machining many investigations have been conducted to identify the best coating to slow the rate of flank wear. In the past, research conducted by Dearnley et al. in 1986, on turning titanium, identified that many coatings such as TiN, TiC, Al_2O_3, and HfN had accelerated flank wear when compared to uncoated WC-Co tools, regardless of whether chemical or attrition based mechanisms dominated [67]. Not tested by Dearnley et al., PVD-TiAlN coatings are sometimes used for the machining of titanium. PVD-TiAlN is generally utilised because it enables exceptional productivity. This is because it increases the heat resistance, hardness, wear resistance, lubricity and oxidation resistance of the tool [92, 68]. However, for the case of titanium turning, Choudhary and S.Paul used tool wear and cutting energy analysis to show that

PVD-TiAlN coatings perform no better than uncoated tools and in some cases reduce the life of tools [93]. For the case of milling titanium, TiAlN coatings on WC-Co tools have been found to be beneficial: Uddin et al., has shown such coatings can improve tool life by up to 44% [23]. In their work the improved tool life was only demonstrated for 16 meters of cut and so their conclusions are only valid for initial stages of the tools life. For the case of drilling, there has been relatively fewer investigations into coating effectiveness on reducing flank wear, a study on Ti-64 by Sharif and Rahim identify that for initial cutting (first 25 holes), a TiAlN coated drill will outperform uncoated carbide in terms of tool wear [94]. TiAlN coatings are widely used for the drilling application regardless of the titanium alloy selected, there is a need to investigate the effectiveness of this coating on other alloys than that of Ti-64 to ensure tooling suppliers do not waste resources on coatings unnecessarily.

2.5 Machinability

The term machinability is used frequently in both academic and industrial literature to address and compare the difficulty of machining different materials. Discussion of machinability can encompass multiple subject areas, which in turn, can be defined within key categories; chip formation characteristics, cutting forces, tool wear and tool life and the materials response in terms of the machined surface condition and subsurface damage (both of which contribute to the surface integrity). The extent to which each of these subjects is discussed within literature often depends on the perspective of the researcher or institute which is dependent on how they will profit from the results, and hence, the cost effectiveness of the research. For example, while tool manufacturers must be mindful of the surface response and machine process conditions, their main goal is often to pursue understanding of how their tools wear to improve tool life to be competitive within their industry. Aerospace manufactures on the other hand, base their assessment of machinability on the speed at which they can produce aircraft which involves maintaining a high material removal rate (MRR) whilst maintaining component reliability and minimising the time taken for surface quality evaluation. Material manufacturers looking to provide new materials for the aerospace industry must be able to offer competitive pricing compared to the alloy they wish to replace. This requires them to demonstrate the improved machinability to both tooling and aerospace manufacturers. In this section several academic studies of machinability are reviewed to address how chip formation, cutting forces, tool wear, tool life and material response are used to assess machinability. In addition, two established methods of machinability assessment which are used within industry are discussed; the V15 and COM-de-coup method.

2.5.1 Chip formation characteristics in titanium machining

One of the most established ways of assessing the chip formation in industry is by using the ISO 3685 standard to assess chip morphology. This grades swarf based on a set of characteristics like length, serration and radius [95]. Generally in metal cutting, optimum chip formation occurs when a continuous chip with uniform thickness forms. That being said, if continuous chips become too long, removal can be an issue and snarling or jamming can occur. For this reason, tool geometry is often utilised to cause advantageous chip breakage during machining [55]. In the case of titanium machining, achieving a chip with uniform thickness is exceptionally difficult. In titanium chips, the strain is compacted into narrow regions which manifests within extreme shear bands [96]. Between such shear bands, there is much less deformation of the material resulting in a serrated chip as shown in Figure 2.15 [97]. Characterisation and understanding of deformation zones in machining is important when considering machinability and can be achieved through advanced EBSD techniques [19]. The location and direction of the sear bands indicates the location and orientation of the shear plane, the shear occurs along this plane when the stress overcomes the yield strength of the material. Once the deformation occurs along the shear plane the energy involved is transformed into thermal energy. Since titanium has low thermal conductivity the heat is concentrated locally and high temperatures are reached. The local concentration causes thermal softening within the shear band and deformation is thus further concentrated within the shear band [98, 99]. As the tool continues to cut, the shear band continues to propagate and rotate until it is more energy efficient to form a new band, this is termed adiabatic shear. This process is cyclic and results in a serrated saw tooth chip formation evident in Figure 2.15.

In titanium twist drilling the wrong process conditions can lead to poor chip evacuation and entanglement as they exit the flutes of the drill [100]. Lower V_f result in longer continuous chips, then as the V_f is increased, the chip increases and chips become shorter and stiffer. Increasing the V_s while keeping the V_f constant reduces chip thickness and results in thinner less stiff longer chips. Moteshini et al., found microstructure plays a significant role in chip form and characteristics; the chip serration from α alloys is much smaller than that of $\alpha + \beta$ alloys like Ti-64 and the serration of metastable β, like Ti-5553 is even more pronounced than $\alpha + \beta$ alloys. This is a result of more extreme adiabatic shear occurring where within the β phase [101]. Since temperature affects the extent of adiabatic shear, it has been evidenced to play a significant role in chip serration and length [102].

2.5.2 Cutting forces in titanium machining

Cutting force, feed force and in drilling, torque, are influenced by almost all aspects of machining, in general force minimisation is desirable to reduce tool wear and improve surface integrity [55]. The magnitude of force can be controlled by altering the chip thickness by modifying the V_f and V_s. More conservative parameters will minimise the force, but for an industry where productivity is critical, manufacturers cannot afford to machine in this way. They must instead aim to have the highest productivity without exceeding excessive force or variation in force. This balance is extremely difficult to achieve and requires a different set of parameters for every material and machining setup. Analytical models are used to predict cutting forces but can lack the accuracy that empirical investigation on a particular setup can provide [56]. This is because there are so many factors which can effect forces and variation in force, this is especially true when machining titanium. In titanium turning, the cyclic nature of the chip formation causes cyclic forces on the cutting edge of the tools. The cyclic loading can cause chatter and instability within the process. Chatter is a term used to describe the resonance or harmonic instability between the tool and workpiece. Motonishi et al., found that more for heavily β stabilised alloys, the effect is more pronounced and the amplitude of the cyclic forces is increased, resulting in more wear [101]. Cutting forces can also be influenced by changes in cutting edge geometry due to BUE, a characteristic of titanium machining. Oliaei et al., demonstrated that a larger cutting edge radius, such as that created by BUE, creates a large negative rake angle which drastically alters the way chips develop and break during cut [103]. Both the feed and cutting forces were shown to increase during the start of machining as the BUEs formed, the feed force increased more than the cutting force. In drilling, variation in force may cause the spindle to vibrate resulting in destabilisation of the cutting process and premature drill tool failure via chipping or fracture. Spindle torque is often used as a measure of friction and indicates higher cutting

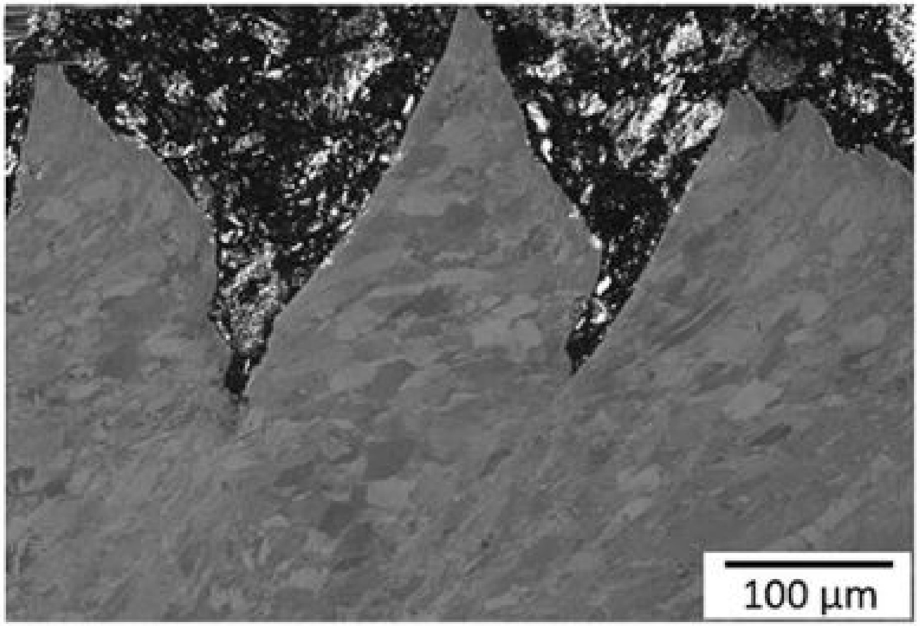

Figure 2.15: SEM micrograph of a Ti-64 serrated chip microstructure [97].

temperatures [53]. Temperature is critical when considering forces, there is evidence that the use of different coolant-lubrication methods can significantly reduce the torque with air blown condition having the highest torque and palm oil minimum quality lubrication (MQL) exhibiting the lowest [104]. The cutting forces involved in titanium drilling are generally similar to those observed in both nickle superalloy and steel drilling [25]. Although this is the case, it has been reported that much higher stresses occur in the localised region around the cutting edge in titanium machining. This is due to titanium's resistance to deformation at elevated temperature and the small contact area between the titanium chip and the rake face of tools [105]. Since the forces involved during machining are an indicator of machinability, some researchers have used them to compare the machinability of different alloys. Kosaka et al., showed that drilling Ti-54M required less torque than drilling Ti-64 at several different RPMs. They used this to indicate that Ti-54M was the more machinable alloy [106]. In their work, they also identified a key relationship between the cutting torque of initial holes and tool life. The higher the torque measured during the drilling of an initial hole the lower the too life, this followed a negative log relationship [107]. Although Kosaka et al., did show the superior machinability of Ti-54M in terms of reduced torque, they did not investigate the surface integrity or microstructural damage in their research. It has since been found that although Ti-54M is more machinable in terms of tool wear there is uncertainty about the quality of the surface integrity after machining [108]. Ti-54M is a good example of how an alloy can be reported to have better machinability when only one aspect of its machinability, i.e tool wear, has been investigated. Ti-54M was developed as affordable alternative to Ti-64. Uptake of the alloy has been minimal not only because of the integrity concerns but also because effective utilisation would require an overhaul of many machining strategies, damage assessment methods and component design which would not be cost effective.

2.5.3 Tool wear and tool life in titanium machining

There have been huge improvements in high performance cutting tool technology [109]. However, poor thermal conductivity inherent of titanium alloys causes heat to be concentrated on the flank and rake of the cutting tool. This, combined with the high tendency for titanium to adhere to the cutting tool and react with the tool substrate, in addition to the cyclic force due to unfavourable chipping, results in extreme thermomechanical loading and therefore rapid tool wear during machining. Within the literature there has been a considerable effort to characterise and understand how tools wear during the machining of titanium in order to provide a basis for tool designers to improve tool life, reduce the wear rate and increase productivity [25]. Since Ti-64 is the workhorse alloy of the titanium industry, much of the current literature is focused on this alloy. However, since the critical wear mode involved in titanium machining is chemical, and there is significant evidence that chemical wear progresses at different rates in different titanium alloys [28, 84], there should be a more concerted effort to investigate the effect of alloy chemistry on chemical crater wear. Studies such as that carried out by the AMRC TMG group endeavour to assess the machinability of many titanium alloys simultaneously [110]. Although this work provides exceptional amounts of data for different titanium alloys, including the specific cutting force coefficients for each alloy, it does not help further understand why tools wear at different rates, and therefore, although it may be of use for optimising machine tools it is not beneficial for improving tool design. Arrazola et al., provide an extremely informative study on the machinability of Ti-64 compared to that of Ti-5553 in turning. In the work they identify that the machinability of Ti-5553 is 56% more than that of Ti-64 by assessing the amount of tool wear, the chip morphology and the specific cutting/feed forces [72]. While assesing the differences between Ti-64 and Ti-5553 machinability and identifying that adiabatic shearing between alloys may increase the loads on the tool, the study does not provide evidence on how more extreme loading results in more rapid diffusion wear and so will only be of limited use to tool designers looking to improve tool wear resistance. That being said, the work by Arrazola et al., has proved an excellent basis for future work to refer to by providing a quantitative measure of machinability between two different alloys. The most beneficial research for tool designers looking to improve their products for machining of titanium alloys come from those who have directly targeted the critical wear mechanism for investigation [29, 87, 84, 85, 70] which are discussed in §2.4.2. Such work has proved tools can be deigned in specific ways to improve chemical wear resistance and therefore are exceptionally valuable to tool manufacturers [90].

The aforementioned studies, and generally the majority of research into tool wear for the machining of titanium alloys is not conducted in drilling investigations. The limited amount of research of tool wear in drilling has been obtained through the drilling of Ti-64. Sharif et al., reviewed titanium machinability in drilling and identified that in terms of tool wear non-uniform flank wear, excessive chipping and micro cracking were the dominant failure mechanism of tools [54]. They identified that flank wear width was proportional to the V_s and that as the wear progresses the adherence of work piece material leads to attrition wear which can result in sever chipping. There is evidence that in drilling the amount of adhered material differs depending on the type of titanium alloy machined. This combined with the fact that the amount of adhered material is linked to tool failure indicates that in drilling tool failure may be closely linked to the interaction between tool substrates and the workpiece alloy [111]. Tools have generally been identified to fail catastrophically from cracks which initiate on the rake face of the tool and propagate along the flank face after significant attrition and diffusion wear have degraded the too material [112].

2.5.4 Machined surface condition in titanium machining

Titanium alloys are often used for critical aerospace applications. Since poor surface condition in terms of surface roughness, residual stress and microstructural hardness can be indicative of poor fatigue life and reliability [40, 113]. This is because scratches, defects and grooves within the surface act as sites of crack initiation. For the case of turning, friction induced damage has been shown to cause a reduction in fatigue life under high cycle fatigue testing. Gao et al., found the friction marks acted as crack initiation sites when samples failed [114]. In milling, the fatigue life of components has been linked to the stress condition of the machined surface. Moussaoui et al., found that by imparting more residual stress into the surface by using a moderate V_s and V_f they could improve the fatigue life. They also found that as a_p does not impact the life of the component significantly it should be maximised to improve productivity. In their study they claimed their optimised machining plan would improve the fatigue lifetime by 2.7 times compared to reference industrial parameters [115]. Cox et al., have found that titanium can adhere to the machined surface and weld fracture sites to the workpiece severely reducing fatigue life [73].

In the drilling of Ti-64, Rahim and Sharif have shown faster V_s reduce surface roughness and consequently improve the surface integrity of holes [116]. They attributed the improvement in surface quality at high V_s to the increase in cutting temperature and a reduction in friction between the tool and workpiece. Rahim and Sasahara have found that the machined surface (Ti-64), can experience thermal softening and subsequent hardening due to localised heating during the drilling process [104]. In work hardened regions the hardness increases depending on the V_f and V_s, higher V_f and V_s, and thus higher temperature, results in higher hardness.

In titanium machining the deformation within the subsurface microstructure of machined components is important. Different types of microstructural deformation can severely impact the integrity of machined parts. Velásquez et al., use a three region system to characterise the subsurface microstructure of machined samples [117]. Figure 2.16 shows the three regions in a Ti-64 sample machined at a V_s of 260 m/min where P1 is the bulk material referred to as the unaffected zone. P2 shows a region of plastic deformation in which the microstructure is deformed in the machining direction, the type of deformation shown within P2, Figure 2.16 is often referred to as swept grains. P3, the highly perturbed region, shows the severe plastic deformation and is closest to the machined surface. In P3 there is intense plastic deformation of the microstructure. This region is significantly affected by thermal softening and subsequent hardening which depends on the thermomechanical loading resulting from the cutting parameters. In extreme cases this region can become what is referred to as white layer, although some refer to white layer as its on region separate to P3. White layer is typically characterised as a region of ultra-fine grains and is extremely detrimental to surface integrity of components. White layer generally exhibits high hardness, low ductility and results in extreme residual stress within the subsurface [118]. The presence of white layer has also been correlated with a significant drop in fatigue performance [119]. In nickle superalloys there is evidence that the fatigue life of drilled samples without white layer is 30 times better than those with it [120].

In drilling, the machined surface condition is often assessed in terms of either surface roughness, hardness or residual stress and not microstructural damage. There have been very few titanium drilling investigations that have examined the microstructure of the drilled subsur-

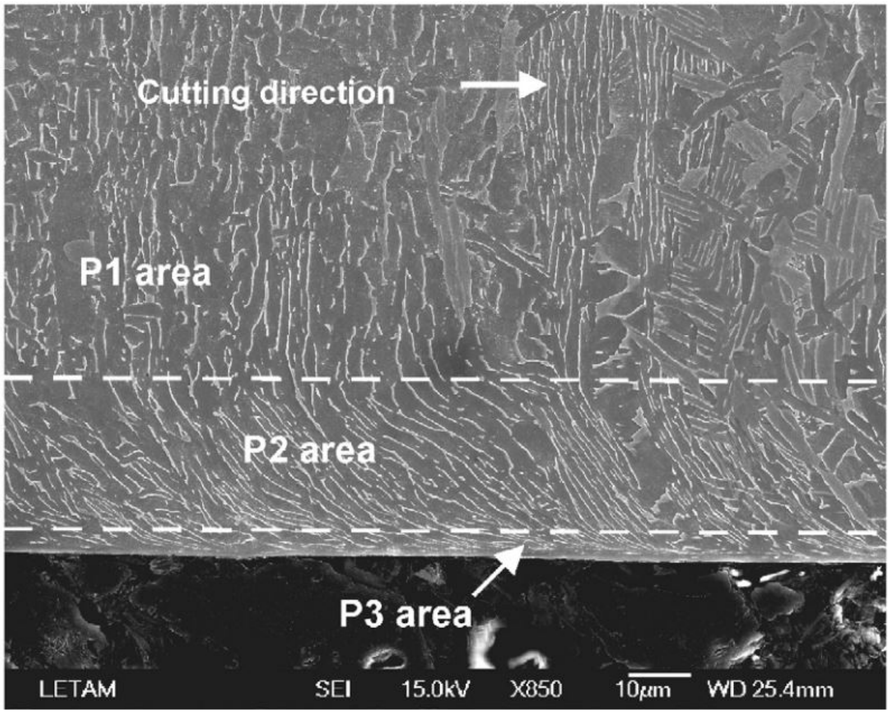

Figure 2.16: Three regions of deformation in the subsurface of Ti-64 machined at 260 m/min. Modified from [117].

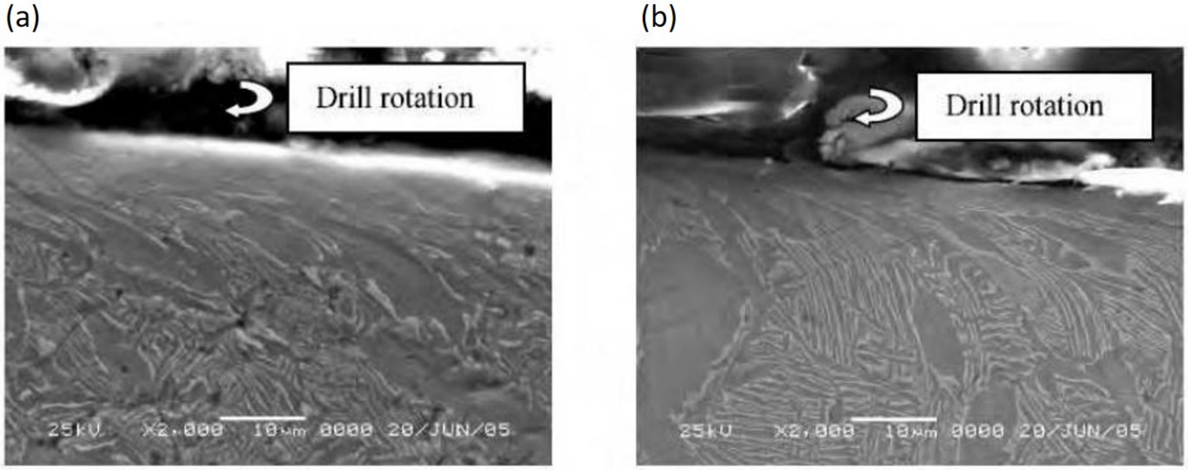

Figure 2.17: SEM image showing the subsurface deformation in Ti-54M when drilling at (a), $V_s = 25$ m/min and (b), $V_s = 45$ m/min using WC-Co tools with 6mm diameters. Modified from [116].

face. Rahim and Sharif have investigated the microstructure hardness under the machined subsurface. They found that for different machining parameters there are significant differences in the microhardness characteristics, they attributed this to changes in heat causing transformation of the α and β phases within the microstructure due to differing temperatures. Rahim has imaged the machined surface using SEM and shown the way in which the machined surface can be seen to be swept in the direction of drill rotation. The extent of the deformation has also shown to decrease as V_s is increased. Figure 2.17 shows the swept grain plastic deformation for a drill used at 25 m/min on the left and 45 m/min on the right. There has been very little investigation into the subsurface damage due to drilling in titanium alloys especially those which are not Ti-64. The subsurface damage and integrity of other titanium alloys, especially those which have higher β stability than Ti-64 and which are used for critical applications must be investigated. Investigations into this could provide essential information to tool suppliers so they can modify their machining strategies when machining more β stable alloys to reduce tool wear and improve material surface integrity.

2.5.5 Methods of machinability assessment within industry

V15 Method

The V15 is a standardised method used for comparing machinability in turning, of different materials or alloys [110]. It aims to encapsulate both tool wear rate and productivity in a single value, the V15, which is the maximum V_s for a particular set of parameters which allows for 15 min of cutting before the tool is considered to fail. The failure point of tools is often measured by the extent of the flank wear and any set of turning tools may have an average and flank wear limit. To standardise the way limits are defined within standard certifications such as ISO3685 [95], although many companies may use their own in-house standards. Through comparing the V15s of different materials it is relatively easy to compare achievable productivity. This often translates to cost effectiveness, especially within rapidly growing industries like aerospace where raising production targets is a primary goal. The V15 does not facilitate understanding of why different materials are more machinable, although it can help to highlight key relationships so more detailed comparison studies between particular alloys can be designed.

COM Method

The COM-Couple Outil Matiere or the “Couple tool-material” investigation method is used to find and define the working zone of a particular tool for a specific application. For example, WC-Co H13A inserts and turning Ti-64. The method enables the minimum and maximum of all relevant cutting parameters to be defined independent of one another. Relational parameters like the material removal rate or tool wear rate, (based on the Taylor model described in §2.3.2), are found and are used to ensure cutting parameters are not all maximised or minimised simultaneously. Auxiliary parameters such as the specific cutting force and f_{rev} are also used to calculate the cutting conditions. These conditions can vary depending on the machining setup. The methodology consists of four stages including; (1) the predetermination, (2) working zone determination, (3) wear and tool life measurement and (4) auxiliary identification. The predetermination test is used to identify if the tool is compatible with the material and to find the maximum V_f and V_s. To do this the V_s is changed for every hole that is drilled (for at least 6 holes). During testing the tools are regularly checked for catastrophic failure. In addition to this, chips are collected and any unexpected phenomena recorded. The V_s is modified continually until the range of V_s in which the tool can operate is found, then a similar process is carried out to determine the V_f range. Feed force is recorded for every hole and the morphology of the chips are assessed according to a set guideline. Other responses that are collected when possible include the cutting power and spindle torque. From the predetermination data the specific cutting forcers are calculated and plotted. Limits of the working zone are defined from the results of the predetermination. The second stage, which involves characterising the working zone of the tool between the previously defined limits is carried out by identifying six incremental points between the zone limits, and a hole is drilled at each point. Again, the specific cutting forces are calculated and plotted against the V_s and V_f. Chips, hole quality and signal stability are also measured in various ways for each hole. From this data the most stable region of the working zone is defined. In the third stage the tool wear is assessed at specific points within the characterised technological working zone. The selected points often depends on whether the investigator is trying to optimise for hole quality, productivity, chip formation etc. The wear measurement used is of flank wear and is assessed based on the Taylor model [62]. In the final stage of testing the auxiliary parameters like specific cutting force are evaluated according to a model.

The COM method of tool material assessment works well for identifying the operational window of cutting tools for specific applications. However, the method is very restrictive as a method of investigating tool wear and material damage characteristics. The COM method also requires four stages of testing which can be very time and resource intensive to carry out using industrial equipment. Since in the COM method only flank wear is measured, there is no possible investigation into what wear mechanisms may be active and therefore no way of understanding why tools are wearing in a particular way or at the rate they are. The method also only enables investigation of qualitative hole quality aspects, like hole diameter and roughness therefore omitting any investigation of microstructural damage, which in titanium alloys is very difficult to quantify due to the diverse range of achievable microstructures and damage modes.

2.6 Chapter summary

This literature review has covered the classification and application of titanium alloys, the chemical interaction that drives tools wear between titanium and WC-Co tools, machining processes including orthogonal cutting, turning and drilling, tool wear in titanium machining and key aspects of machinability assessment. The literature discussed under these topics establishes the background and fundamental ideas required for the experimental section of this work.

The literature review has highlighted key avenues that need to be further investigated to improve the machinability of titanium alloys. There is significant opportunity to improve drilling strategies for titanium alloys, especially those which are relatively expensive for industry to benchmark, like metastable β alloys such as Ti-5553. To do this efficiently a methodology which enables rapid microstructural subsurface damage and tool wear assessment should be developed, enabling rapid machinability comparison of alloys such as Ti-5553, with more thoroughly researched alloys like Ti-64. Since in all machining operations the chemical interaction between titanium and WC-Co contributes critically to wear, and since the rate of chemical wear is seemingly dependant on the β stability of alloys, detailed investigation of crater wear in Ti-5553 could provide an exceptional oppurtunity to elucidate the mechanism by which crater wear manifests in titanium machining.

2.7 Summary of work

This body of work has been conducted to pursue those avenues highlighted within the literature review, to have significant potential in improving the machinability of titanium alloys. Therefore, in this thesis, several experimental sections are presented which endeavour to further understand the machinability of the metastable β titanium alloy, Ti-5553. In the first experimental section, §4, the machinability of alloys with different levels of β stability is explored using established methods. During three investigations; turning, drilling and orthogonal cutting, several aspects of machinability were investigated, including; tool wear, surface integrity, chip formation and the force and torque response. The results highlighted that for the alloys tested; Ti-64, Ti-6246 and Ti-5553, machinability reduces with increasing β content. In §5, a new method employing velocity force maps (VFM) was developed, enabling rapid assessment and comparison of drilling induced microstructural damage at defined forces for Ti-64, Ti-6246 and Ti-5553. The methodology also enabled the comparison of PVD-TiAlN coated and uncoated tools for a range of cutting feeds (V_f) and cutting speeds (V_s), drawing into question whether such coatings are effective when drilling different titanium alloys. The results of §5 show how subsurface damage depth decreases with increasing alloy strength: uncoated tools caused a smaller damage depth than PVD-TiAlN coated tools. Analysis of the torque data indicated distinctly different optimum cutting parameters for each alloy and for both coated and uncoated tools. Tool wear characteristics were distinctly different depending on whether tools were coated or not: coated tools showed evidence of adhesive and abrasive wear mechanisms while for uncoated abrasion was the dominant wear mechanism. Adaption of the VFM methodology for investigating machinability will allow tool designers and machinists to improve machining processes and tool tolerances for new titanium alloys, making their application more affordable. In §6, the evolution of tool wear and hole quality were investigated in a series of three experiments. Several important results were obtained. Uncoated tools were shown to contribute to a more efficient cutting process (in terms of the specific cutting energy) compared to coated tools at the start of drilling: but as the tools started to wear, the efficiency of uncoated tools decreased and the efficiency of coated tools increased. Throughout §6, substantial BUE was shown on all tools used: the BUE was more prominent at faster V_s and was shown to reduce the stability of the drilling operation. Where there was more BUE and less stability, more material tended to adhere to the machined surface, reducing surface integrity. The re-adhered material was responsible for relatively high R_{max} results. Tool wear did not contribute to the Ra and R_{max} results, as over the course of 227 holes there was no change in the Ra. In addition, tools which were coated with PVD-TiAlN were shown to have slightly improved roughness to those tools which were uncoated at slower V_s (33.6 m/min). At higher V_s (46.4 m/min), roughness results were not significantly different for coated and uncoated tools. When considering other aspects of hole quality including; cylindricity, straightness, perpendicularity, entrance burr height and exit burr height, there were no significant differences between coated and uncoated tools. However, there was a relationship between hole location and the exit burr height and hole perpendicularity. This was thought to result from differences in rigidity of the workpiece within the clamping system. The tool wear analysis and hole quality assessment provides valuable information to tool suppliers about the response of current state of the art tools when machining metastable β titanium alloys and will help accelerate both tool and process improvement. In §6, the ability to correlate specific wear features with increases in torque was also demonstrated. In the future this could be used advantageously during in-process tool wear monitoring. In the final experimental section, §7, chemical crater wear, which is critical to tool failure during titanium machining was investigated thoroughly by analysing tools used to turn Ti-5553. SEM, X-EDS, STEM, TEM EDPs and WDS enabled the mechanisms involved in the development of crater wear to be elucidated: Co was shown to diffuse rapidly from the tool substrate once titanium has adhered to the rake face and then was followed by decarburisation of the WC. Two distinct zones of decarburisation were found, one which exists between WC grains and the adhered Ti-5553 and which is characterised by a fringe like W (bcc) layer. Once formed, this layer mediates the decarburisation from the substrate. The second zone, which occurs at prior Co rich regions or binder pockets, resembles a Kirkendall morphology and has been shown to be the site of rapid decarburisation, leading to C being lost from deeper within the tools subsurface. During decarburisation, particularly within the Co-rich, heavily β rich titanium regions, titanium carbides form. Such carbides have been evidenced at the interface and within the adhered Ti-5553, since they are highly abrasive, they cause the weak W(bcc) to break away from the tool, accelerating crater growth. Thermodynamic modelling has been used to analyse the phases that exist at the interface between the adhered titanium and the tool substrate. Results indicated that Ti_2Co and possibly a liquid phase may exist at the interface where there is significant amounts of Co. The presence of a liquid phase would explain the relatively high rate of decarburisation which occurs in some regions. The results of §7 provide invaluable information to tool suppliers who can modify their tool grades to improve performance when machining titanium alloys, possibly by modifying the tool substrate on the rake face of tools where craters form. Overall, the work in this thesis contributes to the overall understanding of metastable β titanium alloys and in particular Ti-5553. The findings can be used to; (1) improve benchmarking and tool design methodologies for such new titanium alloys and (2) provide the knowledge required to make intelligent design decisions when creating the next generation of WC-Co machine tools. Both of these outcomes will help improve the cost effectiveness of using metastable β alloys within industry.

Chapter 3

Experimental Methods

This chapter provides details of the tools, workpiece materials, and common experimental methodologies used throughout the thesis. §3.1 will include information on the tool and workpiece materials including relevant tool geometry, material composition and prior processing condition. §3.2 will cover workpiece sectioning and metallographic preparation techniques, including focused ion beam polishing. §3.3 will include details of the methodologies used for optical microscopy, scanning electron microscopy (SEM), energy dispersive X-Ray spectroscopy (X-EDS), electron probe micro analyser (EPMA), wavelength dispersive spectroscopy (WDS), transmission electron microscopy (TEM) and Alicona imaging. §3.4 includes the key methods used to normalise and analyse thrust force and torque in drilling such as the method for thermal drift compensation and data preparation for velocity force map (VFM) creation. In §3.5, the method used for the surface roughness probe will be outlined and details on the coordinate measuring machine (CMM) that has been used will be provided. In §3.6, the process used to create ternary phase diagrams of the Al-Ti-Co system will be described.

3.1 Titanium alloys

Table 3.1 includes the titanium alloys used as workpiece material in this thesis and includes their chemical composition, heat treatment condition and hardness. The hardness values were measured on a standard Vickers hardness testing machine. The alloys in Table 3.1 are listed in order of increasing molybdenum equivalency (Mo_{eq}). Mo_{eq} is used to characterise the beta stability of an alloy and is calculated using equation 3.1 [121]. For the alloys used Ti-64 had the lowest Mo_{eq} and Ti-5553 the highest.

Table 3.1: Name of alloy, nominal composition in Wt. %, heat treatment and Vickers hardness (Hv) (+/-10) and the billet dimensions - diameter D (mm) x length L (mm).

Alloy	Nominal Comp(wt. %).	Heat Treatment	Mo_{eq}	Hv	D x L
Ti-64	Ti-6Al-4V	Beta annealed	-3.32	345	150 x 200
Ti-6246	Ti-6Al-2Sn-4Zr-6Mo	As forged	0	325	200 x 250
Ti-17	Ti-5Al-2Sn-4Mo-2Zr-4Cr	Heat treated and aged	4	370	200 x 20
Ti-5553	Ti-5Al-5Mo-5V-3Cr	Sub-transus heat treated and aged	8.35	410	150 x 200

$$Mo_{eq} = 1.0[Mo] + 0.67[V] + 0.44[W] + 0.28[Nb] + 0.22[Ta] + 2.9[Fe] + 1.6[Cr] + 1.25[Ni] + 1.70[Mn] + 1.70[Co] - 1.0[Al] \tag{3.1}$$

The machinability of all four of these alloys was investigated in §4. Ti-64, Ti-5553 and Ti-6242 were investigated within the context of drilling machinability for alloys with varying β stability in §5. The focus of §6 was on further understanding the drilling machinability of Ti-5553 in the context of tool wear. Following this, in §7, the tool and workpiece interaction between Ti-5553 and WC-Co tools was studied.

3.2 Tools and tool substrate

Tungsten carbide grains bound in a cobalt matrix (WC-Co), were the tool materials used throughout all experimental work. This is because, as outlined in §2, WC-Co tools make up the significant majority of tools used for titanium alloy machining in industry. For all turning conducted in this programme of work, H13A WC-6%Co inserts were used. Further details of the insert geometry are tabulated in Table 3.2, which also includes the binder content and WC grain size of the tool substrate. Figure 3.1a,b includes a representation of the inserts and the location of the relevant geometric features. Further details of the inserts, including the recommended cutting parameters can be found in the Sandvik Coromant tool guide [122].

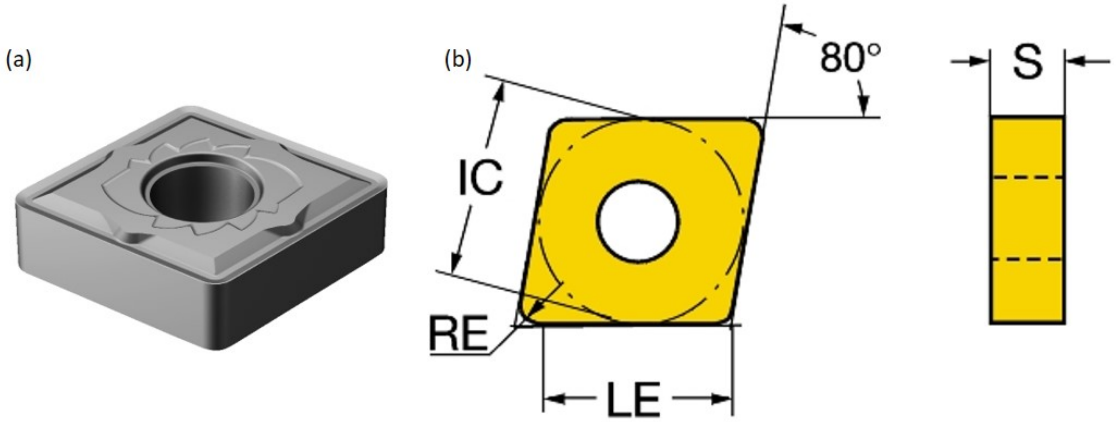

Figure 3.1: (a) - Generic representation of a CNMG 12 04 08 SM H13A insert. (b) - A diagram showing the relevant geometry [122].

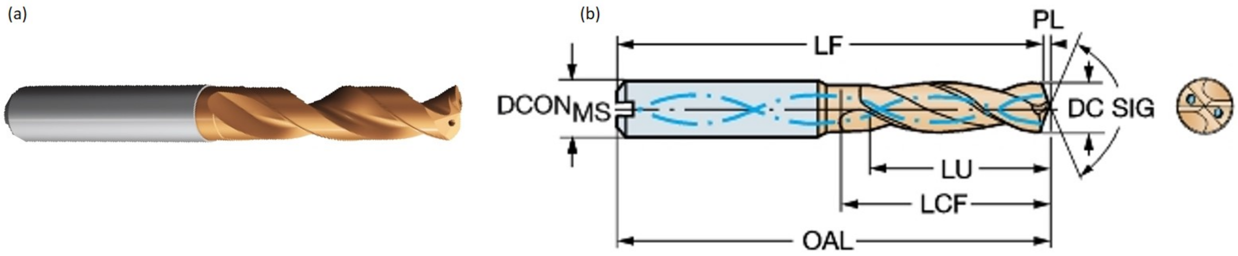

Figure 3.2: (a) - Generic representation of an R846-0690-30-A1A drill (3D render), where the bronze colour represents a TiAlN coating. (b) - A diagram showing key geometric features of the drill.

The drill tools selected for study throughout this work were R846 Corodrill twist drills, their model number is R846-0690-30-A1A. These tools were either used with a PVD-TiAlN coating or left uncoated. A 3D render of the drill and a schematic diagram showing relevant geometric features are included in Figure 3.2 (a,b). Important tool properties, including relevant nominal geometric features, the WC grain size, Co binder % and the coating thickness are given in Table 3.3.

Table 3.2: Model code, relevant insert geometry as labelled in Figure 3.1, Co binder % and typical WC grain size.

CNMG 12 04 08 SM H13A	
Corner Radius (RE)	0.794 mm
Cutting Edge effective length (LE)	8.5 mm
Inscribed Circle Diameter (IC)	12.7 mm
Insert Thickness (S)	4.73 mm
Co Wt.%	6%
WC Grain Size	1.0-1.3 μm

Table 3.3: Model code, relevant tool geometry, Co binder %, WC grain size and coating thickness where applicable. Abreviations are identical to those used in Figure 3.2

R846-0690-30-A1A 1220	
Cutting Diameter (DC)	16 mm / 6.9 mm
Useable Length (LU)	21.9 mm
Chip Flute Length (CFL)	34 mm
Point Angle (SIG)	140°
Functional Length (LF)	77.8 mm
Overall Length (OAL)	79 mm
Point Length (PL)	1.2 mm
Connection Diameter (DCON)	8 mm
WC Grain Size	0.8 - 1 μm
Co binder %	12 %
Coating Thickness	3 (+/-1) μm

3.3 Sample preparation

In §3.3 the processes of wire electrical discharge machining (EDM) (§3.3.1), precision cutting (§3.3.2) and metallographic preparation i.e grinding and polishing (§3.3.3) are introduced.

3.3.1 Sectioning - wire electronic discharge machining

The process of electrical discharge machining (EDM) is a non-conventional method of achieving high tolerances when metal cutting. The process involves the discharge of electrical pulses along a thin wire, between a workpiece and an electrode. High potential gradients accelerate electrons from the dielectric which cascade and create plasma. With each electrical pulse the plasma forces small particles of the conductive workpiece to break free. The wire is often guided using computer numerical control (CNC) to generate a programmed geometry. Using current to locally melt the workpiece means the surface finish of EDM components is extremely consistent and results in no residual stress in the machined surface since the wire never makes contact with the material [123]. By using a wire to supply the current the technology can be used to create and section complex geometries. This is particularly useful for sectioning titanium alloys and was utilised in; (1) §4 to section samples for orthogonal cutting tests and holes, (2) in §5 to carry out precise microstructural analysis on the machined surface of holes.

3.3.2 Sectioning - precision cutting

All sectioning, other than that carried out via wire EDM, was done using a Struers Secotom-50 precision cutting machine equipped with MetPrep type 50 abrasive cutting wheels. Before sectioning, the location of the cut was marked on the sample and the size of the cut was measured. Then, the samples were clamped and held securely within the standard "quick clamp" [124]. Using the machines X, Y and Z controller, the abrasive blade was brought close to the marked location. The size of cut that was input into the Secotom and was always larger than the measured distance of the cut, ensuring the machine would never stop midway through as the blade could become stuck in the workpiece. The rotational speed of the blade was set to 2200 RPM and the V_f was varied between 0.1 and 0.5 mm/min, depending on the samples thickness. Throughout cutting operations, temperature was regulated via the re-circulation of water and Struers Corrozip fluid [125].

It is difficult to section tools in a way which does not damage the worn region and enables effective analysis of the wear. In order to analyse the phenomena known as crater wear - which occurs when machining titanium using WC-Co tools in turning, pre-used tools were mounted in Bakelite with the flank face of the inserts placed face down in the mounting press. The tool and Bakelite was then ground away, following the process outlined in section §3.3.3. During grinding the change in the height of the Bakelite sample was measured until approximately 500 μm had been removed. Then, the samples were viewed under optical microscope to ensure the crater region was visible. Once this check had been made, the polishing steps (also outlined in §3.3.3) were carried out, creating a mirror finish. Where sectioning the top of drill tools was necessary for Alicona and analysis, the Secotom-50 precision cutting machine was used with a diamond tipped cutting blade at an RPM of 2000 and a feed rate of 0.05 - 0.25 mm/min.

3.3.3 Metallographic preparation

Metallographic preparation for microstructural analysis via optical and secondary electron microscopy was required in §4, 5 and 7. Once samples were sectioned using the techniques outlined in §3.3.1 and §3.3.2, samples were mounted in conductive Bakelite using a Simplimet 2000. Resulting Bakelite samples were 32 mm diameter cylinders, with the area of interest located on one of the two flat sides. The metallographic preparation process could then be carried out. Two different methods were used depending on whether the sample was a titanium alloy or if it was a combined titanium WC-Co sample, each sequential step is detailed in Tables 3.4 and 3.5 respectively. All such preparation was carried out on a Buehler Automet 250 with a plate speed of 249 RPM and head speed of 50 RPM.

Table 3.4: Metallographic preparation sequence including the grinding and polishing process for titanium.

Stage	Surface	Application	Force (N)	Time (s)
Grinding	SiC Grinding Paper (P400)	Water	25	60
Grinding	SiC Grinding Paper (P800)	Water	25	60
Grinding	SiC Grinding Paper (P1200)	Water	25	60
Grinding	SiC Grinding Paper (P2500)	Water	25	60
Polishing	Stuers MD-Chem (np)*	Water	20	120
Polishing	Stuers MD-Chem (np)*	9:1 Colloidal Silica (0.05μm) to H_2O_2 (and drip water)	20	300
Polishing	Stuers MD-Chem (np)*	Water	20	60
Polishing	Stuers MD-Chem (np)*	9:1 Colloidal Silica (0.05μm) to H_2O_2 (and drip water)	20	300
Polishing	Stuers MD-Chem (np)*	Water	20	300

*np - neoprene pad

Table 3.5: Metallographic preparation sequence for samples containing both titanium and WC-Co.

Stage	Surface	Application	Force (N)	Time (s)
Grinding	SiC Grinding Paper (P400)	Water	25	60
Grinding	SiC Grinding Paper (P800)	Water	25	60
Grinding	SiC Grinding Paper (P1200)	Water	25	60
Grinding	SiC Grinding Paper (P2500)	Water	25	60
Grinding	SiC Grinding Paper (P4000)	Water	25	60
Polishing	Stuers MD-Largo (pp)*	6 μm diamond suspension (MetPrep)	20	300
Polishing	Stuers MD-Largo (pp)*	3 μm diamond suspension (MetPrep)	20	300
Polishing	Stuers MD-Largo (pp)*	1 μm diamond suspension (MetPrep)	20	300
Polishing	Stuers MD-Chem (np)*	Water	20	60
Polishing	Stuers MD-Chem (np)*	9:1 Colloidal Silica (0.05μm) to H_2O_2 (and drip water)	20	300
Polishing	Stuers MD-Chem (np)*	Water	20	300

*pp - polishing pad *np - neoprene pad

3.4 Imaging techniques

3.4.1 Light optical microscopy

Light optical microscopes and camera systems are used throughout this work. Samples used for microstructural and damage assessment were mounted in Bakelite and surfaces were prepared following the routine in §3.3.3. A Nikon LV150 fitted with cross-polarised light filters, was the main instrument used for the optical microscopy. Cross polarisation enabled a clear distinction between grains due to differences in contrast from the differing grain orientations. Buehler Omnimet software was used to save and post process images. For imaging tool wear an Olympus SZX10 light microscope and Clemex Vision software were utilised.

3.4.2 SEM and EDS

For polished samples prepared using the method outlined in §3.3.3, a Zeiss Evo LS25 was used to obtain high resolution images of the resultant microstructure in machined surfaces. Generally the SEM operational parameters were consistent, but in some cases they varied between the ranges shown in Table 3.6. In some cases backscattered imaging was required to better define microstructural features and the type of damage; backscatter makes it easier to differentiate between the α (hcp) and β (bcc) phases as more electrons are directly reflected onto the detector from the bcc lattice. The Zeiss SEM had an Oxford Instruments X-EDS detector which was utilised for elemental analysis in §7.

Table 3.6: Zeiss Evo LS25 SEM operational parameters.

Parameter	Surface
Voltage	10 – 20 keV
Spot Size	3.5
Working Distance	8 – 12 mm
Detectors	Secondary Electron (SE), Backscatter Electron (BSE)

3.4.3 FIB and TEM

Focused ion beam (FIB) technology utilises a focused beam of ions generated from a liquid metal ion source (LMIS) such as gallium [126]. Once brought into contact with a tungsten needle, the heated LMIS will move to the tip and form a Taylor cone. The radius of the cone is extremely small, ~2 nm, due to the balance between surface tension force and the force caused by the applied electric field. The electric field then causes ionisation and electron emission from the gallium atoms. The beam is then accelerated and later focused via electrostatic lensing. In the present work, a Thermo-Fisher-Scientific Helios 650 FIB was used to prepare samples for TEM. This consisted of removing material from the sample to generate a thin lamellar like sample less than 100 nm thick. FIB enables exact locations on the cutting tool to be examined in TEM due to the high resolution of FIB for locating and extracting such lamellar morphologies. The process of FIB cross sectioning lamellar consists of; application of Pt protection layer, ion milling to separate the lamellar, trimming at low current and polishing at low voltage.

Transmission electron microscopy (TEM) can achieve extremely high resolution compared to optical microscopy due to the relatively low de Broglie wavelength of electrons compared to photons. Unlike SEM which measures reflected electrons scattered by Bragg diffraction, TEM directly measures the transmitted electrons. Although this results in higher resolution imaging, it does require very thin samples that are time intensive to prepare. Not only can TEM be used to generate high resolution images of the prepared samples via scanning transmission electron microscopy (STEM), but diffraction analysis using TEM is an invaluable tool when identifying how atoms have bonded, and what elements are present (spectroscopy). Similar to FIB, TEM machines have a tungsten emission source (or single crystal) filament. Then, a voltage of 100-300 keV is applied to cause emission and acceleration of electrons via thermionic and field electron emission into a vacuum. The TEM machine utilised in this work was a Thermo-Fisher-Scientific Titan G2 microscope which is a fully computerised TEM with 300 kV capability, 0.07 nm resolution and a 1 nm probe size. All TEM micrographs were acquired with a single tilt beryllium holder. Figure 3.3 includes a secondary electron image taken during the sectioning of a lamellar from a WC-Co crater via FIB for TEM analysis including the location of the applied Pt layer.

3.4.4 EPMA

Electron micro probe analysers (EPMA) are used to identify the chemical composition of solid materials. Similar to SEM, EPMA technology utilises electron beams. Electrons from a cathode are accelerated by a positive anode. By focusing electrons into a tight beam via magnetic lensing, excitation occurs, and characteristic X-ray radiation can be produced. Such X-rays can be counted via wavelength dispersive X-ray spectroscopy (WDS), in which Bragg diffraction is used to select and group X-rays that are of interest. To determine the element or chemical composition the number and intensity of X-rays must be compared

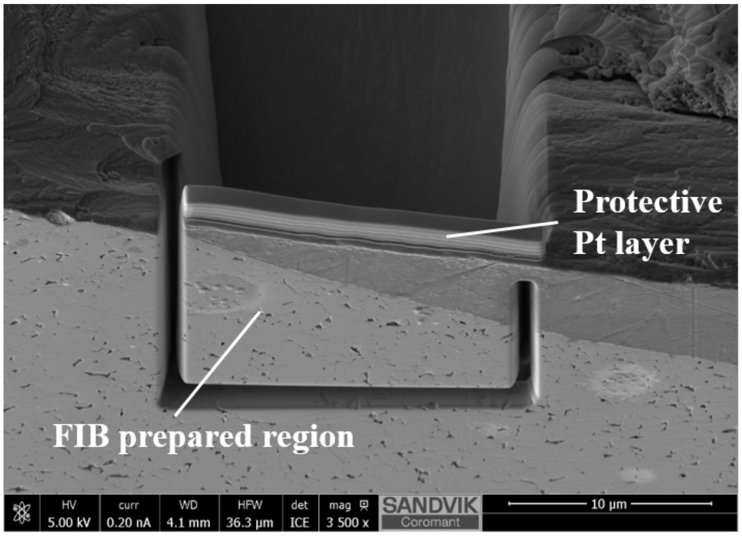

Figure 3.3: An SEM image showing the FIB prepared region on a WC-Co tool including the location of the protective Pt layer [127].

to the intensities recorded from a known element or composition. The resolution of this technique is nominally between 0.3 and 3 μm^3. The EPMA was conducted with the scan length, step size and acceleration voltage given in Table 3.7.

Table 3.7: Details of the electron micro probe analyser including; machine used, scan length, scan step size and acceleration voltage.

Machine Model	JXA-8530F
Line Length	10 μm
Line Step Size	0.05 μm
Probe Current	40 nA
Dwell Time	10 ms
Map Size	36.6 μm * 27.27 μm
Acceleration Voltage	10 keV

The XMapTools MATLAB software package was used to construct images and analyse the EPMA data. First, the data from the probe was imported into MATLAB. When the data is collected the intensity of each element measured by the micro analyser probe was recorded in a separate channel. There was also an additional channel created which included the composite intensity. When these were imported into MATLAB, each channel was saved as a separate vector. Then, within the XMapTools UI the vectors were selected and renamed to reflect the element that they represented. Since each channel contained a single vector, the software required the pixel dimensions of each scan. For all the EPMA scans, the dimensions were 192 x 256 pixels. For each scan taken, each channel was processed into an image. To analyse the data several different functions were used. The sliding window method, which can be selected from the sampling menu, consisted of sampling the datasets using a 190 x 25 window set to scan from top to bottom of each map, providing an intensity profile for each element measured by the EPMA. This method was especially effective for analysing how the concentration of elements changed at interfaces. Another XMapTool utilised in the analysis of the EPMA was the RGB option within the module menu. To use this three elements (channels) need to be selected. Then each channel is highlighted in a different colour (red, green and blue) and the intensity of each colour can also be controlled depending on what you are trying to highlight from the scan. The RGB module was particularly useful when highlighting the location of specific elements within a map.

3.4.5 Surface Topography

To assess the surface topography of machined holes and measure the tool wear on twist drills, 3D images and measurements were made using an InfiniteFocusSL Alicona. This equipment enables dimensional, positional and geometric measurements to be made using focal variation. The Alicona functions by taking multiple images from different heights of a surface or object. To take the images, white light is focused using a beam splitter onto a specimen and the reflected light hits the objective lens and a photosensitive sensor which exists behind the beam splitter. Images are taken at repeated intervals while the optical sensors are moved vertically ensuring that for each location on the object is in sharp focus for at least one image. The Alicona software stitches all the in-focus regions together by analysing the focal variation along the vertical axis, providing a high resolution image with a depth of field. The images can be used to create a 3D point cloud or 3D object. Alicona also provide MeasurementSuite5.3.4 software that enables form fitting, colour mapping and profile form measurement.

In this work, the 3D form fitting module within the MeasurementSuite has been used to remove the form from 3D datasets, so the resulting local depth variations could be resolved. Where the Alicona has been used to analyse holes, the 3D form that was removed was that of a cylinder. The software automatically detected the size and location of the cylinder, the only error was due to poor hole cylindricity. These errors were easily accounted for by calculating a second polynomial form removal after removing the cylinder.

The ability to produce a colour map to represent the changes in depth on a hole surface was useful in understanding the effect of coated and uncoated tools on surface roughness presented in Chapter 6 and the CIRP conference paper titled “Surface roughness response to drilling of Ti-5Al-5Mo-5V-3Cr using Ti-Al-N coated and uncoated WC/Co tools”.

The profile form measurement tool within MeasurementSuite enables the user to draw a line onto a 3D object. Once drawn the profile over which the line runs is shown. For a cutting edge, the profile looks like a rounded triangle. Once this profile is created the software can be used to fit any type of shape to the profile. By fitting a circle to the rounded part of the cutting edge, an estimate of the cutting edge rounding can be obtained. For each 3D image of a cutting edge the profile can be drawn at any location along the cutting edge, allowing for any difference in ER due to BUE to be avoided. The ability to measure the edge roundness on the cutting edge using the profile form measurement tool allowed for an alternate way of measuring wear. This was required since typical methods were hindered by the large amount of BUE that occurs during the machining of Ti-5553.

3.5 Force and torque: Data acquisition and analysis

Key software packages have been used throughout the thesis to analyse and present force and torque results. In this section, some of the key programs and functions will be introduced to aid discussion of results in future chapters.

3.5.1 Force and torque measurement

In §4, 5 and 6, force and torque were recorded for drilled holes using a Kistler dynamometer. This equipment utilises piezoelectric crystals that can sense the build-up of charge within material due to an applied mechanical stress. These sensors enable very accurate measurement of directional force and torque during machine operation. The acquired data was received using the Kistler software DynoWare. Details of the spindle mounted Kistler and signal conditioner utilised in this work are highlighted in Table 3.8. Figure 3.4 (a) shows the dynamometer, the Fx, Fy, Fz, Mz channels and their corresponding axes. Figure 3.4 (b) shows the dynamometer within a DMU monoBLOCK 100 machining centre including; the brace which affixes the dyno in place; the collet to hold the tool and; the stator with a high speed connection cable.

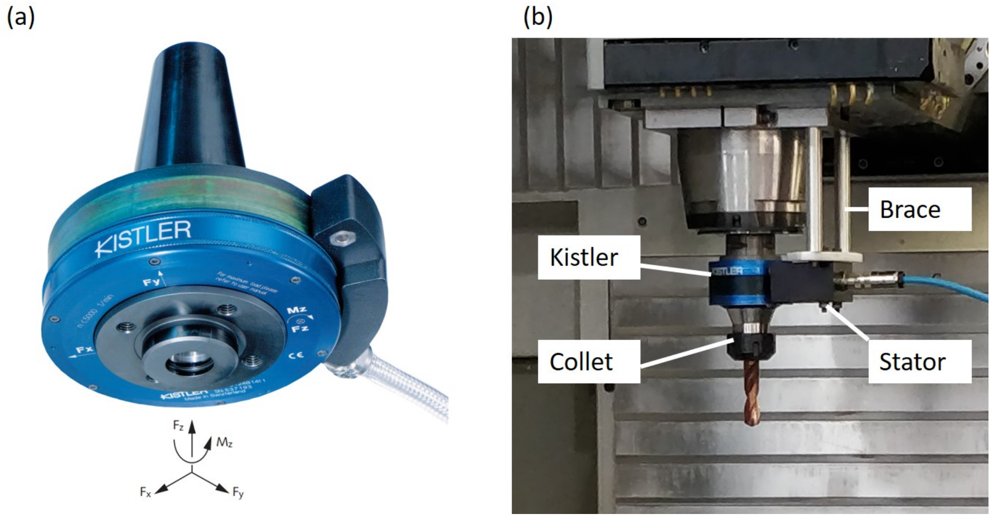

Figure 3.4: (a) - The Kistler dynamometer and axes of measured forces. (b) - The Kistler dynamometer, stator and collet setup, braced within a DMU monoBLOCK 100 machining centre.

3.5.2 Thermal drift compensation

Before force or torque results could be analysed or presented, the data was processed in MATLAB to normalise for thermal drift which is a characteristic caused by the piezoelectric crystal heating up during the machining operation. The way in which thermal drift effects the results can be seen in Figure 3.5 which shows the force increasing as 8 holes are drilled. To normalise for this effect the following was done: First, the start and end of each hole was identified using the movVar() and findpeaks() functions within MATLAB. The movVar()

Table 3.8: Details of the RCD Kistler dynamometer including; model code, conditioner, sampling range, and measuring ranges.

Kistler Model	Type 9170A3112
Signal Conditioner	Type 5238B
Sampling Frequency	0 - 10000Hz
Sensor Measuring Range (Fz)	0 - 20 kN
Sensor Measuring Range (Mz)	0 - 200 Nm

function was used to calculate the moving variance using equation 3.1, for Fz and Mz where the response for each can be considered a vector A made up of N scalar values, where μ is the mean of A. Since different sampling rates were used in different chapters generally the movVar() window size was equivalent to 0.15 s of time in cut. For example where a sampling rate of 19200 Hz the window size was ∼3000 samples.

$$V = \frac{1}{N-1}\sum_{i=1}^{N} |A_i - \mu| \tag{3.2}$$

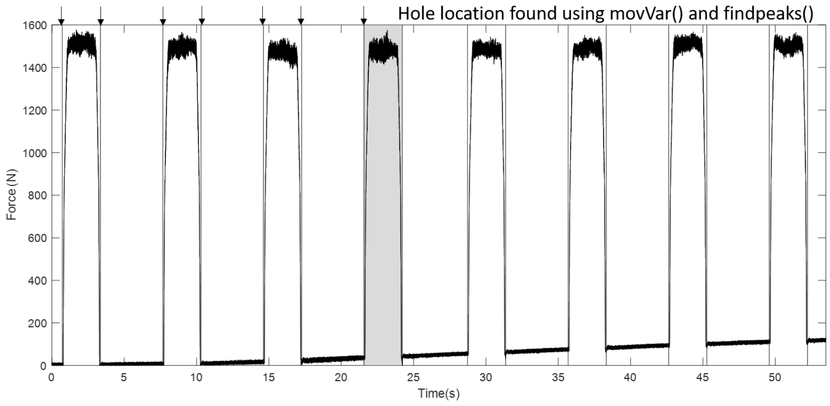

Figure 3.5: Graph showing the Kistler Fz data for eight 6.9 mm holes drilled in a 10 mm Ti-5553 plate.The highlighted area indicates hole selection through MATLAB movVar() and findpeaks() functions.

Once the moving variance was obtained the findpeaks() function was used to find the peak variance. Since at the start and end of each hole the variance becomes extremely large using findpeaks() with a threshold $4 * 10^8$ was suitable to find the start and end of each hole. Then, holes were cropped into separate datasets with a 0.5 second buffer added to the beginning and end. An example of such a dataset for Fz is given in Figure 3.6 which shows the data for

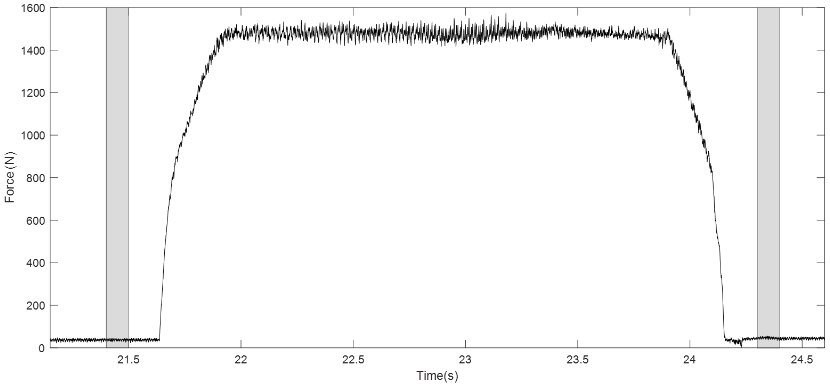

Figure 3.6: Graph showing cropped data for hole 4 which is highlighted in Figure 3.5. Highlighted regions show where mean() function is used to find the force offset before and after the hole is drilled.

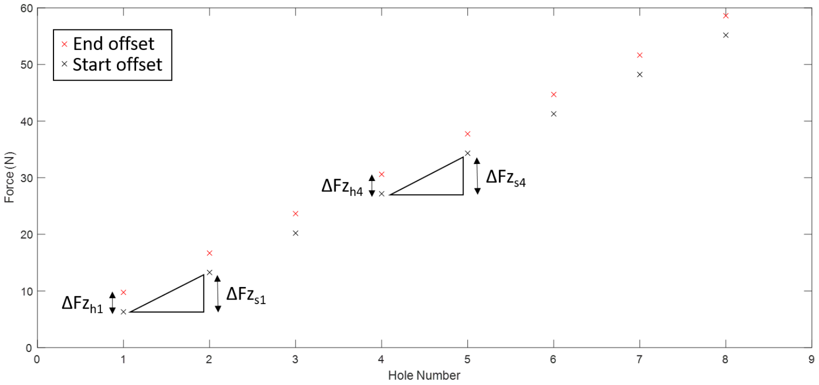

Figure 3.7: Scatter plot showing the average Fz offset at the start of a hole (black), and end of a hole (red).

hole 4 of the 8 hole set given in Figure 3.5. Once each hole was saved as a separate vector within MATLAB, the average force at the beginning and end of the hole was calculated using mean() for the data highlighted in Figure 3.6, on either side of the hole. This was the data from 0.1-0.2 s before and after the hole was drilled. The resulting average values are plotted in Figure 3.7 where the starting and ending average offset is marked in black and red respectively for each hole. Once the offsets are obtained, there are two stages to compensate for the drift. In the first stage, the drift across each hole must be compensated, in order to do this, the value of the offset for the start of each hole must be subtracted from the offset at the end of the hole this is represented in Figure 3.7 by $\Delta F_{h,n}$, where n is the hole number. Then, a linear fit is made between the offset at the start of each hole and the offset at the end. This equation, which follows the form $y = mx + c$ is used to subtract a value mx from each data point of the hole. For the second stage of thermal compensation, the difference between the start offset of each hole, $\Delta F_{s,n}$, as labelled in Figure 3.7, is subtracted from each data point in the Fz vector for each cropped hole. Using this method, both the drift that occurs over a hole and in between drilling holes is compensated for. In the example in Figure 3.5, the drift is shown to be significant across 8 holes (∼50 N) which shows the importance of drift compensation when using piezoelectric dynamometers especially when many hundreds of holes are drilled in succession.

3.5.3 Steady state cutting data acquisition

In §5 and §6, the average force and torque recorded within the steady state cutting region are used to create VFMs to understand how force and torque vary over the life of the tool. Many holes were analysed in both chapters, and therefore some level of automation was required to select the necessary data required for further analysis. Once the data for each hole was isolated and corrected using the method described in §3.5.2, each data point was assigned a depth. To do this the movVar() function was used to identify the point at which the tool was fully engaged and the point just before the tool exited from the material. In the example hole given in Figure 3.8, which was a 20 mm hole, depth is labelled. Once the depth of each data point was assigned the data could be cropped at the relevant location, for example, between 5 and 10 mm. This cropped data was then averaged using the mean() function and could be used as a single data point in a VFM or force against hole number plot.

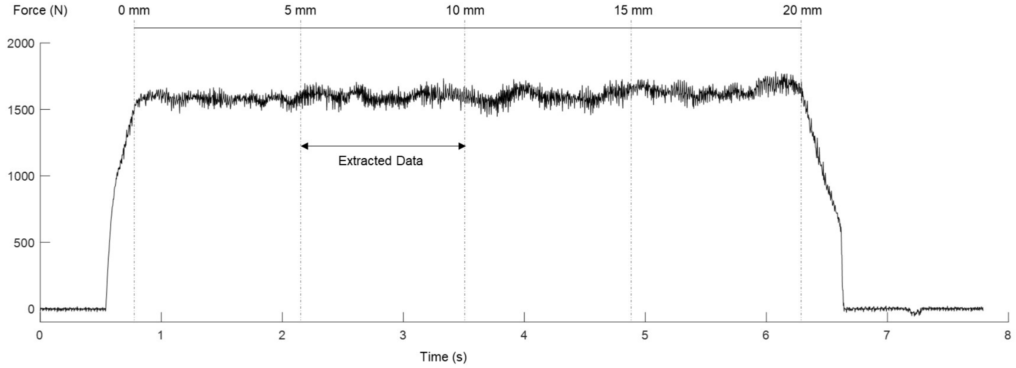

Figure 3.8: Fz signal from an example hole showing where data is extracted from for future processing. The cutting parameters used for this hole were $V_s = 40$ m/min and $V_f = 250$ mm/min [128].

3.5.4 MATLAB - standard variation and variance

In §3.4.2 the force and torque for each hole were split into individual vectors. Then in §3.5.3, a portion of data was cropped within the steady state cutting region of each hole. From this data set the standard deviation and variance for each hole was calculated. To do this the std() and var() MATLAB functions which operate based on equation 3.2 and 3.1 were used.

$$S = \sqrt{\frac{1}{N-1}\sum_{i=1}^{N}|A_i - \mu|^2} \tag{3.3}$$

From these the error in the standard deviation and variance were obtained by dividing by the square root of the vector length.

3.6 Tool geometry and hole quality measurement

The Helicheck Pro is a fully automated high performance measuring machine used to measure complex geometries like those on R846 drills which are used in §4, §5 and §6. The machine utilises several LED light sources, various cameras and a control unit with a positional resolution of 0.004 µm [129]. The most important geometric features measured by the helicheck are labelled in Figure 3.9; the primary and secondary clearance angles, distance to corner, gash length, gash radius, blend radius and edge rounding measurements of the cutting edge at 10% ($A\Delta R$), 60% ($B\Delta R$) and 90% ($C\Delta R$) of the radius.

3.6.1 Surface roughness measurement

A Mitutoyo surface roughness portable tester (178-561-02E) was used to measure the Ra and R$_{max}$ of machined surfaces in §4. In §6, a Diavite DH-8 surface roughness tester, equipped with a CLA-400 2 μm measuring head, was used to measure Ra and R$_{max}$ of machined holes. When measuring surface roughness, three line scans were made along the inside of the hole on the machined surface. Each of the scans were 1 mm equidistant, as shown in Figure 3.10. Each line scan was 4.8 mm long and was made at hole depths of 2.5 mm to 7.3 mm. Details of the sample length, cut off wavelength and vertical resolutions are tabulated in table 3.9. The arithmetical mean deviation (Ra) of the line scans is calculated using equation 3.3 where l is the length of the scan and Z(x) is the point by point deviation between the profile and the mean line.

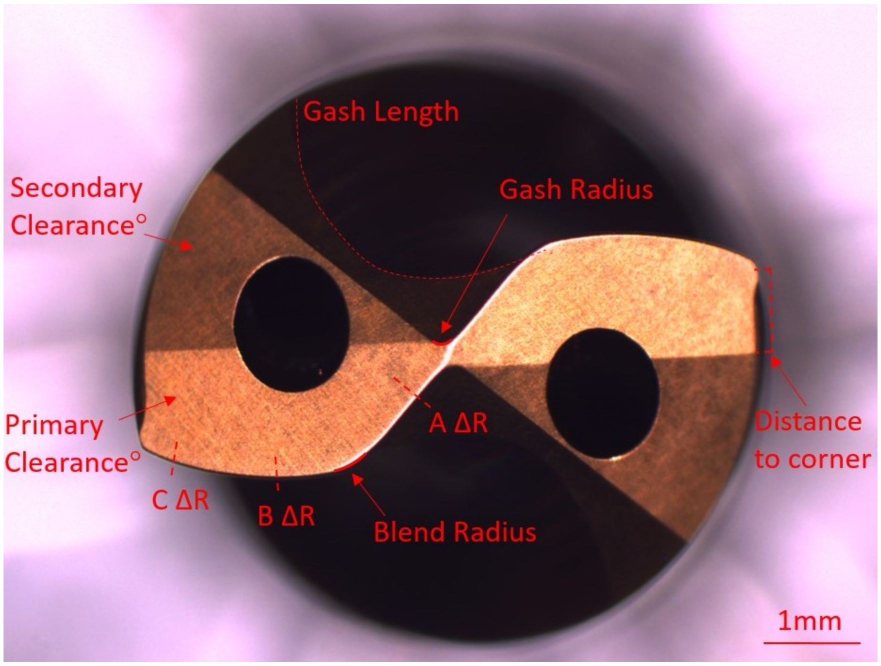

Figure 3.9: An annotated diagram showing the location of the following geometric features which were measured using a Helicheck Pro machine; Primary and secondary clearance angles, gash length, gash radius, blend radius, $A\Delta R$, $B\Delta R$ and $C\Delta R$ which have been measured using a Helicheck Pro.

$$\frac{1}{l}\int |Z(x)|\,dx \tag{3.4}$$

R$_{max}$ was measured as the maximum distance measured between the highest peak and lowest trough as measured from the mean height.

Table 3.9: Details of the settings used with the Diavite DH-8 surface roughness probe including; scan length, sample number, cut off wavelength and vertical resolution.

Parameter	Value
Scan Length	4.8 mm
Sample Number	4800
Cut-off Wavelength	800 μm
Vertical Resolutions	0.1 - 2 μm

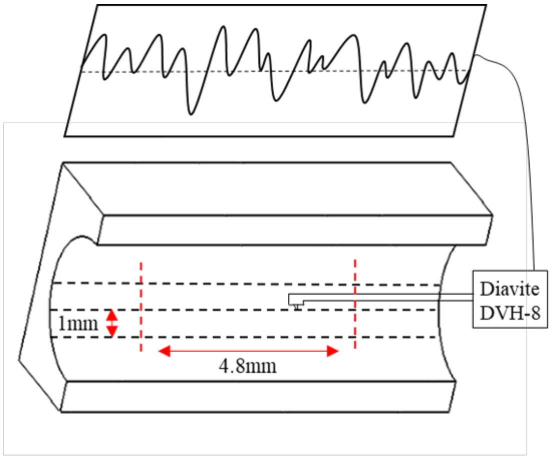

Figure 3.10: Graphical representation showing how the Ra and R_{max} were measured on the machined surface of drilled holes using the Diavite DVH-8 roughness probe. Adapted from [130].

3.6.2 Coordinate measuring machine

The coordinate measurement machine (CMM) is utilised throughout industry to assess the quality of machined features. It is particularly useful when measuring aspects of hole quality since CMM machines can automate the process for a large set of holes. In §6, hole quality characteristics were measured on a Zeiss Accura measurement machine fitted with a VAST navigator is used to compare the quality of coated and uncoated holes. The aspects of hole quality that were evaluated were: cylindricity (deviation from perfect cylinder), perpendicularity (error in the hole center axis angle), straightness (error due to curve of hole axis) , surface roughness, Entrance burr height (average and max) and exit burr height (average and max).

3.7 Thermodynamic modelling

To investigate the interaction of Co on the rate of crater wear in §6, ThermoCalc thermodynamic modelling software was employed to analyse the Co-Al-Ti system. A modified TCNi8 database, provided by Nathalie Dupin [131] and crosschecked with the binary alloy database TCbin was used to generate 3D ternary phase diagrams at temperatures relevant to the crater region of tool wear. To achieve this the FORTRAN based console was used in the following manner.

First the user database is defined using the command line:

Go data → switch → user database → define-system → Co Al Ti → get data.

Then the system conditions were defined by going to the poly3 module and setting the temperature and pressure to 1273.15 K, 101325 Pa (in this example) and N = 1. Followed by setting the mole fraction of Co to 1e-2 and the mole fraction of Al to 5e-3 and calculating the equilibrium:

Go poly → set-condition T=1273.15 P=101325 N=1 → set-condition X(co) = 1e-2 → set-condition X(Al)=5e-3 → calculate-equilibrium;

Next, the axis variables were defined with X(Co) on the first (left) axis between 0 and 1 mole fraction in steps of 0.01. X(Al) was on axis 2 (bottom), again between 0 and 1 mole fraction in steps of 0.01:

Save-axis-variable 1 X(Co) 0 1 0.01 → save-axis-variable 2 X(Al) 0 1 0.01;

Once the axis were set the data could be mapped using the **map** command. Once mapped the POST module was used to prepare the ternary diagrams for presentation. The X and Y axis were set to show the mole percent of Al and Co and the axis were rasterised:

Set-diagram-axis X mole-percent Al → set-diagram-axis Y mole-percent Co → set-raster-status yes;

The label type, scaling status, and tile status were set:

Set-label f → set-scaling-status y n -0.01 1.01 → set-tiling-status 1;

To ensure the diagrams were consistent with the Ti-Al and Ti-Co binary systems the binary module was used. To create a binary diagram the following commands were used where the pressure is defaulted to 101325 Pa and the gas constant to N = 1:

Go bin → define system Al Ti (Co Ti) → Get Data → Set Condition Calculate equilibrium → go post → plot.

Then at the temperature for which the ternary's were calculated the binary was examined checking if it was consistent with the Co = 0 and Al = 0 axis for the Al Ti and Co Ti system respectively. For all diagrams presented in this work, the binary at this axis, was identical to the ternary.

Chapter 4

Machinability assessment of Titanium alloys

This chapter consists of three different machinability investigations. Each experiment was conducted to further understand and compare the machinability of titanium alloys with different levels of β stability for different machining operations. §4.1 utilises the concept of the V15 for comparing the machinability of Ti-5553 to Ti-6246 when turning with WC-Co tools. Then, once the V15 is established for both alloys, further trials were carried out where the primary purpose was to identify the change in flank wear and surface roughness (Ra) with time. In §4.2, the drilling machinability of Ti-5553 and Ti-64 are compared via force, torque and tool wear analysis. In §4.3, a novel method employing an arbitrary strain path (ASP) testing machine is used to compare the machinability of Ti-64, Ti-6246 and Ti-17 in a small scale orthogonal cutting test. The purpose of ASP testing is to identify the feasibility of such small scale tests for the assessment of machinability compared to more expensive techniques such as the V15. §4.4; addresses the effectiveness of the three different methods for assessing machinability, discusses the key differences and similarities between results and sets out the premise for future chapters.

4.1 Turning Ti-5553 and Ti-6246 using WC-Co H13A uncoated inserts

In this investigation, the machinability of Ti-5553 is compared to that of Ti-6246 in two tests; a V15 outer diameter (OD) turning investigation using CNMG H13A WC-Co cutting inserts followed by a time dependant machinability investigation. To establish the V15 of each alloy, turning was carried out at a range of V_s from 40 to 110 (m/min) at a constant depth of cut

(a_p = 1 mm) and F_{rev} = 0.1 mm/rev. Flank wear was measured as the primary indicator of process performance. Both chip geometry and Ra were also measured. The V15s of Ti-5553 and Ti-6246 were identified as approximately 71 m/min and 74 m/min respectively, with the more β-stabilised alloy, Ti-5553, confirmed as the least machinable in terms of optimum productivity and wear rate. Once the V15s were established, a time dependant trial was carried out on each material. This consisted of OD turning for 5 s, 15 s, 30 s, 60 s, 120 s, 180 s, 300 s, 600 s and 900 s at 70 m/min for Ti-5553 and 75 m/min for Ti-6246, (V15s +/- 1 m/min). For the V15 investigation, Ra results indicated 60 m/min and 40 m/min, to be the best V_s to reduce Ra for Ti-5553 and Ti-6246 respectively. For the time dependant wear testing, Ra varied significantly for different lengths of time in cut in both materials showing a certain level of wear on the tool can improve machinability, possibly by stabilising the cutting process. Examination of the tool chips indicated it may be possible to deduce the optimum parameters solely through comparing the swarf morphology at different V_s.

4.1.1 Experimental setup - turning

Separate cylindrical Ti-5553 and Ti-6246 billets were clamped within a Cincinnati Hawk-SL 300 lathe machine (Figure 4.1a). Table 4.1 highlights the nominal composition, heat treatments and billet dimensions of these alloys. The workpiece setup within the machine is shown in Figure 4.1b. Solid inflexible jaws were used to clamp the billet material and then a centre support was used to maintain billet stability. H13A inserts were held at an oblique angle, in a Sandvik Coromant T-max tool holder during OD turning. The edge rounding (ER) of all test inserts was measured using an Alicona Sl; further details are provided in §3.4.5. As the edge radius of cutting inserts has been known to effect the turning operation and rate of wear, the ER of each insert was measured. Tools with ER larger than one standard deviation from the mean were omitted from the investigation. Hocut795B coolant was applied to the cutting edge through the tool holder. Table 4.2 includes the model number for the tool inserts and tool holder as well as further details on the coolant used throughout the investigation.

Table 4.1: Material nominal compositions (wt. %), heat treatment, billet diameter and billet length for the V15 and progressive tool wear turning tests.

Material	Nominal Composition (wt. %).	Heat Treatment	Diameter (mm)	Length (mm)
Ti-5553	Ti-5Al-5Mo-5V-3Cr	Sub-transus heat treated and aged	150	157.6
Ti-6246	Ti-6Al-2Sn-4Zr-6Mo	As Forged	198	250

Table 4.2: Tool insert and tool holder model number, coolant type, flowrate (litres/min) and concentration.

Tool Insert	Tool Holder	Coolant Type	Coolant Flowrate	Coolant Pressure	Coolant Concentration
H13A CNMG 1204 08-SM	C5-DCLNL -35060-12	Hocut 795B-EU	5.4 (L / min)	40 Bar	5%

Figure 4.1: A photograph of the Hawk-SL 300 lathe including the Ti-6246 workpiece, centre support, tool holder and insert.

4.1.2 The V15 method - turning

To find the V15 of each material, the V_s was varied while the V_f and radial a_p were kept constant. Table 4.3 contains the V_f, radial a_p and major clearance angle. Testing was conducted by varying the V_s in Table 4.4, in order from left to right. Once the V15 was determined (test 4 in Ti-5553 and test 7 in Ti-6246), a repeat run at the V15 was carried out to test the repeatability of the V15 wear rate. For each speed a new cutting insert was selected, and after each 15 min test, the flank wear of the tools was measured on a Zeiss light optical microscope. As flank wear varied along the cutting edge, both VB and maximum flank wear (VB_{max}) values were measured where the VB was obtained from at least 5 measurements, taken along the whole length of the flank. Figure 4.2a shows an example of how the flank wear was measured for an insert used for 15 min to machine Ti-6246 at a V_s of 75 m/min. Figure 4.2b shows how the rake face of the tool was imaged for each insert. As in the ISO3685 the VB limit was set to 0.25 mm and the VB_{max} to 0.5 mm [95]. To obtain an estimate of the V15, VB and VB_{max} measurements were plotted against V_s and the location at which the data intercepted the pre-set limits identified. This can be seen in Figure 4.5 in §4.1.4.

Table 4.3: (F_{rev}), a_p and major clearance angle for V15 and time dependant wear turning.

Parameter	Value
Feed Rate , F_{rev}	0.1 mm/rev
Radial Depth of Cut , a_p	1 mm
Major Clearance Angle	0°

Table 4.4: V_s (m/min) used in V15 tests in testing order.

Test #	1	2	3	4	5	6	7	8
Ti-5553	40	110	90	70	70			
Ti-6246	40	110	60	90	70	80	75	75

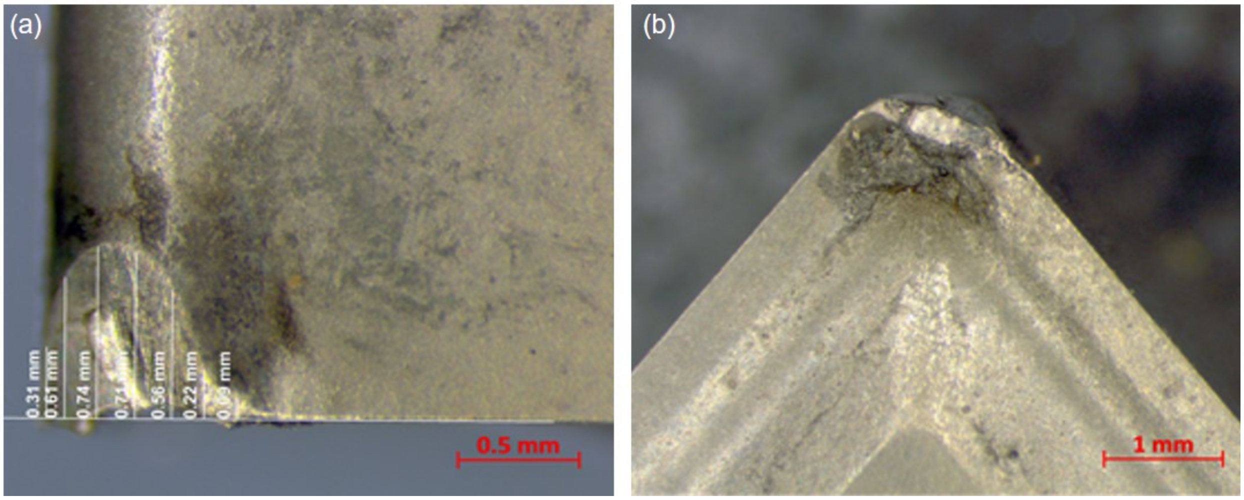

Figure 4.2: (a) - Annotated photograph indicating the method used to measure flank wear. (b) - a photograph of the worn rake face of the tool. Both photographs were of an insert used to machine Ti-6246 at V_s = 75 m/min for 15 min.

4.1.3 Time dependant wear method - turning

In the second phase of the machining trial, the focus was to understand how the tool wear, primarily flank wear, varied with time in cut for both Ti-5553 and Ti-6246. New inserts were used to machine for the times listed in Table 4.5. The table also includes the billet diameters for each test run. In this series of tests, the same a_p and F_{rev} as detailed in Table 4.3 were used. For each material the V_s was maintained at the previously determined V15s. During this test the billet was turned in such a way as to leave a surface for roughness analysis at each time in cut. This resulted in a billet with staggered surfaces and decreasing diameter from the clamped portion of the workpiece. Figure 4.3 shows the billet after machining is complete, the first arrow (1) shows the two surfaces resultant from the inserts used for 600 and 300 s. Arrow (2) and (3) indicate the machined surface for tools used for 120 s and 60 s cuts respectively. Arrow (3) identifies the region where machined surfaces made for 45 s, 30 s, 15 s and 5 s were located.

Table 4.5: Time in cut and resulting billet dimensions for each test run of time dependant wear investigation on Ti-5553 and Ti-6246.

Material	Time in cut (s)							
Ti-5553	600	300	120	60	45	30	15	-
Ti-6246	600	300	120	60	45	30	15	5
	Billet Diameter (mm)							
Ti-5553	123	121	119	117	115	113	111	-
Ti-6246	174	172	170	168	166	164	162	160

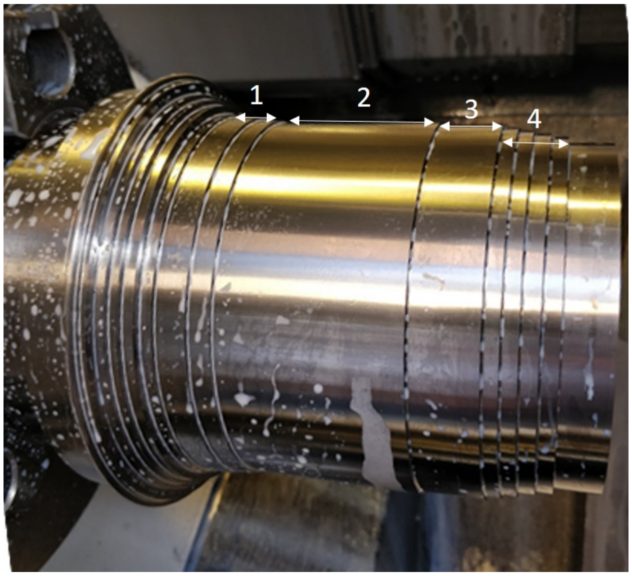

Figure 4.3: A photograph of the Ti-6246 workpiece after time dependant wear trial. 1 indicates machined surfaces after 600 s and 300 s. 2 and 3 mark the machined surfaces for the 300 s and 120 s tests respectively. 4 indicates the surfaces for 45 s, 30 s, 15 s and 5 s.

4.1.4 Results and discussion - turning

The results section includes four topics; (1) the edge rounding measurements for the inserts, (2) the V15 and time dependant flank wear measurements, (3) the Ra measurements and (4) the chip morphology.

Edge Rounding

Figure 4.4 shows a histogram with bin size 1 µm for the ER results. The measured ERs varied from 29.5 μm to 38.5 μm. The cutting inserts selected for testing were all within one standard deviation of the presented data set in order to reduce error associated with variation of the cutting edge geometry.

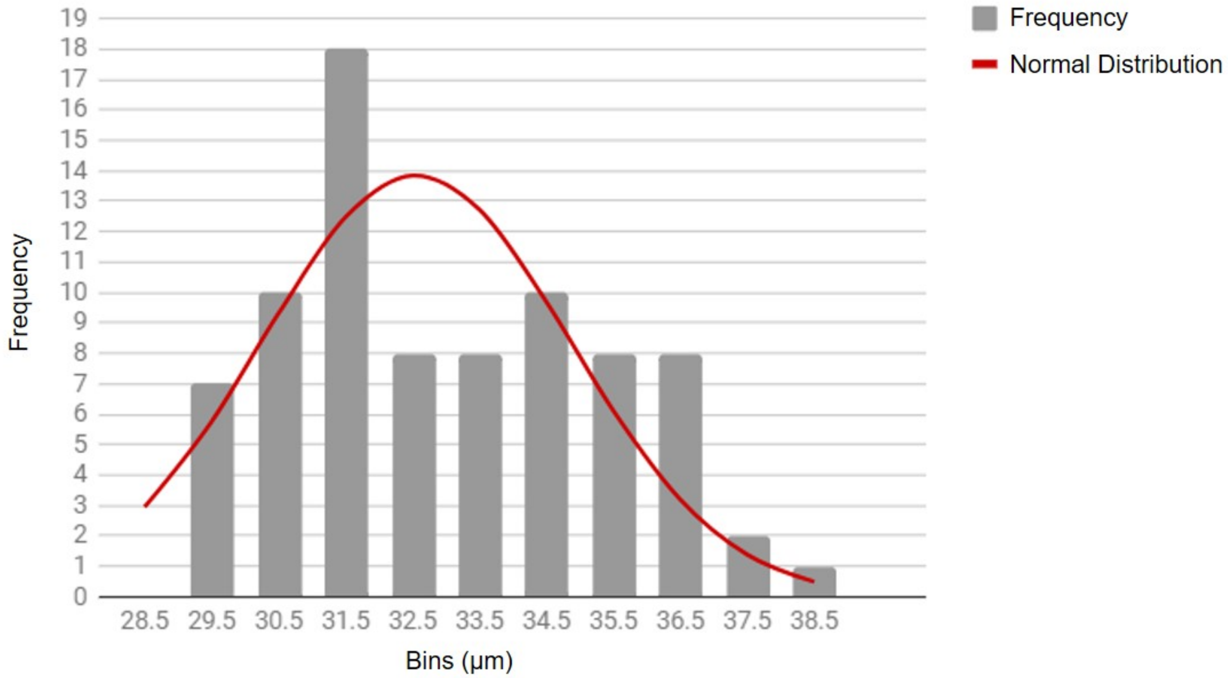

Figure 4.4: Histogram showing ER distribution, as measured on Alicona, for 80 cutting edges (20 inserts).

Flank Wear

The VB and VB$_{max}$ results for the V15 trial are shown in Figure 4.5a and Figure 4.5b respectively. The results show that the VB and VB$_{max}$ vary significantly over the 40 - 90 m/min test parameters. On each graph a horizontal line has been included to show the average (0.25 mm) and maximum (0.5 mm) flank wear limits of the tools. Results recorded above this line, such as 80 m/min for Ti-6246, failed the V15 test. Therefore, for both average and maximum flank wear criteria, Ti-5553 and Ti-6246 failed at all test speeds above 75 m/min. Since the flank wear measurements made at 70 m/min were well under the VB and VB_{max} the V15 was calculated based on interpolation (from the 70 m/min data point, to the 90 m/min data for Ti-5553, and the 80 m/min data for Ti-6246). This provided a conservative estimate of the V15 as the Taylor model for tool wear suggests exponential, non linear increase, meaning that the precise V15 will be higher than these estimations suggest. The V15 for Ti-5553 and Ti-6246 were determined to be 71 m/min and 74 m/min (74 - 78 m/min) respectively. The uncertainty in the V15 for Ti-5553 could not be accurately assessed due to the catastrophic breakage of the tool used at 90 m/min. The VB and VB_{max} results also show increased flank wear for Ti-5553 at all tested V_s completed for both alloys. This result and the estimates of the V15 confirm the reduced machinability of Ti-5553, from the perspective that less material can be removed before the tools fail the tool wear criterion. Figure 4.6a and Figure 4.6b show the VB and VB_{max} measured for each time used in the time dependant wear trial, where V_s were kept at 70 m/min (Ti-5553 V15), for Ti-5553 and 75 m/min (Ti-6246 V15), for Ti-6246. Thus showing how the wear varies as the time in cut is extended for close to optimum V_s (V15). Again, horizontal lines are included at the VB and VB_{max} flank wear limits used in the prior V15 trial. Every data point in Figure 4.6a and Figure 4.6b was recorded with a new cutting edge. For inserts used for less than 60 s, the VB is less than 0.05 mm and does not seem to depend on the time in cut. The same is true for VB_{max} which are all under 0.1 mm. From 120 s and onward the Ti-5553 tools were measured to have more flank wear than those used to machine Ti-6246. This further supports the fact that Ti-5553 is the less machinable alloy. The Ti-5553 tool used to machine for 600 s reaches the VB flank wear limit, which is in sharp contrast to the V15 trial where the insert used at 70 m/min, only reached 0.15 mm of flank wear after 900 s in cut. Similarly in the time dependant wear trial for Ti-6246, the insert used to machine for 900 s measured a VB of 0.45 mm and a VB_{max} of 0.75 mm, well above the wear limits despite being roughly at the estimated V15. For worn flanks of tools used to turn Ti-5553 at all V_s (except 40 m/min), there was excessive adhered material and BUE on the cutting edges. In contrast, the wear on the inserts used to machine Ti-6246 had very little adhered material on the cutting edge.

Surface Roughness Measurements

The surface roughness results, Ra, for both the V15 and time dependant wear investigations are shown in Figure 4.7a and 4.7b respectively. Both alloys show distinctly different trends for Ra with V_s. Although similar at 40 m/min, the Ra measured for Ti-6246 at 60 m/min of 0.37 μm is almost twice as high as that of Ti-5553 at the same V_s, which was 0.21 μm. Similar Ra was measured at 70 m/min. In the time dependant wear trial Ra for Ti-5553 is shown to increase to 0.7 μm at 120 s in cut. This demonstrates that for Ti-5553 turning, the tool wear incurred for the first 120 s to 300 s exacerbates the Ra. Then after the cutting wear on the cutting edge has stabilised, possibly with a consistent BUE, the Ra reduces. In contrast, the Ti-6246 roughness increases until the insert has been used for 600 s, suggesting a different tool wear mechanism and that the lack of BUE may be influencing the resultant

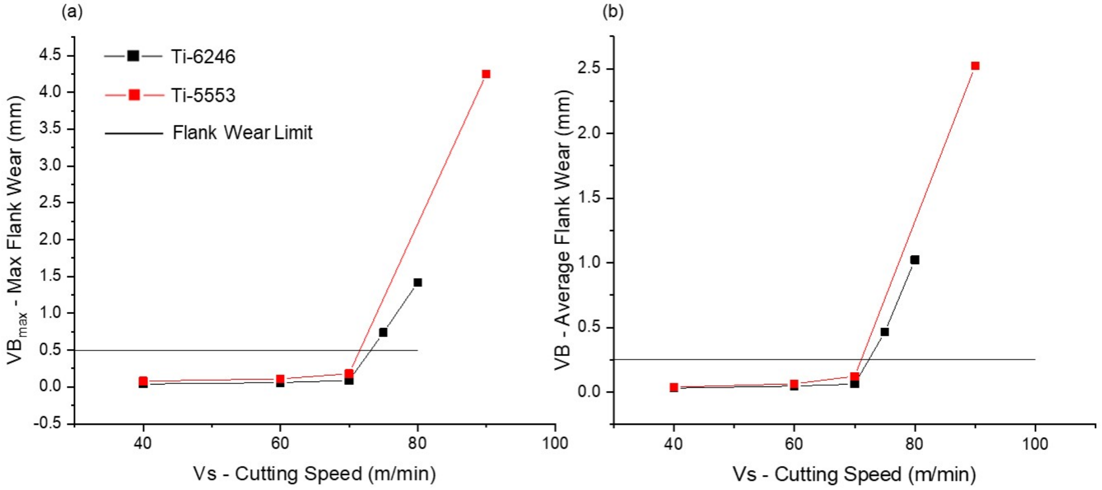

Figure 4.5: Graphs (a) and (b) show the VB and VB_{max} flank wear measured on the inserts used in the V15 tests.

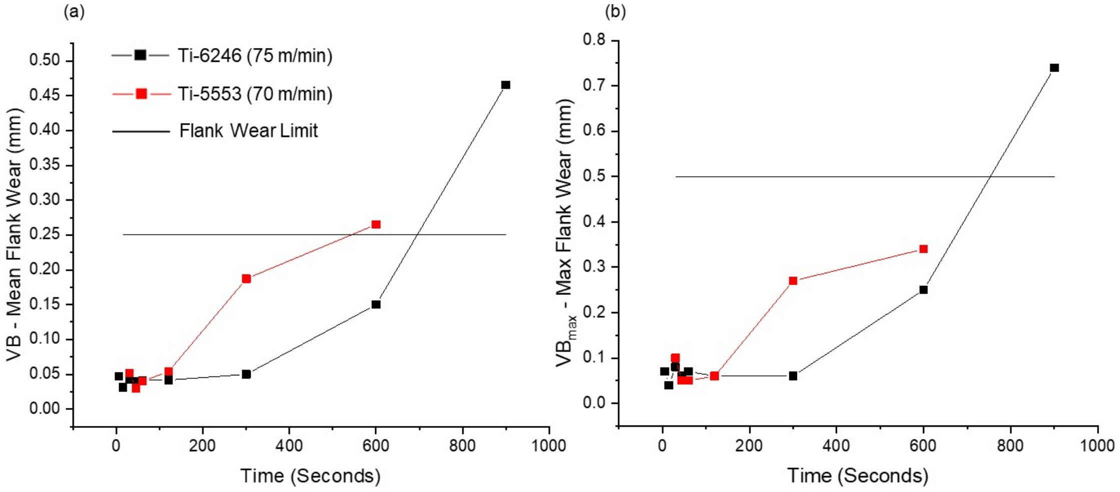

Figure 4.6: Graphs (a) and (b) show the VB and VB_{max} flank wear measured on inserts used for the time dependant tool wear test.

Ra. The experimental error is low, (0.03 μm), as five repeat measurements were taken for each roughness result. Table 7 includes the measured Ra of the machined surface for the three tests completed for 900 s. From these values, the standard error is calculated to be 0.02 μm for Ti-5553 and 0.04 μm for Ti-6246. These uncertainties cannot be considered for the different V_s which were tested, as there is no repeats at any other V_s, other than the V15. However, they are somewhat useful in understanding the uncertainty in the time dependant wear trial where all tests were conducted at the V15 parameters.

In the time dependant wear trial, the Ra increased during the first 120 s coincides with the early development of flank wear, and for Ti-5553, the formation of BUE. The Ra is shown to reach a threshold before starting to decrease as indicated by the peaks in the Ra line graphs of Figure 4.7b. The Ra decreases for Ti-5553 because the BUE becomes stable and uniform, while for Ti-6246 the Ra decreases because the cutting edge is blunted and has a larger ER. These phenomena are shown to happen at distinctly different times for the inserts used to cut each material. In Ti-5553, it happens much quicker as the wear is more rapid and the higher tendency for BUE means a uniform edge is formed earlier on.

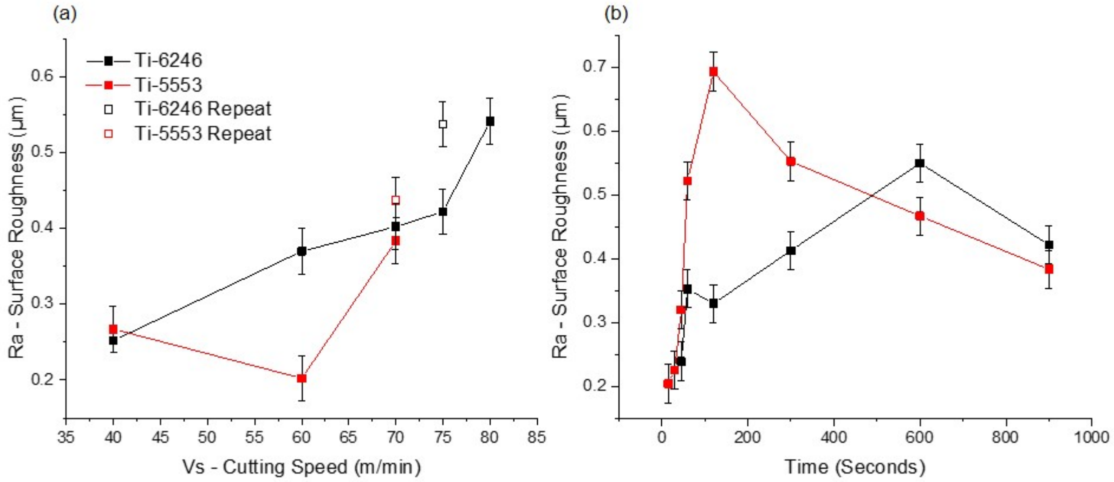

Figure 4.7: Ra results for (a) the V15 test, and (b) the time dependant wear test. The error bars indicate the measurement error (+/- 0.03 μm).

Table 4.6: Ra for all machined surfaces where inserts have been in cut for 900 s.

Material	V_s (m/min)	1	2	3
Ti-5553	70	0.375	0.436	0.387
Ti-6246	75	0.413	0.542	0.431

Chip Morphology

Macroscopic photographs and micrograph high contrast silhouettes of the swarf collected during the V15 trials for V_s of 40, 60 and 70 m/min are shown in Figure 4.8. The samples were each selected from swarf that was representative of the chip geometry after 15 min. The characterisation and analysis is based on the ISO 3685 Standard [95]. A helical geometry was evident for all collected samples. The photographs of swarf generated during Ti-6246 turning, at 40 m/min, indicate there was snarled swarf that has larger coil to coil separation than the samples taken from the Ti-5553 turning at the same V_s. For both alloys, the micrographs of the swarf resultant from 40 m/min turning have low serration and thus low frequency shear banding, indicative of very poor machining [132, 55]. The Ti-5553 swarf generated at 60 m/min was snarled with larger coil to coil separation than the Ti-6246 swarf. Despite being created under similar conditions, the Ti-6246 chips were generally longer but had more uniform separation. The micrographs for 60 m/min indicate a more serrated chip for Ti-6246 than Ti-5553. At 70 m/min, the swarf was snarled for both alloys. Furthermore, at 70 m/min chips from both alloys were generally shorter than at the other V_s, with the Ti-6246 chips being the shortest. At this V_s the micrographs indicate significant serration in the Ti-6246 swarf, which corresponds to high frequency shear banding and thus shorter chip length. In terms of swarf generation, the photographs and micrographs suggest an optimum V_s of 60 m/min for Ti-5553 which had the best serration characteristics. For Ti-6246 the shortest chips and worst serration characteristics (most serrated), was evidenced at 70 m/min.

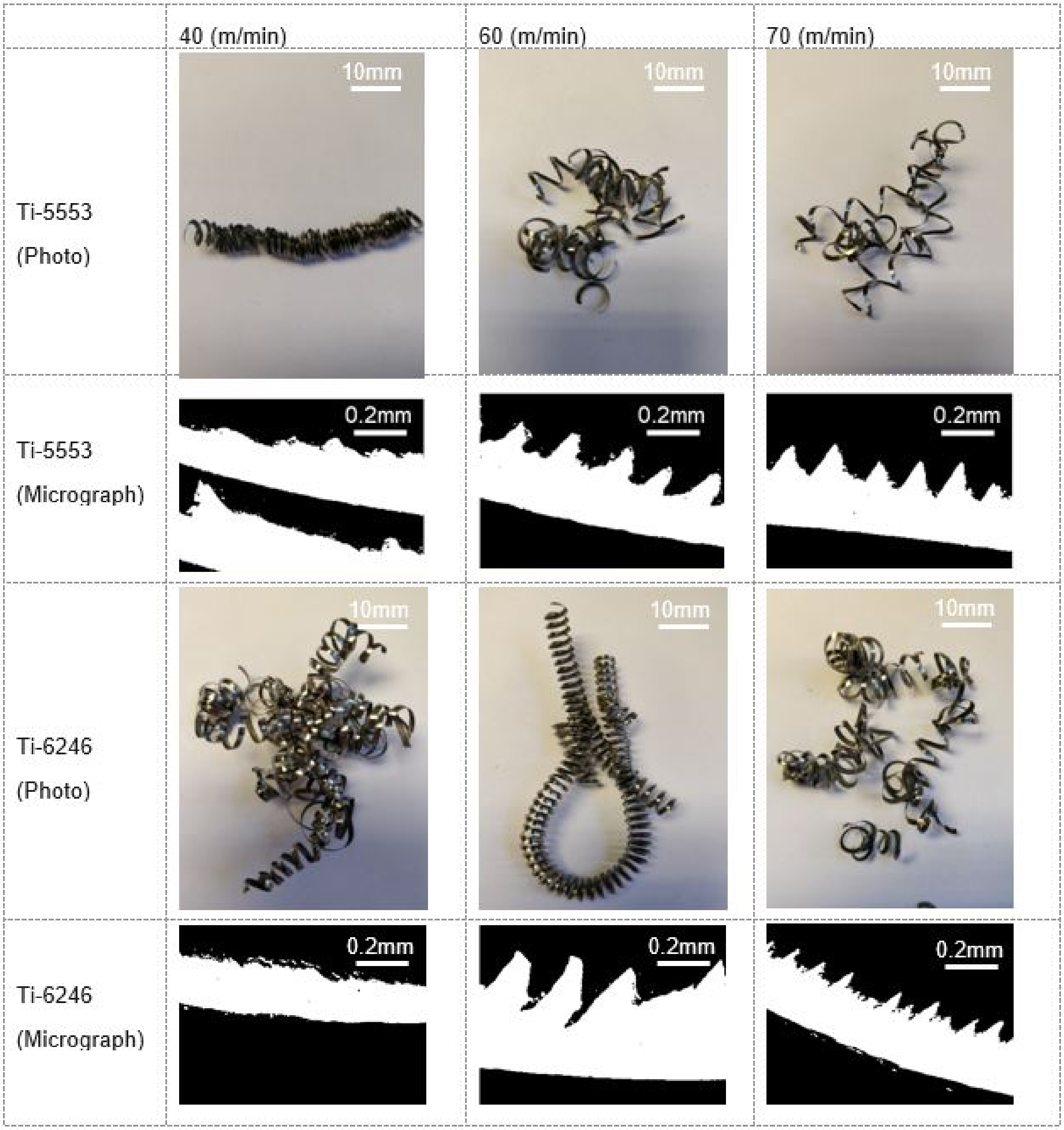

Figure 4.8: Photographs and high contrast micrographs of swarf from V15 trials at 40, 60 and 70 m/min for Ti-5553 and Ti-6246.

4.2 Drilling Ti-5553 and Ti-64 with WC-Co tools

As more metastable β alloys are utilised within the aerospace industry, the process of accurate machinability comparison is becoming ever more valuable to tool designers. Therefore, the drilling machinability of state of the art Ti-5553 (used in large landing gear forgings for the Boeing 787) and Ti-64, was investigated for 16 mm diameter PVD-TiAlN coated R846 solid carbide WC-Co tools. During testing, constant machining parameters were employed, including: V_s = 37.1 m/min and f_{rev} = 0.227 mm/rev. Throughout testing, the water emulsion coolant Hocut 795B was used. Spindle thrust force and torque were measured using a Kistler spindle dynamometer, processing and analysis of this data was done using MATLAB software. Hole roughness was measured using a Mitutoyo-surf portable surface roughness tester. Optical micrographs of the tool wear were taken for each alloy and the various wear modes are discussed in relation to both the forces and roughness data. Higher forces, torque, Ra and tool wear indicated poorer machinability for Ti-5553. As has been previously identified in milling and turning literature [72, 133], the propensity for BUE and adhered material to stick to the tool during the machining of Ti-5553 has been evidenced for drilling in this investigation. This was thought to contribute to an increased chipping propensity at the outer corners of tools used to drill Ti-5553. An interesting correlation between torque and force for each alloy was identified as an important response requiring further study. The result could be used to indicate tool wear during cut and would be invaluable for in process tool monitoring.

4.2.1 Experimental setup - drilling

Two cylindrical billets, one Ti-5553 and one Ti-64, were mounted within a DMU monBLOCK DECKEL MAHO machining centre. The clamping setup can be seen in Figure 4.9 where the Ti-5553 billet is affixed to the base of the machining centre. The tools were 16 mm PVD-TiAlN coated R846 WC-Co solid round drilling tools. For each alloy 2 tools were used and for each tool, 23 holes were drilled. Table 4.7 includes the cutting parameters and relevant information about the through tool coolant which was used during all drilling trials. To process the force and torque data, Kistler software DynoWear was used to record the data live from the dynamometer, then MATLAB was used to crop the data of each drilled hole and correct for thermal drift using the method described in §3.5.2. In MATLAB, the average force per hole was measured within the steady state cutting region. To measure the Ra of the machined surface of drilled holes, a Mitutoyo 178-561-02E surf was inserted 20 mm into each hole and the average from a series of 3 measurements was taken; following the method described §3.6.1. For each tool that was tested, images of the outer corner and rake faces were taken.

Figure 4.9: Photograph of Ti-5553 billet clamped within the DMU 100 monoBLOCK machining centre before drilling.

4.2.2 Experimental results - drilling

In this section several results are introduced: (1) The average thrust force and drill torque for both tested alloys. (2) The relationship between force, torque and hole number. (3) The relationship between Ra and the number of holes drilled. (4) Images and discussion of the tool wear on the margin and rake of the tool.

The average thrust force (Fz) and torque (Mz) for each alloy for repeats 1 and 2 are shown in Figure 4.10a and Figure 4.10b. The average thrust force is 1000 N (40%) higher for the drilling of Ti-5553 in comparison to Ti-64, during the steady state part of the drilling operation. The torque is shown to be 3-5 Nm higher in Ti-5553 for the first half of the drilled hole, then 5-10 Nm higher during the second part. This is roughly a 20% increase in torque for the duration of the drilled hole. The repeat runs for Ti-5553 are almost identical with slight deviation towards the end of each hole in both force and torque. There is slightly more deviation between the Ti-64 repeats where a significant increase in force on repeat 2

Table 4.7: V_s, V_f, coolant type, coolant concentration and coolant pressure for drilling trials.

Parameter	Value
Cutting Speed, V_s	37.1 m/min
Feed Rate, V_f	0.227 mm/min
Coolant Type	Hocut 795B
Coolant Concentration	7%
Coolant Pressure	20 Bar

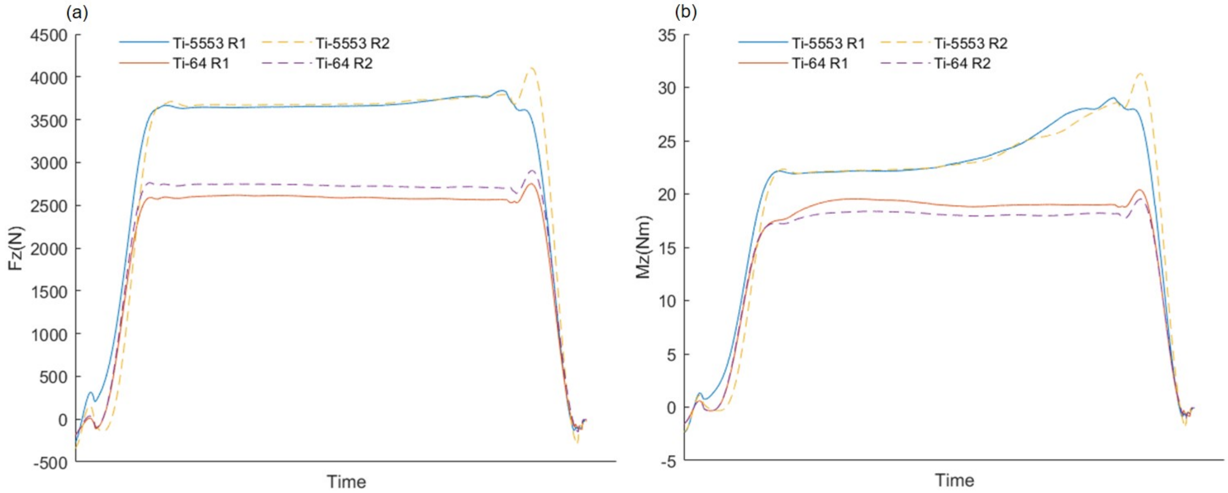

Figure 4.10: Graphs showing the average thrust force (Fz), (a) and torque (Mz), (b) for 23 holes drilled in Ti-5553 and Ti-64 repeats 1 and 2.

corresponds to a significant decrease in torque for repeat 2. Figure 4.11a shows the average thrust force deviation from the mean thrust force of each hole for the progressive 23 hole set for Ti-64 and Ti-5553, for each repeat. There was a significantly steeper positive trend in the measured forces for Ti-5553. Due to this, the range of forces experienced by the tool used to machine Ti-5553 during the test (200 N) was approximately double the range of that of the Ti-64 tool (100 N). The torque results had a very similar trend, Figure 4.11b shows the deviation in the force results on the Y axis and the deviation in the torque results on the X axis for both alloys. The linear fit for repeats 1 and 2 of Ti-64 are plotted through the data. The linear fit for Ti-5553 repeats 1 and 2 are included as the same line, since there is no significant difference between the regression lines. The significance of the fits are presented in Figure 4.11b and are given in Table 4.8 which includes the P and R values. The P value (probability value) is the probability value and indicates the probability of getting a result that is the same or more extreme than the observation. The R value, or the correlation coefficient, is used to quantify the strength and direction of a linear relationship. In Figure

Table 4.8: P (Probability value) and R (correlation coefficient) value for Ti-64 and Ti-5553 fits between thrust force (Fz) and torque (Mz) data - regression lines for which are shown in Figure 14b. R1 and R2 indicate the repeats.

	P Value	R Value
Ti-64 R1	0.19	0.112
Ti-64 R2	0.0001	0.544
Ti- 5553 R1 & R2	0.0000001	0.834

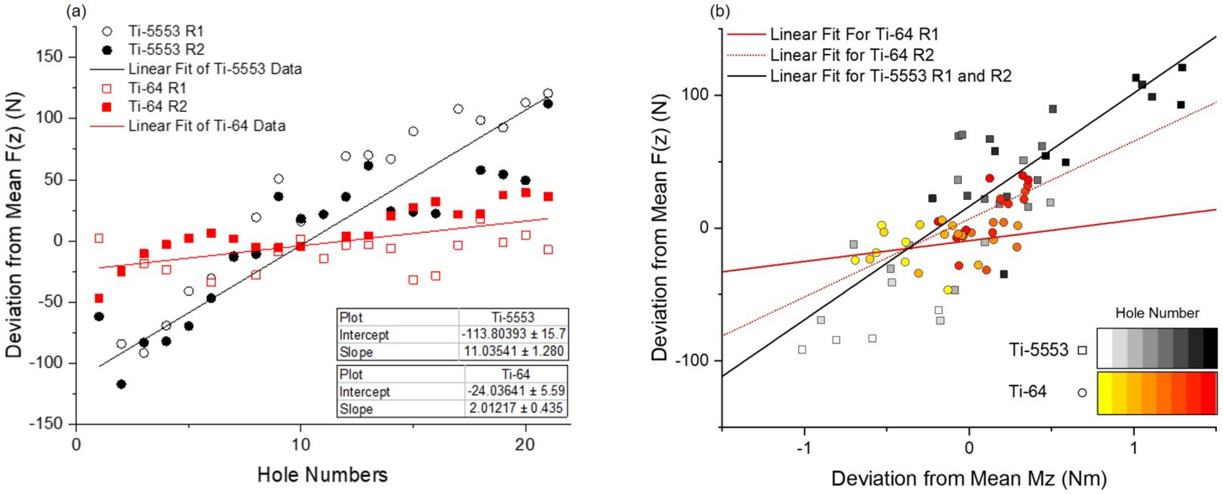

Figure 4.11: (a) - Graph of thrust force (Fz) variation from mean for each hole drilled in Ti-64 and Ti-5553 (R1 and R2). (b) - Graph of thrust force (Fz) and torque (Mz) deviation correlation from mean per hole drilled.

4.11b, the hole number is included as the color gradient indicates, in general the force and torque increase as hole number increases.

Figure 4.12 is included to show the final condition of the outer corner and rake face of each tool (for one side of each tool). It is clear from these images that the wear on the Ti-5553 tools is significantly greater. The wear mechanisms evident are also slightly different for the two alloys. The wear on the rake face for Ti-5553 drilling was more abrasive and less uniform suggesting a different type of sliding and sticking action during chip motion. There is significantly larger BUE and adhered material on the Ti-5553 tool outer corners, which seems to coincide with an increase in chipping that is observed in the rake face images.

The hole roughness measurements are presented in Figure 4.13. The mean Ra for Ti-5553 was 0.766 μm (+/- 0.03 μm), which was 14% higher than the mean Ra for Ti-64, which

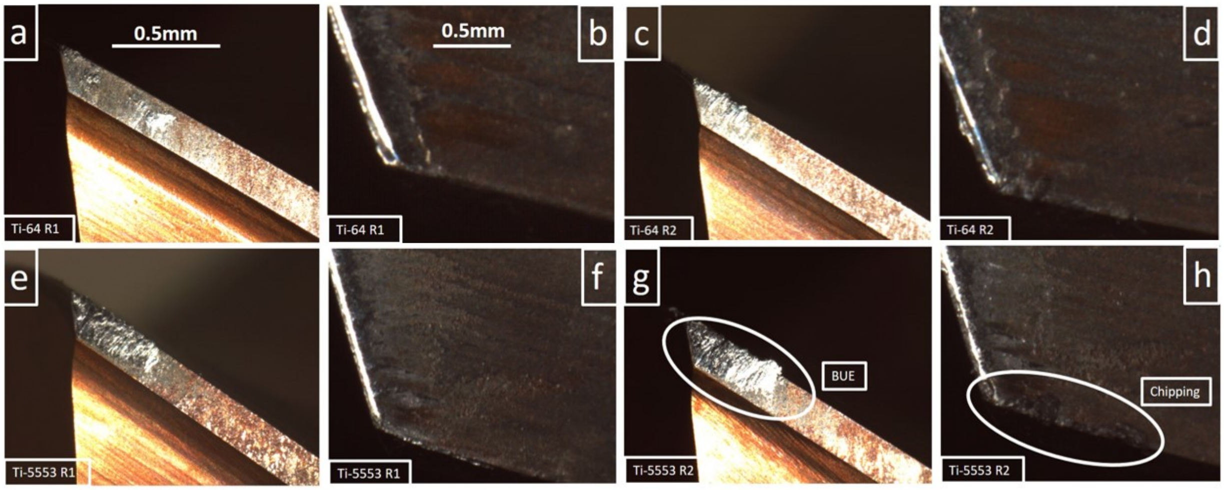

Figure 4.12: Photographs of outer corner margin wear (a, c, e, g) and rake wear (b, d, f, h) for tools used to drill Ti-64 and Ti-5553. The photographs were taken after the final hole. (RX = Repeat X)

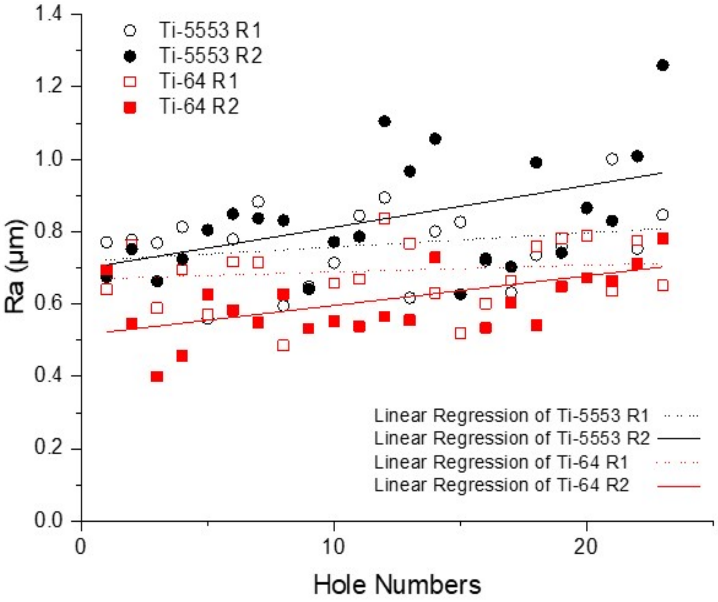

Figure 4.13: Graph showing how Ra correlates with hole progression in Ti-5553 and Ti-64.

was 0.677 μm (+/- 0.03 μm). There was no statistical significance in the linear regressions for Ti-5553 as compared to Ti-64, but both do exhibit a similar positive trend. The errors indicated are the associated the measurement errors.

4.2.3 Discussion - drilling

The tools used to drill the Ti-5553 exhibited significantly more wear than Ti-64. As the same number of holes was drilled for each material (and repeat), this indicates an accelerated wear rate. No exact estimate can be made from these results as to when the tools will fail since so few holes were drilled, however, it can be said that tools used to drill Ti-64 will have significantly longer life. As the thrust force and torque increase with each hole drilled, it is probable that the changing tool geometry, due to tool wear, is influencing them. This is supported by the greater increases in force and torque associated with the Ti-5553 drilling. The higher average forces measured for the Ti-5553 drilling highlights the significant difference between the strength of Ti-5553 and Ti-64. Although this will contribute to the reduced machinability of Ti-5553, the results suggest that there are other contributing factors to consider. For example, the increased tendency for Ti-5553 to adhere to the WC-Co tools and PVD-TiAlN coating, suggests the alloy chemistry is playing a role in the machinability. This hypothesis is supported by research by Hatt et al [28], who has identified key differences between WC-Co tool interaction between $\alpha + \beta$ and metastable β alloys. It has been found in milling and turning [108, 134], that increased cutting forces can reduce part integrity by imparting residual stress into the machined surface. The increased Ra measured for the Ti-5553 surface is indicative of such damage: within industry such holes would require further finishing operations, such as reaming, before they are ready for assembly. To better understand the differences between the subsurface damage for both alloys, sectioning and mounting of the material for high magnification imaging of the subsurface would be required. The relationship between force and torque, identified in Figure 4.11 could present a significant opportunity for in-process monitoring of drill tools, if the changes in force and torque can be correlated with the changing wear of the tools. The results suggest that the steeper the force versus torque gradient, the faster the tool will wear. In the future, it may be possible to estimate the tool life from such gradients, and thus estimate the amount of tool wear at any particular hole during the tools operation.

4.2.4 Conclusions - drilling

- Tools used to drill Ti-5553 had relatively more wear to those used to drill holes in the Ti-64. This was a result of the higher forces and varied wear mechanism that occurred for the metastable β alloy. Again, Ti-5553 is verified to be the less machinable alloy.
- Tools used to drill Ti-64 were observed to have more uniform wear on the rake faces due to the differing change in sticking and tool workpiece material action, resulting in more abrasion on the Ti-5553 tools.
- The relationship between thrust force and torque correlates with the increase in tool wear via chipping BUE and rake face degradation. This may be extremely useful for

dynamic tool wear monitoring during drilling processes.

4.3 Orthogonal cutting using a novel arbitrary strain path testing machine for Ti-64, Ti-6246 and Ti-5553.

The arbitrary strain path testing machine (ASP) shown in Figure 4.14a was used to force 15x15x60 mm samples (shown in Figure 4.14b) of Ti-64, Ti-6246 and Ti-5553 against the cutting edge of two separate WC-Co H13a inserts (shown in Figure 4.14c), at 90 degrees. Hydraulic rams connected to load cells enabled the axial load force of the orthogonal cutting tests to be measured during chip generation. The ASP was programmed to move the samples down against the tools at 10 mm/s for 20 mm. The first 2 - 3 mm of this motion was used to bring the samples and tools into contact with the remaining distance for creating chips and shearing the sample.

The ASP load cell recorded the axial load force at 1024 Hz. These forces were then processed and analysed using MATLAB 2017 software. To correlate the forces with the chip form behavior and assess the feasibility of the ASP approach, chips of Ti-6246 were mounted in Bakelite, polished using colloidal silica buffered with H_2O_2 and then imaged using cross polarised light on a Nikon optical microscope.

4.3.1 Experimental results - orthogonal cutting

In Figure 4.15 the axial load of the ASP machine is plotted for the full length of the orthogonal cut for Ti-64, Ti-6246 and Ti-17. The initial increase in force shown in each plot represents material coming into contact with the stationary insert. For each alloy the loads increase to a similar level and can be seen to oscillate as the cut progresses. The average oscillation for Ti-6246 is largest at 5 kN versus 3 kN for Ti-17 and 2.25 kN for Ti-64. Both Ti-6246 and Ti-17 loads oscillate with a more rapid frequency to that of Ti-64, where the periodicity is less clear.

Figure 4.16 shows a direct comparison of the Ti-6246 microstructure and coreresponding load force. The red colour in the micrograph is used to highlight increases in amplitude of the load force and correlated with the shear-banding within the chip. Figure 4.16 shows how the force on the work material increases and decreases twice. For the shown region, when the load cell records the highest forces, there is much more deformation evident in the micrograph and it is possible to see the shear zones within the chip. The dark line at the

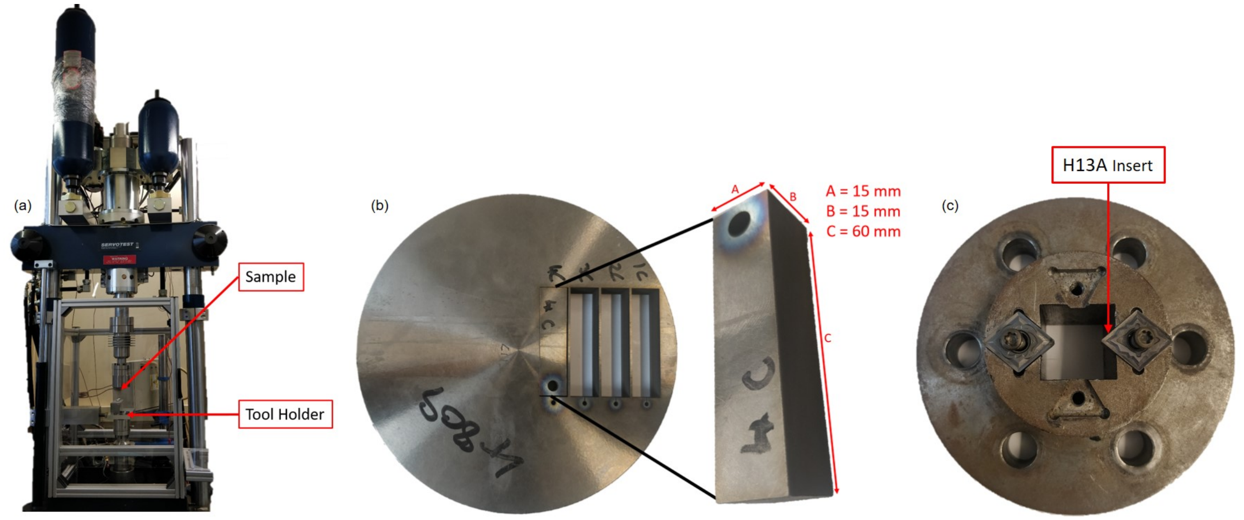

Figure 4.14: Photographs of the: (a) - ASP machine. (b) - Ti-17 material showing location of extraction with wire EDM and ASP sample dimensions. (c) - Tool holder and H13A inserts.

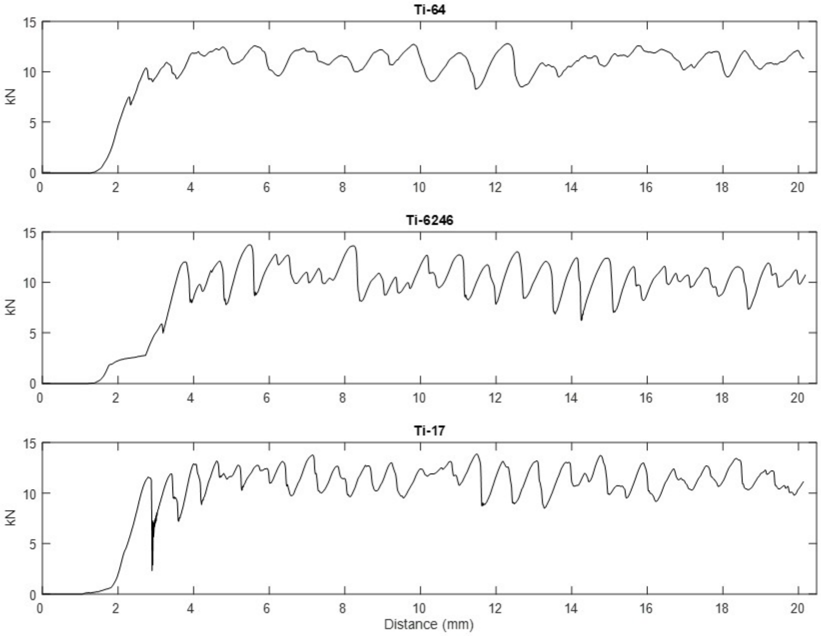

Figure 4.15: Axial load force during orthogonal cutting Ti-64, Ti-6246 and Ti-17 at 10 mm/s using the ASP.

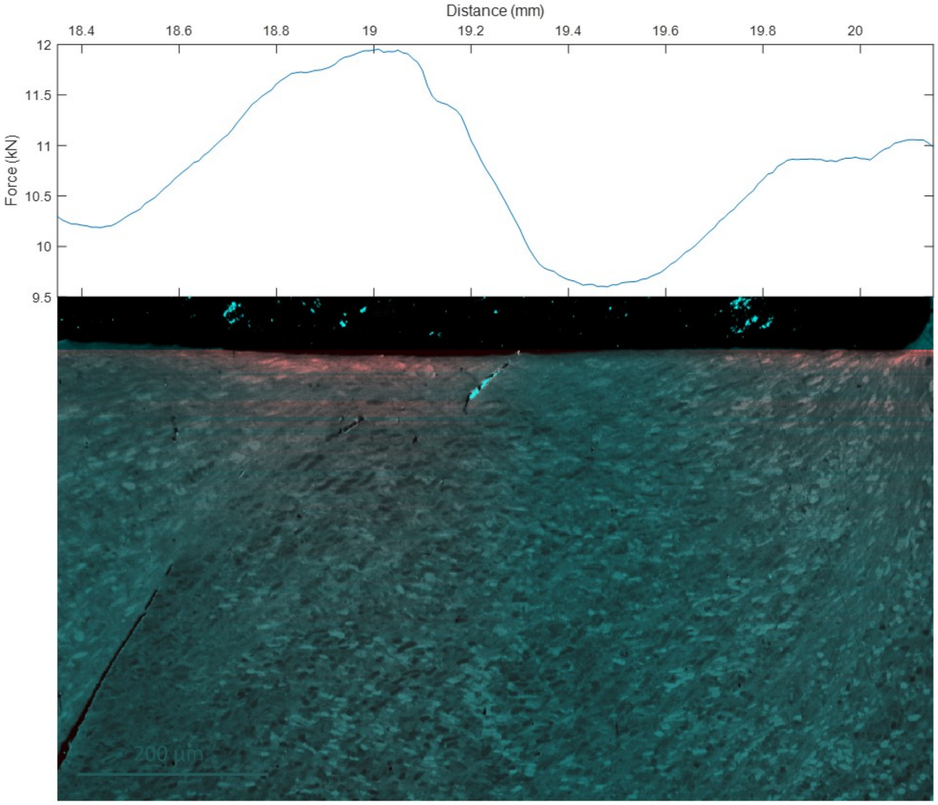

Figure 4.16: Optical micrograph combined with a heat map showing how axial load forces correlate to chip deformation in a Ti-6246 chip made using the ASP.

bottom left of the micrograph is the separation in the chip material caused by the shear force.

4.3.2 Experimental discussion

The oscillation of the load cell forces is indicative of chipping during the orthogonal cuts. This is supported by the scale comparison of the Ti-6246 chip microstructure and the load force. Cyclic forces have been identified to cause rapid tool wear in machining and are characteristic during titanium machining [135, 136]. The load required to form a chip is lowest in Ti-64, putting the tool under the least strain and indicating there will be less tool wear, and therefore, slightly better machinability. In Ti-6246 the required load for chipping is very similar to that of Ti-17 but the subsequent decrease in force is slightly larger, suggesting more deformation in the chip material. This could indicate a more severe damage depth for the machined Ti-6246 due to the shear zone accommodating more of the strain during the removal of material and chip formation [108]. However, as damage in the machined surface was not examined in this investigation, this could not be verified. Although the ASP method has determined that both Ti-6246 and Ti-17 are more difficult to machine than Ti-64 in terms of chipping, it does not examine the effects of temperature and prolonged contact of tool and workpiece material. Both of which have been identified to be critical in the failure of tools used to machine titanium alloys.

4.3.3 Conclusions - orthogonal cutting

The results indicated that Ti-64 had better machinability than Ti-6246 and Ti-17 as the cyclic forces were lower, resulting in less stress on the tool. The results for the Ti-6246 and Ti-17 were similar, and therefore, from the results obtained, it is difficult to declare which of the two has the better machinability. The fact the wear is not examined represents a significant drawback for the method, however, the ASP does enable machinability in terms of chip formation and shear to be investigated at a relatively low cost. It also showcases the possibility of examining specific load cell forces for the corresponding chip microstructure and deformation, something that would be extremely difficult to replicate within an industrial test, but could be critical for accurate, rapid, machinability assessment of new or untested alloys. The full potential of the ASP method is demonstrated by Dredge et al. in their work to understand machinability characteristics of Ti-64 and Ti-407 [97].

The forces extracted from the load cells are not comparable in magnitude to those experienced during machining yet they are still valuable for comparing chip form characteristics and to characterise the cyclic stresses undergone by the tools during machining. This type of analysis could be more effective if the a_p in these trials could be reduced and made more realistic. The ASP method does not replicate the exact thermomechanical conditions analogous to machining and therefore the tool workpiece interaction is not the same.

As the tool and workpiece interaction is critical in determining tool life due to crater wear in titanium machining, another type of test, such as tool workpiece diffusion couples at realistic temperatures and pressures should be considered. Therefore, for maximum effectiveness, ASP machinability testing should be combined within a set of small scale machinability tests that could be carried out for a fraction of the cost required for typical machinability testing that is currently undertaken within industry.

4.4 Chapter summary

The objective of this chapter was to compare the machinability of titanium alloys with different β stability in order to identify key areas of research to pursue in the thesis. In the turning investigation (§4.1) on Ti-5553 and Ti-6246, the V15 method of machinability assessment identified that Ti-5553, a metastable β alloy, had a lower V15, and hence poorer machinability than Ti-6246 - a near-β alloy. The swarf collected during the turning trial supports this finding, indicating that the optimum V_s for turning Ti-6246 was faster than for Ti-5553. In the time dependent wear trial the flank wear over time relationship was different for each alloy. One possible explanation is that the Ti-5553 is interacting with the cutting insert in a way that accelerates the flank wear earlier in the tools life. This is supported by the increased propensity for BUE to form on the cutting edge of tools used to machine the Ti-5553, showing an increased affinity between Ti-5553 and WC-Co. Although the Ra measurements for each alloy were adequate for a roughing operation, the difference in cutting edge geometry of the tools used to machine Ti-5553 exhibiting significant BUE, versus those used to turn Ti-6246, resulted in significant differences in the Ra of the machined surfaces, for both the different V_s tested and the different lengths of time in cut. If surface finish is a priority, machinists should consider that early in the life of tools used to machine Ti-5553, when a stable cutting edge is not yet established, there may be unusually high Ra. In the drilling machinability investigation (§4.2), a different wear mechanism was seen for each alloy (Ti-5553 and Ti-64). Those tools used to drill the Ti-5553 had significantly higher force and torque at the same cutting parameters and there was a key relationship between the thrust force, torque and tool wear. The tools were also observed to have more wear after the 23 holes were drilled, and thus Ti-5553 was confirmed to be the less machinable alloy. The images of the tools showed that for those used to drill Ti-5553, there was more adhesion of workpiece material and thus BUE on the cutting edge. The visual evidence suggested this increased adhesion was leading to more rapid abrasive wear on the rake faces of the tool. In the ASP experiment (§4.3), Ti-64 was found to be the most machinable alloy as the cyclic forces were lowest, which would result in the least stress on the tool and less damage imparted into the machined subsurface. For all three experiments, the reduced machinability of titanium alloys correlates with increased β stability. There was also significant evidence suggesting that the reduction in machinability was not solely due to the increased strength of Ti-5553 but also due to the excessive formation of BUE, possibily due to an increased propensity to react with the tool material and resulting in more wear.

The results of this chapter identify a clear difference in the type and amount of tool wear on WC-Co tools when machining titanium alloys with different levels of β stability. They also highlighted the potential for cutting force data to facilitate machinability comparison. As the results did not enable any kind of subsurface damage assessment of the machined surface, something which is addressed very little within the literature, especially for drilling, this should be addressed in the future. In order to investigate the extent of subsurface damage, whilst continuing to explore the nature of tool wear, a new method of machinability comparison must be developed. Therefore, in §5 velocity force maps (VFM)s are used to further understand titanium alloy machinability in terms of subsurface damage.

Chapter 5

A novel method for investigating titanium alloy drilling machinability using velocity force maps

This chapter presents a new method for investigating titanium alloy drilling machinability via force, torque and microstructural analysis of holes drilled at different V_s and V_f combinations. The technique utilises a response surface methodology in order to directly compare machinability at similar thrust forces by creating so called velocity force maps (VFMs). The work in this section has been published in the international journal; Advances in Mechanical and Industrial Engineering (AIME) [128]. The methodology has also been presented at and published in the proceedings for the 14th international conference on titanium (2019).

5.1 Introduction

Creep resistant α, general purpose $\alpha+\beta$ and high strength metastable β titanium alloys are all used within the aerospace industry. However, the $\alpha+\beta$ alloy Ti-64 accounts for over 50% of the total usage. Generally, this has resulted in tool and process design for all titanium alloys being developed based on Ti-64 drilling data and research. For tool suppliers, the cost of carrying out machinability investigations on less common alloys in order to identify the correct cutting parameters, develop alloy specific tools, or fully optimise current tools is not worth the expense; especially if there is not a guarantee of increased productivity. Instead, tools designed for Ti-64 machining are used for all titanium alloys in combination with significant tool life and cutting parameter tolerances that reduce productivity and result in unnecessary costs. Typically for drilling, tools are PVD-TiAlN coated tungsten carbide, cobalt binder (WC-Co) drills. To optimise or improve these tools for different alloys, current practice necessitates multiple tests to failure which requires thousands of holes per tool, often with many repeats. This accrues significant tooling and material costs, especially for metastable β alloys that are expensive. If tool life and parameter tolerances were improved, through the development of specific tools for different titanium alloys, without the excessive amounts of material and time currently required to develop such tools, both tool suppliers and aerospace manufacturers would benefit. In addition, if the testing and benchmarking of tools can be done within a reduced time frame, it will be possible for tool suppliers to benchmark more tool characteristics, which will result in more rapid innovation.

Currently the process of identifying the operational window of tools in terms of cutting parameters is accelerated through the use of analytical models which estimate the amount of tool wear and hole quality depending on the V_f, V_s and tool geometry [137]. Such models can reduce time spent prototyping new tools, due to their extensible nature and that there are no lead times for developing the new tools to be tested. Unfortunately, current analytical models are not able to account for the effects of certain coatings on tool performance, nor provide any information on the subsurface deformation of drilled holes. The latter is relatively important when drilling titanium alloys, as highly dissimilar microstructures deform differently, which influences how holes have to be finished machined. Models which predict the force and torque in drilling do not consider their influence on part integrity, this is relatively important for titanium alloys since they are used for critical components [56]. Models often require mechanical data, which is not always available for titanium alloys, and especially metastable β alloys. In addition, the interaction between titanium and WC-Co is not well understood and differs depending on alloy chemistry [84]. The same is true of the tool coating workpiece interaction.

Short tool life is a significant contributor to overall cost in titanium alloy machining due to high strength, low thermal conductivity and high chemical reactivity [138, 54]. As discussed previously, the interaction of tools with different titanium alloys varies. As a result, newly developed alloys must often be benchmarked for machining with the current state of the art tools. Often drilling is used in the first benchmarking stage. When benchmarking the machinability of Ti-54M against that of Ti-64 Kosaka and Fox identified that tool wear in drilling can be correlated to the initial thrust force and torque during the operation at various RPMs [107, 106]. However, in their research, they did not investigate, nor consider the important relationship between V_f and V_s on the thrust force and torque, and thus the tool life. Tool suppliers need to understand this relationship for each alloy they are developing for, so they can simultaneously optimise tool design and recommend the most efficient cutting parameters for productivity.

When considering the machinability of titanium alloys subsurface microstructural characterisation of the material being machined is important. Variation in the subsurface deformation can have considerable impact on the fatigue life of components. In milling and turning, several studies have elucidated this relationship [73, 108, 139]. In drilling, Rahim and Sharif, have considered the effect of drilling on the subsurface microstructure in Ti-64, however, there has been no study to investigate this over a range of titanium alloys [116]. As the microstructure of metastable β alloys, such as Ti-5553, is significantly different to those of α+β alloys like Ti-64, it can be expected that the resulting subsurface deformation will also be different.

In order to consider the best machining parameters for current tools when machining different titanium alloys, a range of alloys with increasing β stability (Ti-64, Ti-6246 and Ti-5553), were drilled at a range of V_f and V_s, with both coated PVD-TiAlN and uncoated WC-Co tools. The primary aim was to develop a rapid method of machinability comparison for different titanium alloys which enabled the investigation of microstructural deformation, tool wear and tool operating windows in terms of V_f and V_s.

5.2 Methodology

5.2.1 Material

The three alloys tested in this work are Ti-64, Ti-6246 and Ti-5553. Further details such as the nominal compositions, Vickers hardness and heat treatment conditions are provided in Table 3.1. The bulk microstructure of each alloy is shown in Figure 5.1. As Ti-64 is β annealed, the size of the prior β grains within Figure 5.1a are extremely large, 50 - 500 μm in size. The Ti-6246 microstructure in Figure 5.1b, consists of α grains in a β matrix populated with an α lamellar basket weave Widmanstätten structure. α grain size is roughly 5 to 10 μm. The Ti-5553 microstructure, shown in Figure 5.1c, consists of large prior β grains and small α grains, $2-5$ μm in size. These three alloys were selected to compare the machinability over a range of alloys with varying β stability. Figure 5.2 is a pseudo-phase diagram that indicates the β-transus temperatures of each alloy. Ti-64 is an α+β alloy, Ti-6246 contains

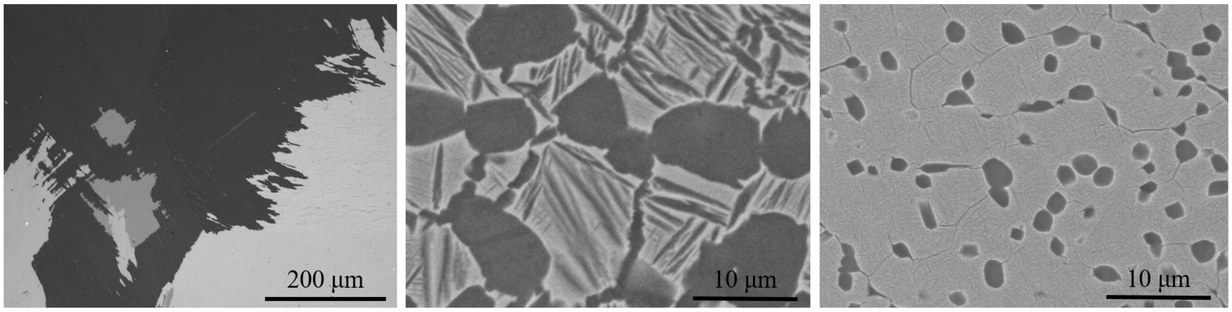

Figure 5.1: Bulk microstructure for (a) Ti-64, (b) Ti-6246 and (c) Ti-5553. (a) Is a cross polarised light micrograph, (b, c) are BSE micrographs.

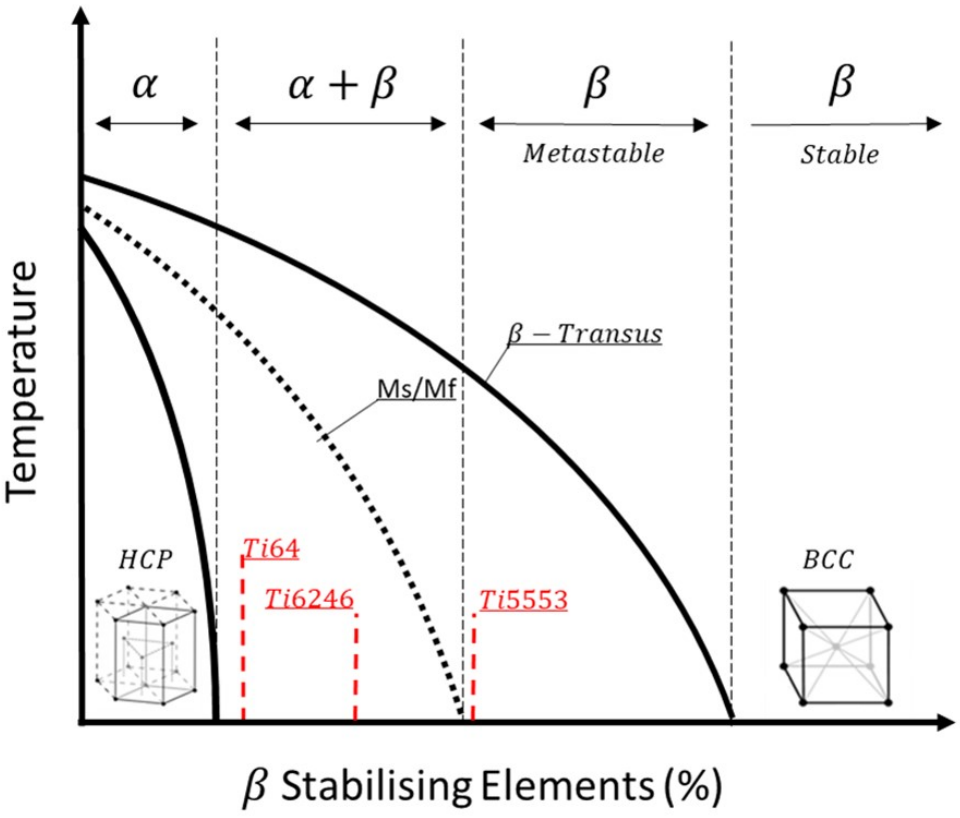

Figure 5.2: Pseudo phase diagram indicating relative difference in T_β temperature for Ti-64, Ti-6246 and Ti-5553.

more β stabilising elements than Ti-64 and although sometimes a point of contention is still described as an α+β alloy. Ti-5553 has relatively more β stabilisers than both Ti-64 and Ti-6246 and is a metastable β alloy.

5.2.2 Tools

PVD-TiAlN coated and uncoated R846 Corrodrill WC-Co twist drills with a 6.9 mm diameter were used in this investigation. Relevant drill characteristics are tabulated in Table 3.3. The uncoated and coated edge radii were 50.1 (+/- 0.5) μm and 55.6 (+/- 0.5) μm respectively. Figure 5.3 is a photograph of the uncoated and coated TiAlN-PVD drill and the unworn rake and flank faces for both. Each tool geometry was measured on a Helicheck Pro machine to ensure no anomalies were present and to characterise the variation of important geometric parameters that could influence results. During testing an Olympus SZX10 light microscope - camera system was used to image the flank chisel and margin of tools at holes 0, 1, and

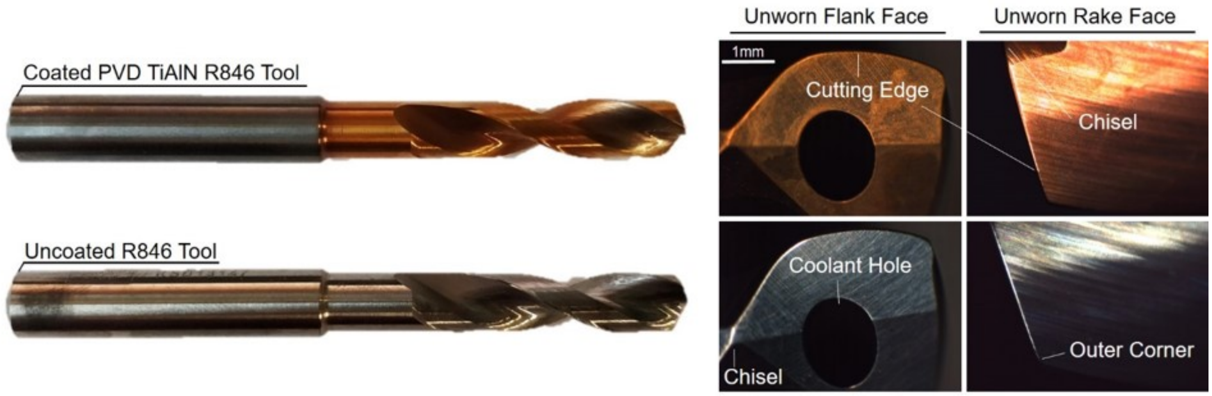

Figure 5.3: Photographs of the uncoated and coated PVD-TiAlN R846 tools and their unworn flank and rake faces

10. Subsequent image processing and scaling was carried out in Clemex vision software.

5.2.3 Machine and dynamometer setup

Throughout the investigation a monoBLOCK DMU 100 machining centre was used. Tools were mounted on the spindle using a hydraulic chuck. A high lubricity soluble oil metal removal fluid, HOCUT 795B coolant (7% Concentration) was supplied through the tool at a pressure of 20 Bar. All testing was completed with a spindle mounted Kistler dynamometer, further details such as the signal conditioner, sampling frequency and sensor measuring ranges are in Table 3.8.

5.2.4 Experimental procedure

For every tool used in this investigation a prior “bedding in” hole was drilled. The purpose of this first hole was to ensure there were no premature failures due to hidden tool defects during testing. The “bedding in” hole was drilled just prior to the actual testing in the material. The drill would be tested at the standard cutting parameters for the material. After, the tool was removed and images of the wear were taken and viewed to check for failure and provide assurance that the tool integrity was fit for further testing. For each of the three alloys that were tested, 10 coated and 10 uncoated tools were used. For each tool, a set of 10 holes plus the initial ”bedding in” hole were drilled. The distance between the centre of one hole and the surrounding holes, or the hole pitch (P) was 7.9 mm. The diagram in Figure 5.4 shows how the V_f and V_s were varied in each material plate. Ten holes were drilled with each tool at a different V_s for each tool (48 m/min for tool 1 to

32 m/min for tool 10). The CNC code was modified so V_f was increased from 208 to 284 mm/min in increments of 8 mm/min for each hole drilled by each tool. Holes were drilled sequentially without removing the tools from the hydraulic chuck or machining centre: for this reason wear could not be imaged for every hole, however, this was deemed necessary to avoid the compounded error that varied runout from releasing and re-inserting tools would cause. Excluding "bedding in" holes, 600 holes were drilled in total: 200 in each alloy with 100 made using coated tools and 100 with uncoated tools. All 600 holes were 20 mm depth, through holes. All V_f and V_s values used in the study were within 20% of the industry standard cutting data, as taken from the CoroPlus tool guide [122]. To check if cutting force and torque surfaces would be comparable at the selected cutting parameters within the tested alloys, cutting force coefficients calculated by the AMRC TMG machining group were used to calculate the expected thrust force that would be measured during testing [110].

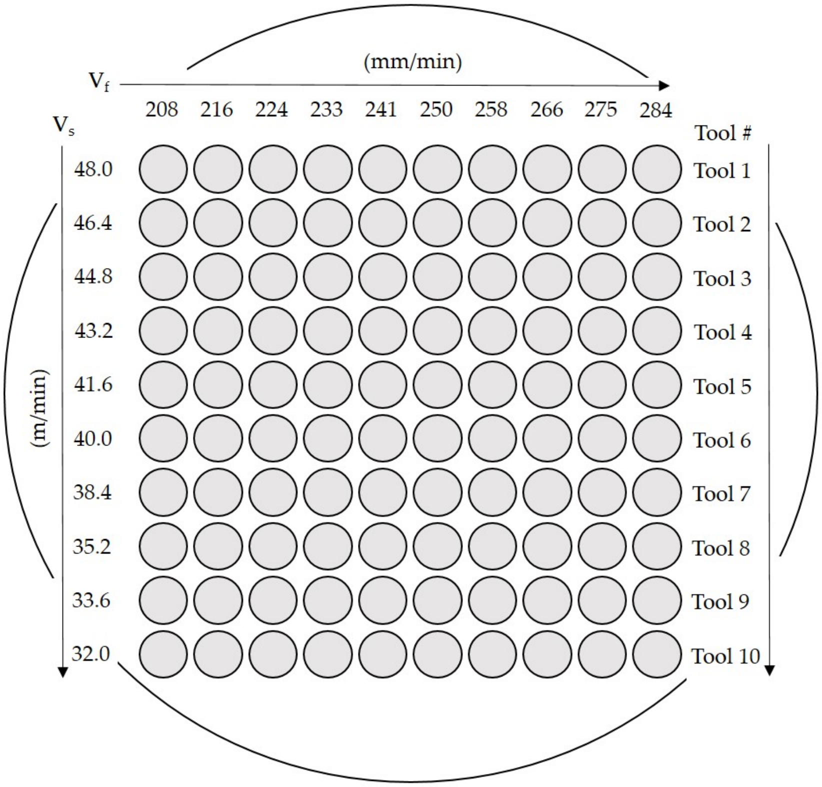

Figure 5.4: The variable V_f - V_s array used to drill holes in each plate where each hole has a different V_f and V_s combination and a new tool was used at each of the 10 V_s. The pitch of the holes (P), was 7.9 mm.

5.2.5 Data processing

All data measured from the Kistler dynamometer was corrected for thermal drift using the method discussed in §3.5.2. Thrust force (Fz) and torque (Mz) measurements were cropped from a section of the steady state cutting region which corresponded to 5 – 10 mm depth in the 20 mm hole, further details are included in §3.5.2. The average (mean) standard deviation (SD) and standard errors (SE) and variance of SD and SE were calculated using Origin Pro 2019 statistical software. Average values were used to plot the response surfaces for each material – tool combination.

5.2.6 Hole extraction and microstructural analysis

Holes given in Table 5.1 were extracted for microstructural evaluation using wire EDM as described in §3.3.1. These holes were only selected once all data was collected in order to ensure subsurface damage of holes drilled in all three materials could be compared for the same thrust force (1600 N). Once extracted from the plates the holes were sectioned parallel and perpendicular to the cutting axis, enabling subsurface characterisation along the length of the hole and for the cross section of the hole respectively. The cross sections of the holes were sectioned between 5 mm and 10 mm depth in every case. Once sectioned cross and parallel sections were ground and polished, following the method set out in §3.3.3, using 1200, 800, and 400 grit paper and a 1 part hydrogen peroxide 9 parts colloidal silica suspension. After preparation electron and light micrographs of the cross and parallel sections were taken.

Table 5.1: The V_f, V_f and F_{rev} of holes selected for microstructural assessment at parameter sets L1, L2 and L3.

	L1	L2	L3
Cutting feed,V_f (mm/min)	275.2	258.4	216.4
Cutting speed,V_s (m/min)	33.6	38.4	46.4
Feed rate, F_{rev} (mm/rev)	0.177	0.146	0.101

5.3 Results

Figure 5.5 and Figure 5.6 are the force and torque response surfaces known as velocity force maps (VFMs) for the array of test parameters defined in Figure 5.4. The VFMs have the V_f – V_s on the X and Y axis and the force and torque measurement on the Z axis. In Figure 5.5

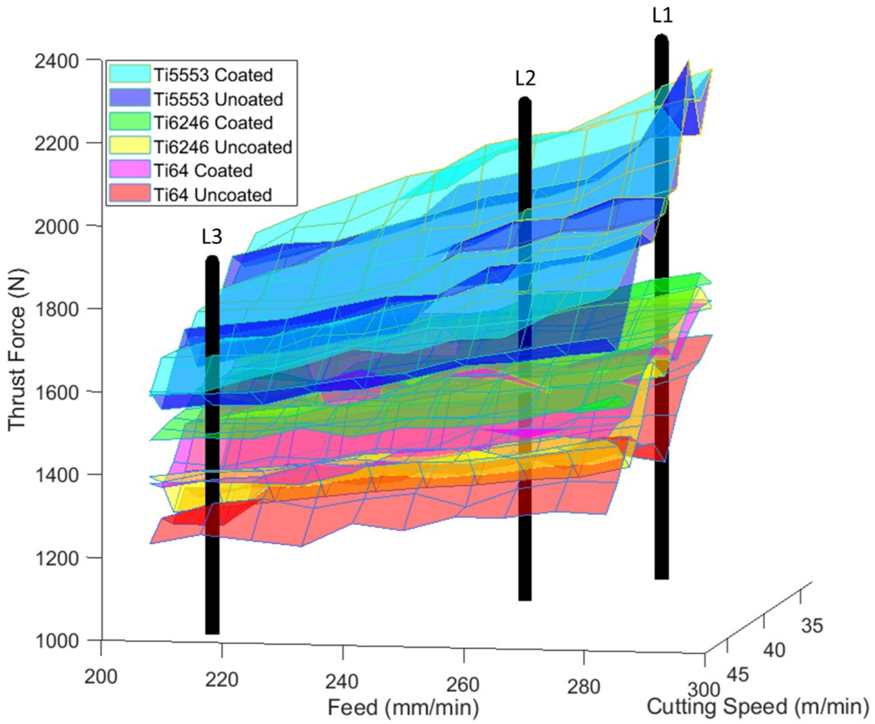

Figure 5.5: 3D visualisation of the Fz data from drilling holes at each parameter set outlined in the variable V_s - V_f array given in Figure 5.4. The L1, L2 and L3 markers indicate the locations selected for microstructural analysis.

and Figure 5.6 there are markers to indicate the data and $V_f - V_s$ for which microstructural assessment was conducted. Figure 5.5 shows, as should be expected, the highest thrust force (Fz), was required to cut the highest strength alloy Ti-5553. Ti-64, which is the workhorse alloy of the aerospace industry required the lowest thrust force. Ti-6246, which lies between Ti-5553 and Ti-64 in terms of β stability and strength, was shown to require a thrust force in-between both although there was some overlap between coated Ti-64 tool and uncoated Ti-6246 tools. In general, for each alloy, coated tools experienced higher thrust forces when compared to uncoated tools. The torque (Mz) results for all alloys and for coated and uncoated tools, shown in Figure 5.6, are more difficult to differentiate between in contrast to the thrust forces. However, some key features are apparent: Ti-5553 VFMs have the steepest gradient from the smallest F_{rev} (lowest V_f – fastest V_s) to the largest (largest V_f – slowest V_s) while Ti-6246 have the smallest gradient.

The mean and variation in SD and SE of the data sets used to construct the VFMs are given in Table 5.2. In general all SE were low, due to the large number of samples recorded by the Kistler between 10 – 15 mm depth. There are some significant differences for the three alloys drilled, highlighted by the statistical descriptions in Table 5.2. Ti-64 had a significantly larger average SD and variation in SD than either Ti-5553 or Ti-6246. In addition, the variation

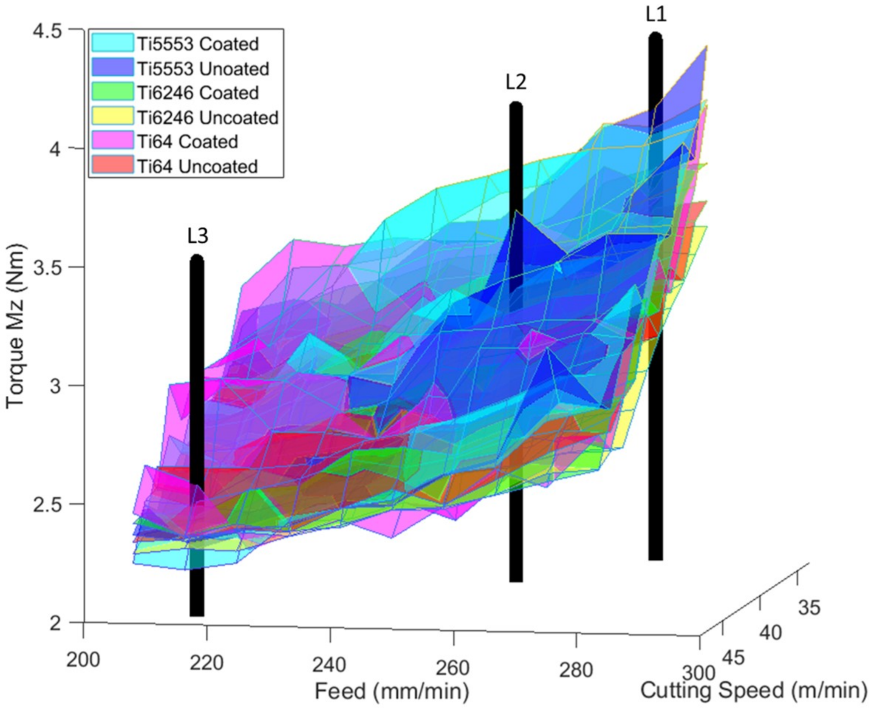

Figure 5.6: 3D visualisation of the Torque data from drilling variable V_s / V_f array defined in Figure 5.4. The L1, L2 and L3 indicate the locations selected for microstructural analysis.

measured for coated tools when drilling Ti-64 was significantly higher than for uncoated tools. There was no significant difference between the values shown for coated and uncoated Ti-6246, and the mean SD for Ti-6246 was the lowest of the three alloys, yet the variation was comparable to Ti-5553. For Ti-5553, the SD and SE are comparable for coated and uncoated tools with the mean SD being 4-5 N higher than that of Ti-6246.

Figure 5.7 and Figure 5.8 are given to enable further analysis of the torque results that were presented in Figure 5.6, in which it is difficult to differentiate between the VFMs for different alloys. In Figure 5.7, the diagonal gradients, which follow increasing F_{rev} as calculated using Equation 5.1, by inputting the V_f and V_s, are plotted against the respective yield strength of each alloy.

$$\frac{Feed}{Revolution} = \frac{V_f \cdot \pi D}{V_s} = \frac{\frac{mm}{min} \cdot \frac{mm}{rev}}{\frac{mm}{min}} = \frac{mm}{rev} \tag{5.1}$$

From this figure it is clear that all the gradients for tools coated with PVD-TiAlN are greater than for uncoated tools, with the smallest difference being for Ti-5553. Another important feature of the graph is that for coated tools, the relationship between the F_{rev} Mz gradient and yield strength is not linear, unlike for uncoated tools. In Figure 5.8, the torque of

Table 5.2: Mean and Var of the standard deviation and the standard error of the force and torque dataset.

	Mean SD	Var SD	Mean SE	Var SE
Ti-64 Coated Fz (N)	42.17	27.69	2.28	8.10E-02
Ti-64 Uncoated Fz (N)	40.47	15.99	2.19	4.68E-02
Ti-6246 Coated Fz (N)	17.32	8.22	0.94	2.40E-02
Ti-6246 Uncoated Fz (N)	17.81	9.34	0.96	2.73E-02
Ti-5553 Coated Fz (N)	22.51	9.16	1.22	2.68E-02
Ti-5553 Uncoated Fz (N)	21.60	7.40	1.17	2.16E-02
Ti-64 Coated Mz (Nm)	0.15	0.0006	0.0084	1.89E-06
Ti-64 Uncoated Mz (Nm)	0.14	0.0002	0.0075	4.98E-07
Ti-6246 Coated Mz (Nm)	0.11	0.0002	0.0058	5.36E-07
Ti-6246 Uncoated Mz (Nm)	0.13	0.0003	0.0070	9.96E-07
Ti-5553 Coated Mz (Nm)	0.10	0.0002	0.0057	5.98E-07
Ti-5553 Uncoated Mz (Nm)	0.11	0.0004	0.0057	1.11E-06

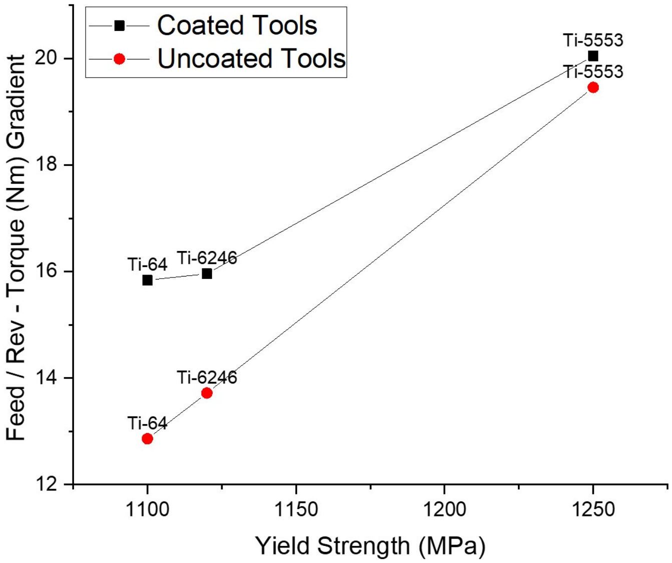

Figure 5.7: Material yield strength plotted against diagonal F$_{rev}$ - torque (Mz) gradients foe Ti-6246, Ti-5553 and Ti-64. F$_{rev}$ calculated using Eq 5.1 from results presented in Figure 5.6

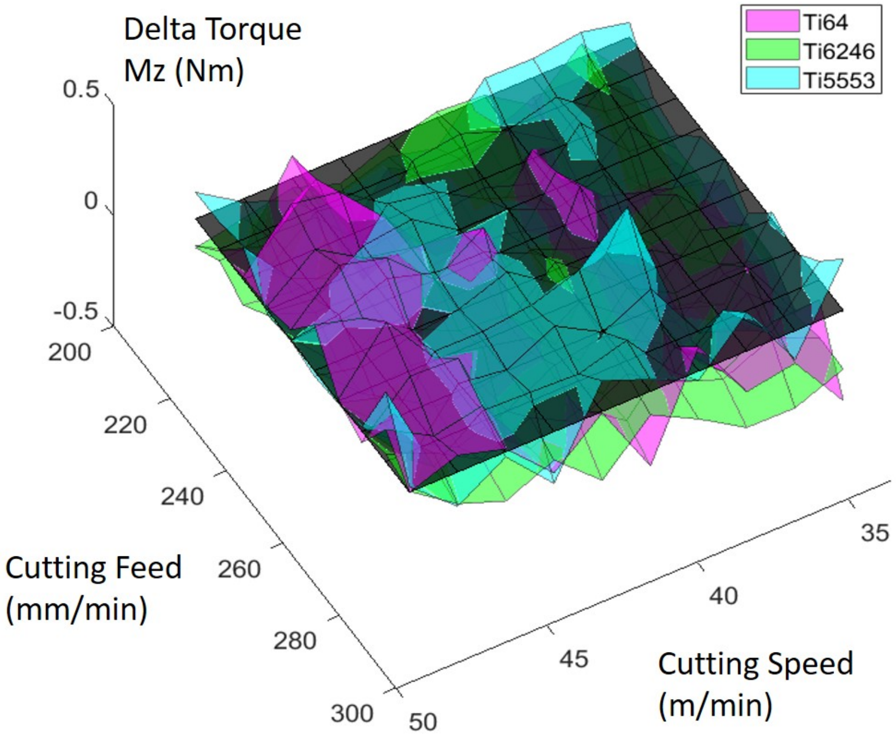

Figure 5.8: 3D visualisation of the difference in torque for coated and uncoated tools in each alloy. The black plane is included to show where 0 Nm is.

coated tools is compared to that of uncoated tools across the VFM array. This is achieved by subtracting the coated data from the uncoated at each $V_f - V_s$ point. The black surface at 0 N is included in the plot to show where there is no difference in coated and uncoated torque: any results above the surface show that at such a V_f and V_s the torque is lower for coated tools. The reverse is also true, anything below the black surface means there was less torque measured for uncoated tools. Figure 5.8 highlights that for each material there is a different relationship between the torque required to cut for coated verses uncoated tools. For Ti-64, there was less torque measured for coated tools at faster V_s, such as 44.8 m/min. The largest difference in torque at these higher V_s was significant at 0.25 Nm which translates to ∼11%. Below V_s = 44.8 m/min torque is lower for uncoated tools at almost all test parameters. As V_s decreases, the difference in torque becomes greater and at the slowest V_s of 33.6 m/min, uncoated tools had 0.4 Nm less torque (∼11%). For Ti-6246 there were very few holes drilled, which required less torque when using coated tools. The largest positive torque was for a hole drilled at V_f = 208 mm/min and V_s = 40 m/min and was 0.065 Nm (∼2.5%) higher than for the uncoated tool. On average the torque measured for coated tools was 4.2% higher than that of uncoated tools, the largest average percentage difference in all three alloys. The largest difference for Ti-6246 was at V_f = 283.6 mm/min and V_s = 36.8 where uncoated tools were measured to have 0.35 Nm less torque than coated tools which is roughly a 10% difference. In Ti-5553 there was much more variance in torque for each hole drilled regardless of whether tools were coated or not. Such variance could be expected to happen when chips jam in the flute of drilling tools resulting in significantly different torques for each hole. Despite this, there is one region in the Ti-5553 dataset which clearly shows a lower torque for coated tools at high V_f and high V_s. The torque for coated tools was 0.33 Nm larger (10%) for V_f = 258.4 mm/min and V_s = 38.4 m/min. Although the data presented in Figures 5.5, 5.6 and 5.8 are all static for the purpose of this chapter, the real benefit of the VFM methodology is that all datasets can be compared in all two or three dimensions by rotating about a desired axis.

The microstructure and subsurface damage for holes drilled with coated and uncoated tools are given in Figure 5.9, Figure 5.10 and Figure 5.11 for Ti-6236, Ti-5553 and Ti-64 respectively. In each Figure (a, c, e) denotes the microstructures from the cross-sectional perspective while (b, d, f) show the microstructure from a perspective parallel to the drilling axis. The V_f and V_s are indicated by the L (1, 2, 3) markers in Figure 5.5 and Figure 5.6. The tables in Figures 5.9-5.11, labelled L (1, 2, 3), give the V_f, V_s, thrust force and torque where C/U-Force/Torque, indicates the coated/uncoated, force/torque. These results demonstrate a novel set of data giving the subsurface damage of holes at equivalent thrust forces of 1600 N for three different titanium alloys. For Ti-6246 (Figure 5.9) 1600 N (+/-10) was the force required at the L2 parameters. For Ti-5553 (Figure 5.10), 1600 N (+/-5) was required at the L3 parameters. In Ti-64 (Figure 5.11), ∼1600 N thrust force was required to drill at L1 parameters for uncoated tools while coated tools experienced slightly higher forces at ∼1660 N.

The use of coated tools generally resulted in a greater subsurface damage depth in both the cross and parallel sections. Images which were taken of the cross section, showed swept grains in the direction of the drill rotation. The size of swept grain layers increased in depth as the material removal rate was increased from L1 to L3. The damage in Ti-6246, which is shown in Figure 5.9, for the micrographs parallel to the drilling direction, show a compressed layer of swept grains under the subsurface in the direction of rotation. For each micrograph the damage depth was measured and is given in Table 5.3. The results provide a quantitative data set that highlights how coated tools result in a greater damage depth than uncoated tools and that such damage decreases with decreasing removal rate. In Figure 5.10, which shows the subsurface damage for Ti-5553, the surface has been plastically deformed and swept in the direction of rotation, as shown in the cross sectional micrographs (a, c, e). In Ti-5553, the damage depth observed was the smallest of all three alloys tested and for all the test parameters, regardless of the higher thrust forces and torque. Unlike with

Table 5.3: Ti-6246 subsurface damage depth measured from parallel SEM micrographs (+/-) 0.2 μm.

Marker Number	Damage Depth (Coated Tools) (μm)	Damage Depth (Uncoated Tools) (μm)
L1	6.1	4.2
L2	4.3	2.4
L3	2.6	1.2

Ti-6246, it is more difficult to measure a difference in damage depth with changing cutting conditions since the deformed layer is much smaller and there is a significant amount of adhered material in some micrographs which biases quantitative measurement. The adhered material on the Ti-5553 hole surface is deposited from the BUE which is often very large in Ti-5553 machining. The Ti-64 results for microstructural subsurface damage shown in Figure 5.11 are at a reduced magnification to the Ti-6246 and Ti-5553 micrographs. It is clear that the damage depth in the β annealed Ti-64 is substantially larger than the other alloys. The type of damage shown is plastic deformation in the form of mechanical twinning which propagates to different extents depending on the orientation of each titanium grain. The large grain size of the β annealed Ti-64 makes the damage depth in this alloy very hard to quantify or compare between those created at different machining parameters, or with coated/uncoated tools. In order to compare the damage of all three alloys at a similar magnification, a micrograph of the cross and parallel sections at V_f = 258.4 mm/min and V_s = 38.4 m/min is shown in Figure 5.12.

To inspect the typical amount of tool wear caused by the limited number of holes drilled with each tool during this investigation, images of the rake flank, outer corner and chisels of each tool used at V_s = 41.8 m/min are presented in Figure 5.13. As tools were used for only a small number of holes and at different parameters, only qualitative observations about the tools can be made from this section of work. More in depth analysis of tool wear at specific cutting parameters will be presented in §6. In the case of the work presented in this chapter, the amount of flank wear on both coated and uncoated tools can be seen to increase with alloy strength, as expected. On the flank of all tools, thermal scarring is evident: for coated tools the severity of this scaring is much increased. Tools used to machine Ti-5553 were observed to have minor chipping on the outer corner, possibly as a result of chip jamming. Such wear will have caused some of the variation seen between coated and uncoated tools across the matrix. As in §4.3, a combination of abrasive and adhesive wear modes were observed for coated tools in all alloys, with mostly abrasive wear being evident on uncoated tools. For the case of Ti-5553, there is significantly more wear on both the coated and uncoated tools. In addition, BUE was more significant in Ti-5553, this was expected due to the large amounts of BUE seen in §4.3. Additionally the images of the uncoated rake presented in Figure 5.13 (especially for Ti-5553), show the extent to which the cutting edge is modified when a portion of the BUE is torn away, possibly resulting in adhered material being deposited on the hole surface.

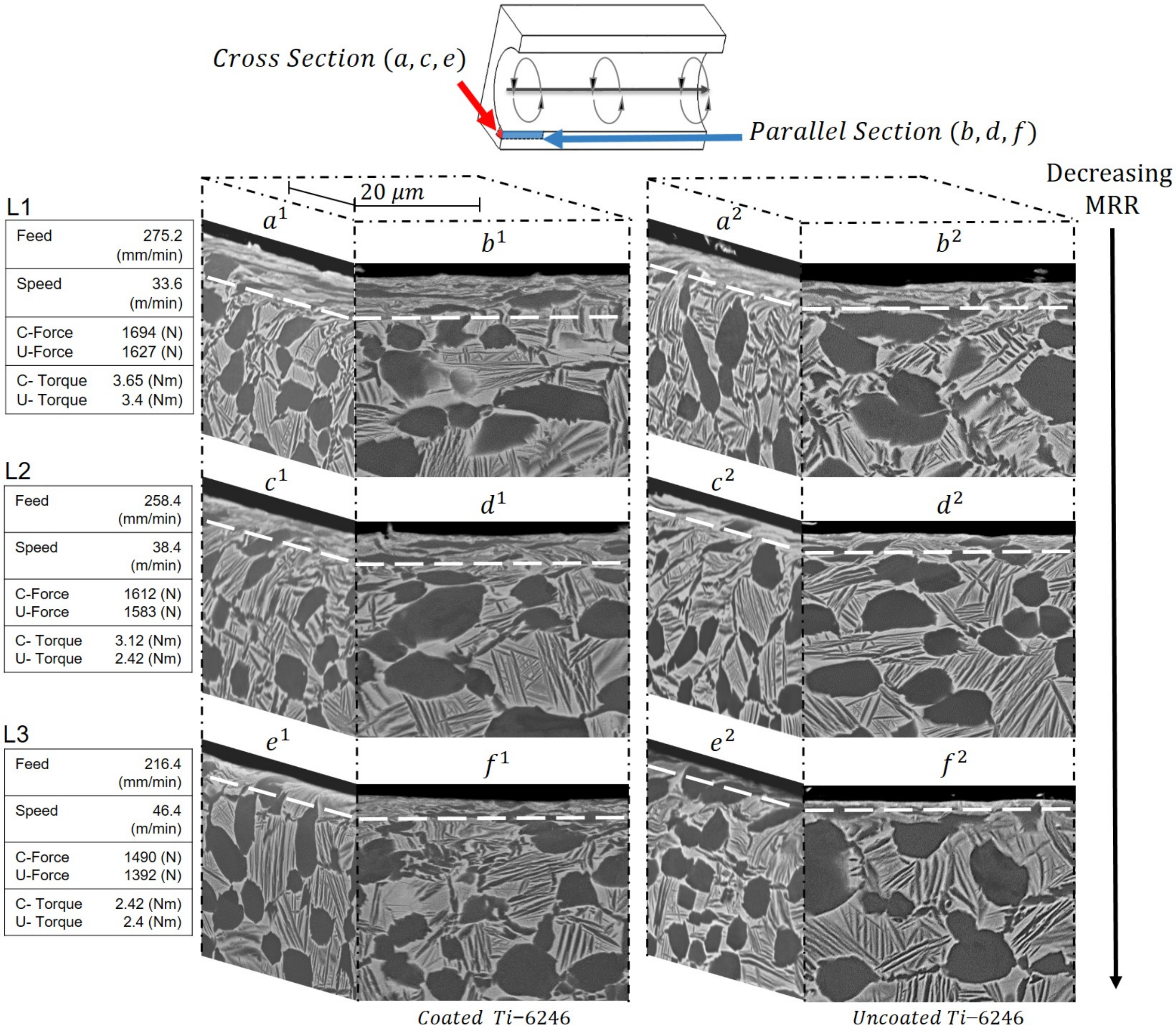

Figure 5.9: Cross section (a, c, e) and parallel (b, d, f) BSE micrographs of Ti-6246 drilled microstructure at a depth of 5 mm for coated^1 and uncoated^2 tools. L1, L2 and L3 correspond to the markers Figure 5.5 and Figure 5.6. For all samples forces were (+/-) 5 N and torque was (+/-) 0.01 Nm. C/U-force/torque indicates the coated/uncoated force/torque.

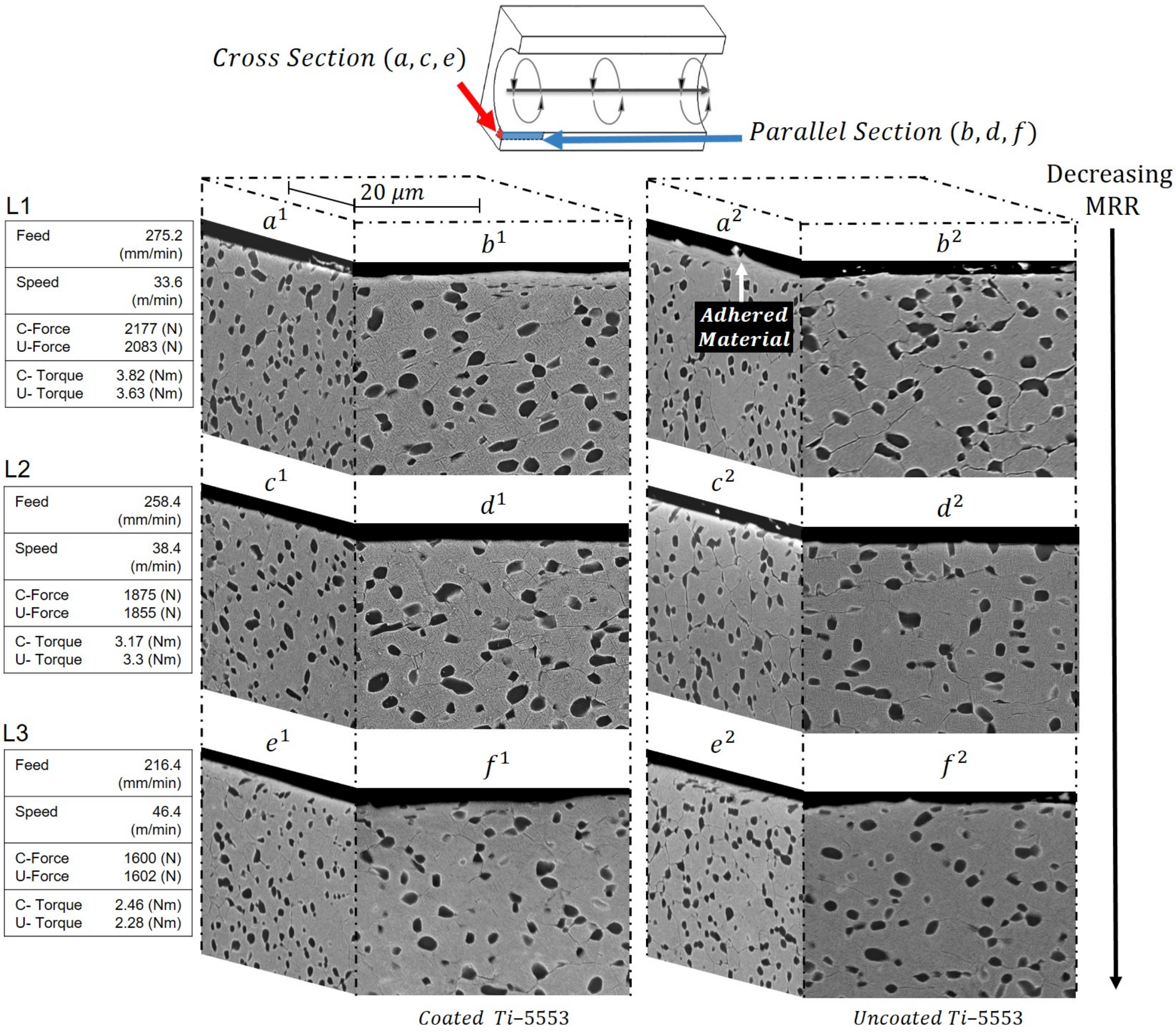

Figure 5.10: Cross section (a, c, e) and parallel (b, d, f) BSE micrographs of Ti-5553 drilled microstructure at a depth of 5 mm for coated^1 and uncoated^2 tools. L1, L2 and L3 correspond to the markers 5.5 and Figure 5.6. For all samples forces were (+/-) 5 N and torque was (+/-) 0.01 Nm. C/U-force/torque indicates the coated/uncoated force/torque.

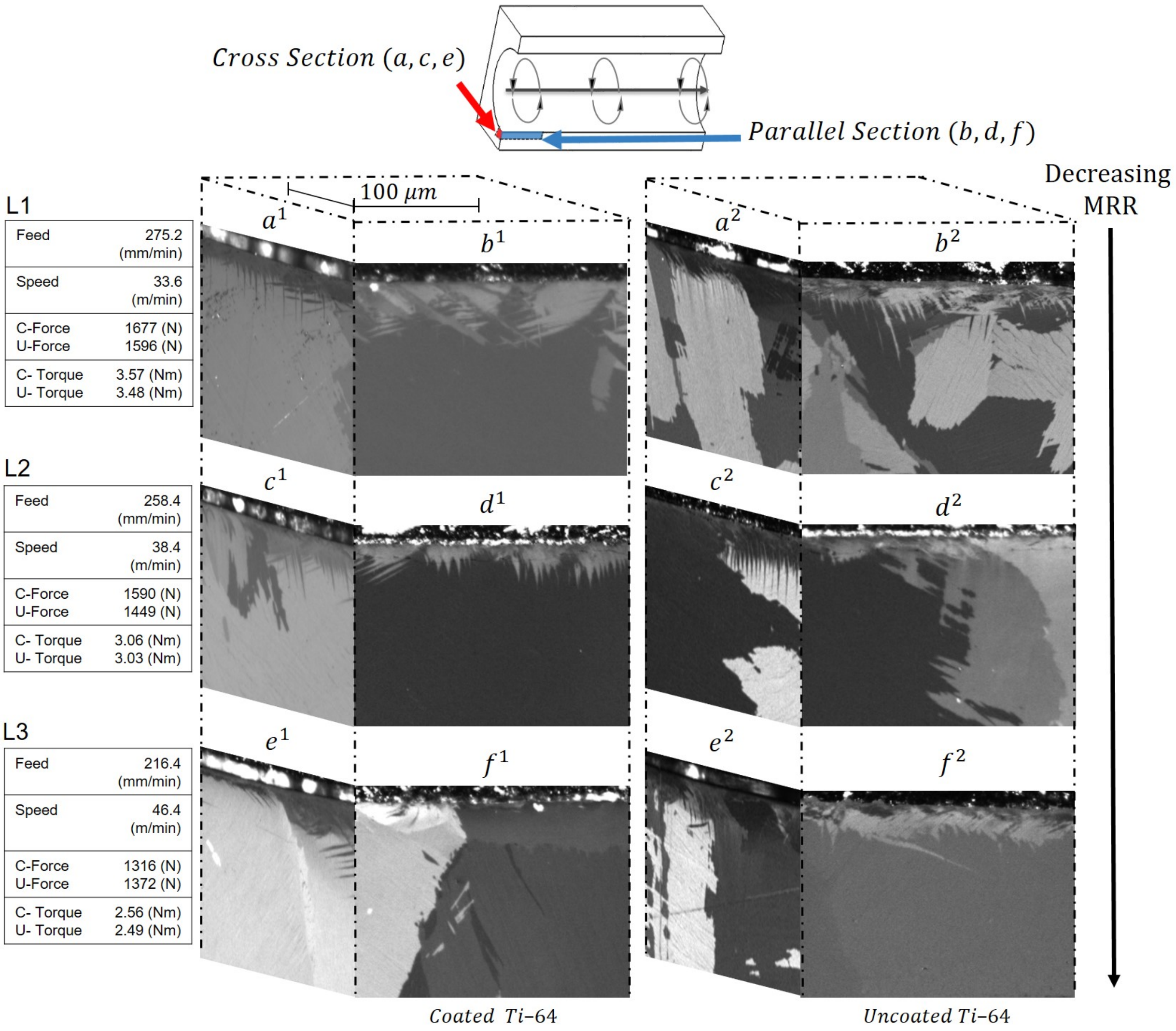

L1

Feed	275.2 (mm/min)
Speed	33.6 (m/min)
C-Force	1677 (N)
U-Force	1596 (N)
C- Torque	3.57 (Nm)
U- Torque	3.48 (Nm)

L2

Feed	258.4 (mm/min)
Speed	38.4 (m/min)
C-Force	1590 (N)
U-Force	1449 (N)
C- Torque	3.06 (Nm)
U- Torque	3.03 (Nm)

L3

Feed	216.4 (mm/min)
Speed	46.4 (m/min)
C-Force	1316 (N)
U-Force	1372 (N)
C- Torque	2.56 (Nm)
U- Torque	2.49 (Nm)

Figure 5.11: Cross section (a, c, e) and parallel (b, d, f) BSE micrographs of Ti-64 drilled microstructure at a depth of 5 mm for coated^1 and uncoated^2 tools. L1, L2 and L3 correspond to the markers 5.5 and Figure 5.6. For all samples forces were as (+/-) 10 N and torque was (+/-) 0.01 Nm. C/U-force/torque indicates the coated/uncoated force/torque.

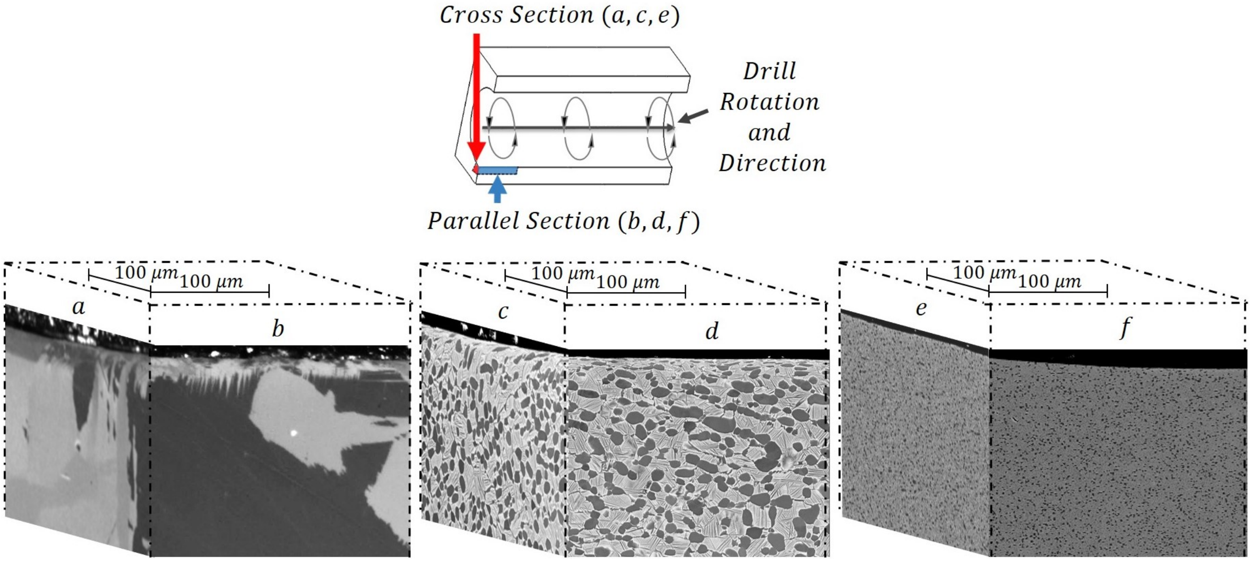

Figure 5.12: Cross and parallel light micrographs of Ti-64 (a, b), Ti-6246 (c, d) and Ti-5553 (e, f) drilled samples at $V_f = 258.4$ mm/min and $V_s = 38.4$ m/min (L2).

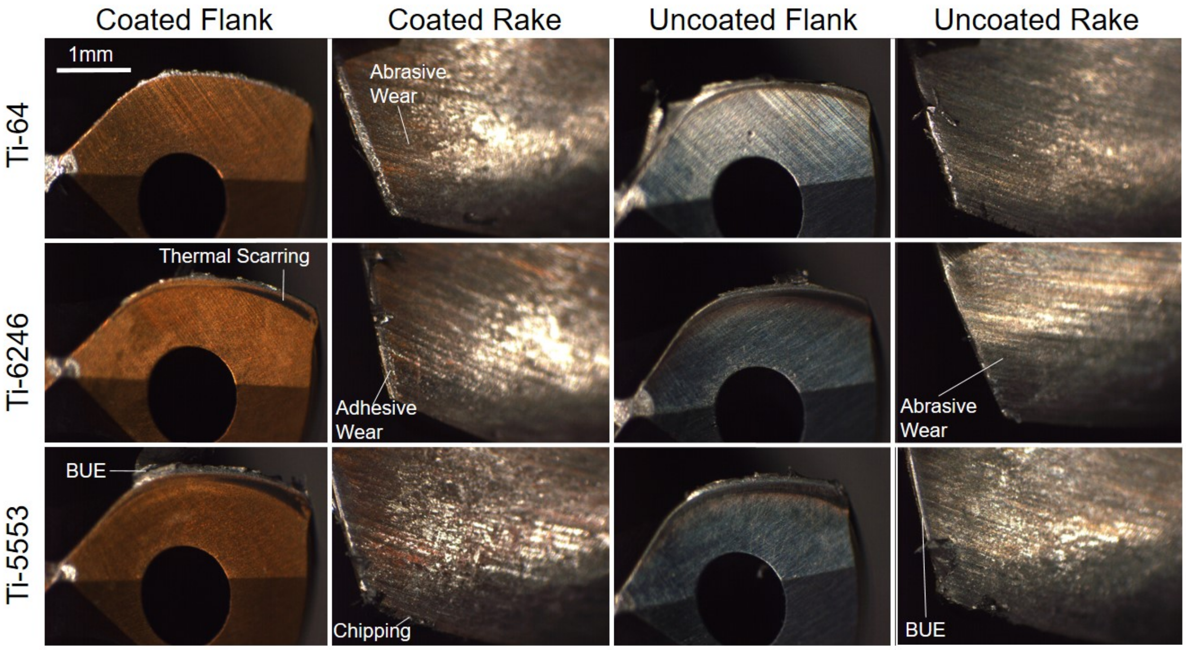

Figure 5.13: Flank and rake face wear macrographs from tools used to drill 10 holes at $V_s = 41.6$ through all tested V_f for coated and uncoated tools in Ti-6246, Ti-5553 and Ti-64.

5.4 Discussion

The VFM maps for thrust force and torque enable a machinability assessment from the perspective of subsurface damage, to be cross analysed with thermomechanical loading across a range of V_f and V_s, without thousands of holes having to be drilled, as would be typical within industry. As predicted, the more β stabilised and the higher strength the alloy, the higher the required cutting forces, demonstrating their poorer machinability for a range of parameters. The coated-uncoated paired design of this study made it possible to determine that coated tools require higher thrust forces during drilling of titanium alloys. It has been identified in the literature that PVD coated tools can have a significantly larger ER than uncoated tools, which causes higher thrust forces during the cutting process [140]. The cutting edge results presented in §5.2.2 showed the coated tools to have an ER which was 5.5 μm larger than uncoated tools, which translates to a 10% increase. Such a significant difference will increase the required thrust forces and will be the main contributing factor to the difference in force that has been observed. Another factor which will have contributed to the higher thrust forces measured for coated tools, is the fact that said tools were shown to have both abrasive and adhesive wear types, which will have caused some destabilisation of the cutting process and hence higher thrust forces. As it was mainly only abrasive wear observed on the uncoated tools, there will have been less adhesive stick-slip action, and thus, the process will have been more stable, resulting in slightly lower thrust forces. As highlighted by Figure 5.7, Ti-5553 machining resulted in a steeper torque vs F_{rev} relationship across the VFM, showing that as the MRR is increased, Mz increases at a rate which is correlated to increasing alloy strength. High values of Mz measured in the VFM could be indicators of more friction between chip material and the tool at the tool chip interface. For the case of Ti-5553, where there is more friction between the tool and chip, there is more wear on the rake face and the tool is wearing faster than in the case of Ti-64 and Ti-6246. This much can be inferred regardless of the limited number of holed drilled with each tool. The increase in wear and friction was likely caused by the increased affinity and reactivity of metastable β alloys and WC-Co tools [84, 72]. The torque vs F_{rev} gradients in Figure 5.7 also highlight that coated tools require a larger increase in torque to increase the MRR than uncoated tools. One reason for this is the increased propensity for coated tools to have adhesive wear that increases the required torque through stick slip action and by reducing the stability of the process. Evidence of the increased contribution to wear by adhesion and galling is shown in Figure 5.13 and is known to happen more frequently at higher MRR. The VFM methodology enables the relationship between V_f, V_s and torque to be characterised. As is showcased by Figure 5.8, the datasets within the VFM can be used to compare changes in drill characteristics, such as the presence of a PVD-TiAlN coating. Torque was found to be 11% lower for most of the test array. The parameters where the coated tools had lower torque than the uncoated tools were at fast V_s at and above 44.8 m/min, where it is hypothesised that the PVD-TiAlN coating is improving the lubricity of the cutting operation, as designed. For the parameters below 44.8 m/min, coated tools required substantially more torque to cut, and therefore for such parameters, the coating is no longer providing the same benefit. This trend does not apply to Ti-6246 where on average the torque was 4.2% lower for uncoated tools. In Ti-5553 the difference in torque for coated and uncoated tools reaches peak efficiency for coated tools at 38.4 m/min and 258.4 mm/min. The differences in the delta torque graphs in Figure 5.8 for the different materials indicates how the tool-workpiece interaction at the cutting edge and possibly chipping behaviour is significantly different for the test alloys. The kind of analysis made possible by the VFM method and showcased in Figure 5.8 makes rapid efficient comparison of material operational windows possible for specific tool characteristics like tool coating, allowing the effectiveness of such tool characteristics to be compared in a relatively cost effective manner. Different tool characteristics like specific changes in tool geometry or material grade could be tested in an identical fashion with the VFM method making it versatile for investigating the performance of said characteristics.

The subsurface of holes drilled in Ti-6246, presented in Figure 5.9, showed extensive plastic deformation within the subsurface, caused by the high temperatures and large strains involved in shearing material during the drilling process. The swept nature of the deformation has been shown to occur in both Ti-64 and Ti-54M previously by Rahim and Sharif [116]. The damage depth for the cross sectional orientation micrographs (a, c, e) was larger when the machining conditions where more extreme and the measured forces were higher. This result is to be expected, as more energy is being imparted into the chip and cut surface; similar results have also been shown in turning [108]. The parallel orientation micrographs in Figure 5.9 (b, d, f) indicate there is a relatively small difference in damage depth and intensity. These parallel images provide a good example of how plastic strain is imparted to the cross and parallel axis of rotation during drilling. The damage measured for uncoated tools was less for L1, L2 and L3 parameters. Such a clear difference between the amounts of subsurface damage has not previously been shown. For Ti-5553 (Figure 5.10), the thrust force required for drilling was much higher for the comparative cutting parameters: however, when comparing the subsurface damage layer at 1600 N (Fz) and 2.4 Nm (Mz) the layer of deformation is much smaller. Although this does not necessarily indicate better surface integrity, it is important for aerospace manufacturers to know, so they can implement the correct finishing processes to maximise part integrity. More adhered material is shown on the machined surfaces of holes in Ti-5553 and only increases with increasing MRR. In the literature, adhered material on the surface of Ti-5553 has been shown to affix fracture sites to the surface, severely reducing fatigue life [73]. The adhesion of Ti-5553 workpiece material to the machined surface has been seen previously in milling operations, but this is the first time it has been demonstrated for drilling [71]. The tendency of machined Ti-5553 to not only adhere to the tool cutting edge in the form of BUE, but to also remain on the part after machining, should be considered in the design of tools for the machining of such alloys. As PVD-TiAlN coatings are being shown to have minimal effectiveness in the machining of Ti-5553, other coatings should be considered: preferably ones that are made to reduce adhesion during machining operations. Cross and parallel microstructures of the β

annealed Ti-64 shows severe plastic deformation (SPD) and mechanical twinning within the subsurface. Crawforth et al., found for twinning within large grained Ti-64, that there is a significant relationship between the size of twins and the grain orientation in turning induced damage; the twin's size and intensity of twins is dictated by the surface shear stress [108]. Within this investigation the same is true, indicated by the change in direction and size of twins which varies significantly between grains but is consistent within each grain. This is shown clearly in the cross polarised light micrographs in Figure 5.11, for which different orientation is indicated by grain contrast. Unfortunately, due to this and the extremely large size of grains within Ti-64, it is very difficult to effectively compare the damage in Ti-64 at different cutting parameters and therefore the micrographs in Figure 5.11 should not be directly compared. Regardless of this, it is clear from the reduced scale in Figure 5.11 that the damage depth is considerably larger in Ti-64 than Ti-6246 and Ti-5553. Figure 5.12 uses the same scale for each micrograph (and each alloy), and clearly shows the differences in damage depths at the L2 parameters. The result presented in Table 5.2, which show the SD and SE of the individual hole datasets measured on the Kistler, show Ti-64 to have the highest SD, Var and SE: this is likely the result of drilling through different orientations of the α phase present in each of the large grains, each requiring a different thrust force to cut and shear at the set parameters. In Ti-6246 and Ti-5553, which are more heavily β stabilised (therefore less α) and have finer grain structures (Figure 5.1), the SD, SE and Var in the thrust force are lower (lowest variation in Ti-5553). This study has highlighted the extent to which microstructural subsurface damage can differ when drilling titanium alloys. Often more thorough assessment of the subsurface is overlooked within industry, where machining speed and tool wear take priority. In cases where subsurface damage has been considered during machinability assessment, it is often only Ti-64 which is investigated. This can result in machinists overlooking and not considering critically important types of subsurface damage when machining other titanium alloys. Therefore, as in this work, it is important that key differences in subsurface damage for alloys with different α and β volume fractions is investigated, characterised and understood. In the longer term this will benefit tool designers who will have the knowledge they require to effectively improve their tool and coating design to maintain machined surface quality and part integrity.

On the subject of PVD-TiAlN coatings and their effect on the drilling machinability of titanium alloys; Rahim and Sharif found WC-Co tools coated with PVD-TiAlN and used to improve the machinability of Ti-64 in drilling by enhancing lubrication and reducing friction [94]. They suggested this was due to the formation of an Al_2O_3 layer on the cutting edge. The present work suggests that a reduction in friction may only occur for specific V_s which differ depending on the alloy; 44.8 m/min and above for Ti-64, 38.4 m/min for Ti-5553 and not at all for Ti-6246. In fact, in most cases the presence of the PVD-TiAlN coating could be increasing friction and reducing stability, as is supported by the torque comparison in Figure 5.8 and by observing that there is more damage at the subsurface for coated tools in the direction of rotation (Figures 5.9-5.12). This result is only apparent when testing a wide array of cutting parameters, as is done when creating VFMs and suggests that in many cases, especially when Ti-64 is not the workpiece alloy, uncoated tools would improve machining conditions. The only caveat to this, is that there is more thermal scarring on coated tools, possibly indicating that the temperature may be higher and that more thermal energy is transferred to the workpiece which would contribute to more damage and would indicate that the coating is protecting the tool from thermal damage via thermal fatigue. That being said, it could just be that thermal scarring is more apparent on PVD-TiAlN than the uncoated carbide. When comparing the results of the present work to that of Rahim and Sharif, it is important to recognise that the Ti-64 alloy they used was substantially different from the β annealed billet utilised here. In addition, subtle changes in tool geometry could also have influenced their results. This highlights one of the major difficulties within machinability literature, which is comparing results which are achieved with subtly different setups where the effect of every minor contribution is not understood for every material. However, the VFM method does provide a comprehensive dataset which can be compared in some aspects to other research and provides a great baseline to work from, particularly when designing new experiments to further investigate certain titanium alloys, like Ti-5553.

The VFM methodology has significant advantages over other testing approaches like the COM-Couple Outil Matière method [141]. Although there are some similarities, the creation of VFMs is much less resource intensive. It also enables more in depth and flexible analysis of the microstructural damage at any force result in the VFM. A significant amount of information can be gathered about the tool and workpiece interaction using the analysis methods presented in this work and the findings can be analysed from the perspective of the tools operational window which is relatively important for tool manufactures.

5.5 Conclusions

This work, which is also accessible in the AIME journal paper "A novel method for investigating drilling machinability of titanium alloys using velocity force maps", aims to develop, test, and use the VFM method to further understand the machinability of Ti-64, Ti-6246 and Ti-5553 using WC-Co twist drills [128]. The novel approach allowed for an in depth machinability study to be conducted in a more resource efficient manner compared to standard methods. VFMs demonstrate how the thrust force and torque measured at the spindle varies for an array of cutting parameters, for PVD-TiAlN coated and uncoated tools. The resultant dataset is extremely valuable for tool designers who wish to compare the operating windows of tools with different characteristics (like coatings). The dataset also enables selection of the correct V_f and V_s for further studies.

The following conclusions about the drilling machinability of Ti-64, Ti-6246 and Ti-5553 have been made possible through the VFM methodology:

- A positive relationship between the diagonal gradients of the torque VFMs and material yield strengths. The trend was more significant for uncoated tools.
- Both abrasive and adhesive wear was shown on coated tools causing higher torque, this was due to higher levels of friction resultant from adhesion and galling. For uncoated tools the mechanism of wear was seen to be abrasive.
- The methodology enabled comparison of microstructural damage at defined forces: The subsurface damage depth reduced with increasing alloy strength, regardless of higher thrust forces and torque.
- The difference in torque between coated and uncoated tools showed the interaction between the coating and workpiece varies significantly for each alloy. This indicated that PVD-TiAlN effectiveness is alloy dependent.

For future application of the VFM method for machinability comparison and assessment, the number of holes used for the array could be reduced, especially if repeat arrays are drilled. An array with 10 holes, repeated three times, would give an accurate response surface for force and torque which could be used to analyse the operational window of tools. The benefit of using a larger array with more holes, such as the one investigated in this work, is that it is easier to compare microstructures at more similar forces. However, if arrays with few holes are drilled, they could easily be used to identify the exact parameters you would obtain similar forces and then holes at such parameters could be drilled and sectioned for microstructural analysis.

Chapter 6

Investigating tool wear and hole quality when drilling Ti-5553 with WC-Co tools

In §5 the VFM method of investigating machinability that focused on microstructural sub-surface damage assessment and initial hole comparison was developed. This chapter focuses is on Ti-5553 drilling machinability from the perspective of tool wear rate and hole quality. In this work the tools used were identical to those used in §5, but were tested for extended periods of time at different V_f and V_s to investigate the failure mechanisms of the tools and identify the optimal operational parameters for drilling Ti-5553. Again, PVD-TiAlN coated and uncoated twist drills were used to assess the utility of such coatings. The machining carried out in this chapter was conducted in two locations on two different machining centres. This enabled work to be validated using a second machining centre which was similar to, but not identical to, the system used previously. In total, three experiments are presented in this chapter: Experiment 1 consists of drilling 1805 holes with a single coated tool at cutting parameters within the centre of the test matrix defined in §5. The thrust force and torque for each hole was measured and is compared to the tool wear progression, as observed in images of the tool chisel, flank, margin and rake faces. Experiment 2 utilises a VFM approach for assessing how changing V_f and V_s influences key aspects of tool life and how they vary with changes in force/torque over 10% – 20% of the tools life. In experiment 2, the surface roughness response at different cutting parameters was investigated in detail; the discussed results were presented at CIRP international conference on surface integrity 2020 and published in the proceedings [130]. In experiment 3, four tools were tested to investigate if results in experiment 2 could be used to predict the behaviour and wear of such tools at untested cutting parameters, on a different machining centre and setup. In addition, several aspects of hole quality were measured on a CMM machine and analysed to investigate if there were any major differences when using PVD-TiAlN coated tools or uncoated tools: results were correlated to the location of the holes in the workpiece and the thrust force/torque was measured for each hole.

6.1 Experimental methodology

6.1.1 Experimental setup

Workpiece material

The Ti-5553 subtransus heat treated and aged billet material was identical to that introduced previously in §3.1 and used in §5. Following evidence in §5 that chip jamming was occurring in the final 5 mm of holes drilled in Ti-5553, the billet material was sectioned into plates with a smaller thickness of 10 mm - half the thickness of those used in §5.

Cutting tools

The tools used were also identical to those introduced in §3.2 and used in §5 - R846 6.9 mm solid carbide twist drills (Figure 3.2). The coated and uncoated tools were produced in separate batches which can introduce variation in the geometry of the drills. Therefore, a comparison of the most important geometric tool features between PVD-TiAlN coated and uncoated tools was carried out using Helicheck Pro machine.

Machining centre and dynamometer

Two machining centres were used in this chapter, the first was the DMU monoBLOCK – dynamometer setup used in §5, including a slight modification to the clamping mechanism, required due to relatively thinner 10 mm plates. The second was a DMG DMC 835 V fitted with the same Type 9170A3112 Kistler dynamometer used previously. The clamping and Kister setup for the DMG DMC 835 V is shown in Figure 6.1.

6.1.2 Experimental procedure

The testing in this chapter was conducted in three parts. In the first experiment, a tool was tested for 1805 holes on the DMU monoBLOCK machining centre. One of the goals of this experiment was to check that the tool life was similar to that predicted by the tool supplier, Sandvik Coromant. In the second experiment, coated and uncoated tools were used; in this investigation the first goal was to analyse the wear rate of the tools at different cutting parameters on the DMU monoBLOCK machining centre. A response surface methodology

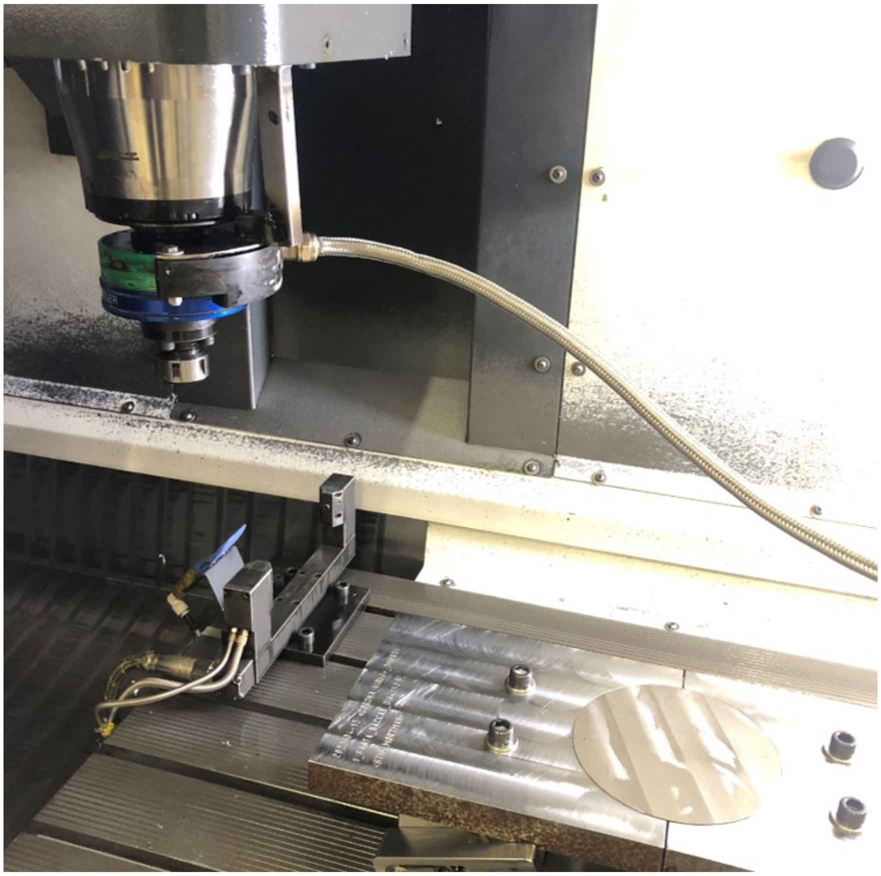

Figure 6.1: The Kistler rotating dynamometer and workpiece clamping setup in the DMG DMC 835 V.

was used to interpolate the specific cutting energy (SCE) and hence efficiency for the range of parameters tested in §5. The second goal in experiment 2 was to investigate the effect of PVD-TiAlN coating on surface roughness. In the third experiment, coated uncoated tools were used in the DMG DMC 835 V; the primary objectives were to test the accuracy of the interpolated tool wear results and to investigate the effects of coating and tool wear on important aspects of hole quality when drilling Ti-5553. The experimental methodology for each experiment is described in more detail below.

Experiment 1

In the first instance, a tool was used to drill 1805 holes at the recommended cutting parameters, shown in Table 6.1 [122]. Thrust force and torque were measured for every hole using the spindle mounted Kistler dynamometer. The results were drift compensated and processed in MATLAB, using the methods established in §3.5.2, to get average force for the region from 2.5 mm to 7.5 mm hole depth which coincides with the steady state cutting region. Tool wear images of the flank, rake, margins and chisel were taken for holes 0 and 1 then every 40 holes after, until all holes were completed. The total time that the drill was in cut was 74 min and 51 s.

Table 6.1: V_s, V_f, F_{rev}, RPM and cutting time per hole for experiment 1.

V_s (m/min)	V_f	F_{rev}	RPM	Time per hole (s)
40	242	0.131	1845	2.48

Experiment 2

In this experiment, 10 tools were used, 5 coated and 5 uncoated. The Helicheck pro was used to ensure all tools were within the manufacturer's tolerance and to compare the variation for the point angle, angle of the primary clearance, angle of the secondary clearance, gash angle, gash radius, ER on section A, section B and section C, chisel length and blend radius. Section A, B and C are at 10%, 60% and 90% of the radius from the point of the drill along the cutting edge respectively. The location of each of these features is shown in §3.6, Figure 3.9, where ΔR can be considered the ER. Each coated/uncoated tool pair was used at a different V_s and V_f. The selected parameters are tabulated in Table 2. These test parameters were selected so response surfaces of force, torque and SCE could be created and used to analyse the performance of tools. A single 10 mm plate was used for each tool. In each plate 227 holes were drilled at each of the tool pair test parameter sets in Table 6.2. Tool wear images were captured on the Olympus ZX10 optical microscope camera at holes 0, 1, 71, 156 and 227. In addition, the Ra and R_{max} was measured using the Diavite DH-8 instrument with a CLA-400 2 μm measuring head for every 5th hole for tool pairs 2 to 5.

Table 6.2: V_s, V_f, F_{rev}, RPM and cutting time per hole for experiment 2.

Pair No.	V_s (m/min)	V_f (mm/min)	F_{rev} (mm/rev)	RPM (rev/min)	Time per hole (s)
1	40	242	0.131	1845	2.48
2	46.4	216	0.101	2141	2.77
3	33.6	216	0.140	1550	2.77
4	46.4	275	0.128	2140	2.18
5	33.6	275	0.177	1550	2.18

Experiment 3

In the third part of this investigation, machining was carried out on the DMG DMC 835 V remotely from the UK Sheffield in Sandviken Sweden. The geometric tolerances of 10 coated and 10 uncoated tools was measured using a Zoller Genius 3, then 2 coated and 2 uncoated tools were selected based on having the most representative geometry. Each coated/uncoated pair were used at the 2 different V_s - V_f combinations shown in Table 6.3 where F_{rev} was kept at 0.131.

Table 6.3: V_s, V_f, F_{rev}, RPM and cutting time per hole for experiment 3.

Pair No.	V_s (m/min)	V_f (mm/min)	F_{rev} (mm/rev)	RPM (rev/min)	Time per hole (s)
1	39.5	240	0.131	1822	2.5
2	35	218	0.131	1615	2.75

6.2 Results and discussion

The results and where relevant discussion of each experiment described in §6.1 are presented within this section, then in §6.3, the broader implications of the results are discussed.

6.2.1 Experiment 1

The average spindle thrust force and torque measured from 2.5 mm to 7.5 mm depth in each hole is shown in Figure 6.2 and Figure 6.3 respectively. The dashed line is included to show a 95% prediction interval as calculated from the estimated SE. Table 6.4 includes the y intercept and gradient for the spindle thrust force and torque.

Table 6.4: The y intercept and gradient per hole and per second for the spindle thrust force and torque in experiment 1. The standard error and R^2 values are also included.

	Intercept	Gradient (per hole)	Gradient (per second)	Standard Error, SE	R^2
Force (N)	1595	0.044	0.0178	17.45	0.64
Torque (Nm)	2.79	1.78e-4	7.18e-5	0.09	0.511

From hole 1 to 1805 and within a 95% prediction interval, thrust force and torque increase by 79.4 N (5%) and 0.32 Nm (11.5%) respectively. As the data has been drift compensated for thermal effects within the dynamometer, it is likely that changes in tool geometry due to tool wear and degradation are responsible for the increase. Changes in the cutting edge radius on the chisel and flanks of the tool will increase the area that is being used to cut, which in turn increases the force and torque required to shear the material [142, 143]. Wear images of the tool from 40 to 1805 holes are shown in Figure 6.4. There is no visible change in the wear on the chisel through holes 40 to 1805. The images of flanks 1 and 2 (F1, F2), show dark thermal scarring near each cutting edge with significant amounts of Ti-5553 workpiece material adherence. On the cutting edges, frittering becomes noticeable between the 626th and 1080th hole and becomes substantial by hole 1805. Frittering can be caused by extensive and repeated tearing away of a BUE. In titanium turning, the "plucking" of tool material in this manner can be exacerbated by the presence of coatings [122]. On the tool margins (M1, M2), extreme amounts of workpiece material has adhered along the length of the imaged section, with substantially more material located near the outer corner of the tool. At this location, in a similar manner to the cutting edge, frittering could be occurring. However, any evidence of this is obscured by the adhered material. M2 hole 853 shows that there has been some removal of tool material from the margin, yet in subsequent images of M2 the chip has

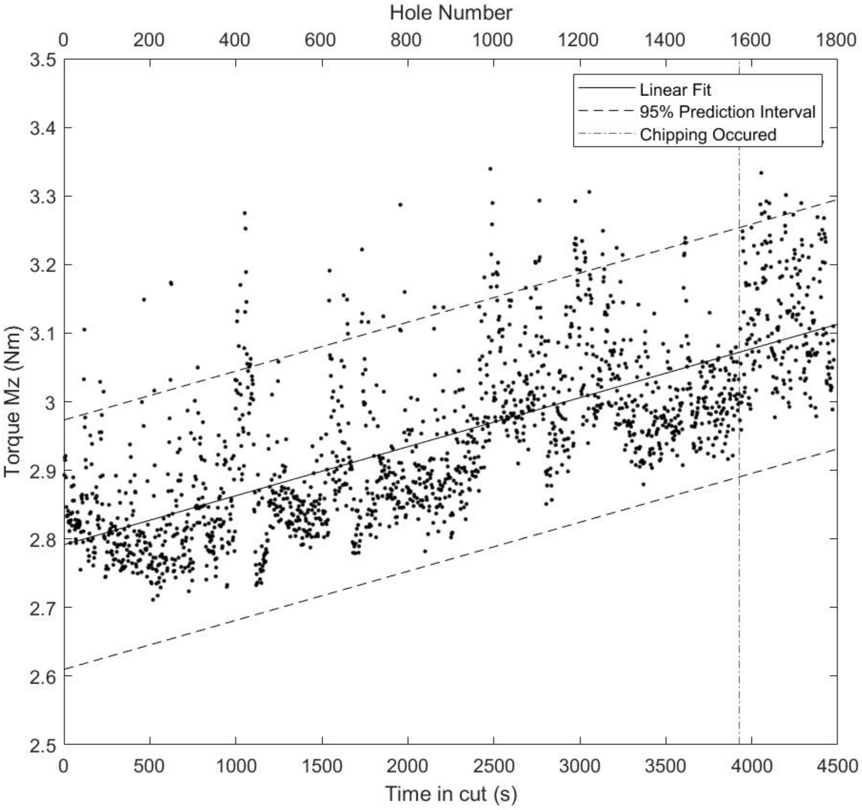

Figure 6.2: Graph showing the average thrust force, Fz (N) of each hole in experiment 1, for a 5 mm section in the steady state cutting region.

been filled with Ti-5553. Further evidence that there has been tool material removed on the margin near the outer corner is shown in the rake images (R1, R2), where the usually flat outer corner is shown to have a rough edge where tool has been damaged. The rake images (R1, R2), show BUE forming on the cutting edge. The BUE is constantly changing the geometry of the cutting edge, as evidenced by its change in size on R2 from hole 156, where it is relatively small compared to 256 where it has increased substantially. Then, by hole 389 it has reduced in size again. Changes in the cutting edge geometry will influence the thrust force and torque. Torque is influenced most by the tool geometry furthest from the centre of the tool, and therefore it can be assumed that the BUE will have a greater influence on the torque than the thrust force. Figure 2 shows that there are instances of average torque for some holes which are significantly higher than the predicted fit and which lie outside of the 95% prediction interval. In these cases it is likely the BUE is so large that it is reducing the stability of the drilling operation [116]. Such instability increases the energy requirement of the process, raising the chances of the chipping on the cutting edge of the tools and reducing the chip evacuation quality.

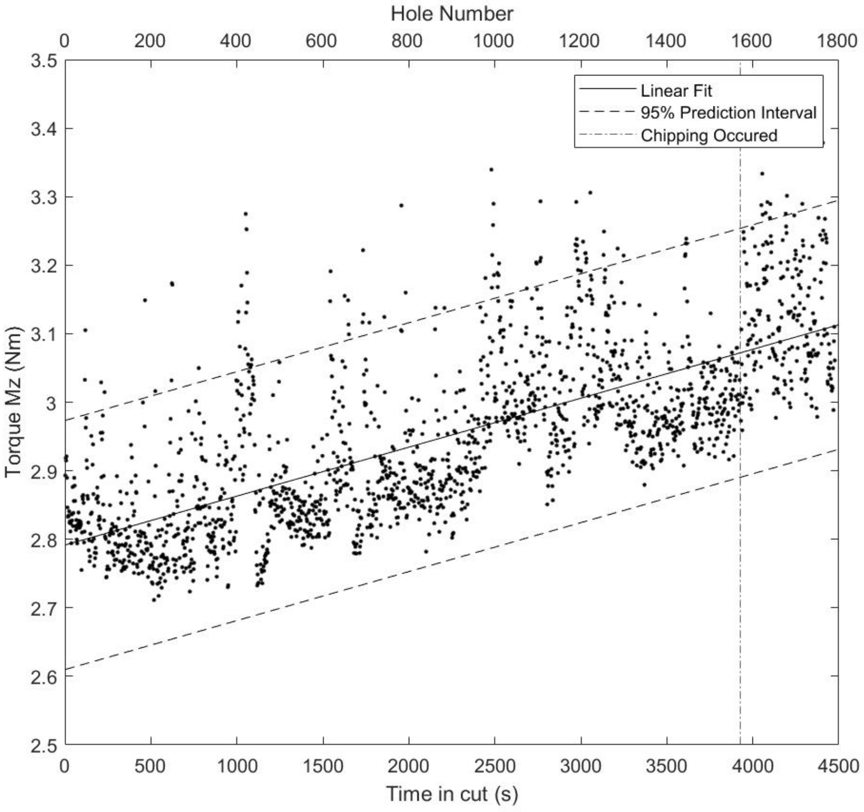

Figure 6.3: Graph showing the average spindle torque, Mz (Nm) of each hole in experiment 1, for a 5 mm section in the steady state cutting region.

The flank wear on F2, as measured from the original location of the cutting edge, for 26 instances throughout the 1805 holes, is shown in Figure 6.5. The data shows two significant increases in flank wear; one between 389 and 456 holes and one between 1500 and 1600 holes. The first coincides with a small chip which can be seen within Figure 6.4, on F2, at hole 626. This small chip was quickly filled in with adhered Ti-5553 and is difficult to distinguish in the images taken after hole 626. The second increase pushes the flank wear over the critical wear limit (0.25 mm) and coincides with a large chip evident on F2 at hole 1534. By industry standards the tool would have been considered to have failed at 1534 holes (3800 s in cut), significantly lower than the given life for the tool ∼2000 holes [122]. In the force and torque results there is no noticeable change in thrust force for the first chip, however, there is a noticeable peak within the torque data around hole 400 which is likely related to the damage and changes in tool geometry. Since the chip is quickly filled in with workpiece material, the torque stabilises. When the large chip occurs at hole ∼1500 there is a small spike in the average thrust force and a significant increase in the torque, as shown in Figure 6.2 and Figure 6.3 respectively. After hole 1534 the torque data has a noticeably larger variation, this is due to the increased instability of the drill, with the extensive change in geometry resultant from the large amount of tool material removed from the chip. The correlation of specific tool wear incidents, with changes in the average torque and thrust force is relatively important for machinists. It demonstrates that Kistler data can be used to identify possible instances of chipping while the tool is in operation, without the need of removing the tool to observe the wear. In the future it may be possible to link specific wear incidents to characteristics within the torque data; hence enabling machinists to monitor the type of wear that is occuring, while the machine is in opertation. It is important to address that within the torque data, there are other instances where the average torque measurements increase for a period of time, for example after 1000 holes (2500 s in cut); in such instances it is possible that either tool material, or a large portion of a stable BUE broke away and induced instability into the process. To further investigate this, the tool would need to be taken out of the machine when such a spike occurs and the damage analysed.

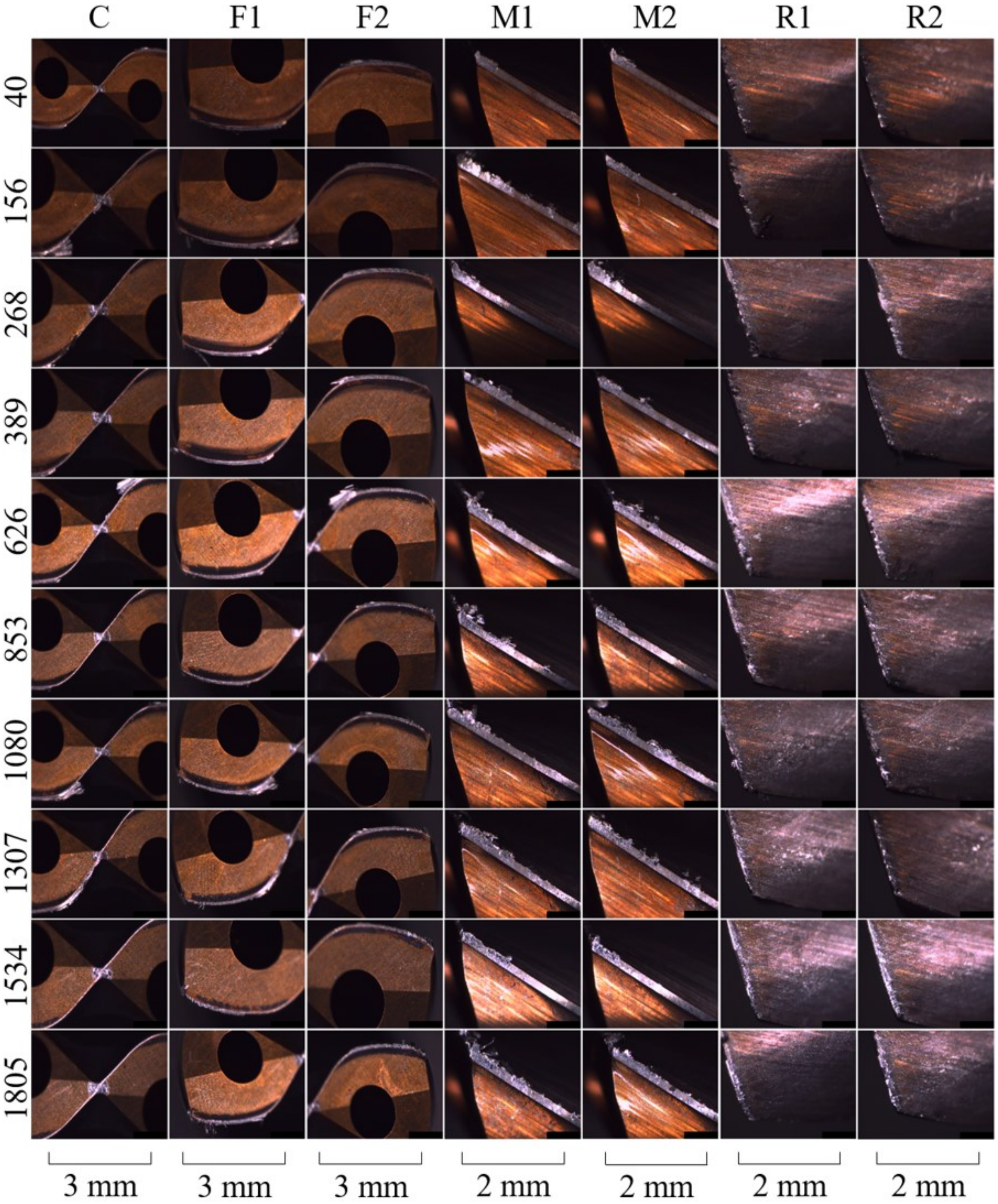

Figure 6.4: Photographs showing the tool wear at the corresponding hole number (on the left), for the chisel (C), flank 1 (F1) and flank 2 (F2), margin 1 (M1) and margin 2 (M2), rake 1 and rake 2 (R1 and R2).

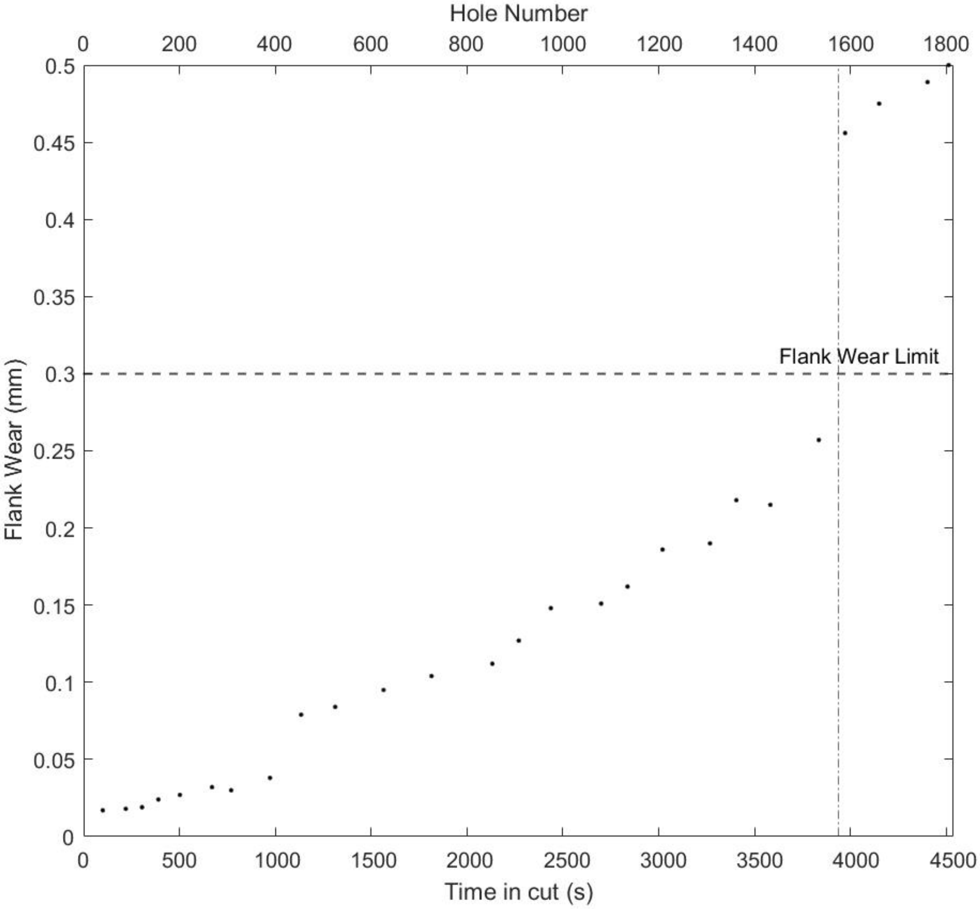

Figure 6.5: Graph showing the flank wear (mm) progression on flank 2 (F2) for 1805 holes and 4500 s in cut. The horizontal line indicates the flank wear limit. The vertical dot-dashed line indicates the time and hole at which the tool chipped.

6.2.2 Experiment 2

Tool geometry

The Helicheck results for the parameters defined in §3.6 are given in Figure 6.6. Generally coated tools were very similar to uncoated ones, however, some small differences were apparent: Tools with the PVD-TiAlN coating tend to have a smaller point and primary clearance angle while there is no difference in the secondary clearance. Both the gash angle and radius were slightly larger for coated tools. The chisel length and blend radius were slightly reduced for coated tools. Uncoated ΔR was lower, with the largest relative difference being near the chisel (A) and the smallest being at the furthest from the chisel (C). The application of coating to the cutting edge is known to increase the ER of tools [144], hence why at location A, B and C the uncoated tools have lower ER. However, the ER at location A is substantially lower and may result from measurement error, due to the increased reflectivity of the uncoated tools. Despite the differences observed for coated and uncoated tools all measurements (except section A, ER for uncoated tools), were within tolerance for the R846 Corodrill twist drills.

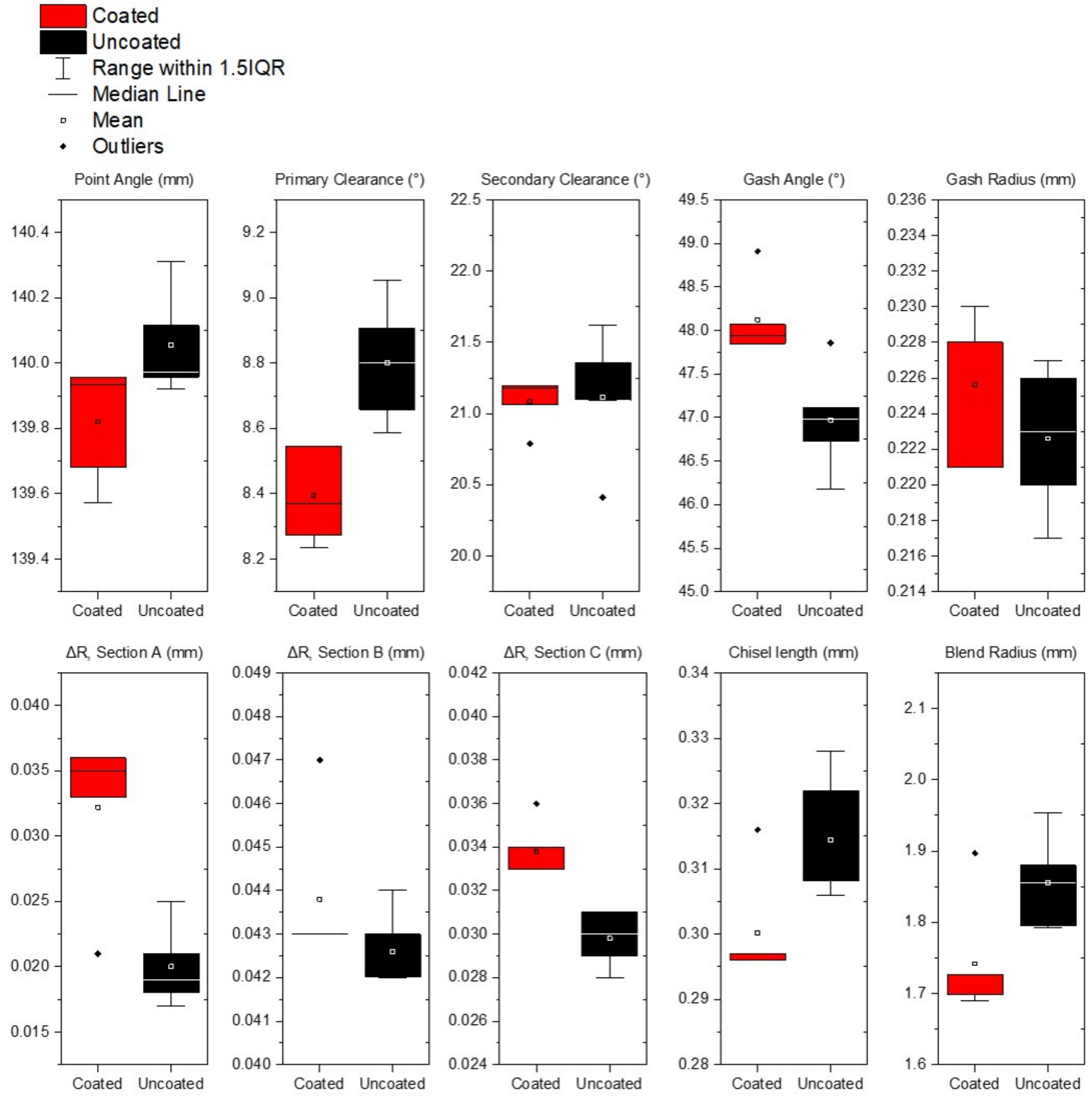

Figure 6.6: Box plots comparing the following geometric features of R846 coated and uncoated tools: point angle, primary clearance, secondary clearance, gash angle, gash radius, ΔR Section A, ΔR Section B, ΔR Section C, chisel length and blend radius. Where ΔR is the ER.

Thrust force and torque

The thrust forces for each coated (a-e) and uncoated tool (f –j), used in experiment 2, at the cutting parameters defined in Table 6.2, are shown in Figure 6.7 and Figure 6.8. Using the polyfit and polyval functions in MATLAB, a linear fit was applied to each data set to determine the average rate of change for Fz and Mz for each tool. The spread of Fz data is relatively similar for each set of cutting parameters tested. However, for Mz, tests 2, 4 (b, d) for coated tools and 1, 2, 4 (f, g, i) for uncoated tools show considerably more variation than other tests. Tests 2 and 4 (b, d) were conducted at the fastest V_s, hence there is a correlation between Mz variation and V_s, suggesting a slower V_s is required to achieve better stability when drilling Ti-5553.

Figure 6.9a (Mz) and Figure 6.9b (Fz) are VFMs constructed by plotting and interpolating between the y intercept of the results in Figure 6.8. As highlighted from the VFMs discussed in §5, thrust force increases with increased chip thickness; that is, as the V_f increases and the V_s decreases. To better visualise the rate of change for the coated and uncoated datasets Figure 6.9c and Figure 6.9d were plotted using the gradient of the results in Figure 6.8. The change in Fz and Mz per hole for coated tools follows a different relationship to that of the uncoated tools. The change in Fz is negative for uncoated tools when used at faster V_s but remains fairly constant for coated tools. Then, at both low V_s and V_f, the Fz increase by the same amount in both coated and uncoated tools. At the most extreme cutting conditions, low V_s and high V_f, where there is the largest F_{rev}, uncoated tools see a positive Fz per hole, while coated tools maintain similar Fz. At the centre point, $V_s = 40$ m/min and $V_f = 240$ mm/min, the rate of change is similar for both coated and uncoated tools (-0.05 N/hole), and is smaller than a linear relationship between V_s, V_f and Fz would predict; therefore suggesting there is a convex relationship. For the case of torque, as shown in Figure 6.9d, the relationship between Mz rates of change per hole is opposite to Fz: Coated tools have a large negative rate of change (Nm/hole) at fast V_s, while for uncoated tools this remains fairly constant. The largest difference in the Mz rate of change between coated and uncoated tools is at a V_f of 216 mm/min and a V_s of 33.6 m/min, which is not the case for Fz, for which they were similar. The only instance where the rate of change in Mz is more positive for coated tools ($1 \cdot 10^{-3}$ Nm / hole) compared to uncoated tools (0.5 Nm / hole) is at $V_s =$ 33.6 m/min and $V_f =$ 216 mm/min; the largest F_{rev} (0.14 mm/ rev). At the centre of the test array, $V_s = 40$ m/min and $V_f = 240$ mm/min, the rates of change in Mz are relatively higher than a linear relationship between V_s, V_f and Fz would predict; suggesting a concave relationship. Figure 6.9e and Figure 6.9f give the SCE and SCE per hole respectively. As the dimensions of SCE are (J/mm^3) as calculated using equation 6.1, the results given in Figure 6.9e present the efficiency of the process at the tested cutting parameters in terms of the required energy to cut a fixed amount of material.

$$SCE = \frac{Torque \cdot \omega}{MRR} = \frac{Torque \cdot \omega}{\pi D^2 \cdot V_f} = \frac{(Nm) \cdot (\frac{Rad}{s})}{(Rad \cdot m^2 \cdot \frac{m}{s})} = \frac{J}{m^3} \tag{6.1}$$

Where ω = *angular speed*

The results show that the SCE is lower at slower V_s for coated and uncoated tools and that at all test parameters uncoated tools required less power to remove an identical amount of material. In Figure 6.9f, the SCE per hole results show convex relationships for coated and uncoated tools. Uncoated tools are shown to maintain fairly static SCE with a maximum increase of 0.005 J/mm^3/s for V_s = 40 m/min V_f = 242 mm/min, at the centre of the test array. On the other hand, for coated tools, SCE decreases for all test parameters apart from at the highest V_f and lowest V_s. This indicates that at least for the first 227 (15-20% of life), holes drilled the coated tools become more efficient, indicating that the coating takes some time to reach maximum efficiency, possibly as it is removed from the main cutting edge.

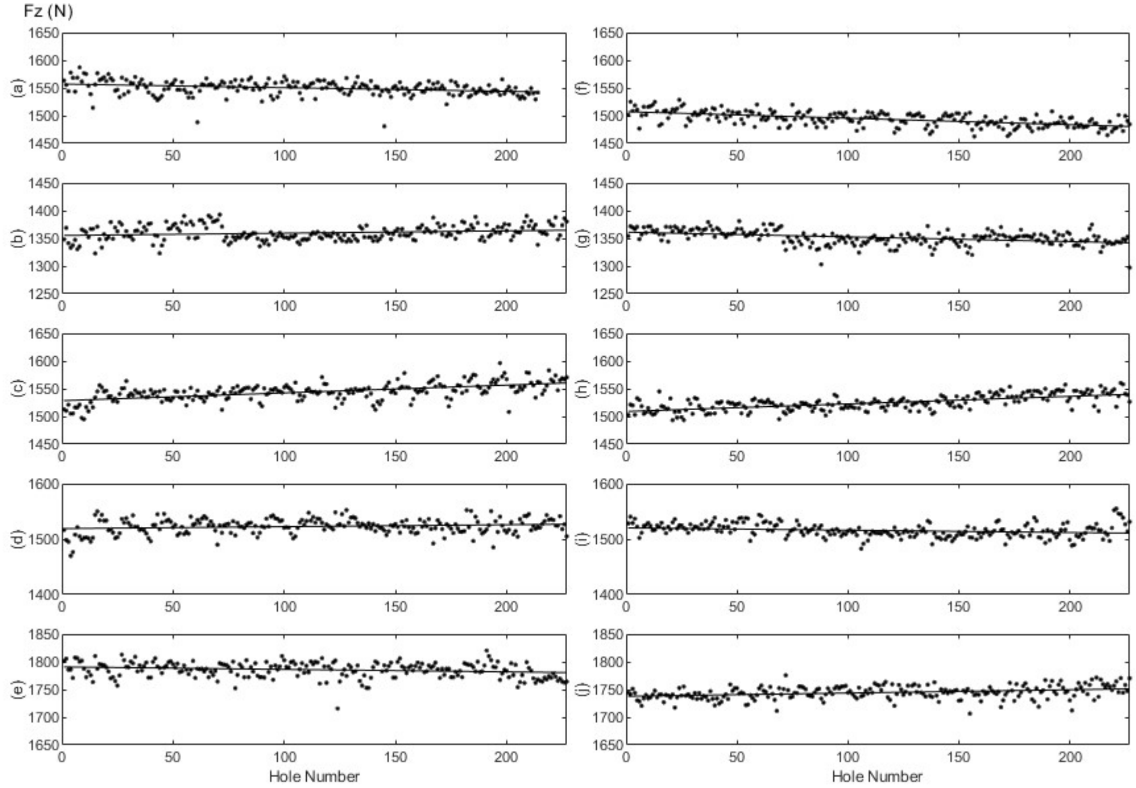

Figure 6.7: Graphs showing the average thrust force, Fz (N), for 227 holes drilled with coated (a – e) and uncoated (f – j) R846 Tools. Each set (a – e) and (f – j) are drilled at the V_f and V_s listed in Table 6.2.

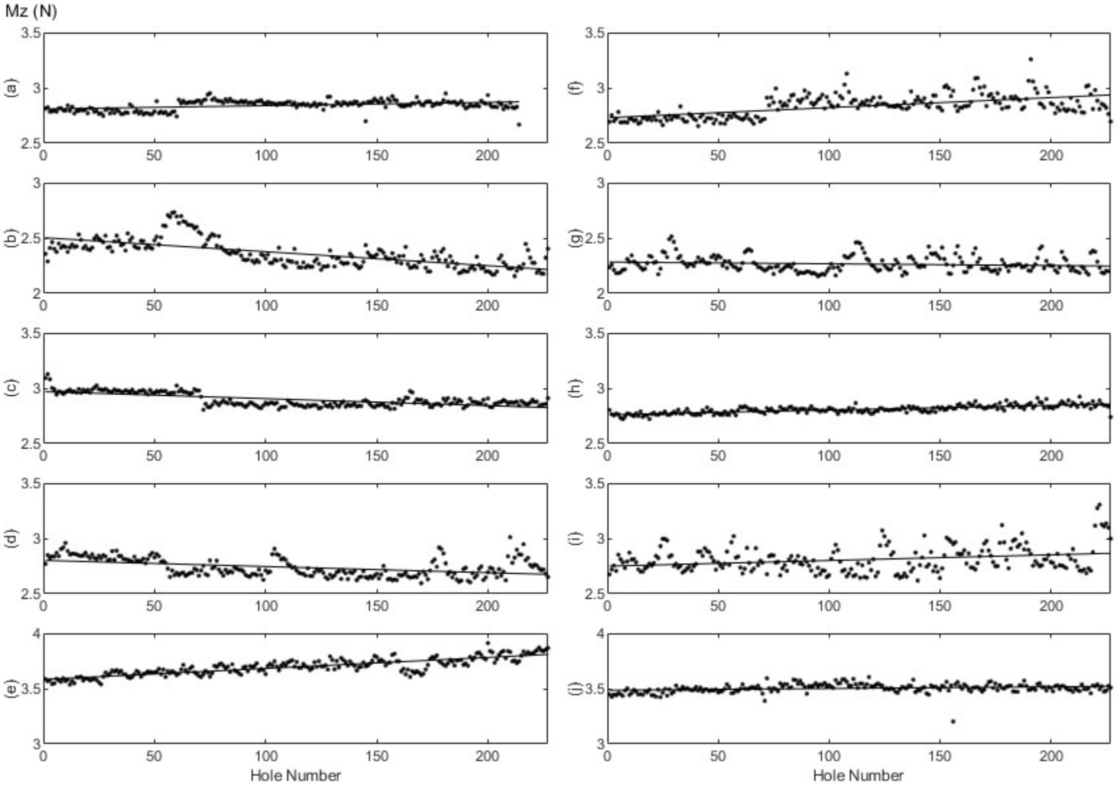

Figure 6.8: Graphs showing the average torque, Mz (Nm), for 227 holes drilled with coated (a – e) and uncoated (f – j) R846 Tools. Each set (a – e) and (f – j) are drilled at the V_f and V_s listed in Table 6.2.

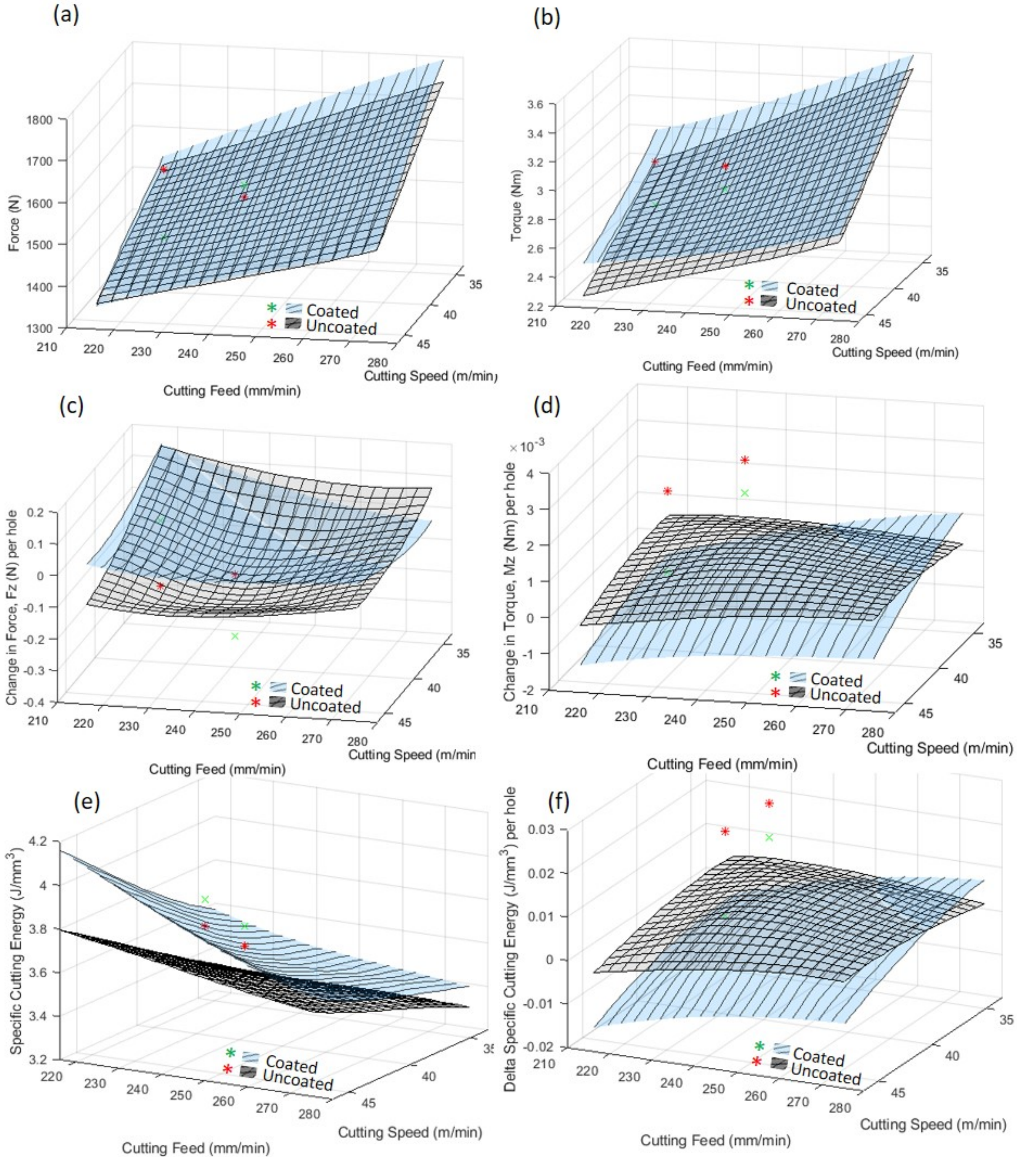

Figure 6.9: VFM Response surfaces for; (a) - initial thrust force (Fz), (b) - initial torque (Mz), (c) - change in thrust force (Fz) per hole, (d) - change in torque (Mz) per hole, (e) SCE and (f) change in SCE per hole. Results from experiment 3 are included for comparison where coated and uncoated values are marked in red and black respectively.

Tool Wear

The mean amount of flank wear on the tools used in experiment 2 is shown in Figure 6.10a, each box shows the 25th -75th percentile of the 24 flank wear measurements recorded for both cutting edges (12 on each), the range of the data is included as whiskers on each plot. The vast majority of flank wear measurements were below 0.1 mm for all tools. The lowest flank wear was measured for the slowest V_s, (33.6 m/min); at this V_s, the amount of flank wear was comparable, regardless of the V_f, for coated and uncoated tools. At the highest V_s (46.4 m/min), uncoated tools wore faster and had more flank wear than coated tools after 227 holes. For coated and uncoated tool 1, which was at the centre of the test array (V_f = 241.6 mm/min and V_s = 40 m/min), the mean flank wear of the coated tool was 0.078 mm, 0.012 mm more than the uncoated tool (0.65mm). The images from which these flank wear values were measured are shown in Figure 6.11a; which gives images of the tool wear after each 227 hole set for the chisel, flanks, margins and rake faces of tools used in experiment 2. As found previously in §5, the wear on coated tools is a combination of abrasive and adhesive wear at all tested V_f and V_s, while wear on uncoated tools is highly abrasive. For both coated and uncoated, considerable BUE is evident on all tools and obscures the cutting edge in most cases. It is for this reason the values measured for flank wear in Figure 6.10 have large ranges. Figure 6.11b shows the results of Alicona ER measurements made at point $C\Delta R$ as shown in Figure 3.9. Each cutting edge is labelled on the bottom x axis as C/U.1 (edge measured to have the largest ER) or C/U.2 (edge measured to have the smallest ER). In some cases the ER was shown to increase from 34 μm to 70 μm, although excessively high measurements may result from BUE hindering accurate measurement of the cutting edge. The largest ER for tool 1 was evident on the coated tool, and for both coated and

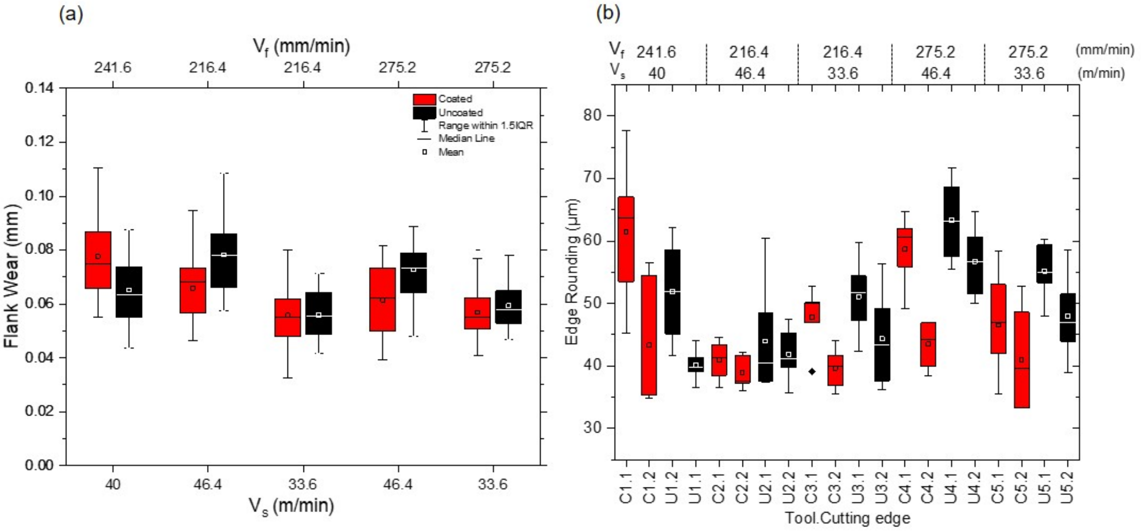

Figure 6.10: Box plots where: (a) - Shows flank wear. (b) - Shows ER for coated and uncoated tools used to drill 227 holes in experiment 2.

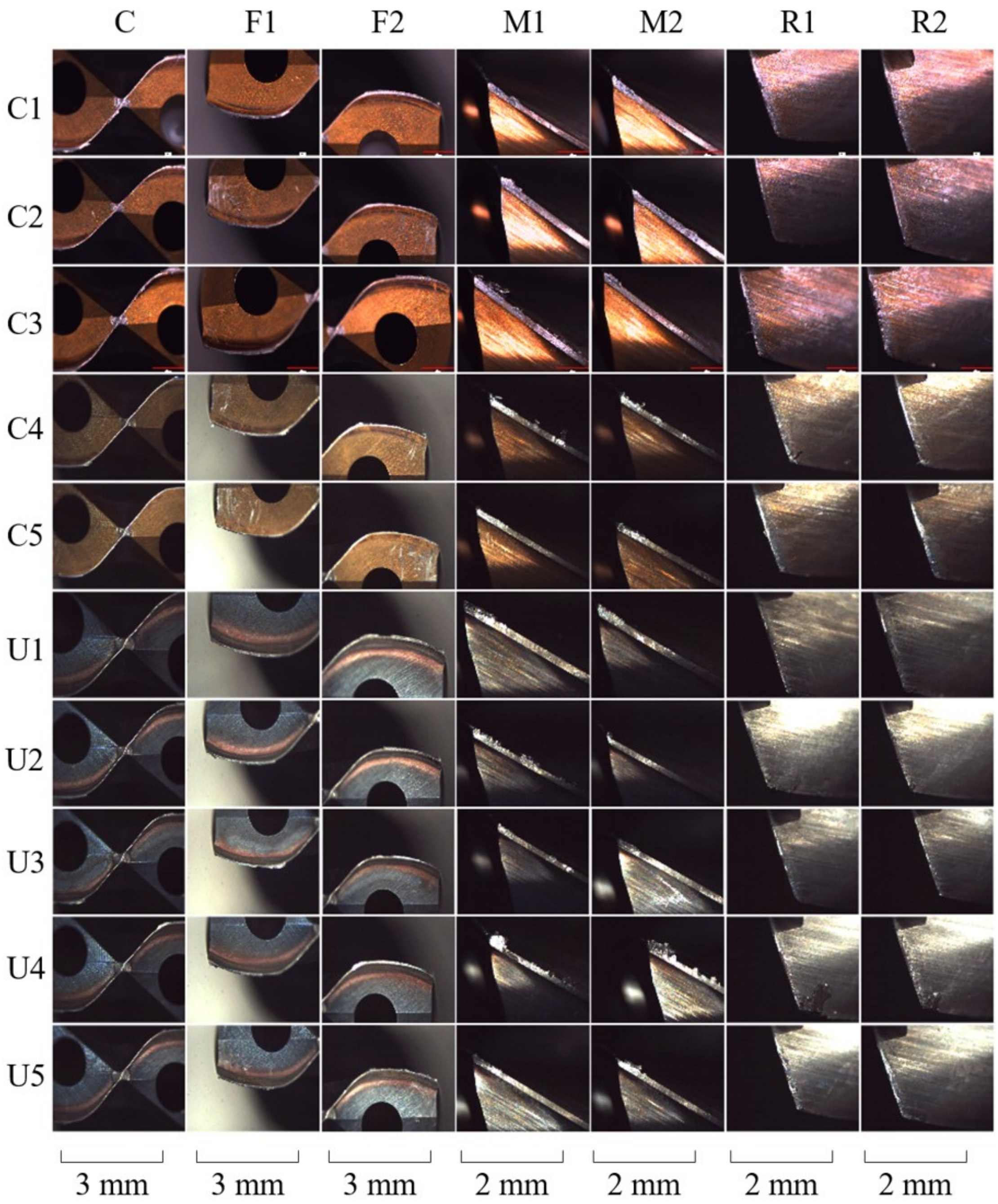

Figure 6.11: Photographs showing the chisel (C), both flanks (F1, F2), both margins (M1,M2) and both rake faces (R1, R2) for each tool (C1 –C5, U1 – U5), used in experiment 2 after 227 holes.

uncoated there was a large difference between the rounding measured on edge 1 and edge 2.

Unlike tool 1, tool 2 ER was smaller and there was a relatively small difference between each cutting edge, showing the least amount of tool material was lost for the most conservative cutting parameters. For tool 3 there was a similar difference between cutting edges 1 and 2 for both the coated and uncoated case. For tool 4 and 5 the uncoated tool had larger ER although for tool 4 there was a larger difference between the two coated edges, whereas in tool 5, the difference between cutting edges was similar.

Surface Roughness

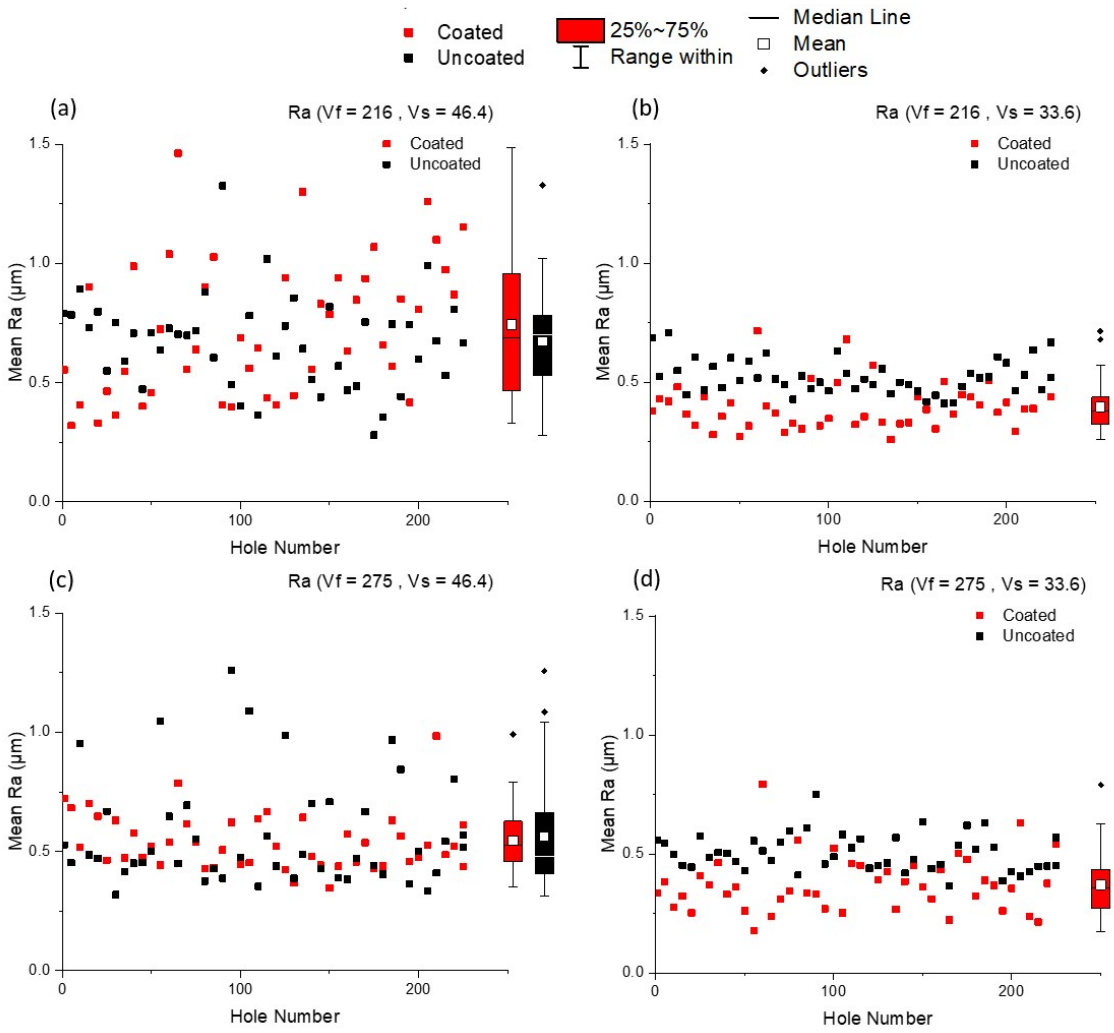

Figure 6.12: Graphs (a-d) show the Ra of holes drilled with coated uncoated tool pairs 2-5 from Table 6.2.

The Ra results as measured by the Diavite DH-8 probe for pairs 2 – 4 as defined in Table 6.2 are presented in Figure 6.12. The R_{max} results are presented in Figure 6.13. The figures show that drilling in Ti-5553 at higher V_s (44.6 m /min), causes a larger variation in Ra and R_{max} and that those tools used at slower V_s (33.6 m/min), results in a lower mean Ra; illustrating that lower V_s are beneficial in improving surface roughness. There is a slight reduction in Ra when coated tools are used at 33.6 m/min regardless of the V_f, showing coating tools with PVD-TiAlN results in a slightly improved roughness response. Sharif and Rahim identified a similar relationship for PVD-TiAlN vs uncoated carbide drills when machining Ti-64: In their investigation, they attributed the differences in Ra between coated and uncoated tools to differences in tool wear. However, as the tools in this investigation reached 20 – 40% of the maximum wear limit and there was no noticeable increase in the roughness from hole 1 to hole 227, the amount of tool wear is not the cause of the disparity when drilling Ti-5553. The average Ra results at 46.4 m/min are highly varied and there is no definitive difference shown between coated and uncoated tools; for the slower V_s of 33.6 m/min there is somewhat lower Ra measured for coated tools which is most likely resultant from the larger average tool ER, which was 10 - 15% larger for the coated tools. Although yet unproven, it must also be considered that the workpiece-coating-tool interaction and the formation of an Al_2O_3 layer could be reducing tool friction and therefore improving stability of the operation and reducing the roughness slightly as discussed [116]. The R_{max} measurements shown in Figure 6.13 are considerably higher for the fastest V_s (46.4 m/min). Of the two tests at this speed, the test conducted at the lower V_f (216 mm/min) showed the highest R_{max} values. The lowest R_{max} values were evident for the slower V_s. As mentioned previously there was less variation in the torque results for the slower V_s which indicated

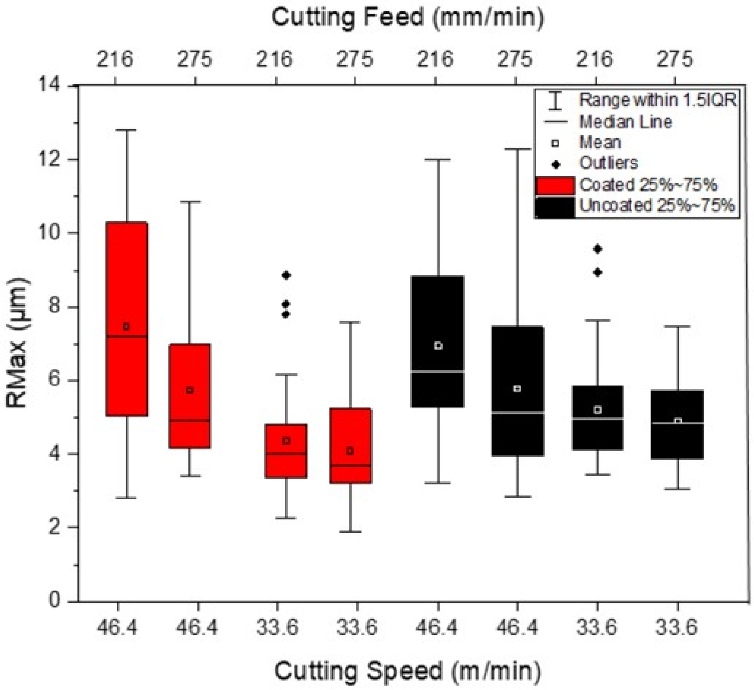

Figure 6.13: Graph showing R_{max} for coated and uncoated pairs 2-5 in Table 6.2.

better process stability at these conditions, this contributes to the improvements in both mean Ra and R_{max} with reduction in speed.

Regardless of the variation due to cutting parameters, R_{max} values, when drilling the Ti-5553 alloy, were higher that would be expected in the drilling of Ti-64. In order to understand why this was the case, Alicona variable focus scanning was used to analyse the elevation on the machined surface of holes from the trial. The diagram on the right of Figure 6.14, indicates the region where the Alicona scans were made. On the left is an elevation colour map which shows the surface of the drilled hole. Labelled on the scan are sites of elevation which were thought to be re-adhered Ti-5553 material from the cutting edge of the tool, which was shown in experiment 1 (Figure 6.4) to accrue an excessive amount of BUE and adhered workpiece material during the drilling process. To confirm if the features seen on the scan in Figure 6.14 were adhered Ti-5553, and to see exactly how it was affixed to the surface of the hole, cross-sectional BSE micrographs of the hole within the same location as the Alicona scan were taken. Figure 6.15 shows a cross-sectional BSE micrograph from each side of the hole. The re-adhered Ti-5553 is clear on both micrographs, in (a) the material is elevated approximately 10 μm above the surface, in (b) the deposit is much smaller measuring approximately 3 μm. The deposited material has a similar morphology and deformed microstructure to that investigated by Cox et al., when milling Ti-5553: They found that the re-adherence of material in this manner would significantly reduce fatigue life due to what was effectively the welding of fracture sites onto the workpiece [73]. Higher V_s will result in higher temperatures that in turn will contribute to more BUE and re-adherence of material, thus resulting in the higher roughness shown in tests at V_s = 46.4 m/min [25]. This is supported by the flank wear results in Figure 6.10a, which show more flank wear was measured for tools at V_s = 46.4 m/min. As flank wear measurement could not accurately differentiate between the cutting edge and BUE, the increased wear is likely due to the presence of BUE. The increased variation in torque for each hole drilled at the higher V_s

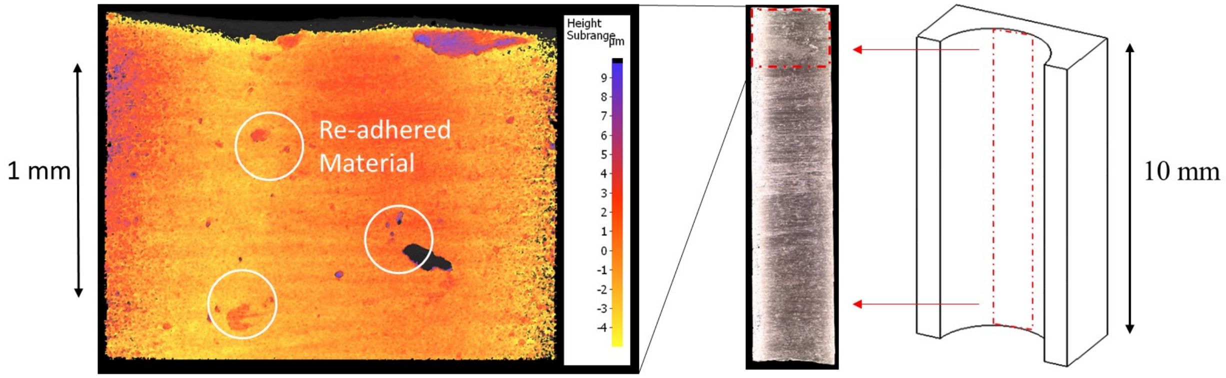

Figure 6.14: Alicona image of re-adhered material on the machined surface hole drilled using a coated tool at V_f = 275 mm/min and V_s = 46.4 m/min including the scan location with in the hole.

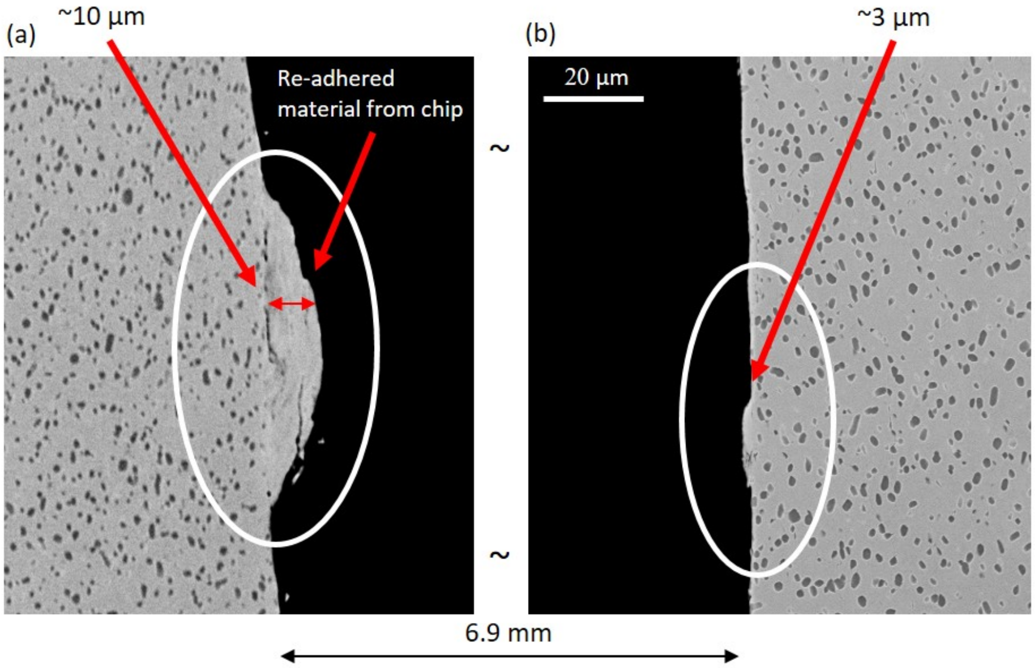

Figure 6.15: BSE micrographs of the drilled hole surface within the Alicona scan region identified in Figure 6.14 for a coated tool used at $V_f = 275$ and $V_s = 46.4$. (a, b) are from opposite sides of the cross section.

also suggests poorer stability, resultant from geometric imbalances between the cutting edges due to variation in BUE.

6.2.3 Experiment 3

Thrust Force and Torque

The thrust force and torque of each hole was measured using the same method as was utilised for experiments 1 and 2. The results for all four tools are shown in Figure 6.16. Again, the gradient of each set of holes was calculated, and the change per hole in Fz and Mz compared to the results of experiment 2. This comparison can be seen in Figure 6.9 (a,b); the green cross represents the coated and the red cross the uncoated tools. Following the same trends found previously in this chapter and in §5, Fz and Mz for coated tools had a larger magnitude than uncoated tools. However, when compared directly to the values measured in experiment 2, the magnitude of Fz is lower than the response surface would indicate, whereas, the Mz is very similar to expected. The change in Fz per hole as given in Figure 6.9c is not comparable between experiment 2 and 3. The fact that the fit significance of the gradient attributed to the Fz is low (due to only 50 holes being drilled), calls into question the accuracy of the result obtained for Fz. Although this also draws into question the validity of Mz, Figure 6.9d does show that coated tools require more torque per hole than uncoated tools despite considerable difference in magnitude between experiment 2 and 3. The SCE results given in Figure 6.9e, show like in experiment 2, that the uncoated tools are cutting more efficiently (in terms of power usage). Direct comparison to the results of experiment 2 indicates minimal change in cutting efficiency for experiment 3; suggesting that regardless of the machining setup similar results for initial holes do occur. However, since the change in SCE per hole for coated tools was lower in experiment 2 than 3, tools may have been wearing in a different way or that 50 holes was not long enough to see SCE decrease significantly. In other words, after 50 holes the coating may not have reached peak performance, or been removed from the cutting edge. For uncoated tools, the change in SCE per hole in experiment 2 and 3 remain similar, further validating the idea that uncoated tools wear at a constant rate.

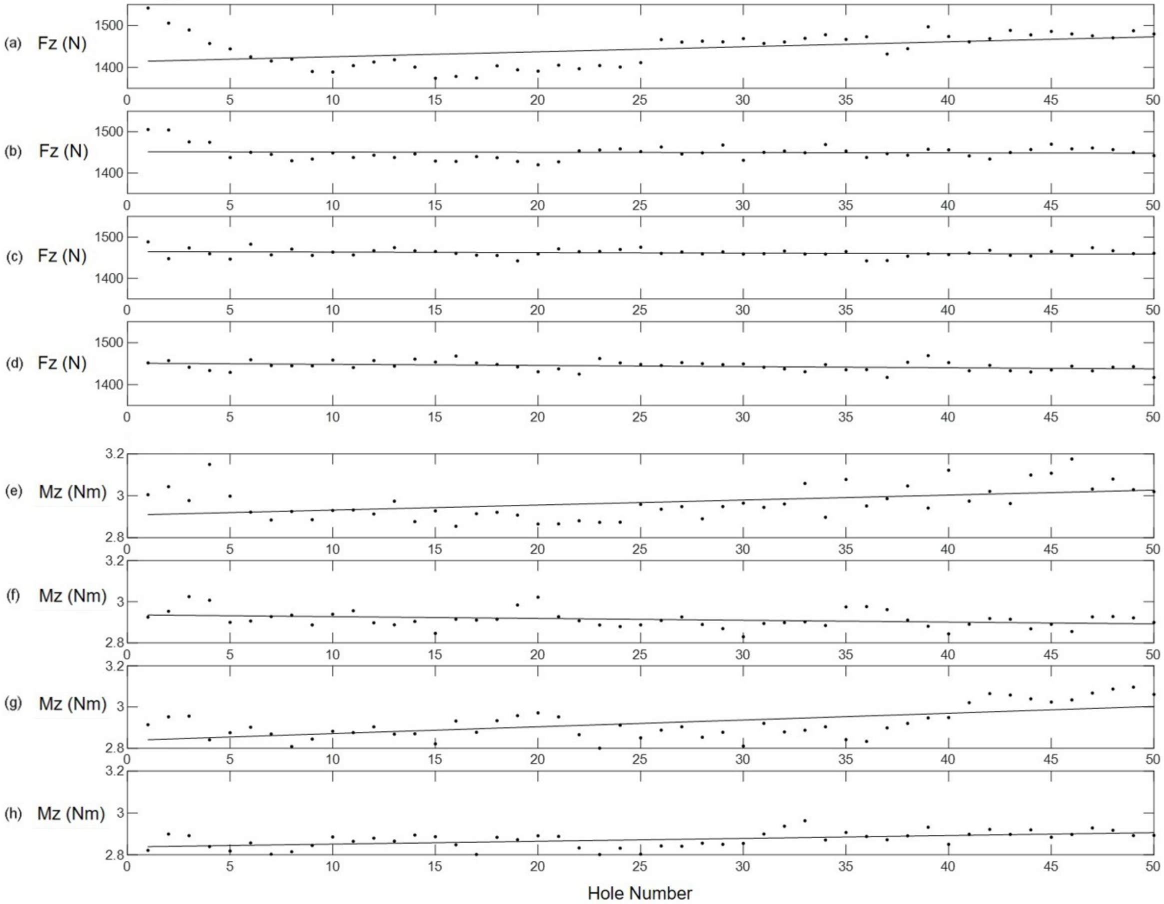

Figure 6.16: Graphs showing the thrust force (a-d) and torque (e-h) results for experiment 3.

Tool Wear

The type of wear observed in experiment three was very similar to what was expected following the previous work in section §6.1 and §6.2. Figure 6.17 shows the top view (T), chisel (C), and both flank faces (F1, F2), for both coated and uncoated tools after the 50th hole drilled with each tool. The tool chisel remained unbroken in all cases, with removal of the coating at a small area surrounding the tool point. On the cutting edges and tool margin/outer corner shown in (F1 and F2), BUE can be seen clearly. Figure 6.18 shows the difference in elevation for each tool from hole 0 to the 50, from two perspectives; - the top of the tool and the side of the tool. Figure 6.19 enables quantitative measurement of the amount of BUE evident on each of the tools after the 50th hole. On cutting edge 1 of C1, the BUE measures between 0.01 and 0.03 mm increasing in size as the radius increases. Similarly, for both the U1 and U2 cutting edges, the amount of BUE increases from the centre outwards from 0.02 mm to 0.4 mm. C2 however, has minimal BUE on the cutting edge, the edges near the point of the tool show a reduction in tool material of roughly 0.01 mm in height. There is adherence of Ti-5553 towards the outer corner, but this only measures 0.01 mm. C2 shows significantly more material adhesion to the tool flute indicating for this tool the chip evacuation was not optimal. The large elevation to the top right of the top down map of C2 was identified as external residue which adhered to the tool after all cutting and photographs were complete, hence why it is not seen in Figure 6.18 (C2).

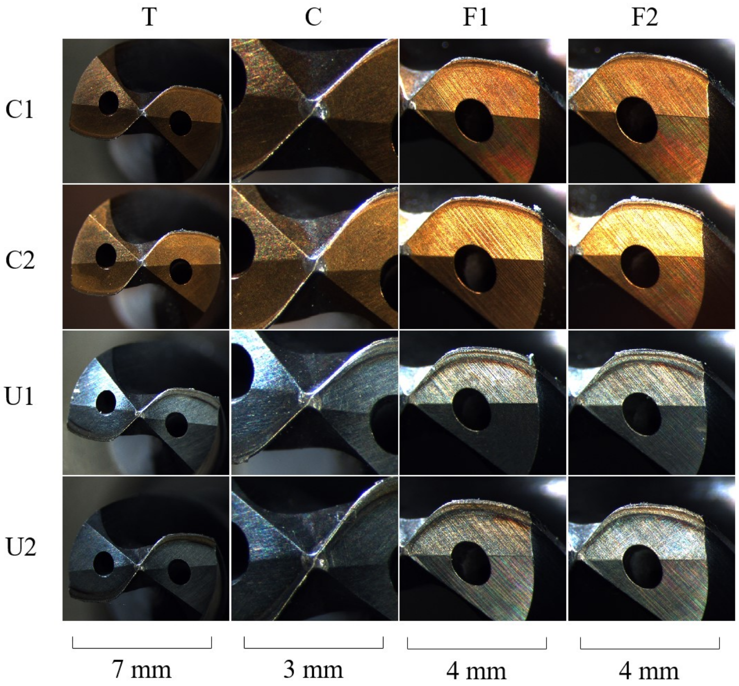

Figure 6.17: Photographs showing the top (T), chisel (C), and both flank faces (F1, F2), for both coated (C1,C2) and uncoated (U1,U2) tools after the 50th hole drilled with each tool.

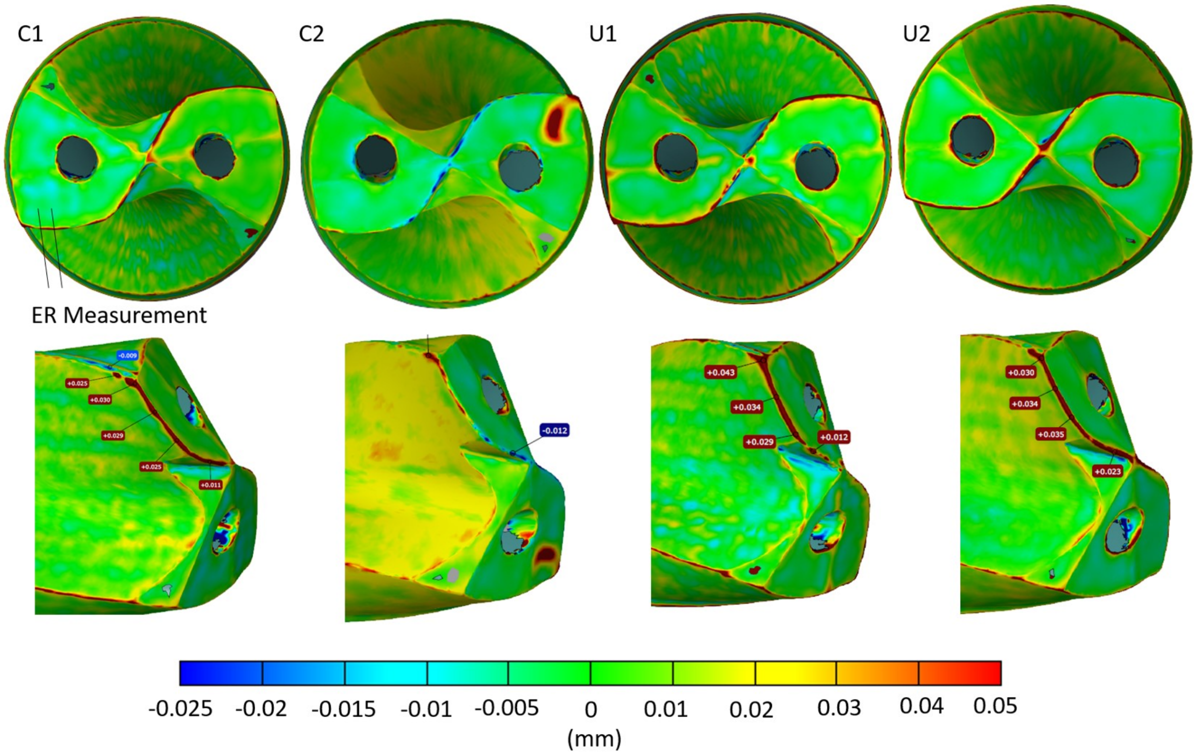

Figure 6.18: GOM images showing tool wear elevation for coated (C1, C2) and uncoated (U1, U2) tools after the 50th hole in experiment 3.

In order to compare the tool wear from experiment 2 to experiment 3, the increase in ER of the tool at the location marked “ER measurement” in Figure 6.18 (C1) for each cutting edge was measured and compared to the predicted change in ER, as calculated from the results presented in experiment 2. The predicted value was calculated via linear interpolation between the Helicheck measurement of each tool before drilling and their ER as presented in Figure 6.10b. Figure 6.19 shows the results of the measured ΔER and predicted ΔER. In all cases, except for C2, results for edge 1 of each tool were relatively close to, but slightly above the predicted. For coated 2, which was observed to deviate significantly in the 3D scans (Figure 6.18), the amount of wear on edge 1 is more than double what was expected. For edge 2, all ERs increased substantially more than predicted, with coated 2 being more than three times as large as predicted. As the prediction for ΔER was made based on a linear interpolation of ΔER per hole, it is possible the increase in ER per hole occurs slightly faster on one cutting edge and slightly slower on the other at the start of the tools life i.e. the first 50 holes. That being said, the results presented in Figure 6.19 for C1, U1 and U2 demonstrate that a wear measurement, such as ΔER, can be somewhat successfully predicted for untested V_f and V_s using wear data measured at the array of parameters tested in experiment 2.

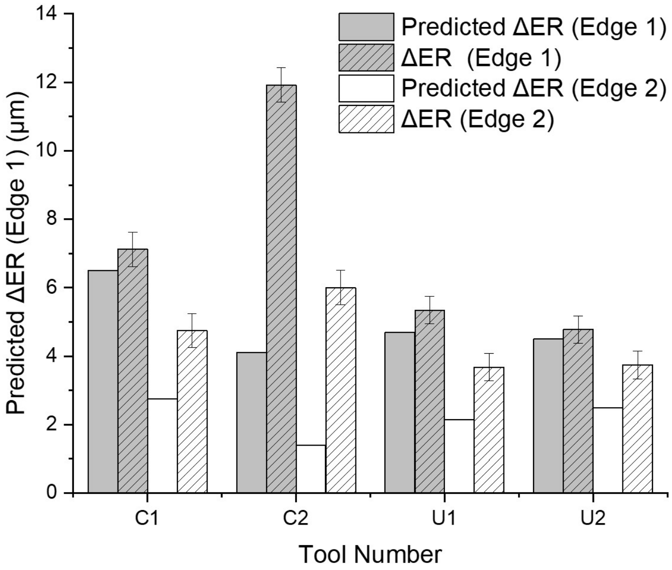

Figure 6.19: Bar chart showing the ΔER and predicted ΔER of tools used in experiment 3.

Hole Quality

The following aspects of hole quality were measured and compared for coated and uncoated tools used in experiment 3; cylindricity, straightness, perpendicularity, entrance burr height, exit burr height and average hole roughness (Ra). The results for all holes are shown in Figure 6.20 as box plots. Although there are no substantial differences between the coated and uncoated tools, some minor differences were observed: The hole roughness measurement indicated comparable results for coated tools to those measured in experiment 2, however, the values measured for coated tools were slightly lower, with several outliers equivalent to the mean Ra identified previously. In the case of entrance burrs, the holes drilled with C1, C2 and U1 were all comparable, but U2 showed a reduction in entrance burr and in some cases a negative burr. The effect of location on the drilled plate was also investigated in order to understand if either the clamping system or differences in material properties with changing billet diameter had any influence on the aforementioned aspects of hole quality. A clear relationship between entrance burr height and hole distance from the centre/edge of the workpiece is demonstrated in Figure 6.21a. There is also a slight relationship between improved hole perpendicularity and distance from the centre of the workpiece, as evidenced in Figure 6.21b. The reason for the correlation between location and entrance burr/perpendicularity is best explained by considering the improved rigidity of the workpiece, by the clamping system employed in experiment 3, which clamped the part at all points around the perimeter.

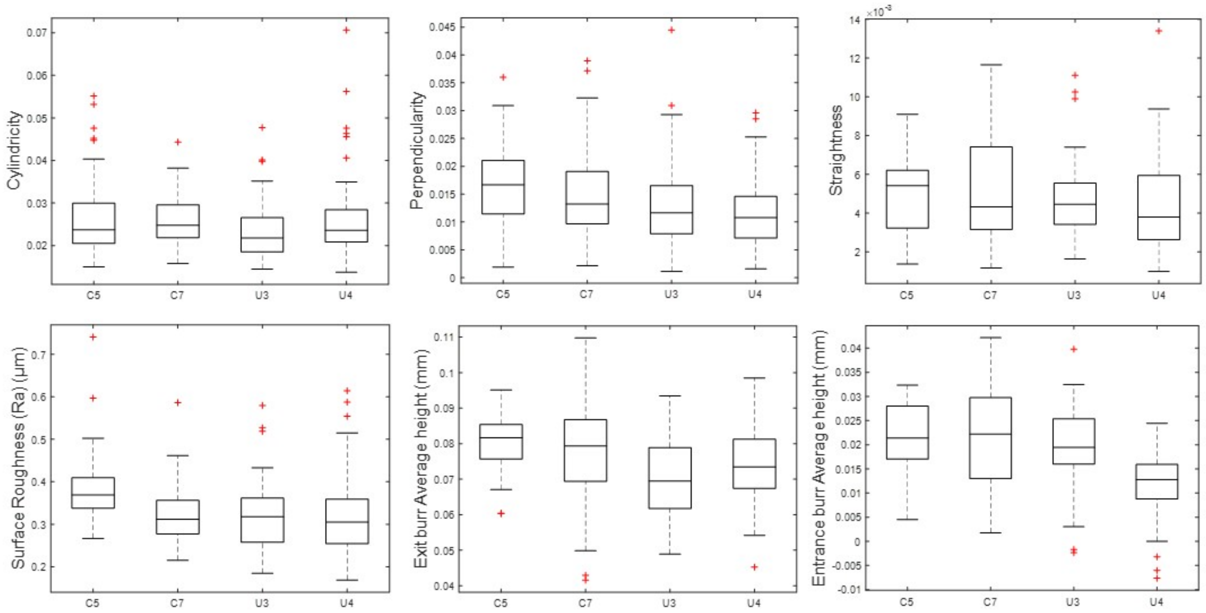

Figure 6.20: Box plots comparing the cylindircity, straightness, perpendicularity, entrance burr height, exit burr height and Ra between coated and uncoated tools used in experiment 3.

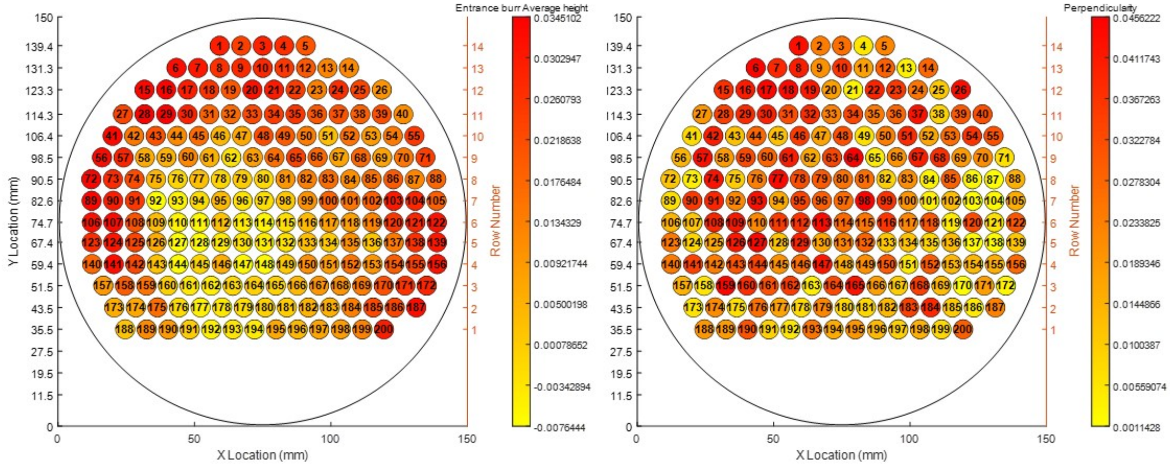

Figure 6.21: Heat maps showing how (a) entrance burr height and (b) hole perpendicularity vary with hole X and Y location. Holes 1-50 and 51 - 100 were drilled with coated tools while holes 101 -150 and 151 – 200 were drilled with uncoated tools.

6.3 General discussion

The work and results presented in §6 are brought together and discussed in relation to relevant literature under two subheadings; Tool wear and hole quality.

6.3.1 Tool wear

In all three experiments the tool wear images shown in Figure 6.4, Figure 6.11 and Figure 6.17 highlight that a combination of abrasive and adhesive wear was evident on coated tools, while uncoated tools were shown to wear mostly via abrasion. A similar observation was made in §5 for tools which had only drilled a limited number of holes [128]. In this chapter, a substantial amount of holes were drilled with all tools, therefore, it is probable that the wear modes remain similar throughout the tools life. As previously shown, a significant amount of BUE remains on the cutting edge, similar behaviour has been seen in both milling and turning of Ti-5553 [72, 73]. The amount of BUE has made the quantification of wear difficult, as evidenced by the large range of flank wear measurements, given in Figure 6.10a. Despite this, the results can still be discussed in relation to the SCE which is presented in Figure 6.9: those tools used at slower V_s, at both low and high V_f, measured less flank wear and a lower SCE than tools used at faster V_s. Therefore, for tools 2 – 4 the amount of flank wear correlates with the SCE of the process. In addition, it appears the tool coating is more effective at reducing the rate of flank wear at $V_s = 46.4$ m/min. At such speeds the cutting temperature is higher, and therefore, it can be said that the TiAlN coating is in some capacity working as intended, providing protection at elevated temperatures. At the centre of the test array where the SCE is shown to increase most per hole, for both coated and uncoated tools, the flank wear was highest for coated tools indicating the coating is not only ineffective at reducing wear rate, but is actively accelerating the wear rate. Coatings are known to increase the propensity for phenomena such as frittering and micro cracking to occur at the cutting edge, this can be exacerbated by the “plucking out” of tool material via adhesive stick-slip of the adhered BUE [122, 39]. Such wear was shown to occur for the coated tool tested in experiment 1. In addition, within the literature, extended contact of adhered titanium in contact with WC-Co tools when turning is known to cause the degradation of tools via chemical interaction, namely the removal of carbon from the WC, leaving free W(bcc) [29, 87]. As such interaction has been proven to be more extensive the more β-rich the titanium alloy, it is probable that such degradation is occurring at the tool and Ti-5553 BUE interface [84]. As reported by Kaplan et al., the decarburisation of the WC leads to the formation of highly abrasive TiC particles within the adhered material. If such carbides form during the drilling of Ti-5553 they will lead to, and exacerbate, abrasive wear which has been evidenced for all tools.

The measurement of ER (Figure 6.10b and Figure 6.19), was less compromised by the presence of BUE, as the geometry (radius) of the real cutting edge was estimated with the BUE discounted. Therefore, the rate at which the ER increases can be used as a more accurate measure of the rate at which tool material is lost, and hence, the rate of tool wear. In this work, the ER was measured at location C because this was closest point to where the tool in experiment 1 exceeded the flank wear limit and failed. At all but the most conservative cutting parameters (lowest F_{rev}), there was a substantial difference between the ER of each cutting edge. This corresponded to zero or negative change in torque per hole at such cutting parameters. It is expected that divergence from symmetry on a drill will cause instability and increase the torque [145], however, although the difference between cutting edges for other tools was apparent, it did not correlate with the response surfaces presented in Figure 6.9. The effect of BUE, masking the real cutting edge and constantly altering the stability mean that it was not possible to correlate the amount of wear directly by measuring the rate of torque or SCE increase per hole.

6.3.2 Hole quality

Aspects of hole quality were measured for experiment 2 and 3. Surface roughness, which is a key parameter for measuring hole quality within industry was measured to be below critical thresholds for hole tolerances, however, as shown in experiment 2, the R_{max} was found to exceed tolerance due to adhered material on the hole surface. Such adherence of Ti-5553 is known to effectively weld fracture sites to the machined surface and reduce the fatigue strength of parts [133, 73]. Since the magnitude and range of R_{max} was substantially higher for faster V_s, regardless of coating, lower V_s should be maintained if the part fatigue critical and/or finishing operations on the hole are difficult when drilling Ti-5553.

The methodology used in §6.2.3 for plotting CMM measurements is effective for understanding how hole location, and thus clamping systems impact relevant aspects of hole quality, and therefore, would be beneficial for testing clamping setups within an industrial environment. Of all the CMM measurements, only average entrance burr and hole perpendicularity were shown to have any correlation with location on the billet: Lower entrance burrs are likely created where the rigidity of the plate is lower, towards the centre while better perpendicularity is more likely where the workpiece is more rigid, i.e, around the perimeter, near to where it is clamped [146]. In addition to the above hypothesis, the mechanical properties and microstructure of titanium billet material, which has been shown to vary with radius, may also influence the burr and perpendicularity. However, based on the results of Suárez et al., the variation would vary round the circumference of billet and would not be as consistent as the results of this work indicate [139]. In addition, the Ti-5553 plates in this work were of smaller diameter than those tested by Suarez et al., and therefore there would be less changes in material due to relative differences in work hardening in certain locations characteristic of the forging process.

6.4 Conclusions

In §6 aspects of tool wear and hole quality for PVD-TiAlN and uncoated R846 WC-Co twist drills when drilling the metastable β titanium alloy Ti-5553 were investigated and examined in relation to thrust force and torque. A response surface methodology was examined for investigating tool wear for a range of cutting parameters. The results presented on hole roughness in §6.2.2 have been presented at the international conference on surface integrity 2020 (CSI 2020) and published in the CIRP annals. The key results and conclusions from the work are as follows:

- Instances of tool wear, such as chipping on the flank of the tool, correlate to spikes within the torque data. If such features can be better characterised, cutting torque could be used to identify when a tool fails, and thus save time during the tool development process.
- As has been previously established, PVD-TiAlN coated tools were again shown to wear via adhesion and abrasion, while uncoated tools wear via abrasion. This occurs for up to 20% of the tools life.
- PVD-TiAlN coated tools become more efficient the longer they are used, suggesting their optimum efficiency is when some or all of the coating is removed.
- BUE acts to stabilise the drilling operation by maintaining the cutting edge and minimising the effect of small chips and wear.
- Too much BUE can cause imbalance and asymmetry in tools which leads to more variation in torque and hence poorer stability.
- More BUE and poorer stability, typically seen at high V_s, causes more adhered material to be smeared on the hole surface resulting in high R_{max} results.
- Slightly better Ra and R_{max} results were achieved for coated tools which was attributed to better stability and larger ER.
- Substantially high values for R_{max} are measured during Ti-5553 drilling. Re-adhered titanium on the surface of the hole is responsible for this and will substantially decrease fatigue life.
- Over 227 holes there was no evidence of changing Ra despite tools wearing considerably (20% - 40%) of life. Therefore, initial tool wear does not influence surface roughness.
- At all but the most conservative cutting parameters, the cutting edges of the tool lose material at different rates, leading to asymmetry.

- There is no significant difference in cylindricity, straightness, perpendicularity, entrance burr height, exit burr height when using PVD-TiAlN coated or uncoated tools.
- Exit burr height and hole perpendicularity are influenced by the location of the hole, possibly because of increased stiffness around the plate perimeter and/or due to heterogeneous textures generated during the forging process.

Analysis of the force torque and SCE over 227 holes showed evidence that at the start of machining, uncoated tools are more efficient than PVD-TiAlN coated tools. However, as uncoated tools wear the cutting efficiency reduces and more energy is required. Whereas, for the majority of coated tools, the efficiency actually improves over the course of the 227 holes, suggesting that tools become more effective as the coating is removed. More holes would have to be drilled to identify if this trend continues and coated tools become more efficient than uncoated or not. The substantial BUE on tools used to drill Ti-5553 demonstrated in this chapter could be significantly reducing the tool substrate integrity. To investigate the mechanism by which this occurs, §7 will focus on further understanding the chemical wear that occurs during the machining of titanium with WC-Co tools.

Chapter 7

The mechanism of crater wear in Titanium machining

This chapter presents work which has enabled the mechanism by which adhered titanium on the rake face of cutting tools causes wear to be further understood beyond that within current literature. As a result a journal article titled "On the mechanism of crater wear in a high strength metastable beta titanium alloy" has been published in the international journal - Wear [127]. A brief introduction of for this chapter is provided, more in depth background on the nature of WC-Co chemical interaction and crater wear is given in §2.4.

7.1 Introduction

Previous chapters have repeatedly shown the affinity for Ti-5553 to adhere to cutting edges during machining operations. Such adherence occurs during the turning of titanium alloys and results in the chemical wear. In turning this chemical wear manifests as crater wear. In order to improve the tool life of WC-Co tools in the machining of Titanium alloys the mechanism of crater wear needs to be further understood so that tool manufacturers can design tools which have better productivity and tool life. The current understanding of crater wear stems from a seminal research paper by Hartung et al., (1982) [26]. In their research, they established that crater wear is the critical wear mechanism in titanium machining. From their results, they claimed that the crater wear process happens at a constant rate dictated by the rate of dissolution diffusion between the WC-Co substrate and adhered titanium on the rake face of the tool. They postulated that a layer of TiC forms in the crater between the titanium and tool substrate and that the size of this layer mediates the rate of tool degradation. Hartung et al., also found the temperature on the rake face of the tool to be upward of 950°C. This has since been found to be around ~1000°C at a pressure of 2 GPa

[80]. Although crater wear is the critical mechanism of wear, no stable TiC layer has been found to form, except when the static situation has been investigated using diffusioncouples [84, 85]. In these studies, Ramirez et al., (2017) found that in addition to a TiC layer, there are Co rich zones, in which there is poor diffusion of titanium matrix solutes. Hatt et al., (2018) found there is a significant inverse relationship between the Molybdenum Equivalency and the amount of TiC which forms at the interface. In the dynamic situation, which occurs during turning, TiC has been shown to form sporadically as particles within the adhered layer [88]. At the interface, a layer of W(bcc) forms due to the decarburisation of the WC which mediates the rate of the decarburisation [29, 87]. The modeling of Co diffusion within the system has shown that the amount of Co heavily influences the rate at which crater wear occurs. This is thought to be due to the Co enhancing the decarburisation via either the Ti_2Co phase or possibly a liquid phase, although no evidence of this has been found yet [87]. The aim of this work is to further understand the role of Co in crater wear. The metastable β titanium alloy Ti-5553 is investigated as since crater wear is known to be more rapid where there is more β phase. In this work several techniques; Optical microscopy, SEM, STEM, TEM, X-EDS, WDS and thermodynamic phase diagram modeling of the Al-Ti-Co system are used to improve the current understanding of the chemical interaction between Ti-5553 and WC-Co at the rake face of the tool during the turning carried out on the HAWK SL300 in §4.1.

7.2 Experimental methodology

7.2.1 Machining

The machining and method of insert selection for this chapter is described in detail in §4.1. The H13A CNMG 1204 08-SM WC-Co uncoated inserts which have 6 wt. % Co binder were used on the Cincinnati HAWK SL3000 lathe to turn both Ti-6246 and Ti-5553. This work focuses on further analysis of those inserts used to turn Ti-5553 at the V15 (70 m/min). In total, 4 inserts are analysed: the first was used to machine Ti-5553 for 30 s, the second for 60 s and the final two for 900 s. The WC grain size of the insert substrate was 1-1.3 μm, the substrate Vickers hardness was 1600 Hv.

7.2.2 Crater wear analysis

Inserts were sectioned in such a way that the crater region was exposed for high resolution imaging and elemental analysis. To achieve this, all inserts were mounted in Bakelite and polished using diamond suspension on a neoprene surface with an applied force of 20 N, the machines and process are discussed in detail within §3.3. For each insert, 500 μm was removed from the cutting edge, after which, samples were washed using water. Then images of the crater were acquired using an optical microscope, from which the crater depth was measured. Figure 7.1a shows exactly where the tool material was polished away. Figure 7.1b is a diagram indicating where the flank and rake faces are relative to the crater and the direction of the chip flow during machining (CFD).

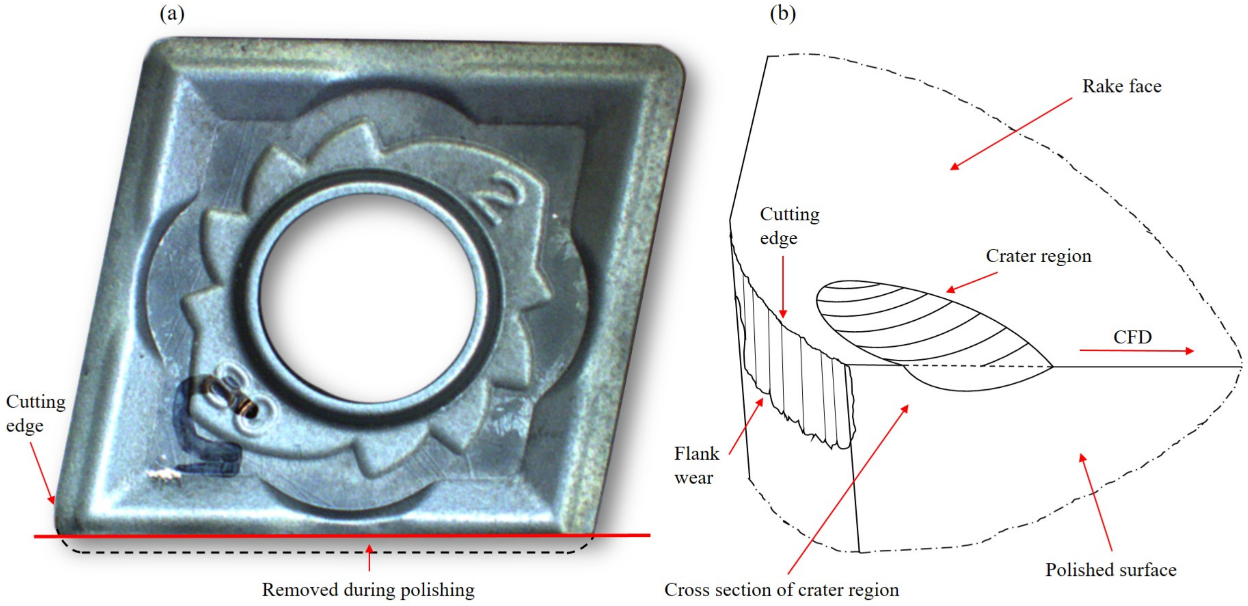

Figure 7.1: (a) - A modified photograph of the cutting insert with the section removed via polishing highlighted. (b) - A schematic diagram of the tool corner showing the polished surface, crater region, cutting edge, flank wear and chip flow direction (CFD) [127].

The rake face of the inserts were imaged using light and scanning electron microscopes at the crater formation location. AZtec Oxford instruments software was utilised in combination with the X-EDS detector to measure the relative quantities of elements within different regions of the crater at the titanium alloy and substrate interface. Improved resolution on the elemental distribution within locations of interest was achieved using an electron micro probe analyser (EPMA), which enabled wavelength dispersive analysis (WDS). Such analysis enabled the location and distribution of lighter elements like C to be resolved. In MATLAB the XMapTools package was used to further investigate elemental distribution via RGB and sliding window methods (described in §3.4.4). Analysis of the data collected using the

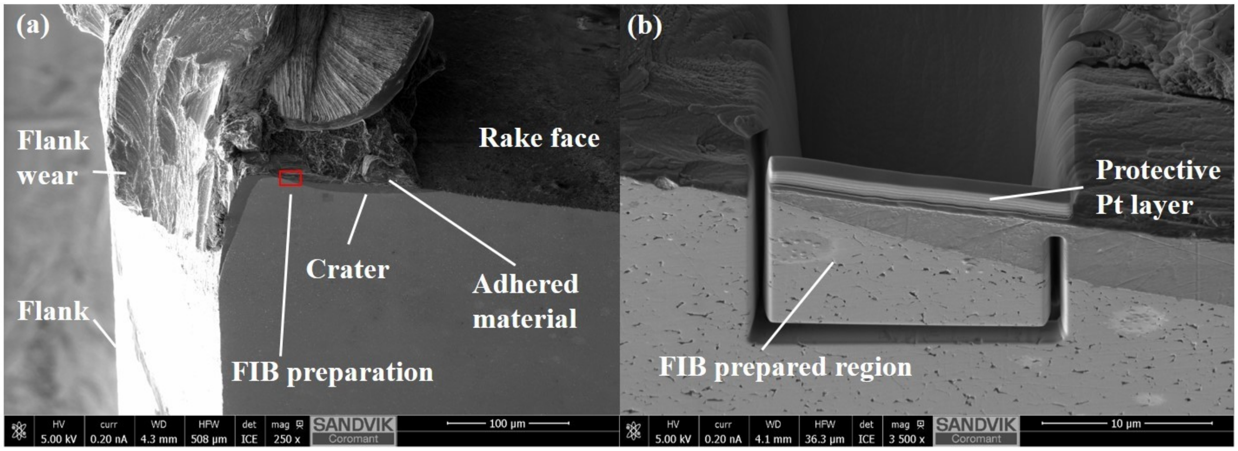

Figure 7.2: (a) - SEM of the tool corner after polishing showing adhered material within the crater region and the exact location of the lamellar extracted for TEM. (b) - Magnified view of the TEM lamellar showing the location of the protective platinum layer. Adapted from [127].

methods described above, demonstrated the need for even higher resolution techniques to be employed if the mechanism of crater development was to be further understood. Therefore, a TEM sample was prepared using a Thermo-Fisher-Scientific Helios 650 FIB. As discussed in §3.4.3, a protective Pt layer was applied to the crater and the FIB was used to extract a lamellar from the location labelled in Figure 7.2 (a). This enabled differentiation between the W(hcp) and W(bcc) phases via EDP analysis. High resolution STEM images of the sample were obtained in combination with X-EDS and energy loss spectroscopy (EELS) maps using a Thermo-Fisher-Scientific Titan G2 microscope, providing a “freeze-frame” of the crater as the wear is developing enabling the chemical wear mechanism to be analysed in detail.

7.2.3 Thermodynamic phase diagram analysis

Themocalc thermodynamic modelling software is used in combination with an improved TCNI8 NI-Alloys database [131]. Further details of how the phase diagrams were generated can be found in §3.7. The Ti-Al-Co phase diagram at atmospheric pressure (10^6 Pa) and 2x10^9 Pa were calculated and are presented and discussed in the context of other results.

7.3 Results

The time used, VB, VB_{max} and crater depth are tabulated in Table 7.1. Generally inserts used to machine titanium alloys are known to wear at a faster rate when machining first starts, before a stable BUE is formed. Thus, inserts #1 and #2 are shown to have substantial amounts of flank wear for the relatively short amount of time they were used in cut (30 and 60 s). On these inserts, there was no measureable crater and there was only limited sporadic deposits of adhered material remaining on the rake face after machining. Of the two inserts used for 900 s (inserts #3 and #4), insert #3 had slightly less flank wear (for both VB and VB_{max}), however, both inserts #3 and #4 had a substantial crater measuring 10 μm in depth. The difference in flank wear for the same crater depth is a result of the flank wear rate increasing substantially once the crater reaches a certain depth (10 μm in this case), as postulated by Hartung et al [26].

Table 7.1: Insert number #, time machining, average (VB) and Maximum (VB_{max}) flank Wear, for inserts selected for further analysis.

Insert #	1	2	3	4
Time	30	60	900	900
VB (mm)	0.034	0.042	0.085	0.11
VBmax (mm)	0.04	0.05	0.13	0.17
Crater Depth (μm)	Na	Na	10	10

Cross sectional and top down views of all four inserts are given in Figure 7.3. In the top down SEM images in Figure 7.3 (e, f, g, h), substantially more thermal scarring is seen for inserts which were used for 900 s. No crater can be seen for either insert #1 or #2, as the region is extremely small and totally covered by a BUE and adhered material; for inserts #3 and #4 the crater is large and partly obscured. Without the cross section images given in (c, d), the crater region is difficult to identify. The cross sections of the inserts, within the crater region, demonstrates the relative increase in BUE on the flank of the tool and adhered material within the crater region, from the start of machining (30 s to 60 s), to when the insert is fully worn (900 s). For insert #1 (Figure 7.3a,e), the crater cannot be seen at all, yet at 60 s (b, f), there is evidence that tool material has been removed within the crater region. Then for insert #3 (c, g), and #4 (d, h), there is a recognisable crater in both cases. The extent of the flank wear by 900 s, as given in Table 7.1, is substantial. The chip flow from the cutting edge and over the crater is evidenced in Figure 7.3d where the shape of the adhered material provides a snapshot of the machining process that occurs during turning [55].

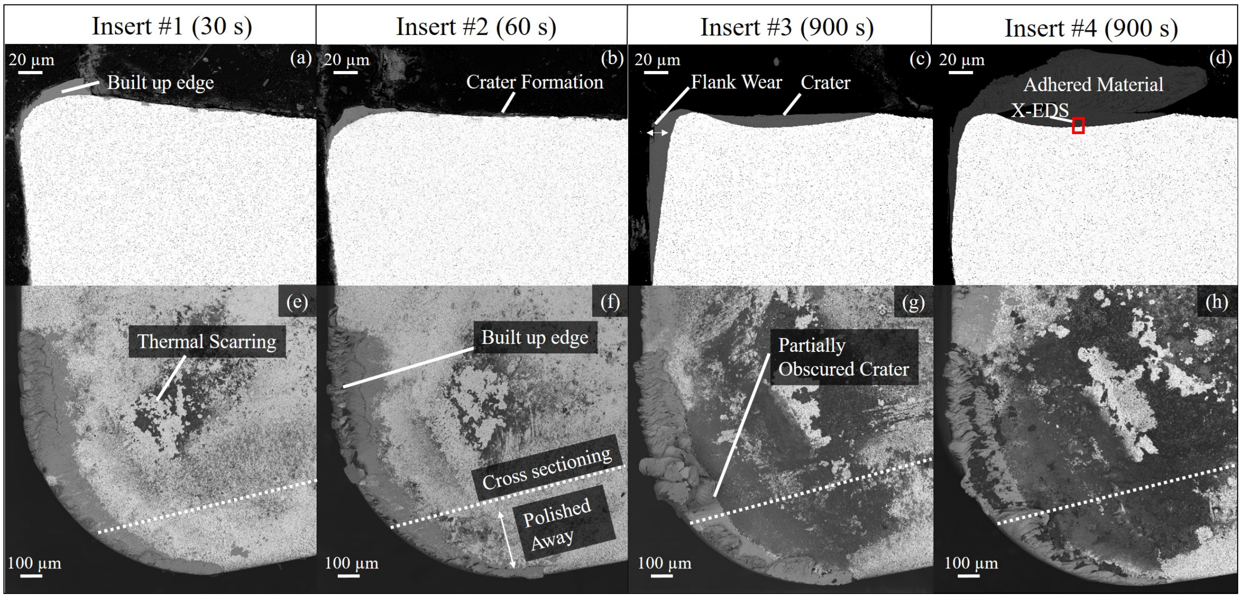

Figure 7.3: (a, b, c, d) - Optical micrographs of the sectioned and polished crater region for inserts 1 to 4. (e, f, g, h) - SEM images of the tool corner rake face, showing which region was polished away for crater analysis [127].

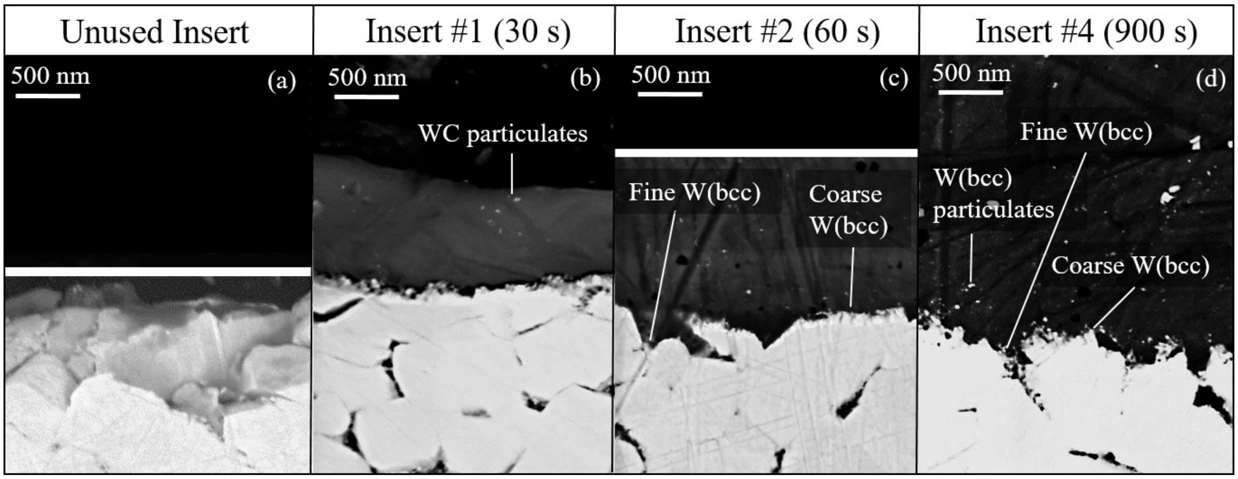

Figure 7.4: SEM micrographs of; (a) - the morphology of the WC-Co tool substrate on the rake face on an unused H13A insert, (b) - the adhered material deposited on the rake face of the tool after 30 s of machining, (c) - the crater at the interface between Ti-5553 and the WC-Co after 60 s, (d) - the crater interface after 900 s showing substantial W(bcc) particulates within the adhered layer and both fine and coarse W(bcc) at the interface [127].

To further show how the crater develops over time, and how the WC-Co tool substrate interacts with the adhered titanium that flows over the rake face of the tool, Figure 7.4 has been included. The SEM micrographs labelled (a, b, c and d), show the crater interface for an unused insert and inserts #1, #2 and #4 respectively. For the unused insert the typical substrate structure and morphology within the region under investigation shows WC grains $1 - 1.3$ μm in size, bound within a Co metal matrix, with each grain having a unique size and geometry. Figure 7.4b shows deposits of Ti-5553 on the rake face of the tool. As soon as the Ti-5553 comes into contact with the substrate the morphology and appearance of the tool material begins to change. Abrasive wear caused small particles of WC to break away from the rake face of the tool, some of which can be seen in the adhered Ti-5553. In addition to this, what looks to be small fringe-like structures begin to form between the Ti-5553 and tool substrate. As the insert is used for more time in cut more tool material breaks away and that in addition to the fringes, some finer structures begin to form at the interface, as is shown in Figure 7.4 (b) (60 s). After 900 s (Figure 7.4c,d), it is clear there is both a coarse and fine morphology of fringe-like structures and that there is substantially more tool material within the crater than at earlier stages of the cutting operation.

In Figure 7.3d, one location where X-EDS has been carried out is labelled in red. The results of the X-EDS scan from this location are shown in Figure 7.5. The count intensity of Al, Ti, C, W and Co over the crater and adhered Ti-5553 interface are included. The results give significant Al and Ti within the adhered material. The counts for the other alloying elements, V, Mo and Cr were not included, as the level of each was indicated to be less than that of the noise within each signal. Also evident within the adhered titanium layer, are occasional peaks in the C X-EDS, which occur when the line scan crosses small dark particulates. Indicating the presence, and thus formation of carbides within the crater. From the scans, the tool substrate is shown to contain W, Co and C, as expected. The X-EDS scan also clearly shows that Co increases between the WC grains due to large peaks in Co and minima in the W signal. In some cases where there is a significant amount of Co, the features will be referred to as Co rich regions. At the interface between the substrate and the Ti-5553, the Al and Ti counts are shown to decrease relatively quickly through the fringe-like morphology. The opposite is true for the C and W count at the interface, which increases as you go from the adhered titanium and into the tool substrate.

The WDS data obtained via the EPMA technique for insert #1, which was used for 30 s, is presented in Figure 7.6. At this time in cut the microstructure of the adhered Ti-5553 at the location of crater formation is still recognisable. For this particular deposit of titanium, the fact that the microstructure is visible, indicates that it was deposited very recently. The microstructure is most heavily smeared at the interface, suggesting that for this recent deposit of material, there is stick-slip adhesion occurring. Even though the adhered material in Figure 7.6 has only been on the tool surface for a relatively short amount of time, small counts of Co were verified within the adhered Ti-5553, suggesting the diffusion of Co has already begun.

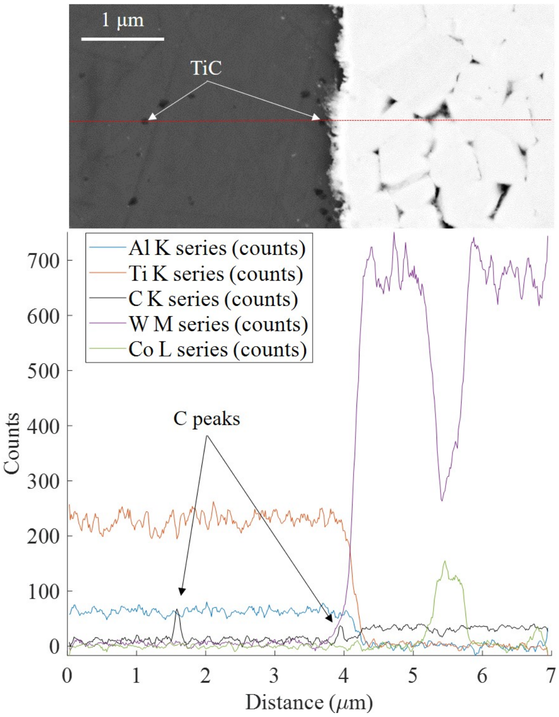

Figure 7.5: The top of the figure shows an SEM image of the crater at the adhered Ti-5553 and WC-Co interface. The location of an X-EDS linescan for Al, Ti, C, W and Co is indicated in red. The graph below the SEM image shows the count and intensity of each of the aforementioned elements and their distribution along the line scan [127].

WDS maps are given in Figure 7.7, which also includes the corresponding SEM micrographs for each; Figure 7.7a is the micrograph of the map in Figure 7.7c and Figure 7.7b is the micrograph for Figure 7.7d. The Ti-5553 and tool substrate interfaces for inserts #3 (a, c) and #4 (b, d) which are so labelled in Table 7.1. In both cases the maps are taken from the deepest point on the crater, which is at the crater centre. On the WDS maps, green indicates where C has been detected. The maps show that at the interface, in prior Co rich regions, there is more C within the surrounding adhered titanium. This suggests the Co is in some way enabling the C depletion at such sites and that more C is being lost from the tool substrate in such locations. Within the SEM micrographs (Figure 7.7a,b), dark particles are shown to form in and around these regions, resembling the TiC particulates previously identified from the X-EDS results in Figure 7.5. Also included in Figure 7.7f is a graph of the count intensity of C (+/-) 0.05 and Co (+/-) 0.1 across the interfaces shown in Figure 7.5a-d, created using the sliding window method explained in §3.4.4. The data is presented to the same scale along the X axis, as the WDS maps. For both C plots there is a decreasing C gradient at the interface, which occurs for around 1 μm, which translates to 20 pixels. From the interface, into the tool, the count of Co is shown to increase suggesting more Co is lost nearer to the adhered titanium. One key difference between the C graphs for insert

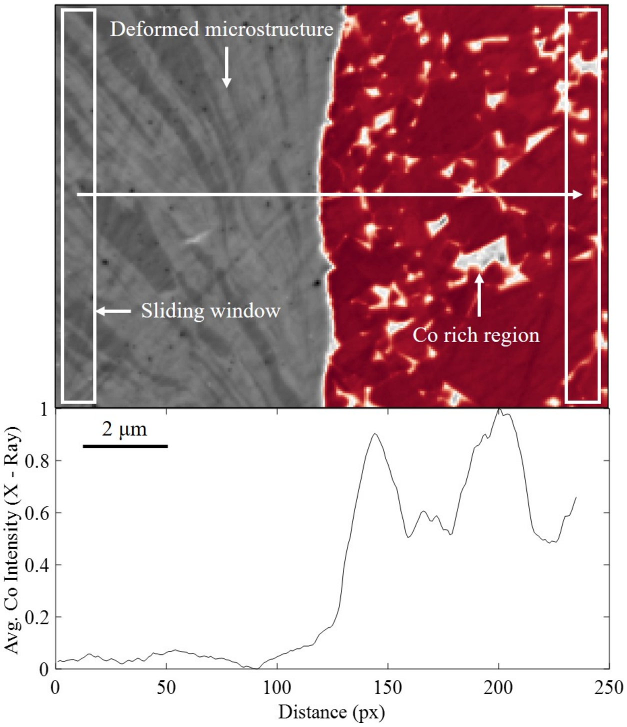

Figure 7.6: In the top of the figure there is a map of the interface constructed from the composite channel of the EPMA. The size and direction of a sliding window scan is labelled on the image. In the bottom of figure is the results of the sliding window scan for the Co intensity. The scale in the top and bottom is identical. [127].

#3 and #4, is that for #3, there is a small peak in the C concentration, but for #4, there is no such feature. Observing the maps in Figure 7.7b,d, one possible reason for the peak seen for insert #3, is the increased number of prior Co rich regions, facilitating more C removal from the tool, resulting in more C and thus more TiC at the interface.

From the lamellar sectioned from the location highlighted in Figure 7.2, TEM was used to obtain STEM micrographs of the interface. The STEM micrographs are shown in Figure 7.8, which also includes X-EDS maps of the STEM region for Ti, W and C on the left hand side. On the right hand side of Figure 7.2, the location marked Zone 2.2 in the top left STEM image is magnified and X-EDS maps of the Ti, W, Co, Mo, V+Cr and Al+W. In addition, EELS was used to make an elemental map of Zone 2.2 (for Ti and C). In the top left STEM image, the two zones previously identified as coarse and fine fringe-like W(bcc), are clearly distinguishable and labelled Zones 1 and 2 respectively. The fine fringes generally occur at the sites of prior Co rich regions, evidenced by the Co X-EDS map, showing how Zones 2.1 and 2.2 have a much higher amount of Co than the rest of the interface (Zone 1). The spectroscopy done on Zone 2.2 on the left hand side of the figure demonstrates that there is a high C content where the prior Co rich regions are, as was found from the

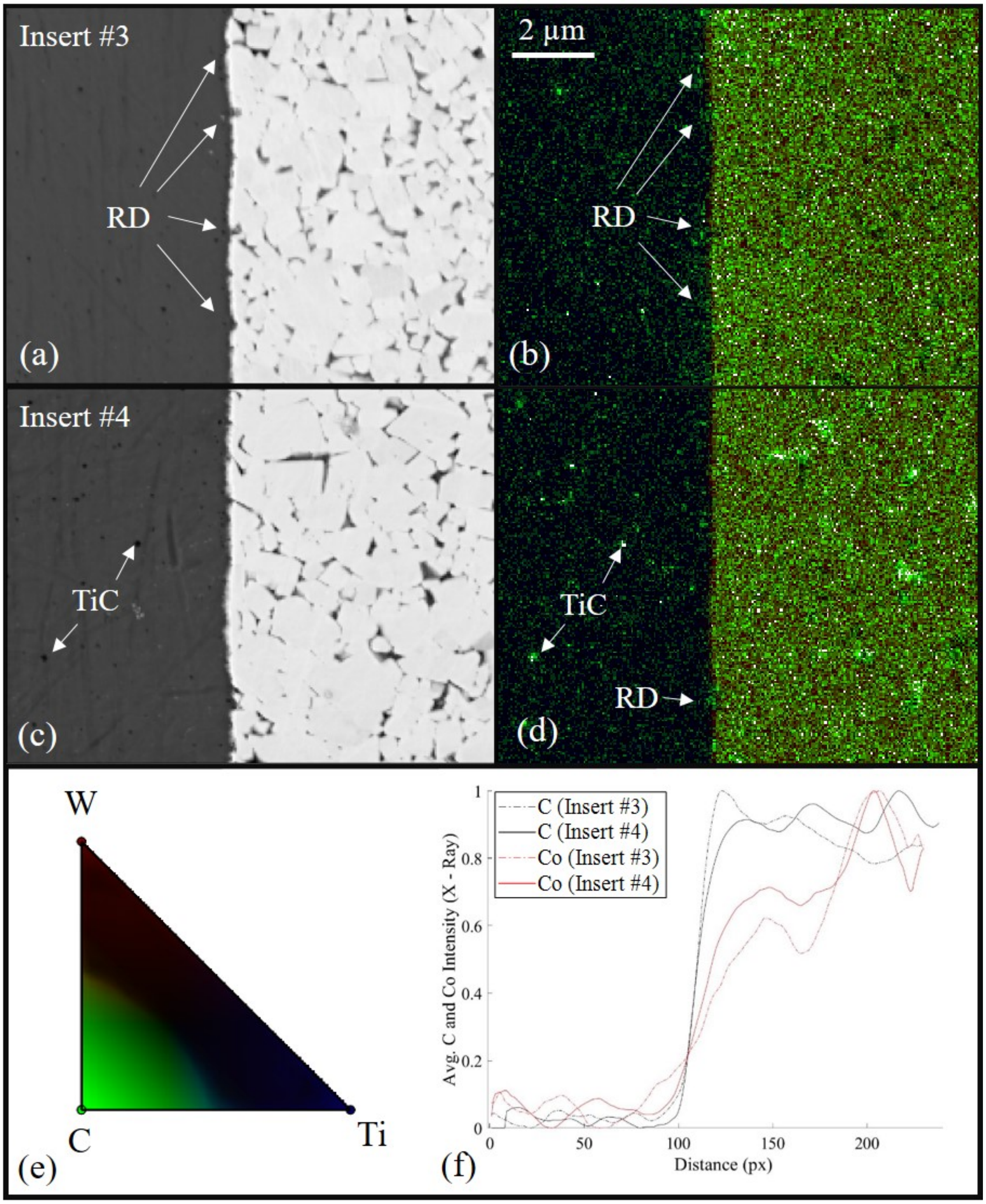

Figure 7.7: (a, c) - SEM images of insert #3 and insert #4. (b, d) - WDS maps for C, W and Ti where is (e) the colour key for (b, d). (f) - Graph of the C and Co across (b, d), where the X axis is at the same scale as the WDS maps [127].

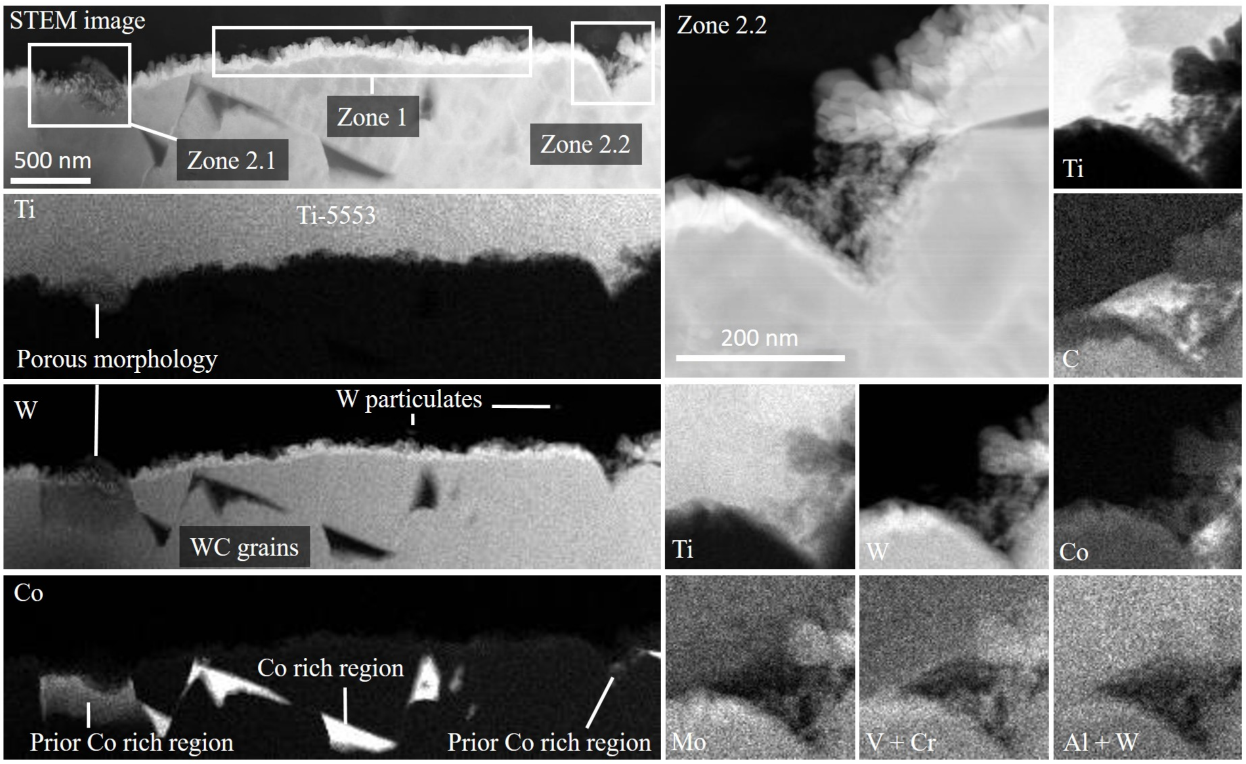

Figure 7.8: On the left there is a STEM image and X-EDS maps for Ti, W and Co of the interface within the crater. On the right a higher resolution of Zone 2.2 is presented with the X-EDS for Ti, W, Co, Mo, V+Cr and Al+W and EELS for Ti and C. All data is from the FIB sectioned lamellar marked in Figure 7.2 [127].

WDS results presented in Figure 7.7. Interestingly, within Zone 2.2 there is also a lack of Ti alloying elements; V, Mo and Cr. At the resolution presented in Figure 7.8, the fine fringes of W(bcc) appear to have a significantly different porous morphology, to that of the coarse fringes which form at the tool titanium interface. The morphology resembles Kirkendall like structure.

The electron diffraction patterns and the location from which they were extracted are given in Figure 7.9. The (110) titanium reflection is indicated in yellow and the (110) W reflection is indicated in red. The bcc phases of Ti and W have very similar radii within the diffraction pattern, but the fact that two distinct rings which measure 2.32 (Ti, a= 3.282 Å), and 2.24 (W, a = 3.165 Å), shows that both phases are present at the interface within Zone 2.2.

In Figure 7.10, the STEM micrographs (a, b, c) show a WC-WC grain boundary at ∼2 μm below the WC-Co and Ti-5553 interface within the crater. The high contrast region between the grains has been confirmed to be W(bcc): the evidence for this is shown in the EDP pattern in Figure 7.10c,d. This demonstrates that the decarburisation is not only occurring at the interface but also within the subsurface of the crater.

The ternary phase diagrams of Al-Ti-Co, calculated within Thermocalc software using a modified TCNI8 database [131], are presented in Figure 7.11a and Figure 7.11b. Within the diagrams (a) and (b) the phases that are stable at both 1015°C and 975°C, respectively, are included: For both, the pressure used was 10^6 Pa (atmospheric pressure). The other key difference between Figure 7.11a and Figure 7.11b, other than the difference in temperature, was the fact that in (a), the Ti_2Co was allowed to form, whereas in (b) it was suspended. From Figure 7.11a it becomes apparent that the Ti_2Co phase is present within the system at low quantities of Al, and around 12 mol. % Co in the titanium, this is entirely possible within Co rich regions which are intersected by the titanium and substrate interface within the crater. In addition, a liquid phase is shown to start to form under equlibrium conditions when the amount of Co is as low as 11 mol. %. In Figure 7.11b, where the Ti_2Co is removed from the simulation, it is clear that without the Ti_2Co nucleation, the liquid phase forms at lower temperatures from around 15 mol. % Co. In both simulations, at both temperatures, the addition of Al within the Ti-Co system reduces the mol. % of Co required to form the liquid phase. In order to test whether the simulations remain consistent at higher pressures,

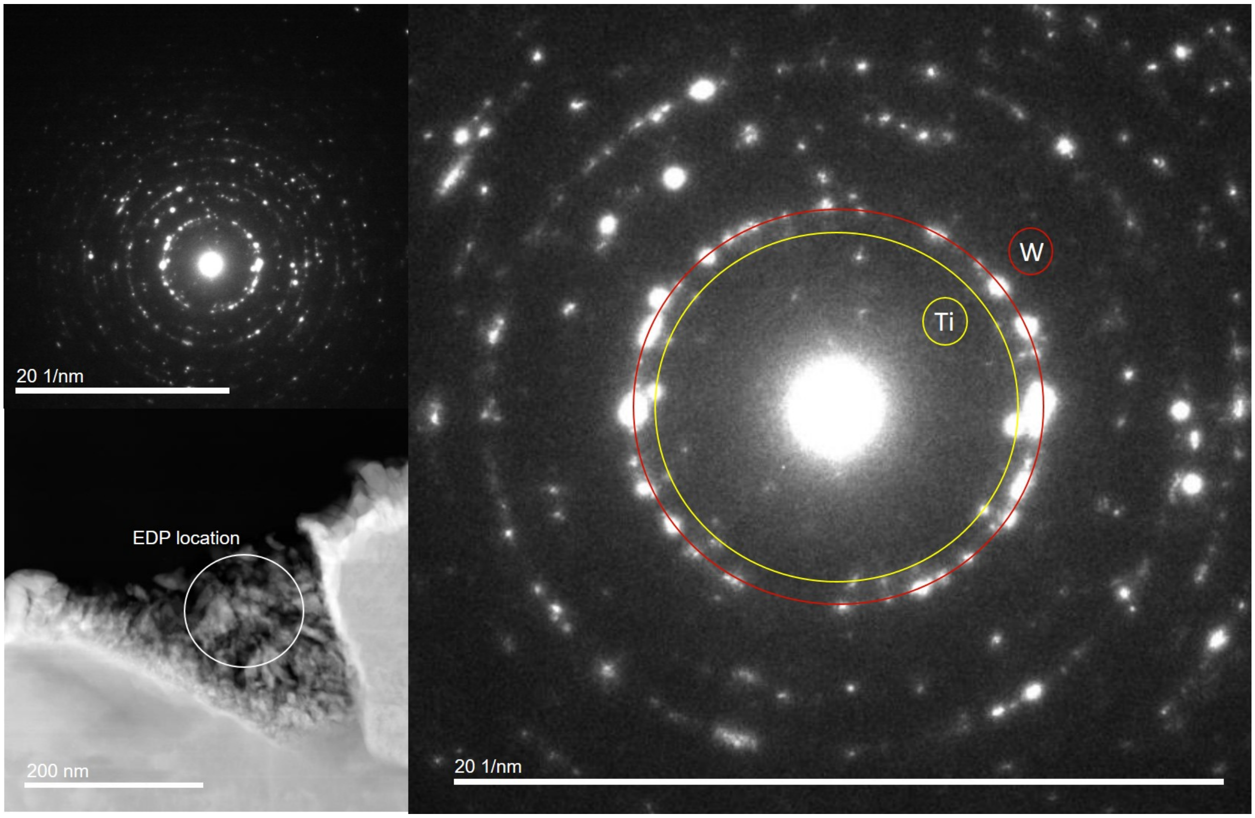

Figure 7.9: EDP patterns from the EDP location marked in the bottom right. Ti 2.32 (Ti, a=3.282 Å), marked in yellow and W2.24 (W, a =3.165 Å) marked in red [127].

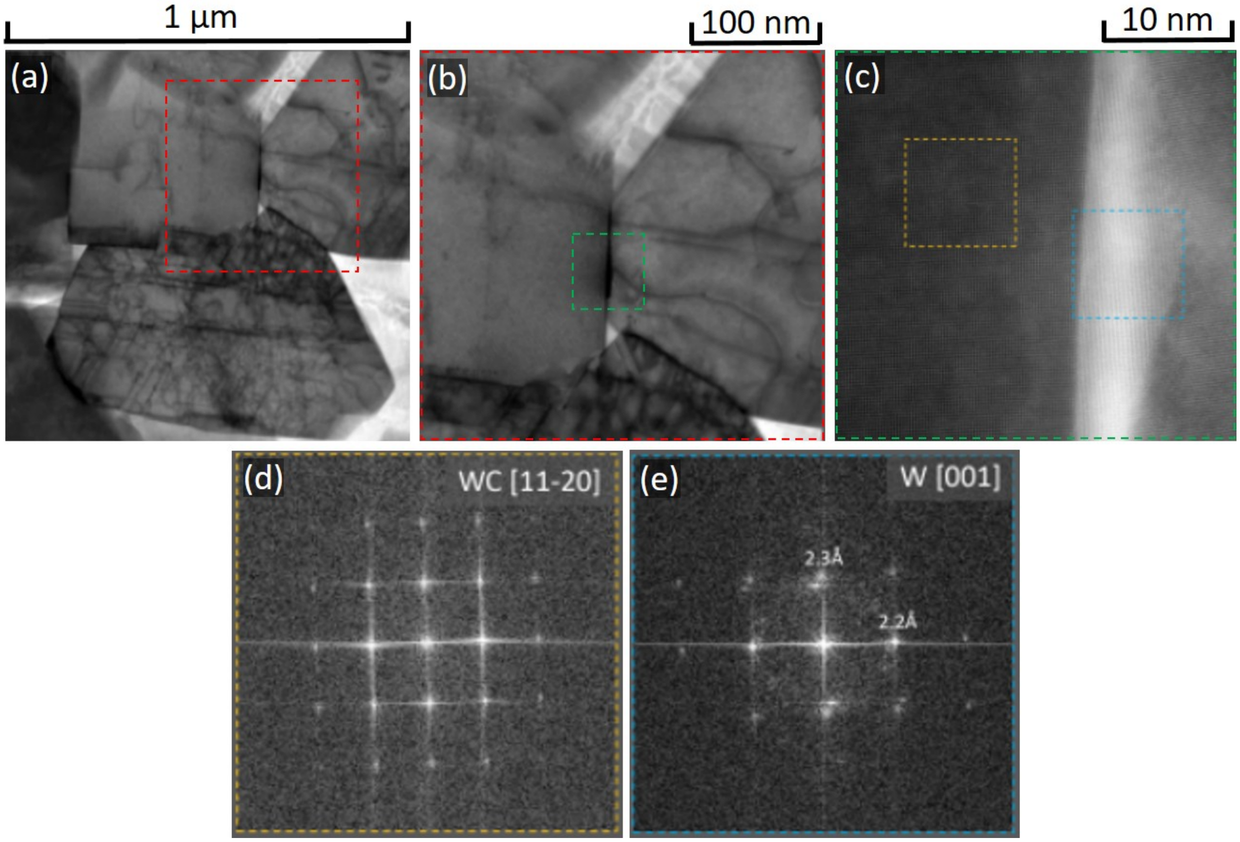

Figure 7.10: (a, b, c) are STEM micrographs of the WC-WC grains at 2 μm below the subsurface of the crater. (d, e) are EDPs of the yellow and blue locations marked in (c).

which have been found to be around 2 GPa at the cutting edge, the same ternary diagrams for Al-Ti-Co were calculated at 2 GPa. Results showed no difference in the liquid formation temperature where Ti_2Co is suspended. For the case where Ti_2Co is not suspended, the additional pressure causes the temperature at which the liquid forms to increase by 5°C, which is negligible within the context of the current study.

7.4 Discussion

In this section, the results presented in Figures 7.3 to 7.11 are discussed within the context of the current literature. Key observations from the results will be drawn from the results to provide a description of the mechanism for crater wear in WC-Co tools when machining titanium alloys. A schematic of the time steps for the proposed crater wear mechanism is provided in Figure 7.12.

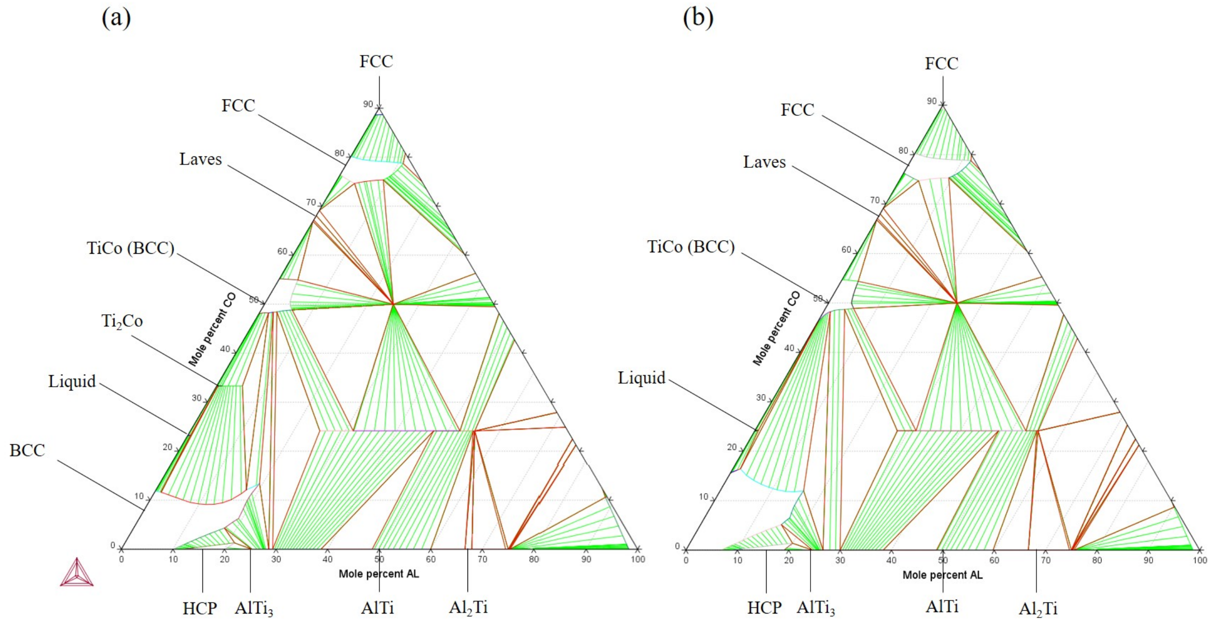

Figure 7.11: (a) Al-Ti-Co ternary phase diagram at atmospheric pressure (10^6 Pa), and 1015°C. (b) Al-Ti-Co ternary phase diagram with the Ti_2Co phase suspended, at atmospheric pressure (10^6 Pa), and 975°C. [127].

The process of turning titanium with WC-Co tools leads to crater wear on the rake face of tools, where temperatures between 900°C and 1050°C are known to occur within the secondary shear zone and where the chips slide against the tool substrate [26, 79, 80]. The bright fringe-like morphology, identified in Figure 7.4 and Figure 7.5, is the result of the WC-Co substrate interacting with the adhered Ti-5553 within the crater zone at elevated temperature, namely the loss of C from the WC and the formation of W(bcc). Odelros et al., (2017) have identified this phenomena before, when investigating WC-Co inserts used to turn Ti-64 with XRD [29]. The present work confirms that similar interaction occurs within Ti-5553, and for the first time, the phase of the fringe-like features has been proven to be W(bcc) since the EDPs given in Figure 7.8 show a reflection for the Ti(bcc) and W(bcc) phases at (a=3.282 Å) and (a=3.165 Å), respectively.

The high resolution STEM, that is presented in Figure 7.9, gives valuable insight into the nature of the interaction between adhered titanium and the tool substrate, and thus the process of crater wear. There are two distinct zones of decarburisation, introduced previously as Zone 1 and Zone 2. Within Zone 1 there are coarse fringes of W(bcc) and generally this zone is present along the majority of the interface. The coarse fringe-like morphology forms because of the immiscibility gap between W and Ti. Once this layer of W(bcc) has formed, it acts to limit the diffusion of C from the tool material into the adhered titanium because of the low solubility of C in W(bcc). Within the crater, where Co rich regions are intercepted by the interface, regions with more Co exist and lead to the formation of a fine porous morphology of W(bcc), labelled as Zone 2 in Figure 7.9. The morphology evident in such a zone resembles that of a Kirkendall morphology which occurs due to a large difference in the effective diffusion rate between two metals [147]. Previously within the literature, the interface characteristics of Zone 2 have only been observed twice, and only when TEM has been utilised [91, 148]. As Co can stabilise the β phase in titanium, the titanium within Zone 2 will be more heavily β stabilised than elsewhere, contributing to increased diffusion of C away from the tool, accelerating the rate of decarburisation. In addition to the contribution of the higher β stability, the ternary diagrams of the Ti-Al-Co system in Figure 7.9 show that Ti_2Co will form within the crater in Co rich regions, in combination with a liquid phase that could greatly enhance the rate of C diffusion into the titanium, thus enhancing the rate of decarburisation. As the presence of Ti_2Co has not yet been proven, and if for some reason the Ti_2Co phase is not able to form, the propensity for liquid formation at the interface in Zone 2 is increased, regardless of the pressure. The formation of such a liquid has previously been hypothesised by Odelros et al., due to the extremely smooth crater floor which remains if the adhered titanium is etched away [29]. In their work, some simple DICTRA thermodynamic simulations were used to back up the hypothesis. In the present work, the calculated phase diagrams using the modified TCNI8 database provides stronger evidence for the hypothesis - that a liquid phase is contributing to the decarburisation of tool material during crater wear.

The TEM, X-EDS and EELS analysis of Zone 2.2 in Figure 7.9, shows evidence that the region is rich in both C and Ti: this coupled with the darker contrast on the STEM micrographs, indicates the presence of TiC. This is further supported by the lack of any titanium alloying elements (Al, Mo, V and Cr), within Zone 2.2. Those alloying elements which are carbide formers, and are not present, such as Mo, V and Cr, could be forming carbides elsewhere, away from the interface. The TiC and other carbides which form within Zone 2, and elsewhere, can be expected to break away at some point and move through the adhered titanium. Such carbides have been previously identified within the adhered material by Kaplan et al. (2018) and Saketi et al. (2019) [87, 88]. In this study, the TiC particulates were seen throughout the adhered material in Figure 7.4 - Figure 7.7. They are highly abrasive, and thus when coming into contact with the relatively low strength W(bcc) layer, will cause the breakaway of material into the crater. These W(bcc) particles are shown to be present within the crater, with increasing frequency, the longer the insert has been used to machine (Figure 7.4). The process of tool decarburisation at the interface, is shown to be more extreme when there are more Co rich regions: as is the case in Figure 7.7, where the imaged region of insert #3 contains many more Co rich regions compared to that of insert #4. Further to this, for insert #3, the C count decreases as the scan progresses into the tool, suggesting the possibility that decarburisation may be occurring within the subsurface of the tool, and not just at the interface. If this is true, it is likely the Co rich regions are the cause of any subsurface decarburisation that is occurring. This was proven to be the case, and is evidenced in Figure 7.10. It has been proven that there is a monolayer of Co between WC-WC grains within WC-Co tool substrates [149]. The decarburisation evidenced below the subsurface, in Figure 7.10, is possible because the Co acts as a diffusion pathway for the C, which leaves the tool via Zone 2, at prior Co rich regions. It is also possible that W(bcc) forms more readily between WC-WC grains, as the stress at the boundary causes low energy planes [150], from which it requires less energy for C to be removed. The formation of W(bcc) at WC-WC grain boundaries will reduce the integrity within the subsurface of the tool substrate, resulting in premature fracture and breakaway of tool material from the crater region.

The original hypothesis regarding the formation of TiC within the crater was that its presence would mediate the dissolution diffusion of the tool substrate and thus the wear rate [26]. Then, Hatt et al., showed that titanium alloys with higher β stability form less TiC by examining the interface between WC-Co tools and different titanium alloys using diffusion couples, hypothesising that a thinner TiC layer would result in faster diffusion and dissolution of the tool, and therefore, more rapid crater wear with increasing β stability [84]. However, as the TiC does not form a layer during the dynamic process of crater wear, and instead forms mostly at sporadic locations across the interface, their previous hypothesis that reduced TiC formation results in more crater wear is not true. It is instead more likely that the higher the β stability of an alloy, coupled with the additional β stabilisation, due to W and Co, causes faster decarburisation within prior Co rich regions, such as Zone 2.2, and that rather than TiC mediating the wear rate, it is the formation of the W(bcc), which is present along the majority of the interface that is responsible. That being said, if the rate of TiC formation with Co regions at the interface is slower for the alloys with higher β stability, then the TiC could still contribute to the wear.

A schematic view of the crater wear process is given in Figure 7.12. The schematic runs through the stages of crater wear with a renewed understanding of the process. Each stage (a – g) is marked with a time stamp that identifies a rough estimate of the time at which reaction occurs. In the first instance, Figure 7.12a shows the tool before machining has started. The WC grains, which are roughly 1 – 1.4 μm exist within a Co matrix. The SEM image in Figure 7.4a gives a real example 3D view of the tool rake face prior to any machining. When machining begins the titanium adheres to the rake face of the tool, this is represented by the dark layer above the WC-Co substrate in Figure 7.12b. This occurs almost instantaneously once machining has begun and the chip starts to flow over the rake face of the tool. The closest real representation of this stage of the process is shown in the SE micro-graphs and X-EDS data from insert #1, in Figures 7.3, 7.4 and 7.5. At this stage, thermally driven Co diffusion is rapid in β-Ti at a rate of (10^{-4} mm^2), much faster than in WC (10^{-7} mm^2) [70, 151]. Since the release of C from the WC requires a WC to W and C phase change, the binder diffuses from the substrate into the adhered titanium before any visible degradation of the WC. This has been verified through the WDS sliding window scan over the interface presented in Figure 7.5, which shows how Co is diffusing into the adhered material when the material is only recently deposited due to the fact that the microstructure of the Ti-5553 is still recognisable. Although this is the case the process of crater wear does not become continuous until the adhered titanium becomes a consistent layer on the rake face of the tool, until this time, the intermittent presence of Ti-5553 on the rake face contributes to the removal of WC from the tool via stick slip adhesion and abrasion, as is indicated by the way the microstructure is most heavily deformed at the interface in Figure 7.5. Since after 60 s in-cut the microstructure is no longer recognisable within the adhered layer, as in Figure 7.4c,d it is likely that from 60 – 900 s, adhered material is consistently present within the crater region and the process of diffusion dissolution crater wear is active. When the adhered titanium is in contact with the tool substrate for extended periods of time, the WC begins to be decarburised. Figure 7.4c,d shows this to be the case as there is clear fringes of W(bcc) forming at the interface. The WC decarburisation occurs across the whole interface but is accelerated and unrestricted at WC grain boundaries, where the Co matrix exists and no coarse layer of W(bcc) forms. For this reason the schematic in Figure 7.12c shows small fringes of W(bcc) forming within Co rich regions before and coarse WC forms elsewhere at the interface. Then, in Figure 7.12d the coarse W(bcc) fringes are shown to form, at a slower rate, on the top of WC grains at the interface. Where the newly formed W(bcc) layer exists C diffusion and therefore decarburisation of the WC is limited due to the low solubility of C in W(bcc). Where C is removed from the tool, metallic carbides form, this means that more carbides form at Co rich regions on the interface than elsewhere. Such carbides are indicated by the black circles within Figure 7.12e. The presence of such abrasive particles at the interface causes the breakaway of the now low strength W(bcc) which is forced into the adhered titanium. As more carbides form at Co rich locations (Zone 2), it is here that most of the W(bcc) is broken away. From when the titanium begins to become consistently adhered to the rake face it takes under 30 s for the crater wear degradation process to get underway. As the crater wear progresses and the Co continues to facilitate the loss of C from the substrate at and below the interface and tool material continues to be removed until underlying grains are exposed to the adhered titanium and they begin to be decarburised. This process is depicted in Figure 7.12g,f which highlights how the crater grows, this will proceed until the crater becomes a critical size at which the propensity for plastic deformation of the cutting edge increases, which in turn leads to an acceleration in flank wear and ultimately the failure of the tool.

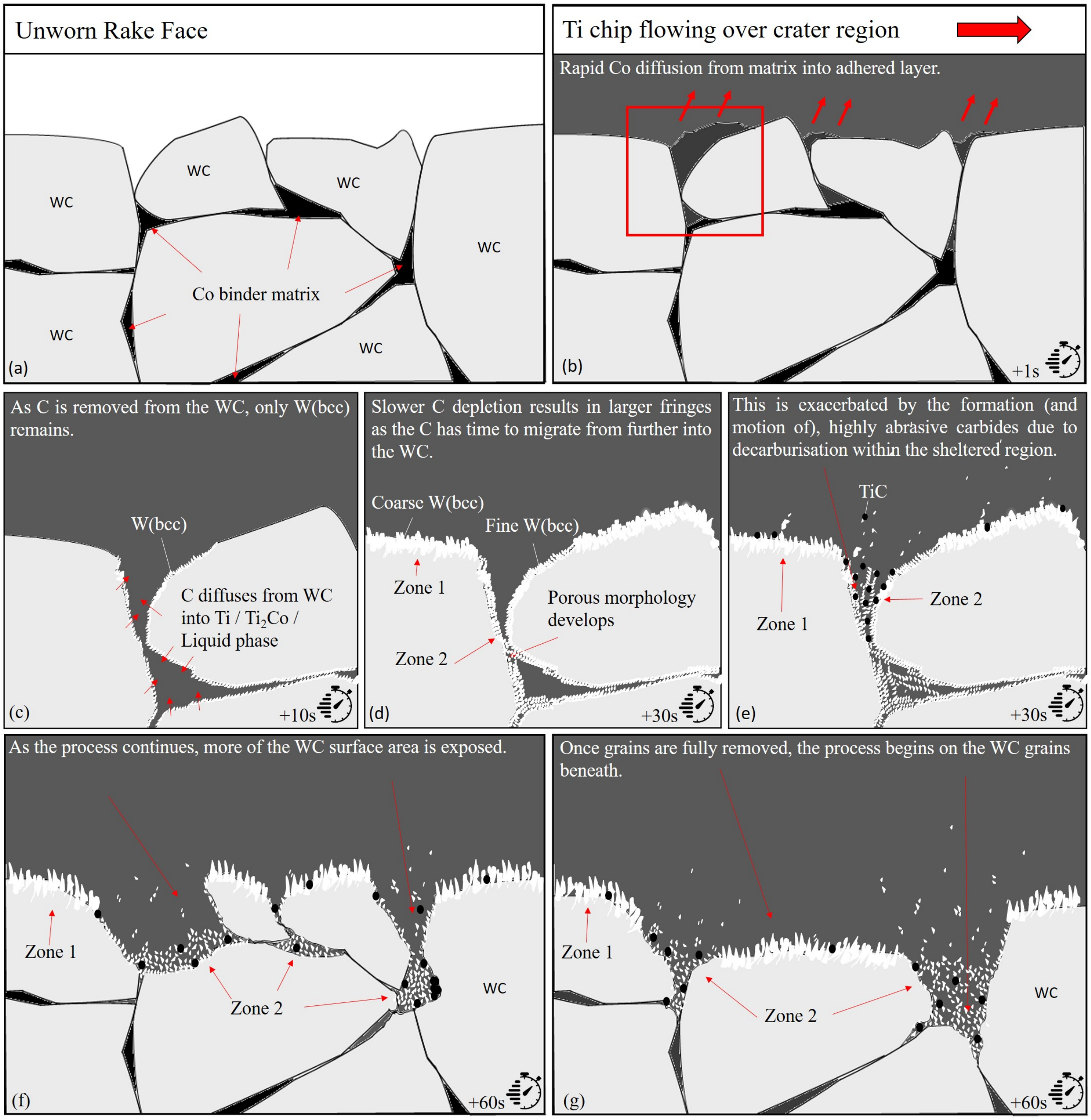

Figure 7.12: (a – g) Show graphical representations, in order, of the WC-Co and adhered titanium interface on the rake face of turning inserts used to machine a Ti-5553 workpiece during crater wear [127].

7.5 Conclusions

The work in §4, §5 and §6, which identified the adhesive tendency of Ti-5553 to stick to WC-Co tools, needed to be understood within the context of the tool-workpiece material interaction, in order to identify what effect adhered titanium has on the tool substrate and tool integrity. This, coupled with the finding by Hatt et al. (2018), that β stability increases the propensity for crater wear, made the investigation of crater wear in the Ti-5553 an essential avenue of research [84]. Therefore, within this chapter, the mechanism by which Ti-5553 interacts with WC-Co to cause crater wear, the critical wear mode of WC-Co tools was investigated. SEM, TEM, WDS, X-EDS and EELS high resolution techniques were utilised to analyse the crater interface on tools used for turning Ti-5553. The following results and conclusions were made and published in the international Journal – Wear [127]:

- Two key zones of tool degradation have been demonstrated at the interface. Zone one consists of large fringes of W(bcc) between WC grains and the adhered Ti-5553.
- The visual evidence and elemental analysis suggest decarburisation and degradation of the tool material is significantly faster within previous binder regions. Thus, such regions are critical to the crater wear rate.
- Thermodynamic modelling suggests the formation of Ti_2Co and liquid phase (for 10^6 Pa and 10^9 Pa); however, the Ti_2Co phase was not observed experimentally. The metastable calculation, excluding the Ti_2Co phase, gives the formation of a liquid phase at even lower temperatures. If a liquid is present, this will cause accelerated decarburisation of the WC.
- The accelerated decarburisation in binder pockets enables the formation of TiC, in contrast to the regions where W(bcc) acts as a diffusion barrier to carbon diffusion. A lack of alloying elements, such as V, which are thought to have formed into free abrasive metallic carbides, e.g. Ti(V,C) are thought to contribute to the crater progression across the whole interface.
- When the chip is sliding over the interface, the wear was observed to be significantly more abrasive than when the crater was fully formed.
- Small particle debris from the W(bcc) are identified in the adhered layer, and volume fraction increased with time in cut.

Through this chapter, and the paper published in Wear [127], understanding of the wear and degradation mechanism for uncoated cemented carbide inserts for turning Ti-5553, a metastable β titanium alloy, has been improved. This was achieved by combining experimental work with thermodynamic modelling of the Ti-Al-Co system. The understanding that this work provides will enable the development of tools and alloys which will improve machinability and productivity in industry.

Chapter 8

Conclusions and Future Work

8.1 Conclusions

This thesis and body of work has been produced and carried out to further understand the machinability of metastable β titanium alloys, with a specific focus on Ti-5553. The key findings and conclusions made in this EngD project and the corresponding implications for the aerospace and machining industries are given in this section.

The VFM method was developed because typical methods utilised within industry, such as the V15 method, do not provide opportunity for detailed characterisation and analysis of machinability. The VFM method enabled the drilling machiability of Ti-5553, Ti-6246 and Ti-64 to be investigated and characterised thoroughly. The investigation carried out using the VFM methodology led to the conclusion that for PVD-TiAlN coated tools, both adhesive and abrasive wear mechanisms occured, resulting in higher torque for coated tools verses uncoated tools, where the wear mechanism was mostly abrasive. This finding will help guide grade engineers and tool designers to improve the coating resistance to said wear mechanisms thus improving tool life and machinability. The VFM method also showed how microstrucutral subsurface deformation of the machined surface in Ti-64, Ti-6246 and Ti-5553 was significantly different depending on the alloy which was being drilled, whether or not the tool was coated and what machining parameters were used. Even for similar forces, the damage depth for Ti-5553 was significantly smaller than for Ti-6246, which in turn was significantly smaller than for Ti-64. This knowledge and the characterisation of the subsurface damage done for each alloy can help guide how machine parameters should be selected for drilling to minimise subsurface damage whilst optimising for productivity within industry. Aspects of the VFM methodology, such as the efficient creation of force and torque response surfaces and the ability to analyse microstrucutral damage formed at different cutting parameters can now be utilised by machinists and tool developers alike to improve efficiency when machining and during the development of new tools. Further investigations done by drilling Ti-5553, utilising a variation of the original VFM method, yielded several more important conclusions. The fact that torque can be used to identify when a tool has a catastrophic wear event could enable tool wear to be accurately monitored during drilling. In turn, this will enable tools to be pushed further, increasing average tool life and improving productivity. The important finding, that an optimal amount of BUE can act to stabilise the drilling operation could help change the way that tool designers think about their design. Often tool developers will try to minimise BUE, but with this knowledge they may be able to work towards a stable BUE and thus achieve a more stable process. The significant amount of adhered material found on the machined surface after holes were drilled highlights that it is important to ensure holes drilled in Ti-5553 are quality inspected or finish machined via reaming or a similar post process. This is especially important for the aerospace industry where the welding of fracture sites to the machined surface could be catastrophic for safety critical components.

Prominent conclusions resulted from the investigation of crater wear on WC-CO tools used to machine Ti-5553. The finding that accelerated decarburisation occurs in binder pockets and that within such regions the tool degradation is significantly faster, will be essential for tool grade developers looking to improve the effectiveness of tools used to machine titanium alloys. The same is true of the conclusion that subsurface decarburisation occurs 2 μm into the substrate, within the crater region; tool grade developers will now need to take this into consideration when trying to imporove the integrity of their tools. The fact that TiC forms desperately within the crater, and not as defined layer, suggests it does not mediate the crater wear rate as previously hypothesised. Instead, the decarburisation of the WC and formation and pressence of a W(bcc) layer, coupled with the number and size of exposed binder pocket regions within the substrate exposed to adhered material controls the rate of crater wear. With the improved knowledge of the mechanism by which crater wear manifests in WC-Co tools used to machine titanium, new tools can be developed which have to tailored substrates and/or coatings that can reduce the accelerated decarburisation of the WC and hence slow the rate of crater wear.

If acted upon, the conclusions made in this thesis, can be used to significantly improve the machinability of metastable β titanium alloys by improving the way they are machined, the way machine tools are developed and the way and direction that future research into their machinability is conducted. Improving the machiability of metastable β titanium alloys will reduce the cost required to utilise such materials within the aerospace industry, increasing their uptake within the industry, contributing to lighter, more fuel efficient and long lasting aircraft.

8.2 Future Work

The work in this thesis has opened several avenues of research. If work is continued within these areas it will enable improvement of titanium alloy machinability, especially those with high β stability like Ti-5553. This section details what research should be considered as future work.

- Drill tools used to machine Ti-5553, and which have accrued substantial wear, such as those in §6 should be sectioned following a similar methodology to that used in §7. High resolution techniques like SEM, TEM, EDS and EELS could then be used to understand exactly how the interaction between WC-Co and adhered titanium manifests in drilling, where crater wear is either harder to recognise, or not as prevalent as in the turning operation. During the investigation, the drill tool may have to be sectioned in several areas to determine the contribution of chemical wear at different places on the cutting edge. It is suggested that finite element modeling using the methodology outlined in [152], could be used to investigate the conditions at different locations along the cutting edge to aid in selection for sectioning of the drill. Due to the complex geometry of the cutting edge, it is suggested that the top of the drill, i.e. the chisel and outer coroners should be sectioned from the shaft first. Then, this could be mounted in Bakelite or epoxy, clamped at the desired angle and sectioned to provide a cross section of the cutting edge, similar to that demonstrated for turning inserts in §7.
- The VFM methodology should be used to assess the subsurface damage of more titanium alloys with different β stability and processing conditions. Then, a database that includes the expected subsurface deformation for drilling different alloys could be developed. As is suggested at the end of §5, a reduced array of holes (with repeats) should be drilled, similar to those used within §6. Once completed, the parameters for which the investigator wishes to assess the machined surface can be selected, drilled and investigated. This would aid validation of the results in §5, whilst simultaneously providing tool and material manufacturers invaluable knowledge about the drilling machinability of titanium from the perspective of microstructural deformation and surface integrity.
- The observation in §7 that decarburisation occurs within the subsurface of WC-Co tool substrates should be further explored. The fact that W(bcc) forms up to 2 μm below the subsurface, could have catastrophic implications for the integrity of the tool and may significantly contribute to the rate of failure of tools once the crater becomes substantial. A combination of diffusion simulation and TEM could be used to identify the mechanism by which C is lost from the subsurface. This would provide invaluable information for tool designers, making it easier for them to implement design changes to mitigate crater wear.

- The difference between diffusion couple results within literature needs to be reconciled with the results obtained when examining the crater on worn tools. As has been shown in the research paper presented in §7 [127], and within other research [29, 148, 91], the interface that forms during crater wear has some distinctly different characteristics to those exhibited at the interface of WC-Co and titanium diffusion couples, despite being at similar temperatures [28, 84, 85]. Some of the main differences include; the TiC layer which exists in diffusion couples but not craters (where TiC is only seen sporadically in the adhered material), the formation of M_6C and $M_{12}C$ eta phases, which are evidenced in diffusion couples but not in craters, a consistent interface in diffusion couples as opposed to an interface containing zones of rapid decarburisation in the crater and subsurface decarburisation in the crater but not in diffusion couples. Therefore, it is suggested that future work focuses on understanding how the chemical reaction between the tool substrate and titanium differs during machining. In addition to reconciling the difference between the static diffusion couple and the dynamic crater interface, simulation of the system could help prove if the hypothesis that a liquid forms and facilitates decarburisation is true if the interfacial phases present at the crater interface within the simulation match those presented in §7.

- To further investigate the idea that force and torque data can be used to monitor when the cutting edge undergoes a change in geometry due to wear like BUE, a similar setup as used in §6.2.1 should be employed. A script could be constructed in MATLAB (or other programming software) to measure the variation in average torque for each hole drilled, live, as machining is taking place. In the event of a sudden spike in torque variation, such as those reported in §6.2.1, the drill tool should be removed from the machining center and checked for any obvious signs of wear. Then, using this technique, the exact time, and thus sample number within the force dataset could be identified. If recognisable features are shown at the time the wear manifests, it would become possible to know what type of wear has occurred on the cutting edge without removing the tool. This investigation could also provide a good test dataset for machine learning algorithms, which if trained correctly, could become efficient at in process monitoring of wear in drill tools.

- Currently it requires a substantial amount of holes to calculate the cutting force coefficients [110]. However, the substantial force and torque dataset obtained in §5 and §6 offers a great opportunity to develop a method for calculating cutting force coefficient's for different materials by measuring the instantaneous force resultant as the drill comes into contact with the workpiece, using and improving the method established by Hamade et al., [153]. Identifying cutting force coefficients would provide a substantial improvement to the VFM method enabling better machinability comparison between alloys in a context which could be applied to other machining processes.

Bibliography

[1] S. Weston, “Personal Communication - Sandvik Coromant sales are in excess of £80 million annually for the titanium machining industry,” 2020.

[2] T. Captain, “Aerospace & defense sector need for innovation,” in *the 34Th Annual International Conference and Exhibition on Titanium in the USA*, 2018, pp. 1–40. [Online]. Available: https://titanium.org/page/TiUSA18Proceedings

[3] Corrective and Preventive Actions (CAPA), “Aircraft leasing accounts for half of world’s commercial aircraft fleet.” [Online]. Available: https://centreforaviation.com/analysis/reports/aircraft-leasing-accounts-for-half-of-worlds-commercial-aircraft-fleet-lessors-shun-widebodies-404111

[4] F. H. Froes, “Titanium - physical metallurgy, processing, and applications,” *ASM International*, pp. 75–94, 2015.

[5] I. Inagaki, T. Takechi, Y. Shirai, and N. Ariyasu, “Application and features of titanium for the aerospace industry,” *Nippon Steel and Sumitomo Metal Technical*, vol. 106, no. 106, pp. 22–27, 2014.

[6] E. K. Molchanova, *Phase diagrams of titanium alloys.* Israel Program for Scientific Translations, 1965.

[7] H. Margolin and P. Farrar, “The physical metallurgy of titanium alloys,” *Ocean Engineering*, vol. 1, no. 3, pp. 329–345, 1969.

[8] J. D. Cotton, R. D. Briggs, R. R. Boyer, S. Tamirisakandala, P. Russo, N. Shchetnikov, and J. C. Fanning, “State of the art in beta titanium alloys for airframe applications,” *Jom*, vol. 67, no. 6, pp. 1281–1303, 2015.

[9] “Web of Science [v.5.35] - All database basic search for beta titanium.” [Online]. Available: www.webofknowledge.com

[10] G. Lütjering and J. C. Williams, *Titanium.* Springer Science & Business Media, 2007.

[11] A. K. Nandy, M. C. Gowrishankar, and S. Paul, "Some studies on high-pressure cooling in turning of Ti-6Al-4V," *International Journal of Machine Tools and Manufacture*, vol. 49, no. 2, pp. 182–198, 2009.

[12] C. J. Pretorius, S. L. Soo, D. K. Aspinwall, P. M. Harden, R. M'Saoubi, and A. L. Mantle, "Tool wear behaviour and workpiece surface integrity when turning Ti-6Al-2Sn-4Zr-6Mo with polycrystalline diamond tooling," *CIRP Annals*, vol. 64, no. 1, pp. 109–112, 2015. [Online]. Available: http://dx.doi.org/10.1016/j.cirp.2015.04.058

[13] C. R. Dandekar, Y. C. Shin, and J. Barnes, "Machinability improvement of titanium alloy (Ti-6Al-4V) via LAM and hybrid machining," *International Journal of Machine Tools and Manufacture*, vol. 50, no. 2, pp. 174–182, 2010. [Online]. Available: http://dx.doi.org/10.1016/j.ijmachtools.2009.10.013

[14] M. Dhananchezian and M. Pradeep Kumar, "Cryogenic turning of the Ti-6Al-4V alloy with modified cutting tool inserts," *Cryogenics*, vol. 51, no. 1, pp. 34–40, 2011. [Online]. Available: http://dx.doi.org/10.1016/j.cryogenics.2010.10.011

[15] G. Rotella, O. W. Dillon, D. Umbrello, L. Settineri, and I. S. Jawahir, "The effects of cooling conditions on surface integrity in machining of Ti6Al4V alloy," *International Journal of Advanced Manufacturing Technology*, vol. 71, no. 1-4, pp. 47–55, 2014.

[16] G. Le Coz, M. Marinescu, A. Devillez, D. Dudzinski, and L. Velnom, "Measuring temperature of rotating cutting tools: Application to MQL drilling and dry milling of aerospace alloys," *Applied Thermal Engineering*, vol. 36, no. 1, pp. 434–441, 2012. [Online]. Available: http://dx.doi.org/10.1016/j.applthermaleng.2011.10.060

[17] H. Yang, W. Ding, Y. Chen, S. Laporte, J. Xu, and Y. Fu, "Drilling force model for forced low frequency vibration assisted drilling of Ti-6Al-4V titanium alloy," *International Journal of Machine Tools and Manufacture*, vol. 146, no. April, p. 103438, 2019. [Online]. Available: https://doi.org/10.1016/j.ijmachtools.2019.103438

[18] F. Nabhani, "Wear mechanisms of ultra-hard cutting tools materials," *Journal of Materials Processing Technology*, vol. 115, no. 3, pp. 402–412, 2001.

[19] R. M'Saoubi, D. Axinte, S. L. Soo, C. Nobel, H. Attia, G. Kappmeyer, S. Engin, and W. M. Sim, "High performance cutting of advanced aerospace alloys and composite materials," *CIRP Annals - Manufacturing Technology*, vol. 64, no. 2, pp. 557–580, 2015. [Online]. Available: http://dx.doi.org/10.1016/j.cirp.2015.05.002

[20] Kennametal, "High-temperature alloy turning guide." [Online]. Available: https://www.kennametal.com/in/en/products/metalworking-tools/turning.html

[21] C. H. Che-Haron and A. Jawaid, "The effect of machining on surface integrity of titanium alloy Ti-6Al-4V." *Journal of Materials Processing Technology*, vol. 166, no. 2, pp. 188–192, 2005.

[22] C. Bandapalli, B. M. Sutaria, D. V. Prasad Bhatt, and K. K. Singh, “Tool wear analysis of micro end mills - uncoated and PVD coated TiAlN & AlTiN in high speed micro milling of titanium alloy - Ti-0.3Mo-0.8Ni,” *Procedia CIRP*, vol. 77, no. Hpc, pp. 626–629, 2018. [Online]. Available: https://doi.org/10.1016/j.procir.2018.08.191

[23] M. S. Uddin, B. Pham, A. Sarhan, A. Basak, and A. Pramanik, “Comparative study between wear of uncoated and TiAlN-coated carbide tools in milling of Ti6Al4V,” *Advances in Manufacturing*, vol. 5, no. 1, pp. 83–91, 2017.

[24] B. Waldenström, O. Ake, and A. Ove, “Cemented carbide insert for turning, milling and drilling. United States Patent, No. 6.211.479 B1,” Apr 24 2001.

[25] E. Ezugwu and Z. Wang, “Titanium alloys and their machinability,” *Journal of Materials Processing Technology*, vol. 68, no. 3, pp. 262–274, 1997. [Online]. Available: http://www.sciencedirect.com/science/article/pii/S0924013696000301

[26] P. D. Hartung, B. M. Kramer, and B. F. von Turkovich, “Tool wear in titanium machining,” *CIRP Annals - Manufacturing Technology*, vol. 31, no. 1, pp. 75–80, 1982.

[27] N. Corduan, T. Himbert, G. Poulachon, M. Dessoly, M. Lambertin, J. Vigneau, and B. Payoux, “Wear mechanisms of new tool materials for Ti-6Al-4V high performance machining,” *CIRP Annals - Manufacturing Technology*, vol. 52, no. 1, pp. 73–76, 2003.

[28] O. Hatt, P. Crawforth, and M. Jackson, “On the mechanism of tool crater wear during titanium alloy machining,” *Wear*, vol. 374-375, pp. 15–20, 2017. [Online]. Available: http://dx.doi.org/10.1016/j.wear.2016.12.036

[29] S. Odelros, B. Kaplan, M. Kritikos, M. Johansson, and S. Norgren, “Experimental and theoretical study of the microscopic crater wear mechanism in titanium machining,” *Wear*, vol. 376-377, pp. 115–124, 2017.

[30] N. Vicente, A. Fedrizzi, N. Bazzanella, F. Casari, F. Buccioti, and A. Molinari, “Microstructure of interface of SPS co-sintered and sinter bonded CP2-Ti and Co-28Cr-6Mo,” *Powder Metallurgy*, vol. 56, no. 2, pp. 143–148, 2013.

[31] M. Jackson and R. R. Boyer, “Titanium and its alloys: processing, fabrication and mechanical performance,” *Encyclopedia of Aerospace Engineering*, 2010.

[32] M. Hunter, “Metallic titanium.” *Journal of the American Chemical Society*, vol. 32, no. 3, pp. 330–336, 1910.

[33] W. Kroll, “The production of ductile titanium,” *Transactions of the Electrochemical Society*, vol. 78, no. 1, p. 35, 1940.

[34] D. N. Williams, R. A. Wood, R. I. Jaffee, and H. R. Ogden, “The effects of zirconium in titanium-base alloys,” *Journal of The Less-Common Metals*, vol. 6, no. 3, pp. 219–225, 1964.

[35] M. Rajadurai and A. R. Annamalai, "Effect of Sn addition on the microstructural characteristics and mechanical properties of the titanium alloy (Ti6Al4V)," *Kovove Materialy*, vol. 56, no. 3, pp. 191–198, 2018.

[36] R. R. Boyer, "An overview on the use of titanium in the aerospace industry," *Materials Science and Engineering A*, vol. 213, no. 1-2, pp. 103–114, Aug 1996.

[37] R. R. Boyer and R. D. Briggs, "The use of β titanium alloys in the aerospace industry," *Journal of Materials Engineering and Performance*, vol. 22, no. 10, pp. 2916–2920, 2013.

[38] J. I. Qazi, B. Marquardt, and H. J. Rack, "High-strength metastable beta-titanium alloys for biomedical applications," *Jom*, vol. 56, no. 11, pp. 49–51, 2004.

[39] E. Trent and P. Wright, *Metal Cutting*, 4th ed., 1987, vol. 7, no. 9.

[40] A. Machado and J. Wallbank, "Machining of titanium and its alloys: a review," *Journal of Materials Processing Technology*, vol. 173, no. 2, pp. 125–135, 2006.

[41] I. Jawahir, E. Brinksmeier, R. M'Saoubi, D. Aspinwall, J. Outeiro, D. Meyer, D. Umbrello, and A. Jayal, "Surface integrity in material removal processes: Recent advances," *CIRP annals - Manufacturing Technology*, vol. 60, no. 2, pp. 603–626, 2011.

[42] M. E. Merchant, "Mechanics of the metal cutting process. II. Plasticity conditions in orthogonal cutting," *Journal of applied physics*, vol. 16, no. 6, pp. 318–324, 1945.

[43] A. K. Pal and F. Koenigsberger, "Some aspects of the oblique cutting process," *International Journal of Machine Tool Design and Research*, vol. 8, no. 1, pp. 45–57, 1968.

[44] J. A. Arsecularatne, P. Mathew, and P. L. Oxley, "Prediction of chip flow direction and cutting forces in oblique machining with nose radius tools," *Proceedings of the Institution of Mechanical Engineers, Part B: Journal of Engineering Manufacture*, vol. 209, no. 4, pp. 305–315, 1995.

[45] T. Ghosh, S. Paul, and S. Paul, "Modeling and experimental verification of chip flow deviation in oblique cutting," *Machining Science and Technology*, vol. 22, no. 1, pp. 99–119, 2018. [Online]. Available: https://doi.org/10.1080/10910344.2017.1336630

[46] A. J. Gwinnett and L. Gorelick, "A brief history of drills and drilling," *BEADS: Journal of the Society of Bead Researchers*, vol. 10-11, no. 1998, pp. 49–56, 1999.

[47] H. Kulke and D. Rothermund, *A History Of India: Fourth Edition*, 1998.

[48] "Britannica, T. Editors of Encyclopedia. Drilling machinery. Encyclopedia Britannica." Dec 2010. [Online]. Available: https://www.britannica.com/technology/drilling-machinery

[49] "RS Components, Everything you need to know about twist drill bits," Dec 2020. [Online]. Available: https://uk.rs-online.com/web/generalDisplay.html?id=ideas-and-advice/twist-drill-bits-guide

[50] "Sandvik Coromant, Solutions for cost effective and high-quality machining of aerospace landing gear beam." [Online]. Available: https://www.sandvik.coromant.com/en-gb/industrysolutions/aerospace/titanium/pages/landing-gear-beam.aspx

[51] Z. Liu, Y. Liu, X. Han, and W. Zheng, "Study on super-long deep-hole drilling of titanium alloy," *Journal of Applied Biomaterials and Functional Materials*, vol. 16, no. 1_suppl, pp. 150–156, 2018.

[52] "3D Solid Modelling Videos: iTwist Drill (Autodesk Inventor 2013)." [Online]. Available: https://nisheeth-inventortalks.blogspot.com/2014/06/itwist-drill-autodesk-inventor-2013.html

[53] P. F. Zhang, N. J. Churi, Z. J. Pei, and C. Treadwell, "Mechanical drilling processes for titanium alloys: a literature review," *Machining Science and Technology*, vol. 12, no. 4, pp. 417–444, 2008.

[54] S. Sharif, E. A. Rahim, and H. Sasahara, "Machinability of titanium alloys in drilling," *Titanium Alloys - Towards Achieving Enhanced Properties for Diversified Applications*, vol. 3, pp. 117–137, 2012.

[55] T. Childs, K. Maekawa, T. Obikawa, and Y. Yamane, *Metal machining: theory and applications.* Butterworth-Heinemann, 2000.

[56] P. Naisson, J. Rech, and H. Paris, "Analytical modeling of thrust force and torque in drilling," *Proceedings of the Institution of Mechanical Engineers, Part B: Journal of Engineering Manufacture*, vol. 227, no. 10, pp. 1430–1441, 2013.

[57] G. R. Irwin, "Studies in large plastic flow and fracture: With special emphasis on the effects of hydrostatic pressure." *Science*, vol. 115, no. 2990, pp. 424–424, 1952.

[58] C. Claudin, A. Mondelin, J. Rech, and G. Fromentin, "Effects of a straight oil on friction at the toolworkmaterial interface in machining," *International Journal of Machine Tools and Manufacture*, vol. 50, no. 8, pp. 681–688, 2010. [Online]. Available: http://dx.doi.org/10.1016/j.ijmachtools.2010.04.013

[59] F. Zemzemi, J. Rech, W. Ben Salem, A. Dogui, and P. Kapsa, "Identification of a friction model at tool/chip/workpiece interfaces in dry machining of AISI4142 treated steels," *Journal of Materials Processing Technology*, vol. 209, no. 8, pp. 3978–3990, 2009.

[60] A. Moufki, A. Devillez, D. Dudzinski, and A. Molinari, "Thermomechanical modelling of oblique cutting and experimental validation," *International Journal of Machine Tools and Manufacture*, vol. 44, no. 9, pp. 971–989, 2004.

[61] "Sandvik Coromant, Wear Guide: Educational material from performance testing in Västberga," p. 30, 2018.

[62] J. Taylor, "The tool wear-time relationship in metal cutting," *International Journal of Machine Tool Design and Research*, vol. 2, no. 2, pp. 119–152, 1962.

[63] S. Berezvai, T. G. Molnar, D. Bachrathy, and G. Stepan, "Experimental investigation of the shear angle variation during orthogonal cutting," *Materials Today: Proceedings*, vol. 5, no. 13, pp. 26 495–26 500, 2018.

[64] Z. Hao, D. Gao, Y. Fan, and R. Han, "New observations on tool wear mechanism in dry machining Inconel718," *International Journal of Machine Tools and Manufacture*, vol. 51, no. 12, pp. 973–979, 2011. [Online]. Available: http://dx.doi.org/10.1016/j.ijmachtools.2011.08.018

[65] S. C. Cohen and D. Tabor, "The friction and lubrication of polymers," *Proceedings of the Royal Society of London. Series A, Mathematical and Physical Sciences*, vol. 291, no. 1425, pp. 186–207, aug 1966. [Online]. Available: http://www.jstor.org/stable/2415495

[66] T. A. Stolarski, *Tribology in machine design.* Industrial Press Inc., 1990.

[67] P. A. Dearnley and A. N. Grearson, "Evaluation of principal wear mechanisms of cemented carbides and ceramics used for machining titanium alloy IMI 318," *Materials Science and Technology (United Kingdom)*, vol. 2, no. 1, pp. 47–58, 1986.

[68] K. Bouzakis, G. Skordaris, S. Gerardis, G. Katirtzoglou, S. Makrimallakis, and M. Pappa, "Surface & coatings technology ambient and elevated temperature properties of TiN, TiAlN and TiSiN PVD films and their impact on the cutting performance of coated carbide tools," *Surface & Coatings Technology*, vol. 204, no. 6-7, pp. 1061–1065, 2009. [Online]. Available: http://dx.doi.org/10.1016/j.surfcoat.2009.07.001

[69] K. Bouzakis, N. Michailidis, G. Skordaris, E. Bouzakis, D. Biermann, and R. M. Saoubi, "Cutting with coated tools: coating technologies, characterization methods and performance optimization," *CIRP Annals - Manufacturing Technology*, vol. 61, no. 2, pp. 703–723, 2012. [Online]. Available: http://dx.doi.org/10.1016/j.cirp.2012.05.006

[70] J. Hua and R. Shivpuri, "A cobalt diffusion based model for predicting crater wear of carbide tools in machining titanium alloys," *Journal of Engineering Materials and Technology, Transactions of the ASME*, vol. 127, no. 1, pp. 136–144, 2005.

[71] A. Ugarte, R. M'Saoubi, A. Garay, and P. J. Arrazola, "Machining behaviour of Ti-6Al-4V and Ti-5553 alloys in interrupted cutting with PVD coated cemented carbide," *Procedia CIRP*, vol. 1, no. 1, pp. 202–207, 2012. [Online]. Available: http://dx.doi.org/10.1016/j.procir.2012.04.035

[72] P. J. Arrazola, A. Garay, L. M. Iriarte, M. Armendia, S. Marya, and F. Le Maître, "Machinability of titanium alloys (Ti6Al4V and Ti555.3)," *Journal of Materials Processing Technology*, vol. 209, no. 5, pp. 2223–2230, 2009.

[73] A. Cox, S. Herbert, J. P. Villain-Chastre, S. Turner, and M. Jackson, "The effect of machining and induced surface deformation on the fatigue performance of a high strength metastable β titanium alloy," *International Journal of Fatigue*, vol. 124, pp. 26–33, 2019.

[74] C. Leyens and M. Peters, *Titanium and titanium alloys: fundamentals and applications.* Wiley Online Library, 2006.

[75] T. K. Assadi, H. M. Flower, and D. R. West, "Creep resistance of certain alloys of the Ti–AI–Zr–Mo–Si system," *Metals Technology*, vol. 6, no. 1, pp. 16–23, 1979.

[76] T. K. Heckel, A. G. Tovar, and H. J. Christ, "Fatigue of the near-alpha Ti-alloy Ti6242," *Experimental Mechanics*, vol. 50, no. 4, pp. 483–489, 2010.

[77] H. Nakajima and M. Koiwa, "Diffision in titanium," *ISIJ International*, vol. 31, no. 8, pp. 757–766, 1991.

[78] F. Frank and D. Turnbull, "Mechanism of diffusion of copper in germanium," *Physical Review*, vol. 104, no. 3, p. 617, 1956.

[79] T. Kitagawa, A. Kubo, and K. Maekawa, "Temperature and wear of cutting tools in high-speed machining of Inconel 718 and Ti-6Al-6V-2Sn," *Wear*, vol. 202, no. 2, pp. 142–148, 1997.

[80] S. Odelros, "Tool wear in titanium machining." Master's thesis, UPTEC K , Uppsala University, ISSN 1650-8297; 12 006, p. 63, 2012.

[81] S. Sun, M. Brandt, and J. P. Mo, "Evolution of tool wear and its effect on cutting forces during dry machining of Ti-6Al-4V alloy," *Proceedings of the Institution of Mechanical Engineers, Part B: Journal of Engineering Manufacture*, vol. 228, no. 2, pp. 191–202, 2014.

[82] O. Hatt, "On the mechanism of tool crater wear during titanium alloy machining," Ph.D. dissertation, MSE, University of Sheffield, 2017.

[83] O. Hatt, H. Larsson, F. Giuliani, P. Crawforth, B. Wynne, and M. Jackson, "Predicting chemical wear in machining titanium alloys via a novel low cost diffusion couple method," *Procedia CIRP*, vol. 45, pp. 219–222, 2016. [Online]. Available: http://dx.doi.org/10.1016/j.procir.2016.01.196

[84] O. Hatt, Z. Lomas, M. Thomas, and M. Jackson, "The effect of titanium alloy chemistry on machining induced tool crater wear characteristics," *Wear*, vol. 408-409, no. February, pp. 200–207, 2018. [Online]. Available: https://doi.org/10.1016/j.wear.2018.05.020

[85] C. Ramirez, A. Idhil Ismail, C. Gendarme, M. Dehmas, E. Aeby-Gautier, G. Poulachon, and F. Rossi, "Understanding the diffusion wear mechanisms of WC-10%Co carbide tools during dry machining of titanium alloys," *Wear*, vol. 390-391, no. February, pp. 61–70, 2017. [Online]. Available: http://dx.doi.org/10.1016/j.wear.2017.07.003

[86] E. Edin, A. Blomqvist, M. Lattemann, W. Luo, and R. Ahuja, "MD study of C diffusion in WC/W interfaces observed in cemented carbides," *International Journal of Refractory Metals and Hard Materials*, vol. 85, no. July, p. 105054, 2019. [Online]. Available: https://doi.org/10.1016/j.ijrmhm.2019.105054

[87] B. Kaplan, S. Odelros, M. Kritikos, R. Bejjani, and S. Norgren, "Study of tool wear and chemical interaction during machining of Ti6Al4V," *International Journal of Refractory Metals and Hard Materials*, vol. 72, no. December 2017, pp. 253–256, 2018. [Online]. Available: https://doi.org/10.1016/j.ijrmhm.2017.12.012

[88] S. Saketi, S. Odelros, J. Östby, and M. Olsson, "Experimental study of wear mechanisms of cemented carbide in the turning of Ti6Al4V," *Materials*, vol. 12, no. 7, 2019.

[89] A. Molinari and M. Nouari, "Modeling of tool wear by diffusion in metal cutting," *Wear*, vol. 252, no. 1-2, pp. 135–149, 2002.

[90] M. I. Sadik, M. Lattemann, and J. García, "Specific carbide substrate design to enhance tool performance in machining of Ti5553," *Procedia CIRP*, vol. 77, pp. 598–601, 2018. [Online]. Available: https://doi.org/10.1016/j.procir.2018.08.203

[91] M. Lattemann, E. Coronel, J. Garcia, and I. Sadik, "Interaction between cemented carbide and Ti6Al4V alloy in cryogenic machining," *19. Plansee Seminar 2017*, no. August 2018, pp. 1–13, 2017.

[92] H. G. Prengel, A. T. Santhanam, R. M. Penich, P. C. Jindal, and K. H. Wendt, "Advanced PVD-TiAlN coatings on carbide and cermet cutting tools," *Surface and Coatings Technology*, vol. 94-95, pp. 597–602, 1997.

[93] A. Choudhary and S. Paul, "Performance evaluation of PVD-TiAlN coated carbide tools vis-à-vis uncoated carbide tool in turning of titanium alloy (Ti-6Al-4V) by

simultaneous minimization of cutting energy, dimensional deviation and tool wear," *Machining Science and Technology*, vol. 23, no. 3, pp. 368–384, 2019. [Online]. Available: https://doi.org/10.1080/10910344.2018.1486421

[94] S. Sharif and E. A. Rahim, "Performance of coated and uncoated carbide tools when drilling titanium alloy Ti-6Al4V," *Journal of Materials Processing Technology*, vol. 185, pp. 72–76, 2007.

[95] "Tool life testing with single-point turning tools," *ISO 3685 Second Edition 1993-11-15*, vol. 1993, pp. 1–48, 1993.

[96] R. Komanduri and Z. B. Hou, "On thermoplastic shear instability in the machining of a titanium alloy (Ti-6Al-4V)," *Metallurgical and Materials Transactions A: Physical Metallurgy and Materials Science*, vol. 33, no. 9, pp. 2995–3010, 2002.

[97] C. Dredge, R. M'Saoubi, B. Thomas, O. Hatt, M. Thomas, and M. Jackson, "A low-cost machinability approach to accelerate titanium alloy development," *Proceedings of the Institution of Mechanical Engineers, Part B: Journal of Engineering Manufacture*, vol. 235, no. 10, pp. 1618–1632, 2020.

[98] N. Cook, "Chip formation in machining titanium," in *Proceedings of the Symposium on Machine Grind. Titanium, Watertown Arsenal, MA*, 1953, pp. 1–7.

[99] M. Shaw, S. Dirke, P. Smith, N. Cook, E. Loewen, and C. Yang, "Machining titanium," Massachusetts Inst. of Tech., Cambridge. Dept. of Michanical Engineering, Tech. Rep., 1954.

[100] R. Li, P. Hegde, and A. J. Shih, "High-throughput drilling of titanium alloys," *International Journal of Machine Tools and Manufacture*, vol. 47, no. 1, pp. 63–74, 2007.

[101] S. Motonishi, Y. Hara, S. Isoda, H. Itoh, and Y. Tsumori, "Study on machining of titanium and its alloys," *Kobelco technology review*, no. 2, pp. 28–31, 1987.

[102] O. Dillon, R. De Angelis, W. Lu, J. Gunasekera, and J. Deno, "The effects of temperature on the machining of metals," *Journal of Materials Shaping Technology*, vol. 8, no. 1, pp. 23–29, 1990.

[103] S. N. B. Oliaei and Y. Karpat, "Investigating the influence of built-up edge on forces and surface roughness in micro scale orthogonal machining of titanium alloy Ti6Al4V," *Journal of Materials Processing Technology*, vol. 235, 2016.

[104] E. Rahim and H. Sasahara, "A study of the effect of palm oil as mql lubricant on high speed drilling of titanium alloys," *Tribology International*, vol. 44, no. 3, pp. 309–317, 2011.

[105] W. Konig and K. Schroder, "Face milling and drilling of titanium alloys," in *Proc. Conf. Influence of Metallurgy on Machinability, ASM Tech. Ser. 7*, vol. 308, 1975.

[106] J. Kosaka, Y. Fanning and S. Fox, “Development of low cost high strength alpha/beta alloy with superior machinability,” in *Proceedings of the 10th World Conference on Titanium*, 2004, pp. 3028–3034.

[107] Y. Kosaka and S. P. Fox, “Influences of alloy chemistry and microstructure on the machinability of titanium alloys.” in *Cost Affordable Titanium, TMS Conference*, 2004, pp. 169–176.

[108] P. Crawforth, “Towards a micromechanistic understanding of imparted subsurface deformation during machining of titanium alloys,” Ph.D. dissertation, MSE, University of Sheffield, 2014.

[109] R. M. Saoubi, D. Axinte, S. Leung, C. Nobel, H. Attia, G. Kappmeyer, S. Engin, and W. Sim, “High performance cutting of advanced aerospace alloys and composite materials,” *CIRP Annals - Manufacturing Technology*, vol. 64, no. 2, pp. 557–580, 2015. [Online]. Available: http://dx.doi.org/10.1016/j.cirp.2015.05.002

[110] TMG Group, “Generic titanium machinability for all AMRC partners,” *ABG031*, no. 01, pp. 1–38, 2013.

[111] A. Mantle, D. Aspinwall, and O. Wollenhofer, “Twist drill of gamma titanium aluminade intermetallics,” in *Proc. 12th Conference of the Irish Manuf. Committee*, 1995.

[112] J. L. Cantero, M. M. Tardío, J. A. Canteli, M. Marcos, and M. H. Miguélez, “Dry drilling of alloy Ti-6Al-4V,” *International Journal of Machine Tools and Manufacture*, vol. 45, no. 11, pp. 1246–1255, 2005.

[113] R. M’saoubi, J. Outeiro, H. Chandrasekaran, O. Dillon Jr, and I. Jawahir, “A review of surface integrity in machining and its impact on functional performance and life of machined products,” *International Journal of Sustainable Manufacturing*, vol. 1, no. 1-2, pp. 203–236, 2008.

[114] T. Gao, Z. Sun, H. Xue, E. Bayraktar, Z. Qin, B. Li, and H. Zhang, “Effect of turning on the surface integrity and fatigue life of a TC11 alloy in very high cycle fatigue regime,” *Metals*, vol. 10, no. 11, pp. 1–15, 2020.

[115] K. Moussaoui, M. Mousseigne, J. Senatore, R. Chieragatti, and P. Lamesle, “Influence of milling on the fatigue lifetime of a Ti6Al4V titanium alloy,” *Metals*, vol. 5, no. 3, 2015.

[116] E. A. Rahim and S. Sharif, “Investigation on tool life and surface integrity when drilling Ti-6Al-4V and Ti-5Al-4V-Mo/Fe,” *JSME International Journal Series C Mechanical Systems, Machine Elements and Manufacturing*, vol. 49, no. 2, pp. 340–345, 2006.

[117] J. P. Velásquez, A. Tidu, B. Bolle, P. Chevrier, and J.-J. Fundenberger, “Sub-surface and surface analysis of high speed machined Ti–6Al–4V alloy,” *Materials Science and Engineering: A*, vol. 527, no. 10-11, pp. 2572–2578, 2010.

[118] M. Brown, D. Wright, R. M. Saoubi, J. Mcgourlay, M. Wallis, A. Mantle, P. Crawforth, and H. Ghadbeigi, "Destructive and non-destructive testing methods for characterization and detection of machining-induced white layer: a review paper," *CIRP Journal of Manufacturing Science and Technology*, vol. 23, pp. 39–53, 2018. [Online]. Available: https://doi.org/10.1016/j.cirpj.2018.10.001

[119] Y. B. Guo, A. W. Warren, and F. Hashimoto, "The basic relationships between residual stress, white layer, and fatigue life of hard turned and ground surfaces in rolling contact," *CIRP Journal of Manufacturing Science and Technology*, vol. 2, no. 2, pp. 129–134, 2010. [Online]. Available: http://dx.doi.org/10.1016/j.cirpj.2009.12.002

[120] C. Herbert, D. Axinte, M. Hardy, and P. Withers, "Influence of surface anomalies following hole making operations on the fatigue performance for a nickel-based superalloy," *Journal of Manufacturing Science and Engineering*, vol. 136, no. 5, 2014.

[121] I. Weiss and S. Semiatin, "Thermomechanical processing of beta titanium alloys—an overview," *Materials Science and Engineering: A*, vol. 243, no. 1-2, pp. 46–65, 1998.

[122] "CoroPlus ToolGuide: Find the right tool for your application." [Online]. Available: https://www.sandvik.coromant.com/en-gb/products/Pages/toolguide.aspx

[123] A. R. Prasad, K. Ramji, and G. Datta, "An experimental study of Wire EDM on Ti-6Al-4V alloy," *Procedia Materials Science*, vol. 5, pp. 2567–2576, 2014.

[124] "Secotom-10. Instruction Manual," Jun 2010, manual No.:15037001. [Online]. Available: https://docplayer.org/19254812-Secotom-10-instruction-manual-manual-no-15037001-date-of-release-0-2010.html

[125] "Corrozip data sheet," pp. 1–8, 2005. [Online]. Available: https://www.struers.com/-/media/Library/SDS/Australia/Cutting

[126] J. Gierak, "Focused ion beam technology and ultimate applications," *Semiconductor Science and Technology*, vol. 24, no. 4, 2009.

[127] A. Graves, S. Norgren, W. Wan, S. Singh, M. Kritikos, C. Xiao, P. Crawforth, and M. Jackson, "On the mechanism of crater wear in a high strength metastable beta titanium alloy," *Wear*, vol. 484–485, no. March, p. 203998, 2021. [Online]. Available: https://doi.org/10.1016/j.wear.2021.203998

[128] A. Graves, S. Norgren, P. Crawforth, and M. Jackson, "A novel method for investigating drilling machinability of titanium alloys using velocity force maps," *Advances in Industrial and Manufacturing Engineering*, vol. 2, no. September 2020, p. 100043, 2021. [Online]. Available: https://doi.org/10.1016/j.aime.2021.100043

[129] "Helicheck Pro - Macro and micro ranges - Key parameters," 2020, Walter Tools. [Online]. Available: https://www.walter-machines.com/en/tool-machining/detail-view/product/helicheck-pro/

[130] A. Graves, S. Norgren, P. Crawforth, and M. Jackson, "Surface roughness response to drilling of Ti-5Al-5Mo-5V-3Cr using Ti-Al-N coated and uncoated WC/Co tools," *Procedia CIRP*, vol. 87, pp. 170–175, 2020. [Online]. Available: https://doi.org/10.1016/j.procir.2020.02.112

[131] N. Dupin, "Personal communication - Provided a modified TCNI8 NI-Alloys database for the Al-Ti-Co system," 2020.

[132] M. Cotterell and G. Byrne, "Dynamics of chip formation during orthogonal cutting of titanium alloy Ti-6Al-4V," *CIRP Annals - Manufacturing Technology*, vol. 57, no. 1, pp. 93–96, 2008.

[133] A. Cox, "Understanding the effect of surface generation rates for finish milling of Ti-5Al-5Mo-5V-3Cr aero-structural components," Ph.D. dissertation, MSE, University of Sheffield, 2017.

[134] D. Ulutan and T. Ozel, "Machining induced surface integrity in titanium and nickel alloys: a review," *International Journal of Machine Tools and Manufacture*, vol. 51, no. 3, pp. 250–280, 2011. [Online]. Available: http://dx.doi.org/10.1016/j.ijmachtools.2010.11.003

[135] S. Sun, M. Brandt, and M. S. Dargusch, "Characteristics of cutting forces and chip formation in machining of titanium alloys," *International Journal of Machine Tools and Manufacture*, vol. 49, no. 7-8, pp. 561–568, 2009.

[136] A. Pramanik and G. Littlefair, "Machining of titanium alloy (Ti-6Al-4V) - theory to application," *Machining science and technology*, vol. 19, no. 1, pp. 1–49, 2015.

[137] A. K. Parida, "Simulation and experimental investigation of drilling of Ti-6Al-4V alloy," *International Journal of Lightweight Materials and Manufacture*, vol. 1, no. 3, pp. 197–205, 2018. [Online]. Available: https://doi.org/10.1016/j.ijlmm.2018.07.001

[138] A. Hosseini and H. A. Kishawy, "Cutting tool materials and tool wear," in *Machining of titanium alloys.* Springer, 2014, pp. 31–56.

[139] D. S. Fernández, B. Wynne, P. Crawforth, K. Fox, and M. Jackson, "The effect of forging texture and machining parameters on the fatigue performance of titanium alloy disc components," *International Journal of Fatigue*, vol. 142, p. 105949, 2021.

[140] C. F. Wyen, D. Jaeger, and K. Wegener, "Influence of cutting edge radius on surface integrity and burr formation in milling titanium," *International Journal of Advanced Manufacturing Technology*, vol. 67, no. 1-4, pp. 589–599, 2013.

[141] "NF, E 66-520-1," *Working zones of cutting tools: couple tool-material, general presentation, ISSN*, pp. 0335–3931, Sept 1997.

[142] P. Stief, J. Dantan, A. Etienne, and A. Siadat, “Mechanistic modelling of worn drill cutting forces with drill wear effect coefficients,” *Procedia CIRP*, vol. 82, pp. 2–7, 2019. [Online]. Available: https://doi.org/10.1016/j.procir.2019.04.332

[143] G. Zhao, Y. Su, and G. Zheng, “Tool tip cutting specific energy prediction model and the influence of machining parameters and tool wear in milling,” vol. 234, no. 10, pp. 1346–1354, 2020.

[144] S. Li, X. Qin, Y. Jin, D. Sun, and Y. Li, “A comparative study of hole-making performance by coated and uncoated WC/Co cutters in helical milling of Ti/CFRP stacks,” *The International Journal of Advanced Manufacturing Technology*, vol. 94, no. 5, pp. 2645–2658, 2018.

[145] J. Xu, K. Yamada, K. Sekiya, R. Tanaka, and Y. Yamane, “Evaluation of stability in drilling by measuring the dynamic components of the resultant force converted from thrust and torque,” in *Proceedings of JSPE Semestrial Meeting 2013 JSPE Spring Conference*. The Japan Society for Precision Engineering, 2013, pp. 187–188.

[146] J. N. Asante, “Analysis methods for machining fixtures with multiple point contacts,” Ph.D. dissertation, MAE, Syracuse University, 2008.

[147] E. O. Kirkendall and A. D. Smigelskas, “Zinc diffusion in alpha brass,” *Trans. AIME*, vol. 171, no. 1942, pp. 130–142, 1947.

[148] R. Lindvall, F. Lenrick, R. M’Saoubi, J. E. Ståhl, and V. Bushlya, “Performance and wear mechanisms of uncoated cemented carbide cutting tools in Ti6Al4V machining,” *Wear*, no. February, p. 203824, 2021. [Online]. Available: https://doi.org/10.1016/j.wear.2021.203824

[149] A. Henjered, M. Hellsing, H.-O. Andrén, and H. Nordén, “Quantitative microanalysis of carbide/carbide interfaces in wc–co-base cemented carbides,” *Materials Science and technology*, vol. 2, no. 8, pp. 847–855, 1986.

[150] G. Östberg, K. Buss, M. Christensen, S. Norgren, H. O. Andrén, D. Mari, G. Wahnström, and I. Reineck, “Mechanisms of plastic deformation of WC-Co and Ti(C, N)-WC-Co,” *International Journal of Refractory Metals and Hard Materials*, vol. 24, no. 1-2, pp. 135–144, 2006.

[151] S. Neumeier, H. U. Rehman, J. Neuner, C. H. Zenk, S. Michel, S. Schuwalow, J. Rogal, R. Drautz, and M. Göken, “Diffusion of solutes in fcc cobalt investigated by diffusion couples and first principles kinetic monte carlo,” *Acta Materialia*, vol. 106, pp. 304–312, 2016.

[152] E. J. Armarego and C. Y. Cheng, “Drilling with flat rake face and conventional twist drills-I. Theoretical investigation,” *International Journal of Machine Tool Design and Research*, vol. 12, no. 1, pp. 17–35, 1972.

[153] R. Hamade, C. Seif, and F. Ismail, “Extracting cutting force coefficients from drilling experiments,” *International Journal of Machine Tools and Manufacture*, vol. 46, no. 3-4, pp. 387–396, 2006.